Cover Page

Universiteit Leiden

Author: Qasim, D.
Title: Dark ice chemistry in interstellar clouds
Issue Date: 2020-06-30

Dark Ice Chemistry in Interstellar Clouds

Danna Qasim

Dark Ice Chemistry in Interstellar Clouds

Proefschrift

ter verkrijging van
de graad van doctor aan de Universiteit Leiden
op gezag van de Rector Magnificus Prof. mr. C. J. J. M. Stolker,
volgens besluit van het College voor Promoties
te verdedigen op dinsdag 30 juni 2020
klokke 13:45 uur

door

Danna Qasim
geboren te Kuwait City, Kuwait
in 1989

Promotiecommissie

Promotores	Prof. dr. H. V. J. Linnartz
	Prof. dr. E. F. van Dishoeck
Co-promotor	Dr. G. Fedoseev
Overige leden	Prof. dr. H. J. A. Röttgering
	Prof. dr. P. P. van der Werf
	Prof. dr. M. K. McClure
	Prof. dr. L. Hornekær Aarhus University
	Prof. dr. M. R. S. McCoustra Heriot-Watt University

To those that have helped and continue to pave the way
to allow anyone
the opportunity to have a role in science.

Contents

Cover Page

Universiteit Leiden

Author: Qasim, D.
Title: Dark ice chemistry in interstellar clouds
Issue Date: 2020-06-30

Introduction

1.1 The star formation cycle

Our Sun and the planets surrounding it are part of a stellar formation cycle. This cycle starts with the gravitational collapse of a large interstellar cloud and ends after a number of different phases, when the Sun implodes and returns much of its material into the interstellar medium (ISM). Astrochemistry is the research discipline that aims to characterize the involved materials and processes, and to understand how these depend on the many physical and chemical conditions. Much effort has been put into constraining the details of each stage over the years. From an astrochemical perspective, some outstanding questions remain, such as what materials are inherited at each stage of the cycle, and which materials become important to the origin of life on Earth and possibly elsewhere. Therefore, this introduction will outline the current star formation cycle, with added attention to the gas and ice chemistry that is relevant to this thesis research.

Figure 1.1 shows a general schematic of Sun-like star formation. As this thesis focuses on the ISM, an outline of the physical conditions for stages a and b of Figure 1.1 is shown in Table 1.1. At the earliest stage exists the diffuse ISM. This medium consists primarily of atoms, molecules, and ions and is largely ultraviolet (UV)-dominated. It also has very low visual extinction (A_V), meaning that the dust and gas densities and columns are low. Here, A_V is best described in relation to the neutral hydrogen atom column: $N_H = 3.08 \times 10^{22} \times A_K$ (Boogert et al. 2013), where $A_V = 8 \times A_K$ (Cardelli et al. 1989). At low densities without sufficient collisions of gas with dust, gas-phase species cannot accumulate to form ices, and thus this medium is driven primarily by gas-phase rather than solid-state chemistry. Even if some ice were to form on the dust grain during this phase, this growth would be hindered by processes such as photodesorption (Watson & Salpeter 1972), which is a process that causes the desorption of species by impacting photons. As the densities increase, a cloud starts to take form. At the edge of the cloud (i.e., the translucent phase), a photon dominated region (PDR) exists that can contain H-, C-, and/or O-bearing simple and complex molecules. Hydrogenation of O, C, and N lead to the formation of simple hydrides, such as H_2O, CH_4, and NH_3, respectively (van de Hulst 1946). More complex species, such as HCOOH, CH_3CCH, and CH_3CHO, have been observed (Guzmán et al. 2014; Öberg 2016). Traveling deeper into the cloud, the densities increase, resulting in dense clouds (10^2 - 10^4 H_2 molecules cm^{-3})

and cores (10^4 - 10^5 H_2 molecules cm^{-3}). Note that although cores always have high density and high visual extinction, this is not always the case for dense clouds. For background star observations (as will be discussed in section 1.2.3), a sight-line with a high A_V may either have a high density or a low density with a long pathlength. This density increase has a substantial influence on the chemistry that occurs. UV-photons become largely blocked from penetrating the cloud/core, and in combination with the fact that the cooling rates by molecular emission peak, the cloud/core temperature drops to ∼10 K. This results in a rich ice chemistry, as the sticking coefficient for all species on micrometer-sized dust grains is unity except for the most volatile atoms and molecules, such as H and H_2. Besides chemical reactions on icy dust surfaces, also gas-phase ion-molecule reactions occur (Agúndez & Wakelam 2013). As the observed abundances in the gas phase sometimes cannot be explained by gas-phase mechanisms alone, such as the case for CH_3OH (Garrod et al. 2006; Geppert et al. 2006), it is generally accepted that solid-state reactions are the dominant process. As will be discussed in greater detail in the next section, it is thought that complex organic molecules (COMs; ⩾ 6 atoms and are C and H bearing) primarily originate from this phase in the solid-state. Much is still unclear, however, about the links between solid-state and gas-phase processes.
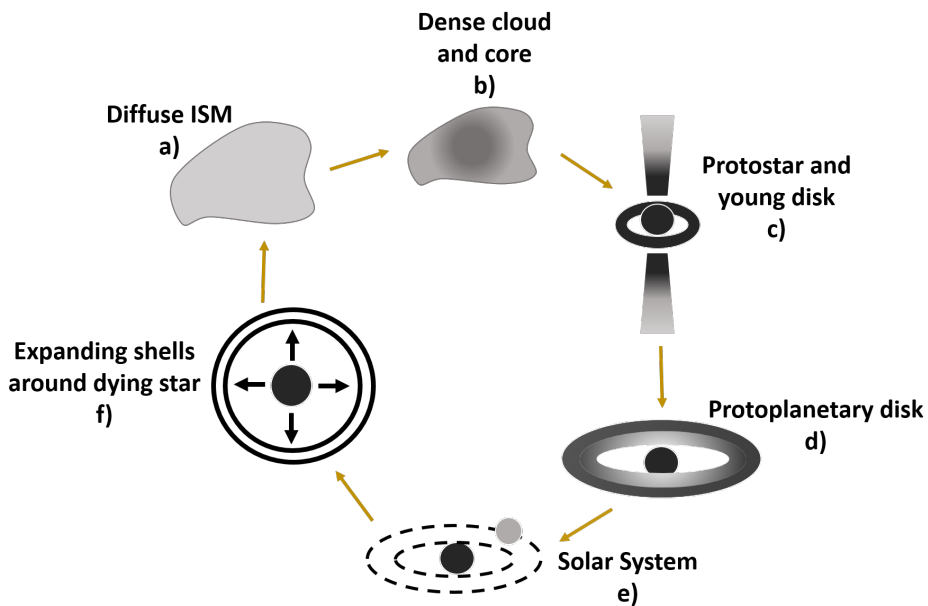
Figure 1.1: The main stages of star formation of a Sun-like star. Adapted from Öberg (2016).

As the dense core increases in mass, its outward pressure becomes less than its inward pressure, and the core eventually collapses under its own gravity (Ward-Thompson 2002). This collapse triggers an increase in the temperature, and at increasing temperatures and densities, a protostar is created, in which it gets most of its luminosity from accretion. Conservation of angular momentum results in an increase in rotation and a decrease in the moment of inertia,

Table 1.1: Physical parameters of the different regions of interstellar clouds, as noted in Table II of van Dishoeck et al. (1993). (a) Dust temperatures are much lower for all noted regions. (b) "Cloud" and "core" are used interchangeably when describing the astrophysical conditions simulated in the experiments presented in this thesis.

ISM region	Density (cm^{-3})	Gas temperature[a] (K)	A_V (mag)
Diffuse molecular	100-800	30-80	$\lesssim 1$
Translucent	500-5000	15-50	1-5
Dense cloud[b]	10^2 - 10^4	$\gtrsim 10$	$\gtrsim 2$
Cold, dark core[b]	10^4 - 10^5	≈ 10	5-25

leading to the formation of a disk and/or outflows (Shu et al. 1987). The starting disk eventually grows in size to form a protoplanetary disk. Observations show that these disks contain organic molecules (Dutrey et al. 1997; Thi et al. 2004; Öberg et al. 2015; Favre et al. 2018; van´t Hoff et al. 2018), although it becomes difficult to probe the less abundant, more complex species (formed in the solid-state), as the spatial scale of disks is relatively small (van´t Hoff et al. 2018). Yet, at early stages, disks are much warmer, and their rich chemical inventory is readily revealed (Jørgensen et al. 2016).

Understanding how the properties of protoplanetary disks link to planet formation is currently (2020) an active field of research. It is theorized that "snow lines", which are regions far enough from the star to allow the freeze-out of gas-phase species (Kennedy & Kenyon 2008), are important to the formation of planets around the new born star. This also applies to our own Solar System. As life exists in our Solar System, detailed knowledge of the many different processes taking place at different locations in a protoplanetary disk, such as better understanding of the role of snow lines in the chemical composition of a disk and in the planet formation process itself, may ultimately show how the building blocks of life arrived on Earth. For example through impacting comets, which are small icy bodies and remnants of the protoplanetary material that carry the chemical memory of the processes in diffuse and dense clouds (Chyba & Sagan 1997; Altwegg et al. 2019). Over time, the star will grow out of the main sequence phase as it becomes depleted of hydrogen, essentially burning up its surroundings. After a number of events involving drastic temperature and pressure changes, for Sun-like stars, its outer layers enhanced in heavy elements will eventually be ejected (Guidry 2019), providing material for the cycle to start over again.

1.2 Translucent, dense cloud, and dark core stages

The dense cloud and dark core stages of the star formation cycle and the preceding translucent stage are what this thesis work is based upon. The studies

presented in the next chapters focus on this step in the cosmochemical evolution, largely through dedicated laboratory experiments and extended with astronomical surveys. The most up-to-date astrochemical constraints of this stage that are relevant to this thesis are discussed in the following subsections.

1.2.1 Observationally constrained ice phases

As mentioned in section 1.1, the formation of the dense molecular cloud in the star formation cycle results in a rich ice chemistry, as temperatures drop, causing gas-phase species except H and H_2 to accrete onto dust grains. These icy dust grains are excellent hosts for chemical reactions to take place, as the surface itself provides a platform for species to congregate, as well as absorbs excess energy from highly exothermic reactions that may cause product dissociation. Astronomical observations show that the ices on grain mantles in interstellar clouds are initially formed in chemical layers, and this layering process is strongly dependent on the dust extinction, or cloud depth (see Boogert et al. (2015) and references therein). A visualization of the first ice phases is shown in Figure 1.2. At a visual extinction (A_v) of 1.6 mag, H_2O ice starts to grow by H- and O-atom accretion (Whittet et al. 2001; Ioppolo et al. 2008, 2010; Cuppen et al. 2010), and is the most abundant ice to be detected, with a typical column density of $\sim 10^{18}$ cm^{-2} (see for example, Boogert et al. (2011)). At this point, photodesorption becomes less likely, which allows species that hit the dust to increasingly stay on the dust surface. Other atoms also accrete, such as C and N, and can be hydrogenated to form CH_4 (Qasim et al. 2020) and NH_3 (Fedoseev et al. 2014), respectively. CO_2 is also found in this ice phase, and is likely formed starting from the reaction between CO and OH species (Ioppolo et al. 2011; Garrod & Pauly 2011; Arasa et al. 2013). It has a typical column density of $\sim 10^{17}$ cm^{-2} (see for example, Boogert et al. (2011)). As the density is around 10^3 cm^{-3} in this phase, mostly atomic species are available with some CO.

At $A_v > 3$, the molecular H_2 density increases to $\sim 10^4$ cm^{-3}, resulting in a "heavy" CO freeze-out, in which < 50% of the CO freezes out onto icy grain mantles (Chiar et al. 1995). This causes an apolar layer to form on top of the previously formed polar layer. Due to the increase in the density, more diatomics, such as N_2 and O_2, should become available. At $A_v > 9$, the density reaches $\sim 10^5$ cm^{-3}, resulting in a "catastrophic" CO freeze-out (Jørgensen et al. 2005; Pontoppidan 2006). This CO-rich ice is hydrogenated and is collectively found to be the dominating pathway to CH_3OH formation in interstellar molecular clouds (Watanabe & Kouchi 2002; Fuchs et al. 2009; Cuppen et al. 2009; Boogert et al. 2011; Wirström et al. 2011). It is noted, however, that the CH_3OH ice formation threshold still needs further constraints. Additionally, CH_3OH is not always detected at $A_v > 9$, thus Figure 1.2 does not represent all interstellar cloud environments. More details about this phenomenon can be found in Qasim et al. (in preparation; Chapter 5).
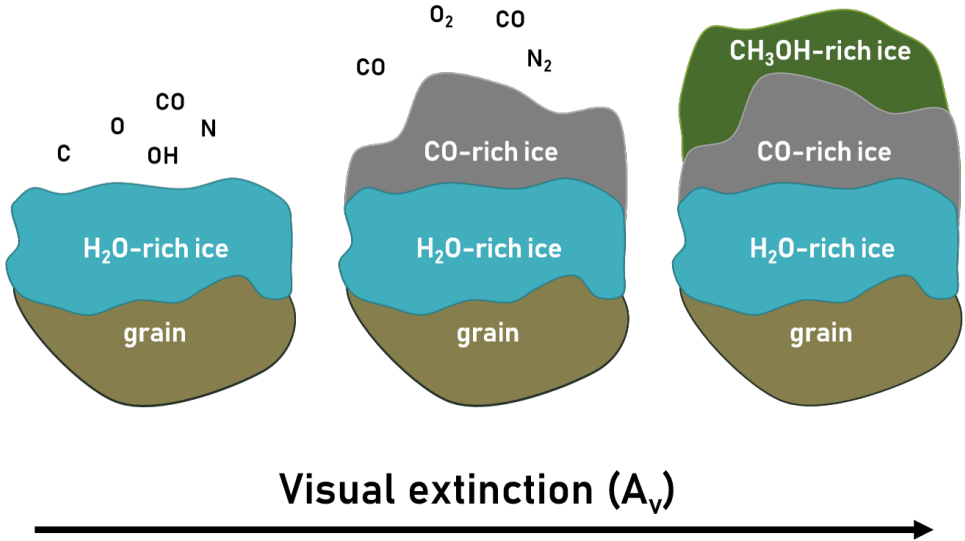
Figure 1.2: The first ice phases, largely as a function of the visual extinction (A_v), as constrained by observations. Gas-phase species relevant to the ice chemistry are noted with black font. Adapted from Boogert et al. (2015).

1.2.2 Non-energetic and energetic ice chemistry

The formation and destruction of molecules in the solid-state in interstellar clouds are largely governed by two processes: 'energetic' and 'non-energetic'. In this specific context, a 'non-energetic' process refers to "a radical-induced process without the involvement of UV, cosmic rays, and/or other 'energetic' particles" (Qasim et al. 2019d). This is also known as 'dark' chemistry. The emphasis on the process being radical-induced is due to the fact that at the low temperatures of ~10 K, radicals are essential for 'dark' ice chemistry to occur. The relevance of the 'non-energetic' process in dense clouds and dark cores is due to the phenomenon in which certain energy sources, such as external UV-photons, become increasingly blocked by the shroud of dust and gas. Note, however, that the atoms used for 'non-energetic' ice chemistry are largely generated from the gas-phase through 'energetic' processes. For example, cosmic-rays can still penetrate dense regions, which dissociate H_2 gas to H-atoms needed for 'non-energetic' solid-state chemistry. Cosmic-rays also cause the production of at least electrons and UV-photons (Herbst & van Dishoeck 2009), which then contribute to 'energetic' processing. A number of laboratory efforts has demonstrated that 'energetic' processing of ices can lead to the formation from simple molecules to biologically relevant species (Allamandola et al. 1988; Caro et al. 2002; Bernstein et al. 2002; Öberg et al. 2009; Materese et al. 2017; Ligterink et al. 2018).

The formation of simple molecules, such as H_2O, NH_3, and CH_4, is primarily due to 'non-energetic' processes, when atomic H, O, N, and C simultaneously accrete (Linnartz et al. 2015). Additionally, the only detected solid-state COM, CH_3OH, is predominantly formed by 'non-energetic' processing (see section 1.2.1). Recent laboratory experiments have shown that UV-irradiation of a

CO:H_2 ice mixture does lead to the simple radical, HCO (Chuang et al. 2018a). UV-irradiation of molecules, such as CH_3OH, also leads to the formation of simple radicals, which can recombine to form rather complex species (Öberg et al. 2009). COMs have been shown to be effectively produced by both, 'energetic' and 'non-energetic' processes (Chuang et al. 2017). When the two processes are combined, radicals that are formed from photolysis become hydrogenated, leading to the formation of simple species in addition to COMs (Chuang et al. 2017). Such COMs include methyl formate, glycolaldehyde, and ethylene glycol – all of which have been detected in observational surveys (Jørgensen et al. 2012).

There are mainly three reaction mechanisms that are considered to take place in interstellar ices: Langmuir-Hinshelwood (L-H), Eley-Rideal (E-R), and Kasemo-Harris (K-H) (Kolasinski 2012). If the reactant species are thermalized with the surface prior to reaction, then the reaction follows an L-H mechanism. If one reactant is thermally equilibrated with the surface and the other is a gas-phase species, then the reaction follows an E-R mechanism. Finally, if one reactant is thermally equilibrated with the surface and the other reactant is on the surface but not fully equilibrated, then the mechanism for reaction is K-H. In this thesis, it is found that the L-H mechanism dominates many of the reactions, as it is found that our H-atoms equilibrate to the temperature of the surface before a reaction is attempted.

As the experiments presented in this thesis typically take place at 10 K and involve atomic hydrogen, it is no surprise that tunneling is an influential aspect for these reactions to proceed. As temperatures drop, the rate constant becomes increasingly dependent on tunneling (Meisner & Kästner 2016). Tunneling is the phenomenon in which a particle has a statistical chance larger than zero to cross an energy barrier. The longer the wavelength of the particle, the more likely it will be able to cross the barrier. From the de Broglie relation, species with the smallest mass will have the greatest wavelength, and this wavelength increases as the temperature decreases (Hama & Watanabe 2013). Thus, at low temperatures of 10 K, atomic hydrogen is the most likely atom to tunnel through a barrier, simply from this perspective. This is observed through a number of reactions studied in this thesis, such as CO + H and C_2H_2 + H, which have barriers that are difficult to cross over at 10 K.

1.2.3 Ice detections

The most abundant ice to be detected in the ISM is H_2O, followed by CO_2, CO, CH_3OH, NH_3, and CH_4 (Öberg et al. 2011). Their relative median ice abundances towards low-mass young stellar objects (LYSOs) are shown in Figure 1.3. There are several ways in which ices are observed. In one case, the star acts as a light source while being remote from the cloud/core. In the observer's line of sight, this star is behind the cloud/core, making it a "background" or "field" star. This kind of observation is used to trace pristine ices, since the star does not process the dust grain or ice. However, dark cores can also contain protostars.

Other ways to observe ice features in the infrared are by exploiting embedded protostars (YSOs embedded in the molecular cloud) and OH-IR stars (stars that are bright in the infrared and exhibit strong OH maser emission), as discussed
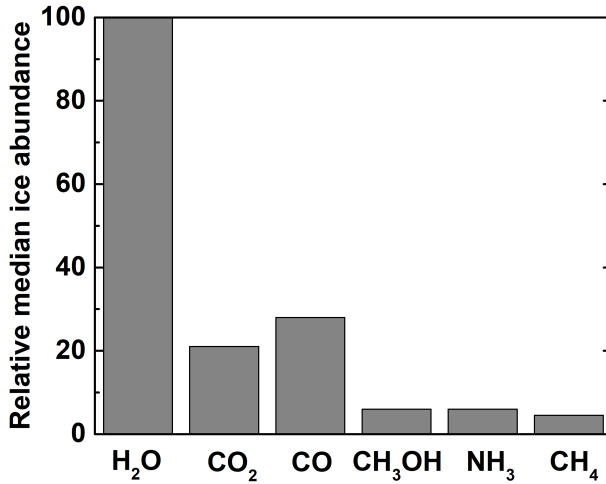
Figure 1.3: Relative median ice abundances of the six most abundant ices detected towards low-mass young stellar objects. Values obtained from Boogert et al. (2015).

in Millar & Williams (1993) and summarized here. Protostars are advantageous in that they are luminous and therefore a good S/N can be achieved, in comparison to background stars, in which their light is more attenuated by the cloud. However with increasing wavelength, the flux decreases, and additionally, the star itself may process the ice. OH-IR stars are unique in that carbon-poor ices can be studied. Their envelopes are oxygen rich, with an elemental C/O < 1. Thus, most of the C is locked-up in CO, as also found in dense clouds and dark cores. Due to the warm temperatures, sticking of CO onto dust grains is inhibited, allowing for ice formation without an abundance of carbon.

In addition to the aforementioned ices, there are also likely identified species (one absorption feature probed and matches laboratory spectra) and possibly identified species (one absorption feature probed and match to laboratory spectra not found; see Boogert et al. (2015) and references therein). These include H_2CO, OCN^-, and OCS (likely identified), as well as HCOOH, CH_3CH_2OH, $HCOO^-$, CH_3CHO, NH_4^+, SO_2, and polycyclic aromatic hydrocarbons (PAH) (possibly identified). Ironically, although there are strong arguments for effective COM formation in the solid-state in dense clouds and dark cores (as discussed in section 1.2.5), CH_3OH is the only COM that has been securely identified directly in the ice. This is, in part, substantially due to the lack of sensitivity provided by previous and current observational facilities, as well as the inherent problem of indistinguishable features in solid-state infrared spectra (Terwisscha van Scheltinga et al. 2018). As will be discussed in the next section, many more COMs have been detected in the gas-phase, in part because gas-phase spectra intrinsically have more resolved features. Additionally, gas-phase spectroscopy can be used to constrain the formation history of detected COMs (i.e., whether they are formed in the solid-state, gas-phase, or

both). For example, Soma et al. (2018) exploit the line profiles of several COMs and compare them to species that are known to be formed in the solid-state (e.g., CH_3OH) and gas-phase (e.g., carbon chain molecules). The line shape is influenced by the distribution of the species (e.g., a narrower line width may mean a more compact distribution). Thus if the spectral line shapes are similar, it means that the species spatially co-exist, and are thought to be formed along a similar formation route (i.e., in the solid-phase or gas-phase or even both). Other example efforts to explain the formation history of COMs through the analysis of gas-phase chemistry are demonstrated in Balucani et al. (2015), Jiménez-Serra et al. (2016), and Lee et al. (2019).

1.2.4 Gas-phase detections

As shown in Table 1.2, there are many more gas-phase than solid-state detections of COMs in dense clouds and dark cores. However, as discussed by Bacmann et al. (2019), there are still limitations to gas-phase observations of COMs in dense clouds and dark cores. Like in solid-state observations, high sensitivity and lengthy integration times are needed, partially because the low temperatures trap a number of COMs in the solid-state. Regardless, more than a handful of COMs has been detected in these environments.

1.2.5 Likelihood of icy complex organic molecules (COMs)

Astrochemical models have shown that gas-phase chemistry alone cannot reproduce the observational abundances of a number of COMs (Herbst & Leung 1989; Millar et al. 1991; Charnley et al. 1992, 1995; Garrod et al. 2006). Thus, the (partial) formation of (certain) COMs in interstellar ices is likely. Solid-state laboratory experiments have pioneered the effort to uncover which COMs can be created in the solid-state under relevant translucent and dark cloud conditions. This is because within the astrochemical 'triangle' that consists of observations, models, and laboratory, specifically experimental laboratory has the advantage to confirm under what conditions species are formed, which is the first piece of information needed to know if such COMs can exist in interstellar ices (as direct ice observations are not currently available).

In the Laboratory for Astrophysics at Leiden Observatory, much dedication has been put into the study of COMs under translucent and dense cloud/dark core conditions, and has further strengthened the argument of COM formation in ices of such interstellar clouds. To do this, an ultrahigh vacuum (UHV) apparatus, SURFace REaction SImulation DEvice (SURFRESIDE), is exploited. This setup allows to somewhat simulate the accretion of atoms, molecules, and molecular fragments in interstellar clouds. Notably, three atomic beamlines are attached to the main vacuum chamber and can collectively produce H-, C-, N-, and O-atoms. These atoms are directed towards a substrate that is typically cooled to 10 K, which is a representative temperature of dust grains in such environments. To our knowledge, this is the only cryogenic UHV apparatus that contains three different atomic beamlines, making it one of the most advanced systems to study the initial formation of interstellar ices. The analytical techniques used to study the ice, reflection-absorption infrared spectroscopy

Table 1.2: A list of COMs that have been detected in the gas-phase in dense clouds and/or dark cores. The reference column lists references in which the detection of the species was first reported. The list of species is predominantly acquired from the census by McGuire et al. (2018).

Species	Cloud/Core	Reference
HC_5N	TMC-1	Kroto et al. (1977)
HC_7N	TMC-1	Kroto et al. (1977)
HC_9N	TMC-1	Broten et al. (1978)
CH_3CCH	TMC-1	Irvine et al. (1981)
CH_3C_4H	TMC-1	Walmsley et al. (1984)
CH_3C_3N	TMC-1	Broten et al. (1984)
CH_3CHO	TMC-1 and L134N	Matthews et al. (1985)
C_6H	TMC-1	Suzuki et al. (1986)
CH_3OH	TMC1, L134N, and B335	Friberg et al. (1988)
HC_2CHO	TMC-1	Irvine et al. (1988)
HC_3NH^+	TMC-1	Kawaguchi et al. (1994)
H_2C_6	TMC-1	Langer et al. (1997)
CH_2CCHCN	TMC-1	Lovas et al. (2006)
CH_3C_5N	TMC-1	Snyder et al. (2006)
CH_3C_6H	TMC-1	Remijan et al. (2006)
C_6H^-	TMC-1	McCarthy et al. (2006)
C_8H^-	TMC-1	Brünken et al. (2007)
CH_2CHCH_3	TMC-1	Marcelino et al. (2007)
$HCOOCH_3$	L1689B	Bacmann et al. (2012)
CH_3OCH_3	L1689B	Bacmann et al. (2012)
HC_5O	TMC-1	McGuire et al. (2017)
HC_7O	TMC-1	McGuire et al. (2017)
C_6H_5CN	TMC-1	McGuire et al. (2018)
$c\text{-}C_2H_4O$	L1689B	Bacmann et al. (2019)

(RAIRS) and temperature programmed desorption (TPD), are however typical within the fields of astrochemistry and surface science.

An intensive study on CH_3OH formation, with CH_3OH being the simplest COM, within the CO + H reaction pathway was performed by Fuchs et al. (2009), and first demonstrated by Watanabe & Kouchi (2002). This pathway, which becomes relevant in the CO freeze-out stage (see section 1.2.1), has also been shown to be promising for the formation of larger COMs. The study by Fedoseev et al. (2015) showed that the simultaneous deposition of CO and H can also lead to the formation of glycolaldehyde and ethylene glycol, and has the potential to form ribose, which is an essential component of ribonucleic acid. Adding H_2CO to the mixture, which is a CO hydrogenation product, results in the additional formation of methyl formate (Chuang et al. 2016). Starting from glycolaldehyde, glycerol and glyceraldehyde can be formed (Fedoseev et al. 2017).

The reaction of C_2H_2 + CO + H was investigated in the work by Qasim et al. (2019a), as C_2H_2 can be hydrogenated to form C_2H_x radicals, which can react to form a unique set of COMs. The C_2H_2 + CO + H reaction network derived from the experimental work of Qasim et al. (2019a) is shown in Figure 1.4. Within the orange square-dotted circle are the radicals and their recombination products in the CO + H reaction network, as constrained from the laboratory experiments by Chuang et al. (2016). In Qasim et al. (2019a), C_2H_2 and its hydrogenated counterparts were added to the network. The saturated radicals (C_2H_3 and C_2H_5) can react with HCO from the CO + H network to form aldehydes (propanal and propenal) and an alcohol (propanol).
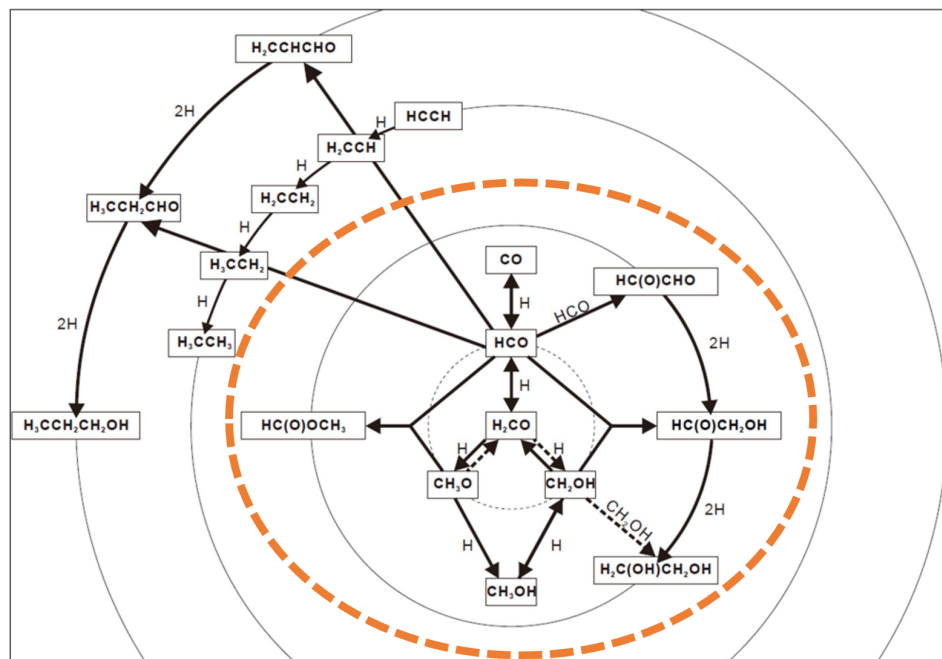
Figure 1.4: The C_2H_2 + CO + H reaction network found in the experimental work by Qasim et al. (2019a). Figure taken from Qasim et al. (2019b), and originally adapted from Chuang et al. (2016).

COM formation starting from the OH radical has also been shown to be favorable. A number of alcohols, such as n- and i-propanol and n- and i-propenol, can be formed starting from the low energy barrier reaction of C_3H_4 and OH (Qasim et al. 2019c). Substituting C_3H_4 with C_2H_2 results in the products, acetaldehyde, vinyl alcohol, ketene, and ethanol (Chuang et al. 2020). As discussed in section 1.2.4, COMs have been detected in the gas-phase, that however are (partially) formed in the solid-state. How COMs, like the ones proposed here, can be released into the gas-phase in a non-thermal way is still an active research topic (Vasyunin & Herbst 2013; Bertin et al. 2016; Chuang et al. 2018b; Dartois et al. 2019).

1.2.6 Role of the James Webb Space Telescope for COMs

The James Webb Space Telescope (JWST), with a current expected launch date of March 2021, will be able to detect solid-state COMs that are more complex than CH_3OH in dense clouds and dark cores – a feat that does not apply to current and previous observational facilities. Ice investigations of COMs in the Laboratory for Astrophysics and in other groups will be combined with chemical models and JWST observations of icy COMs to understand COM formation in various interstellar environments. Some of the advantages of using JWST to detect solid-state COMs in dark interstellar environments, as proposed in the MIRI Consortium and McClure et al. (2017), are briefly summarized below.

Space-based observatories have the advantage of complete wavelength coverage due to the absence of Earth's telluric contamination. However, previous space-based observatories, such as Spitzer and the Infrared Space Observatory (ISO), probed ices with low spectral resolution (Spitzer: R ~ 60-120) or low sensitivity (ISO). An example of blended ice features from Spitzer is shown in Figure 1.5.

Using JWST's NIRCam Wide Field Slitless Spectroscopy (WFSS) mode, a spectral resolution of ~1500 in the 2.5-5.0 μm region will be possible, which will allow separation of the broad infrared ice bands into distinct signatures (McClure et al. 2017). A S/N of 100 will be required to detect COMs at ~3.6 μm that are 3% of the continuum. For the 5-8 μm region, the MIRI medium-resolution spectrometer (MRS) will be used, which has R ~ 3000, to distinguish between less abundant COM species (McClure et al. 2017). A S/N of 300 will be needed, as the laboratory data predict COM features at only 1% of the continuum in this region. An additional advantage for ice observations with JWST is that an ice map with over 100 background stars can be covered at A_V ~ 5-100 mags (McClure et al. 2017). To compare, the largest ice map created included only ten lines of sight (Pontoppidan et al. 2004). Such a map will not only expand the collection of sources with ice detections, but will also allow direct comparison of the ice composition and morphology from the edge of the cloud to its densest regions. The JWST Guaranteed Time Observations program, MIRI EC Protostars Survey (van Dishoeck et al. 2017), will provide complementary results to understanding the ice as well as gas-phase chemistry, particularly towards protostars.
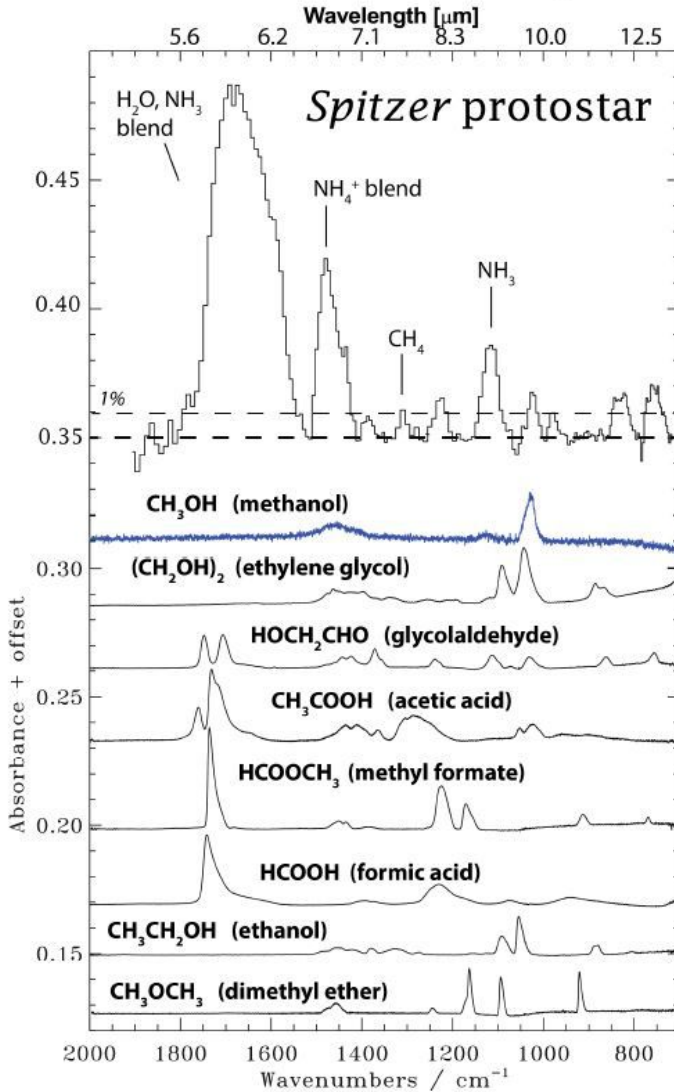
Figure 1.5: (Top) Spitzer ice spectrum taken towards RNO 90 (inverted, continuum and silicate subtracted), in which COMs are 1% of the continuum, requiring a S/N of 300 for detection. Beneath the Spitzer ice spectrum are laboratory solid-state infrared spectra of COMs. Unlike Spitzer, JWST will be able to spectrally resolve the infrared bands of COMs, although they still will be blended. Figure taken from McClure et al. (2017).

1.2.7 This thesis

In this era of astrochemistry, technological advances now allow us to delineate the physical and chemical properties of protoplanetary disks, which provide more clues as to how disks connect to planetary systems. But to fully understand how the disk came to be, knowledge of its birth place – the molecular cloud – is required. To date, there are still gaps in knowledge about the physics and chemistry of molecular clouds, and how the cloud transforms into a disk.

The aim of this thesis is to address the 'dark', or 'non-energetic', *ice* chemistry in molecular clouds/cores that is not thoroughly understood or even realized. The time frame that 'dark' ice chemistry peaks is thought to be the starting point at which a number of simple molecules and COMs are formed, typically on icy grain surfaces. Thus, the species formed in this phase are the starting ingredients to chemical evolution, from the clouds to nascent planets. Having a complete understanding of the initial ice chemistry will shed light to the chemistry in the next stages of stellar evolution.

To investigate such ices, laboratory simulations of realistic interstellar ice analogues are performed with SURFRESIDE^3 in the Leiden Laboratory for Astrophysics. To complement the laboratory work, astronomical observations are presented, along with quantum calculations to grasp the formation mechanism(s), relative abundances, and astrochemical relevance of each molecule studied. CH_4, which is the simplest molecule to be investigated, is observationally constrained to be formed from the sequential hydrogenation of solid C in the polar ice phase. It is experimentally shown that this is possible, which further validates the conclusions from observational surveys. This CH_4 can be a precursor to CH_3OH formation, as shown in a dedicated laboratory paper on the reaction of CH_4 and OH. In turn, the findings from the laboratory paper are supported by a follow-up observational study of CH_3OH ice towards numerous background stars. Other simple molecules, such as HCOOH and CO_2, are currently constrained to be formed largely from CO ice. Taking into consideration the abstraction of atoms, it is shown that reactions involving H_2CO can also contribute to the solid-state inventory of HCOOH and CO_2. The formation of COMs, which is thought to occur once CO freezes out, is now experimentally constrained to take place also when H_2O ice is formed – a time period earlier than expected. Alcohols and aldehydes are demonstrated to be possible ice constituents existing on top of carbonaceous grains. A larger variety of COMs, also to be formed in the H_2O-rich ice phase, is proposed in this thesis. Future work will involve COM formation in H_2O-rich ices starting from atomic C, a missing reaction channel in astrochemical models due to the lack of experimental studies. A summary of the aforementioned investigations divided into chapters is provided below.

Chapter 2 details the experimental apparatus, SURFRESIDE^3, that is used in this thesis to study the 'non-energetic' formation of simple and complex organic molecules in interstellar clouds/cores. A background on the fundamentals of the experimental techniques, RAIRS and TPD, is provided, and how they are used in practice in SURFRESIDE^3 is discussed. The transition from SURFRESIDE^2 to SURFRESIDE^3, which mainly involves the addition of an atomic carbon source, is explicitly described. A separate vacuum apparatus is built to test and perform initial calibrations of the atomic carbon source. This

includes constraining the atomic carbon beam size to fit within the area of the substrate, and providing proof-of-concept experiments such as C + $^{18}O_2$, which shows the formation of $C^{18}O$ and $C^{18}O_2$. With the C-atom source integrated into SURFRESIDE, atomic C fluxes of low 10^{11} - high 10^{12} cm^{-2} s^{-1} are measured, which are values high enough to probe C-atom induced chemistry in SURFRESIDE[3]. These values are also complementary to the H-atom flux measured in SURFRESIDE[3], which should be higher than the C-atom flux in experiments in order to mimic the overabundance of H-atoms in comparison to C-atoms in interstellar clouds. SURFRESIDE[3] is the first experimental apparatus designed to study the formation of COMs starting from C-atoms in realistic interstellar ice analogues. Such COMs are expected to be most prevalent in the translucent phase (H_2O-rich ice phase) of interstellar clouds.

Chapter 3 presents the first experimental study under controlled laboratory conditions of CH_4 formation in the way that it is observationally constrained to be formed: from the sequential hydrogenation of C in a H_2O-rich ice at low temperatures (~10 K). Not only is it proven that CH_4 can be formed in this way, but it is also shown that the formation rate is about twice as high compared to an experiment without water (5.6×10^{11} versus 3.5×10^{11} molecules cm^{-2} s^{-1}), which should be taken account into astrochemical models. The presence of water increases the residence time of hydrogen in the ice, thus increases the probability of hydrogen to react with carbon. The competing H-abstraction reactions by H-atoms are relatively ineffective compared to H-addition reactions under the presented experimental conditions, and are not expected to be effective on interstellar icy grains once CH_3 is formed in the reaction chain, thus providing a more secure route to CH_4 ice formation in the ISM. As CH_4 is best observed with space-based observatories, this study becomes timely with the anticipated launch of the JWST, which will have a sensitivity high enough to directly probe CH_4 in the H_2O-rich ices of quiescent clouds.

Chapter 4 investigates another pathway to form CH_3OH ice in interstellar clouds. This pathway starts from CH_4, which subsequently puts new constraints on the CH_3OH ice formation threshold. Although H-abstraction from CH_4 using H-atoms is ineffective under cold interstellar cloud conditions, such an abstraction becomes more promising when OH-radicals are used, which results in the presence of CH_3 radicals that can react with OH to form CH_3OH. It is shown that this process works at 10 K, and is 20 times less efficient than the sequential hydrogenation of CO to form CH_3OH, which is the dominant pathway to CH_3OH formation in interstellar clouds. This has two main consequences: 1) Since CH_4 ice is present before CO freezes out, this indicates that the CH_3OH ice formation threshold should be below the CO freeze-out point. 2) The relative inefficiency of the CH_4 + OH route to form CH_3OH may partially explain the low CH_3OH upper limits found in observational surveys of background stars.

Chapter 5 is a follow-up study on Chapter 4 from an observational perspective. To investigate whether CH_3OH ice is initially formed when CH_4 ice is formed, a sample of 41 stars behind quiescent interstellar clouds/cores are observed at A_V = 5.1 - 46.0 mags. To increase the sensitivity of the CH_3OH ice feature at 3.537 μm, a method to reduce photospheric lines, and thus lower the upper limits, is demonstrated. As the JWST will also suffer from photospheric line contamination, this method can also be applied to future JWST

observations as well as to previously collected data. 1 new CH_3OH ice detection is reported, which brings the total to 8 detections in quiescent environments. With this new detection, an updated CH_3OH formation threshold of A_V = 6.8 ± 3.9 mag is measured, which shows that more detections are still needed to confirm the threshold, as the value is only 1.7σ. As only upper limits are measured below A_V = 6.8 mag, this indicates that CH_3OH is still constrained to be formed after CH_4 ice is formed. However, due to the large variations between upper limits and detections at high A_V, the possibility that less efficient, alternative pathways to CH_3OH formation, such as the CH_4 + OH route, is still open.

Chapter 6 demonstrates through experimental investigations coupled with computational calculations from the literature that HCOOH and CO_2 ices are formed in the CO-rich ice phase, in addition to the H_2O-rich ice phase. It is found that both, HCOOH and CO_2 can be formed starting from H_2CO, which is a product of the CO hydrogenation pathway. Starting from H_2CO, HCOOH is formed from two formation routes: H + HOCO and HCO + OH. CO_2 is predominantly formed from H + HOCO. It is suggested from the presented results that observational surveys targeting HCOOH ice, which has not been positively identified thus far, should probe within a certain A_V range that is past the H_2O-rich ice phase and before CH_3OH ice is sufficiently formed. This is because the overall abundance of HCOOH (and therefore the S/N) should be higher when probing deeper into the cloud/core, however probing too far may result in spectral signatures of CH_3OH that may potentially overlap with those of HCOOH.

Chapter 7 presents a study on the formation of propanal and 1-propanol under dark cloud conditions within the CO hydrogenation network. By adding hydrocarbon radicals to the network, COMs such as propanal and 1-propanol can be formed. Propanal is formed at the low temperature of 10 K by the reaction between HCO and H_2CCH/H_3CCH_2 radicals. 1-propanol is subsequently formed from the hydrogenation of propanal. From an activation barrier point of view, the pathway to propanal formation is promising in the ISM. The pathway to 1-propanol may be a minor route based on the presented activation energies, which however only represent some of the scenarios that may lead to 1-propanol formation from propanal hydrogenation. Atacama Large Millimeter/submillimeter Array (ALMA) observations towards the low-mass protostar, IRAS 16293-2422B, provide a 1-propanol:propanal upper limit ratio of < 0.35 - 0.55. This parallels the experimental work, as there should be less 1-propanol compared to propanal if 1-propanol is solely formed from the hydrogenation of propanal.

Chapter 8 highlights that a number of alcohols can additionally be formed in the H_2O-rich ice phase of interstellar clouds, and likely with a higher efficiency depending on the starting materials chosen and their availability. Hydrocarbons ultimately originating from carbon-rich star environments, such as propyne ($H_3CC{\equiv}CH$), are expected to accrete onto carbonaceous dust grains that are formed from the nucleation of PAHs. It is demonstrated in a combined experimental and theoretical effort that propyne can react with nearby OH radicals formed in the H_2O-rich ice phase to produce an assortment of alcohols, including n- and i-propanol, n- and i-propenol, and potentially three isomers of propanediol. The n- and i-propanol abundance ratio of 1:1 aligns

with computational calculations that the barriers for propyne + OH to form both isomers are low, indicating that this reaction would be effective on icy dust grains if the reactants were next to each other on the surface. The findings are linked to the potential of forming astrobiological species, as polyynes containing $H_3C\text{-}(C{\equiv}C)_n\text{-}H$ structures may transform into more complex alcohols, such as fatty alcohols, which are thought to have been components of primitive cell membranes.

Bibliography

Agúndez, M. & Wakelam, V. 2013, Chem. Rev., 113, 8710

Allamandola, L., Sandford, S., & Valero, G. 1988, Icarus, 76, 225

Altwegg, K., Balsiger, H., & Fuselier, S. A. 2019, Annu. Rev. Astron. Astrophys., 57, 113

Arasa, C., van Hemert, M. C., van Dishoeck, E. F., & Kroes, G.-J. 2013, J. Phys. Chem. A, 117, 7064

Bacmann, A., Faure, A., & Berteaud, J. 2019, ACS Earth Space Chem.

Bacmann, A., Taquet, V., Faure, A., Kahane, C., & Ceccarelli, C. 2012, Astron. Astrophys., 541, L12

Balucani, N., Ceccarelli, C., & Taquet, V. 2015, Mon. Not. R. Astron. Soc. Lett., 449, L16

Bernstein, M. P., Dworkin, J. P., Sandford, S. A., Cooper, G. W., & Allamandola, L. J. 2002, Nature, 416, 401

Bertin, M., Romanzin, C., Doronin, M., et al. 2016, Astrophys. J. Lett., 817, L12

Boogert, A., Chiar, J., Knez, C., et al. 2013, Astrophys. J., 777, 73

Boogert, A., Gerakines, P. A., & Whittet, D. C. 2015, Annu. Rev. Astron. Astrophys., 53, 541

Boogert, A., Huard, T., Cook, A., et al. 2011, Astrophys. J., 729, 1

Broten, N., MacLeod, J., Avery, L., et al. 1984, Astrophys. J., 276, L25

Broten, N., Oka, T., Avery, L., MacLeod, J., & Kroto, H. 1978, Astrophys. J., 223, L105

Brünken, S., Gupta, H., Gottlieb, C., McCarthy, M., & Thaddeus, P. 2007, Astrophys. J. Lett., 664, L43

Cardelli, J. A., Clayton, G. C., & Mathis, J. S. 1989, Astrophys. J., 345, 245

Caro, G. M., Meierhenrich, U., Schutte, W., et al. 2002, Nature, 416, 403

Charnley, S., Kress, M., Tielens, A., & Millar, T. 1995, Astrophys. J., 448, 232

Charnley, S., Tielens, A., & Millar, T. 1992, Astrophys. J., 399, L71

Chiar, J., Adamson, A., Kerr, T., & Whittet, D. 1995, Astrophys. J., 455, 234

Chuang, K.-J., Fedoseev, G., Ioppolo, S., van Dishoeck, E. F., & Linnartz, H. 2016, Mon. Not. R. Astron. Soc., 455, 1702

Chuang, K.-J., Fedoseev, G., Qasim, D., et al. 2020, Astron. Astrophys.

Chuang, K.-J., Fedoseev, G., Qasim, D., et al. 2017, Mon. Not. R. Astron. Soc., 467, 2552

Chuang, K.-J., Fedoseev, G., Qasim, D., et al. 2018a, Astron. Astrophys., 617, 1

Chuang, K.-J., Fedoseev, G., Qasim, D., et al. 2018b, Astrophys. J., 853, 1

Chyba, C. & Sagan, C. 1997, in Comets and the Origin and Evolution of Life (Springer), 147–173

Cuppen, H., Ioppolo, S., Romanzin, C., & Linnartz, H. 2010, Phys. Chem. Chem. Phys., 12, 12077

Cuppen, H., van Dishoeck, E. F., Herbst, E., & Tielens, A. 2009, Astron. Astrophys., 508, 275

Dartois, E., Chabot, M., Barkach, T. I., et al. 2019, Astron. Astrophys., 627, A55

Dutrey, A., Guilloteau, S., & Guelin, M. 1997, Astron. Astrophys., 317, L55

Favre, C., Fedele, D., Semenov, D., et al. 2018, Astrophys. J. Lett., 862, L2

Fedoseev, G., Chuang, K.-J., Ioppolo, S., et al. 2017, Astrophys. J., 842, 1

Fedoseev, G., Cuppen, H. M., Ioppolo, S., Lamberts, T., & Linnartz, H. 2015, Mon. Not. R. Astron. Soc., 448, 1288

Fedoseev, G., Ioppolo, S., Zhao, D., Lamberts, T., & Linnartz, H. 2014, Mon. Not. R. Astron. Soc, 446, 439

Friberg, P., Madden, S., Hjalmarson, A., & Irvine, W. M. 1988, Astron. Astrophys., 195, 281

Fuchs, G., Cuppen, H., Ioppolo, S., et al. 2009, Astron. Astrophys., 505, 629

Garrod, R., Park, I. H., Caselli, P., & Herbst, E. 2006, Faraday Discuss., 133, 51

Garrod, R. T. & Pauly, T. 2011, Astrophys. J., 735, 15

Geppert, W. D., Hamberg, M., Thomas, R. D., et al. 2006, Faraday Discuss., 133, 177

Guidry, M. 2019, Stars and Stellar Processes (Cambridge University Press)

Guzmán, V. V., Pety, J., Gratier, P., et al. 2014, Faraday Discuss., 168, 103

Hama, T. & Watanabe, N. 2013, Chem. Rev., 113, 8783

Herbst, E. & Leung, C. M. 1989, Astrophys. J. Suppl. Ser., 69, 271

Herbst, E. & van Dishoeck, E. F. 2009, Annu. Rev. Astron. Astrophys., 47, 427

Ioppolo, S., Cuppen, H., Romanzin, C., van Dishoeck, E. F., & Linnartz, H. 2008, Astrophys. J., 686, 1474

Ioppolo, S., Cuppen, H., Romanzin, C., van Dishoeck, E. F., & Linnartz, H. 2010, Phys. Chem. Chem. Phys., 12, 12065

Ioppolo, S., Van Boheemen, Y., Cuppen, H., van Dishoeck, E. F., & Linnartz, H. 2011, Mon. Not. R. Astron. Soc., 413, 2281

Irvine, W., Hoglund, B., Friberg, P., Askne, J., & Ellder, J. 1981, Astrophys. J., 248, L113

Irvine, W. M., Brown, R., Cragg, D., et al. 1988, Astrophys. J., 335, L89

Jiménez-Serra, I., Vasyunin, A. I., Caselli, P., et al. 2016, Astrophys. J. Lett., 830, L6

Jørgensen, J., Schöier, F., & van Dishoeck, E. F. 2005, Astron. Astrophys., 435, 177

Jørgensen, J. K., Favre, C., Bisschop, S. E., et al. 2012, Astrophys. J. Lett., 757, L4

Jørgensen, J. K., van der Wiel, M., Coutens, A., et al. 2016, Astron. Astrophys., 595, A117

Kawaguchi, K., Kasai, Y., Ishikawa, S.-I., et al. 1994, Astrophys. J., 420, L95

Kennedy, G. M. & Kenyon, S. J. 2008, Astrophys. J., 673, 502

Kolasinski, K. W. 2012, Surface science: foundations of catalysis and nanoscience (West Chester, PA: John Wiley & Sons)

Kroto, H., Kirby, C., Walton, D., et al. 1977, in Bulletin of the American Astronomical Society, Vol. 9, 303

Langer, W., Velusamy, T., Kuiper, T., et al. 1997, Astrophys. J. Lett., 480, L63

Lee, J.-E., Lee, S., Baek, G., et al. 2019, Nat. Astron., 3, 314

Ligterink, N., Terwisscha van Scheltinga, J., Taquet, V., et al. 2018, Mon. Not. R. Astron. Soc., 480, 3628

Linnartz, H., Ioppolo, S., & Fedoseev, G. 2015, Int. Rev. Phys. Chem., 34, 205

Lovas, F. J., Remijan, A. J., Hollis, J., Jewell, P., & Snyder, L. E. 2006, Astrophys. J. Lett., 637, L37

Marcelino, N., Cernicharo, J., Agúndez, M., et al. 2007, Astrophys. J. Lett., 665, L127

Materese, C. K., Nuevo, M., & Sandford, S. A. 2017, Astrobiology, 17, 761

Matthews, H., Friberg, P., & Irvine, W. M. 1985, Astrophys. J., 290, 609

McCarthy, M., Gottlieb, C., Gupta, H., & Thaddeus, P. 2006, Astrophys. J. Lett., 652, L141

McClure, M., Bailey, J., Beck, T., et al. 2017, JWST Proposal ID 1309. Cycle 0 Early Release Science

McGuire, B. A., Burkhardt, A. M., Kalenskii, S., et al. 2018, Science, 359, 202

McGuire, B. A., Burkhardt, A. M., Shingledecker, C. N., et al. 2017, Astrophys. J. Lett., 843, L28

Meisner, J. & Kästner, J. 2016, Angew. Chem. Int. Ed., 55, 5400

Millar, T., Herbst, E., & Charnley, S. 1991, Astrophys. J., 369, 147

Millar, T. J. & Williams, D. A. 1993, Dust and chemistry in astronomy, Vol. 2 (CRC Press)

Öberg, K. I. 2016, Chem. Rev., 116, 9631

Öberg, K. I., Boogert, A., Pontoppidan, K. M., et al. 2011, Proc. IAU Symp. 280, 7, 65

Öberg, K. I., Garrod, R. T., van Dishoeck, E. F., & Linnartz, H. 2009, Astron. Astrophys., 504, 891

Öberg, K. I., Guzmán, V. V., Furuya, K., et al. 2015, Nature, 520, 198

Pontoppidan, K., van Dishoeck, E. F., & Dartois, E. 2004, Astron. Astrophys., 426, 925

Pontoppidan, K. M. 2006, Astron. Astrophys., 453, L47

Qasim, D., Fedoseev, G., Chuang, K. J., et al. 2020, An experimental study of the surface formation of methane in interstellar molecular clouds

Qasim, D., Fedoseev, G., Chuang, K.-J., et al. 2019a, Astron. Astrophys., 627, A1

Qasim, D., Fedoseev, G., Chuang, K.-J., et al. 2019b, arXiv preprint arXiv:1906.06508

Qasim, D., Fedoseev, G., Lamberts, T., et al. 2019c, ACS Earth Space Chem., 3, 986

Qasim, D., Lamberts, T., He, J., et al. 2019d, Astron. Astrophys., 626, A118

Remijan, A. J., Hollis, J., Snyder, L. E., Jewell, P., & Lovas, F. J. 2006, Astrophys. J. Lett., 643, L37

Shu, F. H., Adams, F. C., & Lizano, S. 1987, Annu. Rev. Astron. Astrophys., 25, 23

Snyder, L. E., Hollis, J., Jewell, P., Lovas, F. J., & Remijan, A. 2006, Astrophys. J., 647, 412

Soma, T., Sakai, N., Watanabe, Y., & Yamamoto, S. 2018, Astrophys. J., 854, 116

Suzuki, H., Ohishi, M., Kaifu, N., Ishikawa, S.-I., & Kasuga, T. 1986, Publ. Astron. Soc. Jpn., 38, 911

Terwisscha van Scheltinga, J., Ligterink, N., Boogert, A., van Dishoeck, E. F., & Linnartz, H. 2018, Astron. Astrophys., 611, A35

Thi, W.-F., Van Zadelhoff, G.-J., & van Dishoeck, E. F. 2004, Astron. Astrophys., 425, 955

van de Hulst, H. C. 1946, Recherches Astronomiques de l'observatoire d'Utrecht, 11, 2

van Dishoeck, E. F., Beuther, H., Caratti o Garatti, A., et al. 2017, JWST Proposal. Cycle 1, ID.# 1290

van Dishoeck, E. F., Blake, G. A., Draine, B. T., & Lunine, J. 1993, in Protostars and Planets III, 163–241

van´t Hoff, M. L., Tobin, J. J., Trapman, L., et al. 2018, Astrophys. J. Lett., 864, L23

Vasyunin, A. & Herbst, E. 2013, Astrophys. J., 769, 34

Walmsley, C., Jewell, P., Snyder, L., & Winnewisser, G. 1984, Astron. Astrophys., 134, L11

Ward-Thompson, D. 2002, Science, 295, 76

Watanabe, N. & Kouchi, A. 2002, Astrophys. J. Lett., 571, L173

Watson, W. & Salpeter, E. E. 1972, Astrophys. J., 174, 321

Whittet, D., Gerakines, P., Hough, J., & Shenoy, S. 2001, Astrophys. J., 547, 872

Wirström, E., Geppert, W. D., Hjalmarson, Å., et al. 2011, Astron. Astrophys., 533, A24

Dark ice chemistry in the laboratory

In this chapter, a general overview of the experimental setups used in this thesis to investigate the 'dark' ice chemistry in translucent and dense interstellar molecular clouds is provided. This includes a summary of the apparatus, SURFace REaction SImulation DEvice (SURFRESIDE), and the construction of an experimental apparatus complementary to the science on SURFRESIDE. Additionally, fundamental background knowledge, such as the mathematical details behind the analytical techniques used in SURFRESIDE, are described.

2.1 Experimental Setup: SURFRESIDE[3]

For over a decade, SURFRESIDE has been continuously upgraded to better probe the solid-state reactions that occur in the darkness of dense interstellar clouds (i.e., regions that are largely shielded by at least external UV photons), as well as in translucent clouds. As discussed in Chapter 1, these regions contain icy dust grains that are initially formed largely by the accretion of atoms. To mimic this process in the laboratory, SURFRESIDE is equipped with several state-of-the-art equipment, called atomic beamlines, that can produce intense beams with specific atoms. This includes a Hydrogen Atom Beam Source (HABS; see Fuchs et al. (2009)), an atomic H, N, O microwave atom source (MWAS; see Ioppolo et al. (2013)), and a C-atom source (Qasim et al. 2020b). Thus, the setup is currently labeled as SURFRESIDE[3] to represent the 3 atomic beamlines. These beamlines are necessary if one wants to investigate the kinetics of formation and destruction, derive abundances, and/or disentangle the formation routes in the ices of interstellar clouds.

Due to the topic of study, the experiments investigated in this thesis solely involve the reaction between radicals and between radicals and small molecules (i.e., to mimic the reaction between simple species and without an 'energetic' source). All of the presented experiments occur in an ultrahigh vacuum (UHV) environment, as necessary to prevent the interference of atmospheric leak contamination. UHV is also necessary to prohibit uncontrolled reactions with water, which is a relatively abundant background gas. Since our ices have thicknesses as that of interstellar ices (< 100 monolayers, ~50 monolayers; 1 monolayer = 1×10^{15} molecules cm^{-2}), assuming a sticking coefficient of unity, it takes 45 minutes for 1 monolayer of contamination to grow on the surface in a
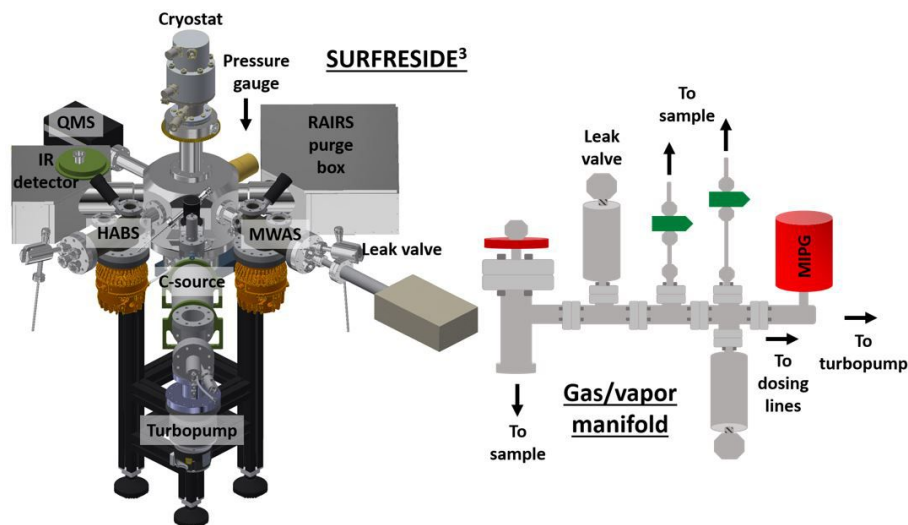
Figure 2.1: (Left) The experimental setup, SURFRESIDE[3], used in this thesis. Image credit: M. Witlox. (Right) The gas manifold that is attached to the setup, which allows gases and vapors to enter the chamber(s).

chamber pressurized at 1.3×10^{-9} mbar (Harrison 2013). Therefore, a pressure of $< 1.3 \times 10^{-9}$ mbar (i.e., UHV pressure) is needed to have a clean ice mixture when growing thin (< 100 monolayers) ices.

Figure 2.1 displays the experimental setup (left) and gas manifold (right). Many of the details of the atomic beamlines incorporated into SURFRESIDE, as well as the other components of the setup, are available in Ioppolo et al. (2013), Chuang (2018, Univ. Leiden), and Qasim et al. (2020b). A closed-cycle helium cryostat (CH-204 SF), coupled with a compressor (HC-4E1), is used to cool the substrate to a base temperature of 7 K. The substrate is where the interstellar ice analogues are grown, and has an inert gold coating. It is inert so that only the ice chemistry is studied (i.e., the reaction of gold and ice is irrelevant to interstellar ice chemistry). The purpose of the gold coating is to create a reflective surface that is required to monitor spectroscopically the formation of the ices over time. Note that the ices formed have thicknesses that prohibit noticeable effects of the surface on the ice chemistry. A cartridge heater is used to heat the sample to a maximum temperature of 450 K, in which sapphire rods are used to prevent damage to the cryocooler. The sample is placed at the center of the main chamber, which reaches a base pressure of low 10^{-10} mbar prior to deposition, as measured by a cold cathode pressure gauge (Pfeiffer Vacuum, IKR270). Analytical tools include a Fourier Transform Infrared Spectrometer (FTIR; Agilent Cary 640/660) and a quadrupole mass spectrometer (QMS; Spectra Microvision Plus LM76). For the IR pathway (discussed in section 2.1.1), boxes purged with filtered compressed air are needed to remove gaseous H_2O and CO_2.

The atomic beamline chambers, which are connected to the main chamber, are discussed below. The HABS (Tschersich & Von Bonin 1998; Tschersich 2000; Tschersich et al. 2008) includes a filament, which thermally breaks apart

H_2 molecules into H-atoms, and is placed inside a UHV chamber (average base pressure of low 10^{-10} mbar at room temperature). H_2 gas is introduced into the HABS by a leak valve, and is prepared in a turbomolecularly pumped dosing line. The MWAS (Oxford Scientific Ltd.) uses electrons, excited by a frequency of 2.45 GHz at a typical power of 275 W, to break apart molecules into fragments. An average base pressure of low 10^{-9} mbar is found, and gases are introduced into the MWAS chamber also by a leak valve, which is connected to a turbo-molecularly pumped dosing line. To collisionally cool the radicals produced by both beamlines, a nose-shaped quartz pipe is attached at both exit channels. The carbon atom source (SUKO-A 40, from Dr. Eberl MBE-Komponenten GmbH (MBE)) chamber reaches an average base pressure of low 10^{-9} mbar. It consists of a tantalum filament that is packed with graphite powder, and is resistively heated during operation. Thus, a dosing line for the C-atom source chamber is not required. However, a new filament is required usually after ~14 hours of operation, and therefore a mini UHV gate valve is incorporated to separate the C-atom source from the main chamber. All three atomic chambers are attached to a water cooling shroud to prevent surrounding components from melting.

The gas/vapor manifold shown in Figure 2.1 is commonly used to prepare the gases/vapors that will enter the main chamber. Like the other gas lines, the manifold is turbomolecularly pumped. Vapors are admitted by an ultratorr connection (see Figure 2.1 manifold drawing, far left with red valve handle), and gases are entered via 1/4" Swagelok (green valves). A mass independent pressure gauge ("MIPG" in Figure 2.1, Pfeiffer Vacuum, CMR361) is used to monitor the pressure, which is useful since calibration for the mass of the gas is not required. This gauge spans from 0.1 and 1100 mbar, and therefore a Pirani transmitter (Pfeiffer Vacuum, TPR280) is also attached in order to probe the pressure down to 10^{-4} mbar (i.e., to ensure that the manifold is effectively pumped). Metal leak valves are used to separate gases within the manifold, and also to minimize leak contamination. Finally, the manifold is connected to two separate dosing lines that are connected to the main chamber by two separate leak valves.

2.1.1 Analytical techniques

Reflection-absorption Infrared Spectroscopy (RAIRS):
The basic principle of infrared (IR) absorption spectroscopy is that the energy of the incoming light must be equivalent to the energy gap between two vibrational states (i.e., resonant frequencies). The way in which a molecule vibrates is known as its vibrational "mode", and in order for a mode to be IR active, a change in the dipole moment of vibration must be induced when transitioning between the ground to the excited vibrational state. This is mathematically described below (Humblot & Pradier 2011):

$$\text{Signal intensity} \propto |\,\Psi_f^* E \mu_{fi} \Psi_i\,|^2 \tag{1}$$

where Ψ_f and Ψ_i stand for final and initial states, respectively, E is the electric field vector, and μ_{fi} is the transition dipole moment. RAIRS is a branch of IR spectroscopy which probes the absorption features of the adsorbed molecules.
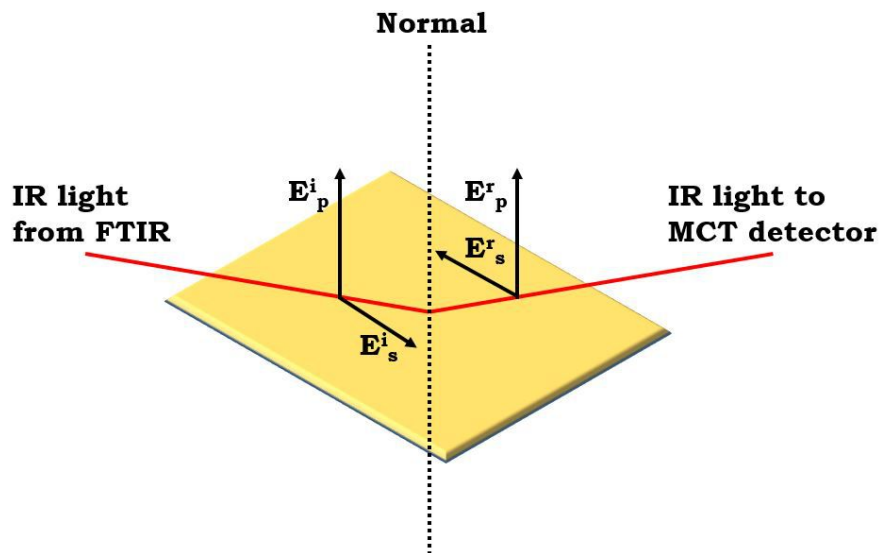
Figure 2.2: The s- and p-components of the electromagnetic field at the surface in a typical RAIRS study. Figure adapted from Humblot & Pradier (2011). On top of this surface is where ices are grown and probed.

It is surface sensitive and comes with an additional selection rule. Figure 2.2 provides a visual of the IR beam pathway when employing the RAIRS technique.

On SURFRESIDE[3], IR light is emitted from a FTIR (allowed spectral range of 6000-700 cm^{-1} and a typically used resolution of 1 cm^{-1}), where it is focused onto the sample by external optics at ~80° to surface normal. This light is composed of two electric field vectors, namely s- and p-polarized. S-polarized gives rise to the longitudinal optical (LO) mode feature, and p-polarized additionally gives rise to the transverse optical (TO) mode feature (Palumbo et al. 2006). As shown in Figure 2.2, the s-component is parallel to the plane of the surface, and the p-component is orthogonal. The s-component of light is essentially negligible, and can be explained by the equation below (Humblot & Pradier 2011):

$$E_s = E_s^i[sin\theta + r_s sin(\theta + \delta_s)] \tag{2}$$

where E^i is the incident electric field at the surface, θ is an arbitrary phase angle, r is the reflection coefficient, and δ is the phase change. At all angles of incidence, δ is near 180° and r is close to unity (Humblot & Pradier 2011), making the electric field at the surface for the s-component close to zero. The p-component of light is split further into parallel and perpendicular components. As the incident and reflected parallel components are opposite in direction, the electric field contribution from the parallel component is negligible. The electric field of the perpendicular component of the p-component of light is described below (Humblot & Pradier 2011):

$$E_{p\perp} = E_p^i sin\phi[sin\theta + r_p sin(\theta + \delta_p)] \tag{3}$$

where ϕ is the angle of incidence. As ϕ approaches 90° to surface normal, the electric field intensity increases until at 90°, in which the increasing δ_p leads to destructive interference. This leads to about 17-25× increase in the sensitivity in comparison to transmission experiments when the grazing incidence angle is just below 90° (Friedbacher & Bubert 2011). Thus, RAIRS is advantageous in comparison to transmission IR in regards to its sensitivity.

In this thesis, RAIRS is particularly exploited to confirm the formation of reaction products *in situ* typically at a substrate temperature of 10 K. There are several ways in which RAIRS alone can be used to identify the species formed. However, it should be noted that for the identification of COMs, RAIRS alone typically cannot be used to secure a detection, as the probability of similar vibrational signatures increases as the molecular complexity increases. As each functional group has a vibrational mode that has a characteristic band strength (units of cm molecule^{-1}, see in the work by Bouilloud et al. (2015)), the relative intensities between the infrared features of the same molecule can be considered a diagnostic tool. As molecules have also different desorption temperatures, the temperature range at which the infrared peaks decrease can further constrain the identity of the species. Finally, according to Hooke's law, a heavier isotope will lead to a red-shift in the vibrational frequency. Thus, isotopic substitution can confirm the target functional group.

RAIRS also has the advantage of determining the amount of product formed by using a modified Lambert-Beer equation:

$$N = \frac{\ln 10 \cdot \int Abs(\nu)d(\nu)}{A'} \tag{4}$$

where N is the column density (molecule cm^{-2}), Abs(ν)d(ν) is the change in absorbance (cm^{-1}), and A' is the band strength. These values are multiplied by ln(10) to convert to optical depth scale, since the spectrometer yields values in absorbance. Particularly for RAIRS experiments, the band strength is the more difficult parameter to obtain, since band strengths are typically measured by transmission IR in the literature. There are two ways in which band strengths are determined in this thesis: 1) The values are taken from laser interference measurements performed on SURFRESIDE by Chuang et al. (2018) and 2) a transmission-to-RAIR proportionality factor is used, in which the band strength of CO (2142 cm^{-1}) from the laser interference experiment performed by Chuang et al. (2018) is included.

Temperature Programmed Desorption (TPD):

A complementary technique to RAIRS is temperature programmed desorption (TPD). It is a well-established method that is regularly used in laboratory astrophysical ice and classical surface science experiments. Particularly in this thesis, the TPD technique is frequently exploited predominantly due to the complexity of the ice mixtures investigated. Such complex mixtures result in the overlap of IR bands, making it difficult to distinguish the features. Especially in a polar ice, IR bands typically broaden, which can then hide other features of interest. This lack in distinction is usually not as severe in TPD experiments, as will be discussed in the following paragraphs. Additionally, the detection limit of the QMS on SURFRESIDE^3 is around 0.005 monolayers,
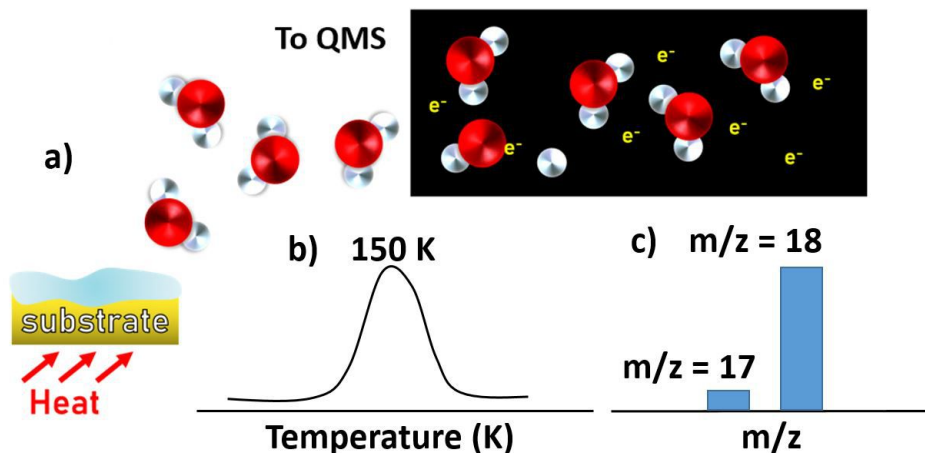
Figure 2.3: Illustration of the basic concept of a TPD experiment (a) and the two molecule-specific parameters typically probed by this method: the desorption temperature and profile (b) and the fragmentation pattern (c).

whereas the FTIR has a detection limit around an order of magnitude less (for species with large band strengths), making TPD a useful technique for probing the COMs that are not abundantly formed.

The basic idea behind a TPD experiment and the information it can provide to constrain the composition of an ice matrix are shown in Figure 2.3. As displayed in Figure 2.3 a, a controlled heat source is used to warm the ice so that the molecules desorb on a linear timescale. This linearity is necessary, as molecules desorb at specific temperatures (e.g., Figure 2.3 b). Some of these molecules will enter the ionization source of the QMS and become ionized and even fragment by accelerated electrons that are emitted from a heated cathode. Since every molecule has a characteristic fragmentation pattern, such a pattern acts as a fingerprint of the dissociated molecule (e.g., Figure 2.3 c). This pattern can be compared to the standards provided in the NIST database[1], or even better, to the standards measured within the same setup in which the experiment was performed. To maximize the number of ions formed, an electron energy of 70 eV is commonly used (also by the NIST database). This value is also ideal, as the dependence of the fragmentation pattern on the change in the electron impact energy around ~70 eV is relatively low. These ions eventually make their way to the mass analyzer, which consists of four poles. The two positively and negatively biased poles act as low-mass and high-mass filters, respectively, and thus the quadrupole only allows the target species to go through based on the m/z value. The remaining ions are then detected by a Faraday cup or a secondary electron multiplier. More information on the thermal desorption of ices can be found in the works of Brown & Bolina (2007) and Burke & Brown (2010), for example.

1 William E. Wallace, director, "Mass Spectra" in NIST Chemistry WebBook, NIST Standard Reference Database Number 69, Eds. P.J. Linstrom and W.G. Mallard, National Institute of Standards and Technology, Gaithersburg MD, 20899, https://doi.org/10.18434/T4D303, (retrieved October 2, 2019).

Similar to RAIRS, isotopically-enhanced gases can also be used to constrain the identity of a feature. Returning to Figure 2.3, the desorption temperature of H_2O in a H_2O ice is around 150 K under UHV conditions, and this can be observed by monitoring m/z values of 18 (H_2O) and 17 (OH). Incorporation of $H_2{}^{18}O$ will result in the rise of m/z = 20 ($H_2{}^{18}O$) and 19 (^{18}OH) at 150 K, along with a fragmentation pattern that is now shifted to m/z = 20 and 19. Repetition of this procedure with 2-3 different isotopically-enhanced gases is ideal to securely constrain the peak's identity.

To use TPD data to identify a species, it is necessary to know what parameters influence the TPD profile and in what ways. The Polanyi-Wigner formula describes the intensity of the desorption peak, under the condition that the rate of desorption is less than the rate of removal of the desorbed species from the UHV chamber. Below shows a simplied version of the formula, as adapted from Kolasinski (2012):

$$I(t) \propto r_{des} = \frac{-d\theta}{dt} = \nu_n \theta^n exp \frac{-E_{des}}{RT} \tag{5}$$

where r_{des} is the rate of desorption, θ is the surface coverage, t is time, ν is the pre-exponential factor, n is the desorption order, E_{des} is the energy of desorption, R is the gas constant, and T is the substrate temperature. This formula can be coupled with the mathematical description of the desorption process:

$$T = T_0 + \beta t \qquad dT = \beta dt \qquad dt = \frac{dT}{\beta} \tag{6}$$

where T_0 is the temperature at t = 0, and β is the ramp rate. Substitution of $\frac{dT}{\beta}$ in equation 5 results in:

$$\frac{-d\theta}{dt} = \frac{\nu_n \theta^n exp \frac{-E_{des}}{RT}}{\beta} \tag{7}$$

Since the maximum intensity (i.e., peak desorption temperature) is when the slope of the TPD profile is zero, the derivative of the above formula with respect to temperature can be set to zero in order to determine how the peak desorption temperature is influenced by other parameters. Rearrangement of Equation 7 after setting the derivative to zero results in:

$$\frac{E_{des}}{RT^2} = \frac{\nu_n}{\beta} exp \frac{-E_{des}}{RT} \tag{8}$$

Thus, the peak desorption temperature is proportional to the heating rate and the desorption energy. Additionally, the ice matrix can also influence the temperature at which molecules desorb. The binding energy of a molecule may shift depending on the ice mixture, which in turn affects the peak desorption temperature. Molecules may also be trapped by less volatile species, resulting in co-desorption (Fayolle et al. 2013, and references therein). It should be noted that the desorption energy and pre-exponential factor can also depend on the coverage of material on the surface.

The TPD method can also provide information on the relative abundances. The general formula is shown below (adapted from Martín-Doménech et al. (2015)):

$$N_{x,y}(mol_{x,y}) = \frac{A_{x,y}(m/z)}{\sigma_{x,y}^+(mol_{x,y})I_{Fx,y}(z)F_{Fx,y}(m)S_{x,y}(m/z)} \tag{9}$$

where x and y represent different molecules, A(m/z) is the integrated QMS area, σ^+(mol) is the ionization cross section, I_F(z) is the ionization factor, F_F(m) is the fragmentation factor, and S_F(m/z) is the sensitivity that is calibrated and specific to each mass spectrometer. The sensitivity values for SURFRESIDE are found in Chuang (2018, Univ. Leiden). The relative abundance is calculated by dividing N_x(mol$_x$) by N_y(mol$_y$).

The RAIR and TPD configurations in SURFRESIDE allow users to combine the two techniques to link the solid-state and gas-phase signatures, which results in a more accurate determination of the ice species formed. A typical procedure is as follows: RAIR spectra are collected during the ice deposition. The ice is then heated using a linear ramp rate (i.e., TPD). During the TPD process, RAIR spectra are collected, which results in RAIR data acquired as a function of the substrate temperature. The gradual disappearance of infrared peaks can be linked to the rise of desorption signals in the TPD, which may ultimately provide more secure assignments for the infrared and mass spectrometry signatures.

2.2 Experimental Setup: Carbon atom source testing chamber

Before implementation of the C-atom source into SURFRESIDE, it was necessary to first test and further optimize the source in a separate testing vacuum chamber. This is because the nature of carbon is not compatible with these types of systems, as carbon can short circuit electronics, attenuate light, create blockage, is difficult to remove, and so on. Moreover, prior to Qasim et al. (2020b), there were no reports (to our knowledge) on the coupling of the SUKO-A 40 source to a UHV setup that contained cryogenic equipment, and thus its behavior under such conditions was unknown. The test setup is shown in Figure 2.4. It is designed to mimic, as close as possible, the conditions of the main chamber of SURFRESIDE. This includes having a base pressure of low $\sim 10^{-9}$ mbar at room temperature, and a gold-plated substrate that reaches a base temperature of 17 K. The horizontal and vertical distances between the carbon filament and the substrate surface are constant between the test setup and that of SURFRESIDE. The details of the C-atom source in SURFRESIDE[3] will be addressed in the next sections. Here, a short recap of the preparations needed to realize this implementation into the main setup is given.
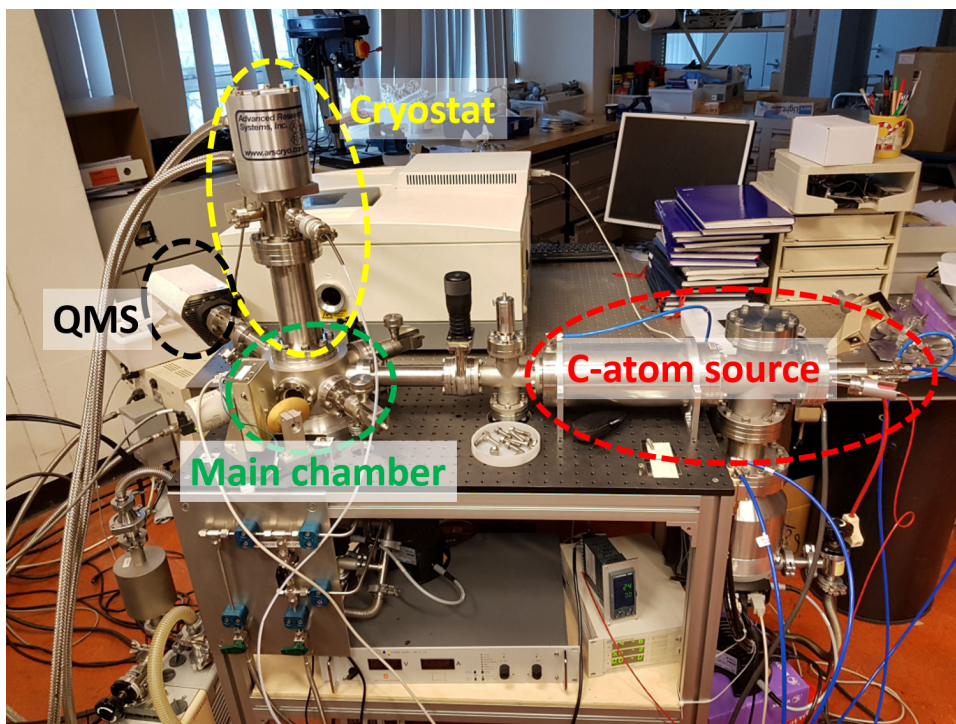
Figure 2.4: The C-atom source testing chamber used to test and optimize the source before its incorporation into SURFRESIDE. Highlighted are the main components, which are the C-atom source (red), the main chamber where ices are grown (green), the cryostat used to create the ices (yellow), and the QMS used to conduct preliminary measurements (black).

One of the main purposes of the testing chamber is to constrain the atomic carbon beam size. Ideally, the beam should not be larger than the substrate surface, but also should cover most of it. This ensures that the components of the main chamber will not be polluted and that carbon chemistry is uniformly distributed on the surface, respectively. To protect the equipment within the test chamber, a long and wide plate is initially used as a substitute for the relatively small gold-plated substrate, as shown in Figure 2.5. As carbon has a high sticking coefficient and is black, the beam size can be directly measured. Copper gaskets with various sized apertures are used to reduce the beam diameter to an ideal value of 21.5 mm, as shown in Qasim et al. (2020b).
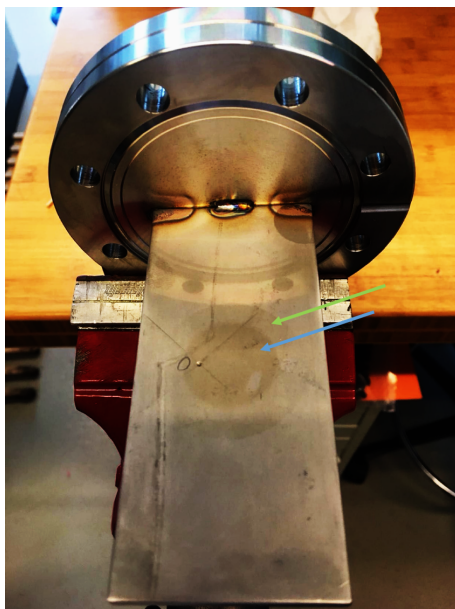
Figure 2.5: Initial results of the atomic carbon beam size using a relatively large plate prior to testing with the gold-plated substrate. The dark circle (blue arrow), with a diameter of 25 mm, represents the majority of the carbon flux. A lighter shaded circle (green arrow), which surrounds the darker shaded circle, is due to residual carbon.

Another main purpose of the testing chamber is to see if solid-state chemistry occurs when using the C-atom source, and under what conditions. These trials are useful, in that experiments can be immediately performed within SURFRESIDE, which limits the atomic carbon pollution in the more expensive apparatus. It is also noted that the survival of the QMS in the testing chamber during an experiment, which is an analytical tool on SURFRESIDE that may be susceptible to short-circuiting by C-atoms, is an important finding. The QMS is positioned in the same geometry with respect to the carbon atom beam as that of SURFRESIDE.

Figure 2.6 shows TPD data of a C + $^{18}O_2$ co-deposition experiment. The peaks of interest are at 37 and 85 K, which likely represent the desorptions of $C^{18}O$ and $C^{18}O_2$, respectively. Note that the desorption temperatures are shifted ~5 K higher than expected, and may be due to a miscalibration of the temperature controller. The desorption signal at 37 K for m/z = 48 is possibly representative of the co-desorption of $C^{18}O_2$ with $C^{18}O$ and the contaminant, CO. The formation of $C^{18}O$ and $C^{18}O_2$ from C + $^{18}O_2$ is confirmed in Qasim et al. (2020b). Such findings show that the C-source is already optimized to conduct solid-state chemistry that is detectable by TPD-QMS, making it available to incorporate into SURFRESIDE.
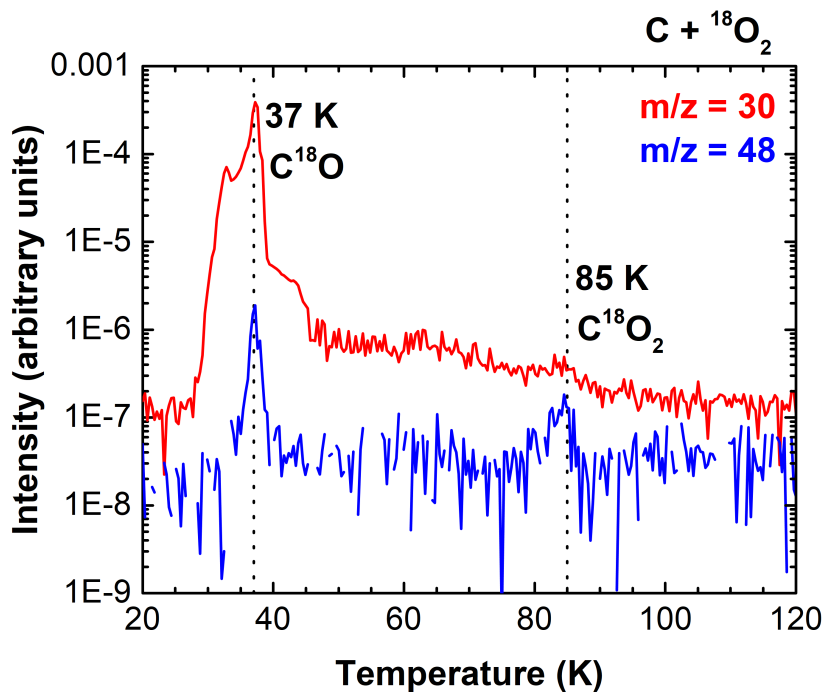
Figure 2.6: TPD-QMS spectra of C + $^{18}O_2$ taken by the testing chamber QMS (Pfeiffer PrismaPlus). Spectra are recorded after ice growth at 17 K. The likely desorptions of $C^{18}O$ and $C^{18}O_2$ are shown at 37 and 85 K, respectively. More details on the C + $^{18}O_2$ reaction are found in Qasim et al. (2020b).

2.3 Introduction

The design, implementation, and performance of a customized carbon atom beam source for the purpose of investigating solid-state reaction routes in interstellar ices in molecular clouds are discussed. The source is integrated into an existing ultrahigh vacuum setup, SURFace REaction SImulation DEvice (SURFRESIDE^2), which extends this double atom (H/D, O, and N) beamline apparatus with a third atom (C) beamline to a unique system that is fully suited to explore complex organic molecule solid-state formation under representative interstellar cloud conditions. The parameter space for this system is discussed, which includes the flux of the carbon atoms hitting the ice sample, their temperature, and the potential impact of temperature on ice reactions. Much effort has been put into constraining the beam size to within the limits of the sample size with the aim to reduce carbon pollution inside the setup. How the C-atom beam performs is quantitatively studied through the example experiment, C + $^{18}O_2$, and supported by computationally-derived activation barriers. The potential for this source to study the solid-state formation of interstellar complex organic molecules through C-atom reactions is discussed.

Complex organic molecules (COMs; carbon and hydrogen bearing molecules with at least 6 atoms) have been detected in the cold and lightless environments of prestellar and starless molecular cloud cores (i.e., in the dark interstellar regions which are shrouded by dust), in addition to other astrophysical environments (Herbst & van Dishoeck 2009; Soma et al. 2018; Bacmann et al. 2019). 3-carbon COMs have now been observed in star-forming regions towards both, high-mass (Belloche et al. 2013, 2016) and low-mass(Lykke et al. 2017) sources. Astrochemical models generally assume that a majority of the detected COMs in such surroundings originate from radical-induced surface reactions, in which the radicals are of molecular form (Garrod & Herbst 2006; Vasyunin et al. 2017). This is supported by a series of recent laboratory and theoretical investigations of solid-state reactions, such as HCO, CH_3O and CH_2OH recombinations, in which the radicals are formed by addition and abstraction reactions within the CO hydrogenation route (Chuang et al. 2016; Butscher et al. 2017; Fedoseev et al. 2017; Álvarez-Barcia et al. 2018; Lamberts et al. 2019).

Another solid-state pathway that offers a route to larger COMs is through direct carbon atom chemistry. This route has been proposed in theoretical works (Tielens & Charnley 1997; Charnley 2001a; Charnley & Rodgers 2005, 2009), applied to observational studies (Requena-Torres et al. 2008), and recently in astrochemical models (Simončič et al. 2020). Neutral atomic carbon derived from the gas-phase is one of the most abundant elements in space,(Phillips & Huggins 1981; van Dishoeck et al. 1988; Herbst 2005) and is primarily available during the early period of ice formation (i.e., before it reacts to form CO

gas). (van Dishoeck 1998; Hollenbach et al. 2008; Taquet et al. 2014). The laboratory study of C-atom chemistry under conditions representative for cold molecular clouds (i.e., ground state atomic carbon on 10 K surfaces in an ultrahigh vacuum (UHV) environment) has turned out to be very challenging, as it is experimentally difficult to produce an intense beam of largely ground state atomic carbon. This is a reason why there is little known regarding the role and relevance of C-atom addition reactions in solid-state astrochemical processes. Recent laboratory works have demonstrated how atomic carbon can react to form simple radicals (Krasnokutski et al. 2016; Henning & Krasnokutski 2019) and COMs(Krasnokutski et al. 2017) within liquid helium droplets. The present work extends on this with the first ice system capable to study C-atom chemistry reactions in interstellar ice analogues.

The focus here is on the design, implementation, and characterization of an atomic carbon source into an existing atomic beamline setup, SURFace REaction SImulation DEvice (SURFRESIDE^2) (Ioppolo et al. 2013), which is dedicated to studying molecular cloud surface reactions. The experimental details of this setup are described elsewhere (Ioppolo et al. 2013). SURFRESIDE^2 has been used to show how H_2O, CO_2, and COMs can form under interstellar cloud conditions (Ioppolo et al. 2010; Chuang et al. 2016; Fedoseev et al. 2017; Qasim et al. 2019b). The two available atomic beamlines currently permit the formation of a number of radicals, including H/D, N, O, OH, and NH_x. The addition of an atomic carbon source further extends the possibilities to study COM formation by the accretion of atoms and small radicals, which is representative of the low density phase of molecular clouds where atoms are not yet largely locked up into molecules (Linnartz et al. 2015; Boogert et al. 2015).

The original design of the atomic carbon source is found in the work by Krasnokutski & Huisken (2014) and the source discussed in this article is a customized SUKO-A 40 from Dr. Eberl MBE-Komponenten GmbH (MBE), patent number DE 10 2014 009 755 A1. The design of the tantalum tube that is filled with graphite powder can be found in the works by Krasnokutski & Huisken (2014) and Albar et al. (2017) Heating of the tube causes the carbon to sublimate and react with the tantalum to produce tantalum carbide, resulting in the conversion of molecular carbon into atomic carbon. Thus, the advantage of this source is that it essentially produces C-atoms rather than C_x clusters (<1% C_2 and C_3 molecules) (Krasnokutski & Huisken 2014). Additionally, carbon atoms are formed by thermal evaporation rather than 'energetic' processing. Therefore, we expect the formation of only ground state C(^{3}P) atoms with moderate kinetic energies. The implementation, design, and calibration measurements of the source are described in section 2.4. Its performance, shown through example reactions which are considered relevant from an astronomical perspective and useful for calibration purposes, is presented in section 6.3. The results are interpreted following computationally-calculated activation barriers that are briefly discussed. Section 2.6 discusses how this source can be used to investigate astrochemically relevant surface reactions, and how it can contribute to the science proposed with the upcoming James Webb Space Telescope (JWST). Section 2.7 lists the concluding remarks by summarizing the pros and cons of the new setup described here.

2.4 SURFRESIDE^3 and atomic carbon source description

The new C-atom source is implemented into an existing setup, SURFRESIDE^2, that has been described in detail before (Ioppolo et al. 2013). The extended system, SURFRESIDE^3, is shown in the 3D representation of Fig. 2.7. This UHV system allows the growth of interstellar ice analogues on a sample surface for temperatures as low as 8 K using a closed-cycle helium cryostat. It comprises of three atomic beam lines. The HABS and MWAS beamlines have angles of 45° to surface normal of the sample. The C-atom source is mounted in between the HABS and MWAS, and faces the plane of the surface of the ice substrate perpendicularly. The result of impacting H/D-atoms by the Hydrogen Atom Beam Source (HABS) (Tschersich & Von Bonin 1998; Tschersich 2000; Tschersich et al. 2008), and/or H/D-, O-, N-atoms, and molecular radicals by the Microwave Atom Source (MWAS; Oxford Scientific Ltd.), and/or C-atoms by the new C-atom source is monitored using reflection-absorption infrared spectroscopy (RAIRS) and/or temperature programmed desorption-quadrupole mass spectrometry (TPD-QMS). RAIRS allows monitoring of the formation of reaction products *in situ*, as well as quantitative measurements of the newly formed products using a Fourier Transform Infrared Spectrometer (FTIR). TPD-QMS is complementary to RAIRS, as it exploits the desorption temperature, mass-to-charge (m/z) value, and electron impact induced fragmentation pattern of the desorbed species to identify newly formed ice products. SURFRESIDE^3 is unique, as it allows to operate three different atomic beam lines simultaneously.

Ices are grown on the gold-plated substrate that is positioned vertically in the center of the main chamber of SURFRESIDE^3, which reaches a base pressure of $\sim 3-4 \times 10^{-10}$ mbar at the start of each experiment. The surface is positioned such that it directly faces the C-atom source beam. A substrate temperature range of 8 – 450 K is achieved by usage of a closed-cycle helium cryostat and resistive heating. The substrate temperature is probed by a silicon diode sensor that has an absolute accuracy of 0.5 K.

2.4.1 Design of the C-atom line

Fig. 2.8 illustrates the cross section of the C-atom source stainless steel chamber, which has a base pressure of $\sim 2 \times 10^{-9}$ mbar when the source is at its standby current of 40 A. Two water-cooled power contacts are used to heat the source by means of a DC power supply that produces up to 1500 W (Delta Elektronika, SM 15-100).

The source is inserted into the vacuum chamber through a 4-way cross (CF 63). At the bottom of the cross hangs a turbomolecular pump attached to an adapter (Leybold 350i, 290 l/s for N_2, CF 100). As shown in Fig. 2.8, the pump is placed behind the source to keep the pump at a distance from the carbon atom beam, as carbon deposits may stick and potentially harm the pump blades by applying weight to them. A water-cooled shroud is attached to the right flange of the 4-way CF 63 cross to prevent surrounding components from melting, as operating temperatures are around 2030°C. A tantalum shield
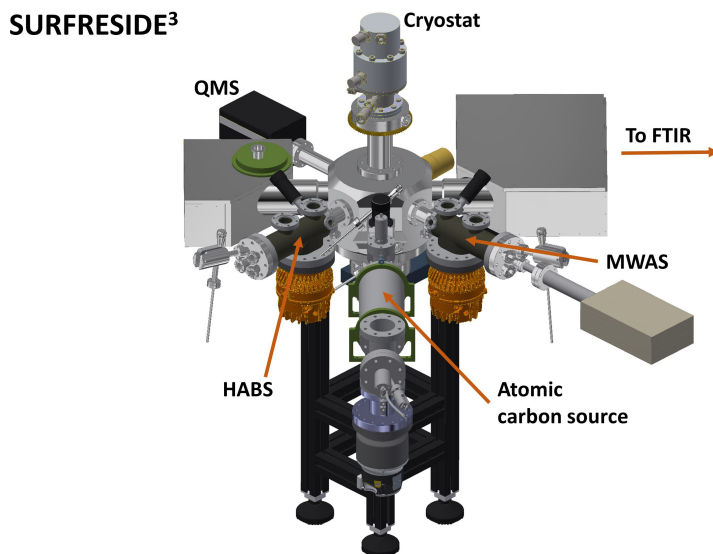
Figure 2.7: A three atomic beam line system, including the new C-atom source introduced here. The three atomic beam lines are capable of generating, H/D, N, O, and C-atoms, in addition to small radicals (e.g., OH, NH). It also contains two regular deposition lines. Both, pre-deposition and co-deposition experiments can be performed. RAIRS and TPD-QMS are used as diagnostic tools.
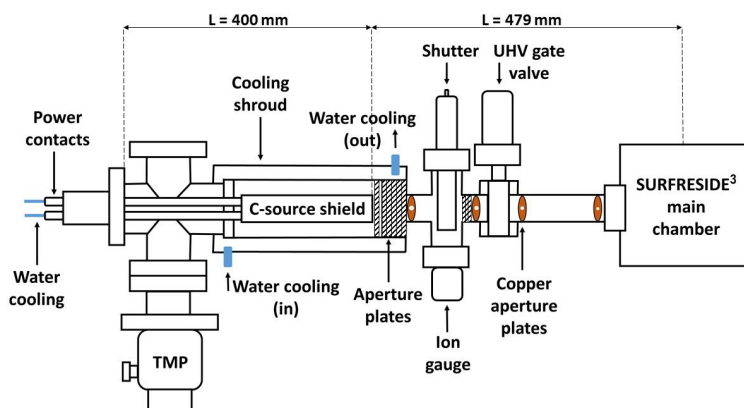

Figure 2.8: Side view schematic of the atomic carbon source vacuum chamber.

is placed around the C-atom source for further protection. To the right of the shroud is a 4-way CF 40 cross piece. The top flange of the cross is attached to a rotary shutter. This shutter is situated in between the path of the emitting carbon atoms and the mini UHV gate valve in order to protect the gate valve from carbon build-up during ramping of the current. The gate valve is installed for the purpose of separating the C-atom source from the main chamber when necessary. At the bottom of the cross hangs a micro-ion gauge (Granville-Phillips, 355001-YG). Various sized aperture plates are installed to spatially restrict the carbon atom beam, where more details are found in section 2.4.2.

Unlike the HABS and MWAS, the exit of the C-source does not have a nose-shaped quartz tube to help collisionally thermalize newly formed atoms before they impact the ices that are on top of the substrate; C-atoms have a much higher sticking coefficient and would coat the tube effectively with a carbon layer. This means that the impacting C-atoms carry the potential to induce thermal processing of the ice, which would not be representative of interstellar conditions. This is an important issue that has been addressed in more detail in the first science result with this new source; in Qasim et al. (2020a) it was demonstrated that in a C + H + H_2O experiment – combining the HABS and C-atom source – the barrierless formation of CH_4 at 10 K predominantly follows a Langmuir-Hinshelwood mechanism (i.e., diffusing reactants thermalize prior to reaction on the surface). This suggests the likelihood of thermalization of the involved reactants, but it is not secured as to whether C-atoms thermalize with the substrate prior to reaction, as the formation of CH in the C + H + H_2O experiment may also proceed by Eley-Rideal (i.e., one reactant is not thermalized prior to reaction). For barrierless reactions, this is not relevant for qualitative studies, as such reactions will proceed regardless of the kinetic energy of the C-atoms. However, for reactions in which a barrier is involved, caution should be taken particularly for quantitative analysis, as the heat of the carbon atoms could open reaction pathways that are not accessible under typical interstellar conditions.

2.4.2 Beam size calibration

The beam size is measured on a gold-decorated substrate that has a width of 24 mm and length of 38 mm, and is positioned at a horizontal distance of 512 mm from the tantalum tube. Fig. 2.9 shows the resulting circular carbon atom beam diameter of 21.5 mm on the gold surface. The beam is narrowed by a combination of stacked oval-like aperture plates (produced by MBE) and circular copper aperture plates (produced in Leiden), as shown in Fig. 2.8. From left to right, the aperture plates by MBE consist of one pyrolytic graphite (PG) plate with an orifice of 18×6 mm, five tantalum plates with an orifice of 19×7 mm, and three tantalum plates with an orifice of 20×12 mm. The PG plate is placed directly after the source to allow the carbon to grow on it without introducing flakes, as thin graphite layers on thin metal parts sometimes create flakes. Multiple plates of the same aperture size are for the purpose of acting as radiation shields. The mean distance between the left-most and right-most aperture plate is 135 mm. The aperture sizes of the copper plates are 21 mm, 20 mm, 19 mm, and 18 mm, respectively, where the plate with the smallest aperture is placed closest to the substrate surface. From left to right,

the distances between the copper plates are 126 mm, 35 mm, and 129 mm. The resulting beam size is optimized in that the majority of the atoms do not go past the sample plate, yet covers a large fraction of the substrate surface in order to have maximum overlap with the FTIR IR beam.

Figure 2.9: The darker circle, outlined by a dashed circle, is carbon deposit that resulted from the atomic beam on the gold surface of the substrate. The entire beam is on the flat surface, and the angle at which the picture is taken makes it appear that the lower part is clipped. A beam diameter of 21.5 mm is measured on a sample plate that has a size of 38 mm × 24 mm. Note that contrast has been added to the image to visualize the area with impacting C-atoms.

2.4.3 Temperature of the graphite-filled tantalum tube

An approximation for the temperature of the graphite-filled tantalum tube, and consequently of the emitting carbon atoms, is measured by a WRe alloy wire that is largely shielded with Al_2O_3 ceramic. A temperature controller (Eurotherm 2408) is primarily used to read out the temperature value. As the thermocouple is placed beneath the tube to protect it from melting, the measured value from the thermocouple is lower than the actual temperature of the heated tube. To know the actual temperature of the graphite-filled tantalum tube, and subsequently the emitting carbon atoms, a pyrometer is used (at MBE) in conjunction with the thermocouple, and the values are shown in Figure 2.10. Note that the C-atoms are assumed to be in thermal equilibrium with the tantalum tube, although in reality, their temperatures are lower, as the energy required to release the C-atoms from the tube (physisorption/chemisorption) is not taken into account. Interpolation of the values provides the approximate temperature of the carbon atoms for every thermocouple reading from 728 - 1567°C. These gas-phase temperature values are important for determining the flux of carbon

atoms on the sample, as the flux is highly dependent on the filament temperature. Note that the pyrometer values are representative of ground state atomic carbon, as the amount of energy required to reach the C(^{1}D) excited state is 14,665 K [2].
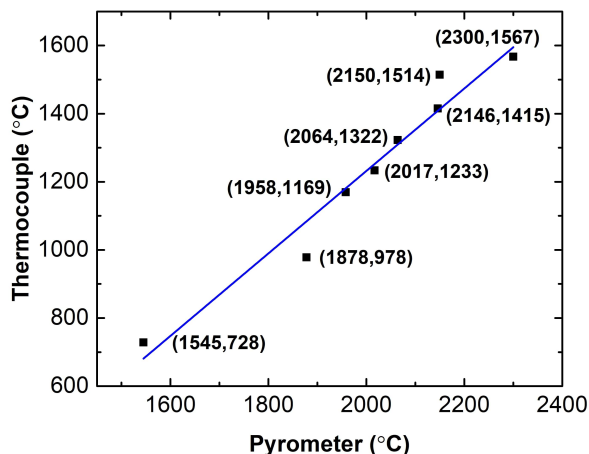
Figure 2.10: A linear fit to the thermocouple versus pyrometer temperature values of the tantalum tube. The values from the pyrometer reflect the approximate C-atom temperatures, whereas the values from the thermocouple are lower due to the distance between the thermocouple and the heated tube.

2.4.4 C-atom flux calibration

In order to characterize the reaction efficiencies in the ice, it is important to quantify the C-atom flux. In Ioppolo et al. (2013), this was demonstrated for the HABS (H/D) and MWAS (H/D, N, O) fluxes. Here, the calibration procedure for the C-atom source is described through a quantitative analysis of various C + $^{18}O_2$ co-deposition experiments. RAIRS is used to probe and quantitate the reaction products. A wavelength range of 4000-750 cm^{-1} with 1 cm^{-1} spectral resolution is used. In section 6.3, it will be explained that C + $^{18}O_2$ acts in a barrierless manner to ultimately form C^{18}O + ^{18}O. ^{18}O can then barrierlessly react with $^{18}O_2$ to form $^{18}O_3$ (Lin & Leu 1982; Ioppolo et al. 2013). Thus, in a very diluted C:$^{18}O_2$ matrix of ~1:500, the $^{18}O_3$ abundance essentially reflects the C-atom abundance at the substrate. This aimed ratio of 1:500 is determined by estimating the C-atom flux using the C-atom flux values from MBE (application of the inverse-square law), and using the Langmuir approximation (1 L = 1.3×10^{-6} mbar s = 1×10^{15} molecules cm^{-2}) to estimate the $^{18}O_2$ flux. Note that an exact ratio of 1:500 is not critical in these specific experiments,

2 Kramida, A., Ralchenko, Yu., Reader, J., and NIST ASD Team (2018). NIST Atomic Spectra Database (ver. 5.6.1), [Online]. Available: https://physics.nist.gov/asd [2019, September 13]. National Institute of Standards and Technology, Gaithersburg, MD. DOI: https://doi.org/10.18434/T4W30F

as the main goal is to just create an overabundance of oxygen. Assuming a linear deposition rate, the flux of $^{18}O_3$, and thus atomic C, can be measured. To calculate the $^{18}O_3$ abundance, a modified Lambert-Beer equation is used, as employed in previous work (Chuang et al. 2018). A setup specific ozone band strength of 4.4×10^{-17} cm molecule^{-1} is applied, and derived by performance of an isothermal consumption experiment of O_3 by H-atoms at a deposition temperature of 50 K. The H-atom bombardment of O_3 ice at 50 K proceeds via an Eley-Rideal mechanism to form products, such as O_2, which desorbs upon formation. Thus, the rate of O_3 consumption by H-atoms is directly proportional to the H-atom flux (i.e., linear) until the surface is only partially covered by O_3. At that point the slope decreases, as the rate of O_3 consumption is hindered by the lack of O_3 at certain binding sites. Thus, the IR absorbance value of O_3 at the transition point is considered to represent a monolayer (ML; 1 ML = 1×10^{15} molecules cm^{-2}) of O_3 ice, and is used to determine the band strength via the modified Lambert-Beer equation. A similar procedure was described in Ioppolo et al. (2013) to determine band strengths with SURFRESIDE².

Table 2.1: The $^{18}O_3$ (C-atom) flux values at various C-atom temperatures, measured from various C + $^{18}O_2$ co-deposition experiments. The C:$^{18}O_2$ ratio is aimed to be ~1:500 in the experiments. [a]Measurement performed with another tantalum tube of the same design.

Thermocouple	Deposition time	$^{18}O_3$ (C-atom) flux
(°C)	(s)	(cm^{-2} s^{-1})
1243	600	1×10^{11}
1287	600	3×10^{11}
1312[a]	600	4×10^{11}
1325[a]	600	7×10^{11}
1445	600	3×10^{12}
1533	600	7×10^{12}

The results are summarized in Table 2.1. An exponential curve can be fit to the values in the last column of Table 2.1 in order to indirectly achieve C-atom flux values between thermocouple temperatures of 1243°C and 1533°C. The fluxes at the extremes are also measured by MBE for this particular source with a quartz crystal microbalance, and values of 1×10^{11} cm^{-2} s^{-1} and 1×10^{12} cm^{-2} s^{-1} are obtained for thermocouple temperatures of 1233°C and 1514°C, respectively. These do not deviate much from the values of 1×10^{11} cm^{-2} s^{-1} (1233°C) and 5×10^{12} cm^{-2} s^{-1} (1514°C) obtained with SURFRESIDE³. The $5\times$ deviation in flux at 1514°C can be due to a number of factors, such as the use of different vacuum chamber designs/geometries (including different pumping capacities), filament designs, and measurement tools. It is clear that for the use of this source in experiments for which flux values are needed, it is important to perform a setup specific calibration. Therefore, the method of measuring the $^{18}O_3$ abundance in an oxygen-rich C + $^{18}O_2$ co-deposition experiment to determine the C-flux should be repeated if changes are made. Note that the inverse-square law is applied in order to compare flux values

to take properly into account the different distances involved in the two used experimental setups.

2.5 Experimental and computational results

The first results of carbon atom chemistry with the SUKO-A in SURFRESIDE[3] are presented below. The two experiments are listed in Table 2.2. These experiments are meant to test the performance of the source by conducting simple reactions that also are considered to be of astrochemical relevancy.

Table 2.2: Description of the performed experiments. Experiment 1 involves co-deposition, and experiment 2 involves pre-deposition. The C-atom fluxes are derived from interpolation of the flux values listed in Table 2.1. The Hertz-Knudsen equation (Kolasinski 2012) is used to determine molecular fluxes. $T_{C\text{-atoms}}$ refers to the temperature probed by the thermcouple. (*) refers to 10 Langmuirs (L).

No.	Exp.	T_{sample} (K)	$T_{C-atoms}$ (°C)	$Flux_{C-atoms}$ ($cm^{-2}s^{-1}$)	Flux $^{18}O_3$ ($cm^{-2}s^{-1}$)	Time (s)
1	C + $^{18}O_2$	10	1315	4×10^{11}	8×10^{13}	3000
2	C + $^{18}O_2$	10	1315	4×10^{11}	*	3000

Isotopically enhanced gas, such as $^{18}O_2$ (Campro Scientific 97%), is used to distinguish reaction products from possible contaminants. Other gases used are H_2 (Linde 5.0) and D_2 (Sigma-Aldrich 99.96%). $^{18}O_2$ gas enters the main chamber of SURFRESIDE[3] through manually operated leak valves from turbo-molecularly pumped dosing lines. Experiments proceed by either a pre deposition or co-deposition manner. In the pre-deposition experiment, molecules are first deposited, followed by C-atom bombardment. In the co-deposition experiments, all species are deposited simultaneously. A major advantage of co-deposition is that product abundance is enhanced due to the constant replenishment of reactants in the ice upper layer. It is also more representative for interstellar processes (Linnartz et al. 2015). Pre-deposition, on the other hand, allows monitoring of the kinetics of formation and consumption of products and reactants, as the initial abundance is known. This method is also preferred when layered ices have to be studied. More detailed information on the application of these two deposition methods can be found in Ioppolo et al. (2014).

Relative molecular abundances are determined by using a modified Lambert-Beer equation, as done previously with the ozone abundance. The infrared band strength of $C^{18}O$ (2086 cm^{-1}) used is 5.2×10^{-17} cm molecule^{-1} (Chuang et al. 2018). For $C^{18}O_2$ (2308 cm^{-1}), a band strength of 4.2×10^{-16} cm molecule^{-1} is used. This value is obtained by multiplying the band strength of 7.6×10^{-17} cm molecule^{-1}, which is from the work by Bouilloud et al. (2015) by a transmission to RAIR setup specific proportionality factor of 5.5, in which the band strength of CO from Chuang et al. (2018) is used.

Fig. 2.11 features the IR signatures of the reaction products of the C + $^{18}O_2$ co-deposition experiment. Such products are $C^{18}O_2$, $C^{18}O$, and $^{18}O_3$. Particu-

larly for the formation of $C^{18}O_2$ and $C^{18}O$, there may be more than one pathway to forming these species. Thus, for a more complete understanding of the C + O_2 reaction network, relevant computationally-derived activation and reaction energies are needed and are shown in Table 2.3. Connecting these energy values to the experimental results can delineate the product formation pathways.

All the density functional theory (DFT) calculations are performed in a gas-phase model, which can be expected to cover the main effects (Meisner et al. 2017a), using Turbomole (TURBOMOLE 2018), accessed via ChemShell (Sherwood et al. 2003; Metz et al. 2014). The unrestricted M06-2X functional (Zhao & Truhlar 2008) is used in conjunction with the def2-TZVP (Weigend et al. 1998) basis set. The geometry optimizations are carried out at the same level of theory using the DL-Find (Kästner et al. 2009) optimizer interfaced via ChemShell. The connecting first-order saddle points (transition states) are obtained using the dimer method (Henkelman & Jónsson 1999; Kästner & Sherwood 2008). Numerical Hessians in DL-Find are used to characterize the optimized geometries as local minima or transition states. Reported energies include harmonic vibrational zero point energies. Intrinsic reaction coordinate (IRC) (Meisner et al. 2017b; Hratchian & Schlegel 2004) calculations are performed to confirm the connections between the transition states and the local minima. Benchmark calculations are carried out using coupled-cluster level UCCSD(T)-F12 (Adler et al. 2007; Knizia et al. 2009), with a restricted Hartree-Fock reference and cc-PVTZ-F12 (Peterson et al. 2008) basis set in Molpro (Werner et al. 2012).

As demonstrated from the computational work, the reaction of C + O_2 barrierlessly leads to the intermediate, linear C-O-O. This process is exothermic by 410 kJ mol^{-1} in comparison to C + O_2 → CO + O, which has a reaction energy of -372 kJ mol^{-1}. In this context, it is noteworthy that both, C and O_2, are in their triplet ground states. As they combine to a singlet state, applying spin conservation results in the generated O-atom to also be in its excited singlet state. Thus, if energy is not dissipated into the ice, the overall process to CO formation is thought to be as fast as an actual barrierless reaction (decay of linear C-O-O to CO + O(^{1}D)). CO can also be formed by the barrierless reaction of C + O_3 → CO + O_2, as listed in Table 2.3. In Fig. 2.12, $^{18}O_3$ is formed by the barrierless reaction of $^{18}O_2$ + ^{18}O, as shown by the increasing signal of $^{18}O_3$. Likely when $^{18}O_2$ becomes limited, $^{18}O_3$ starts to be consumed by C, as shown by the decreasing signal of $^{18}O_3$. Yet in the co-deposition experiment, it is unlikely that $C^{18}O$ is formed from C + $^{18}O_3$, since the matrix of $^{18}O_2$ hinders the reaction between C and formed $^{18}O_3$.

If energy is dissipated into the ice, which is probable to occur as energy dissipation appears to occur within picoseconds (Arasa et al. 2010; Fredon et al. 2017; Qasim et al. 2019b), linear C-O-O can decay to CO_2. However, it should be noted that a continuous reaction path to CO_2 is not found in the present computational simulations due to strong multireference character in the wave function, which is why CO_2 formation from C + O_2 is noted as tentative in Table 2.3. CO_2 can also be formed by CO + O(^{3}P), albeit has a high barrier of 25 kJ mol^{-1}, if O(^{3}P) is in fact formed. CO + O(^{1}D) is barrierless to CO_2 formation (Talbi et al. 2006). The abundance ratio of 12:1 for $C^{18}O$:$C^{18}O_2$ measured in experiment 1 shows that $C^{18}O$ is the more favored product, and thus $C^{18}O_2$ formation is relatively inefficient under our experimental conditions
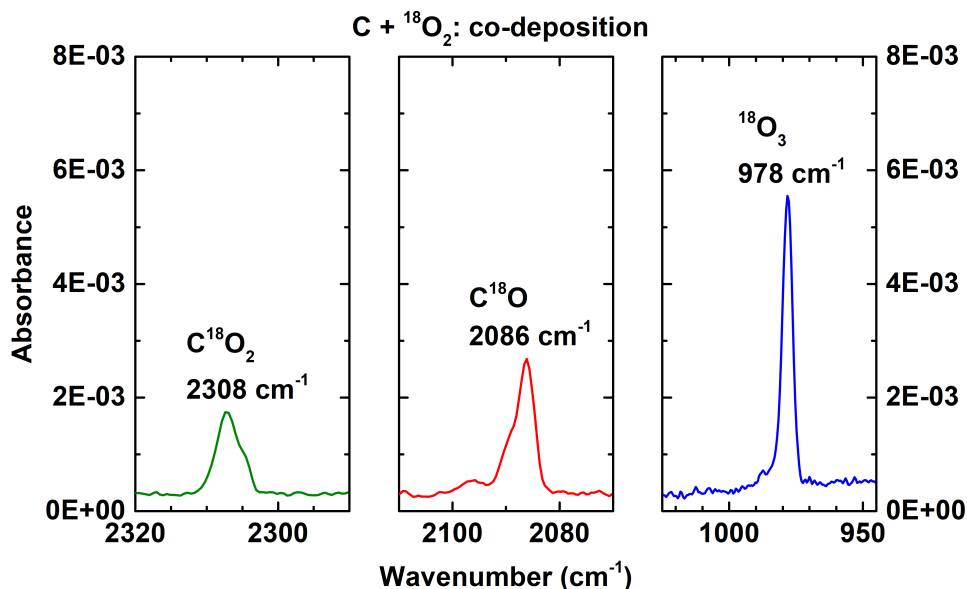
Figure 2.11: A RAIR spectrum acquired after co-deposition of atomic C and $^{18}O_2$ on a 10 K surface (exp. 1). The features of the reaction products, $C^{18}O_2$ (left), $C^{18}O$ (middle), and $^{18}O_3$ (right), are highlighted. A $C^{18}O:C^{18}O_2$ abundance ratio of 12:1 is measured.

Table 2.3: Activation and reaction energies for C + O_2, CO + O(^{3}P), C + O_3, C + CO_2, and C_2O + CO calculated at the M06-2X/def2-TZVP level of theory. Additionally, a benchmark is performed with the CCSD(T)-F12/VTZ-F12 functional. [1] Formation of the intermediate, linear C-O-O, is further discussed in the main text. [2] Tentative (see main text for more details). [3] Barrierless if energy from the formation of the linear C-O-O intermediate goes into the reaction (see main text for more details).

Reaction	Product(s)	Activation energy (kJ mol^{-1})	Reaction energy (kJ mol^{-1})
C + O_2[1]	CO + O(^{1}D)	0[3]	-372
	CO_2[2]	-	-1106
CO + O(^{3}P)	CO_2	25	-527
C + O_3	CO + O_2	0	-981
C + CO_2	CO + CO	29	-540
C_2O + CO	C_3O_2	30	-346

The results of the C + $^{18}O_2$ experiments demonstrate that the C-atom source performs well under our astrochemically relevant experimental conditions to study solid-state reactions. Particularly, the available C-atom flux is sufficient to yield high quality spectra, which allows qualitative and quantitative analysis of the involved chemical pathways.
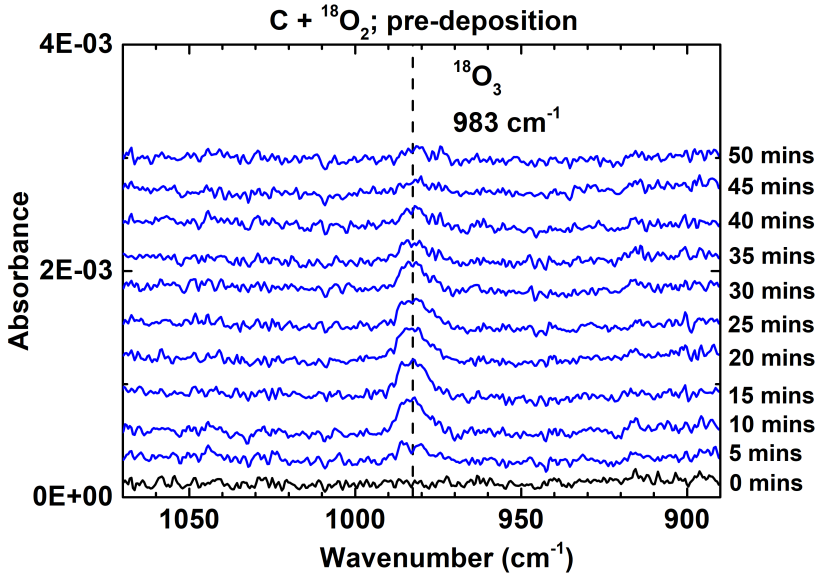
Figure 2.12: RAIR spectra acquired after pre-deposition of atomic C and $^{18}O_2$ on a 10 K surface (exp. 2). 10 L of $^{18}O_2$ is first deposited, followed by carbonation for 50 minutes. The increase and subsequent decrease of the $^{18}O_3$ band is highlighted. RAIR spectra are offset for clarity.

2.6 Astrochemical implications

The new experiments described here are needed to understand how carbonaceous species, and particularly COMs, can be formed by carbon atom chemistry in the early phase of molecular cloud evolution. Such chemistry is expected to be most applicable to the H_2O-rich ice phase, which has a visual extinction (A_V) of $1.5 < A_V < 3$ (Boogert et al. 2015). At such cloud depths, atomic carbon is present, and becomes increasingly locked up in gas-phase CO at greater extinctions ($> 3\ A_V$) (van Dishoeck 1998; Boogert et al. 2015). This carbon then has the chance to react with atomic hydrogen on grain surfaces, for example, to form simple species such as CH_4 (Öberg et al. 2008). The intermediate hydrocarbon radicals, CH_x, may also have the opportunity to react with other species in the H_2O-rich ice phase to form COMs. It should be noted that deeper into the cloud when CO freezes-out, C can also be formed by the dissociation of CO by cosmic-ray-induced processes (Herbst & van Dishoeck 2009; Requena-Torres et al. 2008).

The reaction of C + O_2 in interstellar molecular clouds may occur, as it is demonstrated to be a barrierless reaction, but not expected to be relatively frequent. Although interstellar O_2 ice has not been detected, O_2 has been detected on icy bodies, such as in the coma of comet 67P/Churyumov-Gerasimenko, and is thought to have primordial origin (Bieler et al. 2015; Taquet et al. 2016). As found in Taquet et al. (2016), the distributions of the O_2 ice abundance at $A_V = 2, 4, 6, 8$, and 10 are similar between the A_V levels. Thus, the astrochemical timescales of relatively abundant C and O_2 should overlap. However, atoms

such as H and O also barrierlessly react with O_2, and are at least an order of magnitude higher in abundance than C at the same timescales (Hollenbach et al. 2008; Taquet et al. 2014, 2016). Therefore, the reaction of C with O_2 in the translucent and dense phases of interstellar clouds is assumed to be minor for O_2 consumption. Nonetheless, the experimental and theoretical work presented here shows that atomic carbon and molecular oxygen can readily react if they would neighbor each other on a dust grain. The C + O_2 products, CO, and possibly $O(^3P)$ and CO_2, are unlikely to further react with each other in the laboratory or in the interstellar medium, as such reactions are associated with high activation barriers, as found in Table 2.3. This includes CO + $O(^3P)$ → CO_2 (25 kJ mol^{-1}), C + CO_2 → CO + CO (29 kJ mol^{-1}), and C_2O + CO → C_3O_2 (30 kJ mol^{-1}). However, the formation of $O(^1D)$ from C + O_2 may explain why CO_2 is formed starting from a 'non-energetic' reaction, in which 'non-energetic' refers to a radical-induced process that does not include an external energy source such as UV, cosmic rays, electrons, and/or simple heating of the ice. The reaction of C + O_3 is barrierless and thus may also occur in space. However, it is expected to be relatively infrequent for the same reasons as that for the C + O_2 reaction.

The general relevance for the astrochemical community of using a C-atom source in a setup fully optimized to study atom addition/abstraction reactions in interstellar ice analogues is that it extends on reaction networks proposed before (e.g., Charnley & Rodgers (2005)), but has not been investigated in the laboratory yet. It is expected that experimental investigations of solid-state C-atom chemistry will provide some of the missing fingerprints for how different carbon-bearing species are formed in interstellar ices. To date, the formation of solid-state COMs and other carbon-bearing molecules under interstellar relevant conditions is largely investigated through the combination of molecular radicals (e.g., HCO, C_2H_3, CH_3O), as this way to build the carbon backbone has been experimentally realized for some time. Although it is an important and relevant way to form solid-state carbon-containing species, it is likely not the explanation for the formation of all such species. This is in part due to the presence of atomic carbon in translucent and dense clouds. As atomic C is highly reactive, it may feasibly evolve into C_xH_y structures. These structures can then react with other radicals to form alcohols and aldehydes, as shown in Qasim et al. (2019a) and Qasim et al. (2019b). Alcohols, aldehydes, and other functional groups may also be formed starting from HCO + C (Charnley & Rodgers 2005; Herbst & van Dishoeck 2009) and/or CCO + H. Thus, this work will help understand the relative significance of radical recombination and direct C-atom addition reactions in various interstellar molecular cloud environments. For this, also astrochemical modeling will be needed, taking into account the available C-atom abundances in different astronomical environments. With the options SURFRESIDE^3 offers, it will become possible to provide information on possible reaction networks and reaction efficiencies and in full dependence of astronomically relevant temperatures.

With the expected launch of the JWST in the near future, ice observations should become more prevalent, which also increases the necessity of laboratory C-atom reactions. To date, telescopes have suffered from telluric contamination (ground-based) and lacked the sensitivity to probe ice molecules more complex than methanol. The JWST will provide telluric free data, sensitivity

and/or spectral resolution in the mid-IR that is orders of magnitude higher than encountered with previous telescopes such as the Infrared Space Observatory (ISO) or Spitzer (Martínez-Galarza et al. 2012), and perform ice mapping. These traits alone make the JWST a desired facility for ice observations, and preparations to search for COMs have already been carried out in the laboratory (Terwisscha van Scheltinga et al. 2018). As possible COMs from C-atom chemistry are expected to be formed primarily in the H_2O-rich ice phase, and not in the CO-rich ice phase, C-atom chemistry experiments may provide insight into the origin of the COMs that will be targeted by the JWST. For example, a COM that is effectively formed by C-atom chemistry, but not by other studied pathways, suggests that the detected COM is formed in the polar phase of the cloud. Currently, not even methanol has been directly and exclusively detected in this phase in quiescent clouds (see Figure 7 of Boogert et al. (2015)), and this is a consequence of the relatively low amount of ice at such low extinctions ($A_V < 3$). Thus, this is the ideal time period to investigate C-atom chemistry, as the JWST may have the sensitivity to detect COMs directly in the polar phase that are formed starting from atomic C.

2.7 Conclusions

For the first time, an atomic carbon source capable of producing fluxes in the low 10^{11} – high 10^{12} cm^{-2} s^{-1} range is incorporated into a modified setup that is designed to study the 'non-energetic' chemical processes of interstellar ice analogues. The source comes with new advantages: 1) An alternative way to investigate carbon chemistry in space along a principle that has not been studied so far. 2) A reliable and straightforward method to calibrate the C-atom flux in SURFRESIDE^3 is available. The flux is adequate to probe C-atom chemistry in SURFRESIDE^3, such as the reaction of C + $^{18}O_2$. The experimental results and computationally-derived activation barriers suggest that atomic carbon can react with O_2 and O_3 ice in interstellar molecular clouds, although more abundant species will effectively compete with C. 3) The beam size can be directly measured, which makes it achievable to operate the source without inducing hazardous carbon pollution into the vacuum system. The use of the source also comes with challenges to keep in mind: 1) The production of carbon layers on the sample surface is unavoidable in an experiment (i.e., all experiments take place on a carbonaceous surface). However, the layers observed have a negligible effect on the RAIR intensity. 2) The flux is highly dependent on the filament temperature, and the filament temperature steadily changes within an experiment partially due to the ongoing release of C-atoms. Thus, the longer the experiment, the greater the deviation of the flux between the start and the end of the experiment. 3) On average, the lifetime of a tube is around 14 hours at thermocouple temperatures of around 1300°C. This complicates experiments due to the necessary replacement of the tube, which can be expensive. 4) The extent of thermalization of the C-atoms to the temperature of the substrate is not fully secured yet, and therefore C-atom reactions involving activation barriers require caution, particularly if quantitative analysis is performed. Future studies will focus on developing a method to measure the extent at which C-atoms thermally equilibrate with the sample.

With the positive performance of the modified setup, it is now possible to test what type of COMs can be formed by C-atom chemistry, primarily in a H_2O-rich ice, as these type of COMs are thought to be mixed primarily with H_2O (and also some CO). Such investigations overlap well with the expected launch of the JWST, which will have a sensitivity in the mid-IR that can possibly pick up signatures of COMs formed in low extinction ($A_V \sim$ 2-3) environments directly – something that has yet to be conducted with current observational facilities.

Bibliography

Adler, T. B., Knizia, G., & Werner, H.-J. 2007, J. Chem. Phys., 127, 1

Albar, J., Summerfield, A., Cheng, T. S., et al. 2017, Sci. Rep., 7, 6598

Álvarez-Barcia, S., Russ, P., Kästner, J., & Lamberts, T. 2018, Mon. Not. R. Astron. Soc., 479, 2007

Arasa, C., Andersson, S., Cuppen, H., van Dishoeck, E. F., & Kroes, G.-J. 2010, J. Chem. Phys., 132, 1

Bacmann, A., Faure, A., & Berteaud, J. 2019, ACS Earth Space Chem.

Belloche, A., Müller, H., Garrod, R., & Menten, K. 2016, Astron. Astrophys., 587, A91

Belloche, A., Müller, H. S., Menten, K. M., Schilke, P., & Comito, C. 2013, Astron. Astrophys., 559, A47

Bieler, A., Altwegg, K., Balsiger, H., et al. 2015, Nature, 526, 678

Boogert, A., Gerakines, P. A., & Whittet, D. C. 2015, Annu. Rev. Astron. Astrophys., 53, 541

Bouilloud, M., Fray, N., Bénilan, Y., et al. 2015, Mon. Not. R. Astron. Soc., 451, 2145

Brown, W. A. & Bolina, A. S. 2007, Mon. Not. R. Astron. Soc., 374, 1006

Burke, D. J. & Brown, W. A. 2010, Phys. Chem. Chem. Phys., 12, 5947

Butscher, T., Duvernay, F., Rimola, A., Segado-Centellas, M., & Chiavassa, T. 2017, Phys. Chem. Chem. Phys., 19, 2857

Charnley, S. 2001a, in The bridge between the Big Bang and Biology: Stars, Planetary Systems, Atmospheres, Volcanoes: their Link to Life, ed. F. Giovannelli, 139–149

Charnley, S. & Rodgers, S. 2005, Proceedings of the International Astronomical Union, 1, 237

Charnley, S. & Rodgers, S. 2009, in Bioastronomy 2007: Molecules, Microbes and Extraterrestrial Life, ed. K. Meech, J. Keane, M. Mumma, J. Siefert, & D. Werthimer, Vol. 420, 29–34

Chuang, K. 2018, Univ. Leiden, PhD thesis

Chuang, K.-J., Fedoseev, G., Ioppolo, S., van Dishoeck, E. F., & Linnartz, H. 2016, Mon. Not. R. Astron. Soc., 455, 1702

Chuang, K.-J., Fedoseev, G., Qasim, D., et al. 2018, Astrophys. J., 853, 1

Fayolle, E. C. et al. 2013, PhD thesis, Leiden Observatory, Faculty of Science, Leiden University

Fedoseev, G., Chuang, K.-J., Ioppolo, S., et al. 2017, Astrophys. J., 842, 1

Fredon, A., Lamberts, T., & Cuppen, H. 2017, Astrophys. J., 849, 1

Friedbacher, G. & Bubert, H. 2011, Surface and Thin Film Analysis: A Compendium of Principles, Instrumentation, and Applications (John Wiley & Sons)

Fuchs, G., Cuppen, H., Ioppolo, S., et al. 2009, Astron. Astrophys., 505, 629

Garrod, R. T. & Herbst, E. 2006, Astron. Astrophys., 457, 927

Harrison, I. 2013, Why is there a need for UHV?, http://faculty.virginia.edu/harrison/STM/tutorials/UHV.html/, [Online; accessed 03-October-2019]

Henkelman, G. & Jónsson, H. 1999, J. Chem. Phys., 111, 7010

Henning, T. K. & Krasnokutski, S. A. 2019, Nat. Astron., 3, 1

Herbst, E. 2005, J. Phys. Chem. A, 109, 4017

Herbst, E. & van Dishoeck, E. F. 2009, Annu. Rev. Astron. Astrophys., 47, 427

Hollenbach, D., Kaufman, M. J., Bergin, E. A., & Melnick, G. J. 2008, Astrophys. J., 690, 1497

Hratchian, H. P. & Schlegel, H. B. 2004, J. Chem. Phys., 120, 9918

Humblot, V. & Pradier, C.-M. 2011, in Biointerface Characterization by Advanced IR Spectroscopy (Elsevier), 1–26

Ioppolo, S., Cuppen, H., Romanzin, C., van Dishoeck, E. F., & Linnartz, H. 2010, Phys. Chem. Chem. Phys., 12, 12065

Ioppolo, S., Fedoseev, G., Lamberts, T., Romanzin, C., & Linnartz, H. 2013, Rev. Sci. Instrum., 84, 1

Ioppolo, S., Öberg, K., & Linnartz, H. 2014, in Laboratory astrochemistry: from molecules through nanoparticles to grains, ed. S. Schlemmer, T. Giesen, & H. Mutschke (John Wiley & Sons), 289–309

Kästner, J., Carr, J. M., Keal, T. W., et al. 2009, J. Phys. Chem. A, 113, 11856

Kästner, J. & Sherwood, P. 2008, J. Chem. Phys., 128, 014106

Knizia, G., Adler, T. B., & Werner, H.-J. 2009, J. Chem. Phys., 130, 1

Kolasinski, K. W. 2012, Surface science: foundations of catalysis and nanoscience (West Chester, PA: John Wiley & Sons)

Krasnokutski, S., Goulart, M., Gordon, E., et al. 2017, Astrophys. J., 847, 89

Krasnokutski, S. & Huisken, F. 2014, Appl. Phys. Lett., 105, 113506

Krasnokutski, S., Kuhn, M., Renzler, M., et al. 2016, Astrophys. J. Lett., 818, L31

Lamberts, T., Markmeyer, M. N., Kolb, F. J., & Kästner, J. 2019, ACS Earth Space Chem., 3, 958

Lin, C. & Leu, M. 1982, Int. J. Chem. Kinet., 14, 417

Linnartz, H., Ioppolo, S., & Fedoseev, G. 2015, Int. Rev. Phys. Chem., 34, 205

Lykke, J. M., Coutens, A., Jørgensen, J. K., et al. 2017, Astron. Astrophys., 597, 1

Martín-Doménech, R., Manzano-Santamaría, J., Caro, G. M., et al. 2015, Astron. Astrophys., 584, 1

Martínez-Galarza, J. R. et al. 2012, PhD thesis

Meisner, J., Lamberts, T., & Kästner, J. 2017a, ACS Earth Space Chem., 1, 399

Meisner, J., Markmeyer, M. N., Bohner, M. U., & Kaestner, J. 2017b, Phys. Chem. Chem. Phys., 19, 23085

Metz, S., Kästner, J., Sokol, A. A., Keal, T. W., & Sherwood, P. 2014, Wiley Interdiscip. Rev. Comput. Mol. Sci., 4, 101

Öberg, K. I., Boogert, A., Pontoppidan, K. M., et al. 2008, Astrophys. J., 678, 1032

Palumbo, M. E., Baratta, G. A., Collings, M. P., & McCoustra, M. R. 2006, Phys. Chem. Chem. Phys., 8, 279

Peterson, K. A., Adler, T. B., & Werner, H.-J. 2008, J. Chem. Phys., 128, 01

Phillips, T. & Huggins, P. 1981, Astrophys. J., 251, 533

Qasim, D., Fedoseev, G., Chuang, K. J., et al. 2020a, An experimental study of the surface formation of methane in interstellar molecular clouds

Qasim, D., Fedoseev, G., Chuang, K.-J., et al. 2019a, Astron. Astrophys., 627, A1

Qasim, D., Fedoseev, G., Lamberts, T., et al. 2019b, ACS Earth Space Chem., 3, 986

Qasim, D., Witlox, M. J. A., Fedoseev, G., et al. 2020b, A cryogenic ice setup to simulate carbon atom reactions in interstellar ices

Requena-Torres, M., Martín-Pintado, J., Martín, S., & Morris, M. 2008, Astrophys. J., 672, 352

Sherwood, P., de Vries, A. H., Guest, M. F., et al. 2003, J. Mol. Struct.: THEOCHEM, 632, 1

Simončič, M., Semenov, D., Krasnokutski, S., Henning, T., & Jäger, C. 2020, Sensitivity of gas-grain chemical models to surface reaction barriers: Effect from a key carbon-

insertion reaction, $C + H_2 \rightarrow CH_2$

Soma, T., Sakai, N., Watanabe, Y., & Yamamoto, S. 2018, Astrophys. J., 854, 116

Talbi, D., Chandler, G., & Rohl, A. 2006, Chem. Phys., 320, 214

Taquet, V., Charnley, S. B., & Sipilä, O. 2014, Astrophys. J., 791, 1

Taquet, V., Furuya, K., Walsh, C., & van Dishoeck, E. F. 2016, Mon. Not. R. Astron. Soc., 462, S99

Terwisscha van Scheltinga, J., Ligterink, N., Boogert, A., van Dishoeck, E. F., & Linnartz, H. 2018, Astron. Astrophys., 611, A35

Tielens, A. & Charnley, S. 1997, in Planetary and Interstellar Processes Relevant to the Origins of Life (Springer), 23–51

Tschersich, K. 2000, J. Appl. Phys., 87, 2565

Tschersich, K., Fleischhauer, J., & Schuler, H. 2008, J. Appl. Phys., 104, 1

Tschersich, K. & Von Bonin, V. 1998, J. Appl. Phys., 84, 4065

TURBOMOLE. 2018, V7.0.01, a development of University of Karlsruhe and Forschungszentrum Karlsruhe GmbH, 1989-2007, TURBOMOLE GmbH, since 2007; available from
http://www.turbomole.com.

van Dishoeck, E. F. 1998, in The Molecular Astrophysics of Stars and Galaxies, ed. T. Hartquist & D. Williams (Oxford: Clarendon Press), 53

van Dishoeck, E. F., Black, J. H., et al. 1988, Astrophys. J., 334, 771

Vasyunin, A. I., Caselli, P., Dulieu, F., & Jiménez-Serra, I. 2017, Astrophys. J., 842, 33

Weigend, F., Häser, M., Patzelt, H., & Ahlrichs, R. 1998, Chem. Phys. Lett., 294, 143

Werner, H., Knowles, P., Knizia, G., Manby, F., & Schütz, M. 2012, Mol. Sci., 2, 242

Zhao, Y. & Truhlar, D. G. 2008, Theor. Chem. Acc., 120, 215

Surface formation of methane in interstellar clouds

Methane is one of the simplest stable molecules that is both abundant and widely distributed across space. It is thought to have partial origin from interstellar molecular clouds, which are near the beginning of the star formation cycle. Observational surveys of CH_4 ice towards low- and high-mass young stellar objects showed that much of the CH_4 is expected to be formed by the hydrogenation of C on dust grains, and that CH_4 ice is strongly correlated with solid H_2O. Yet, this has not been investigated under controlled laboratory conditions, as carbon-atom chemistry of interstellar ice analogues has not been experimentally realized. In this study, we successfully demonstrate with a novel C-atom beam implemented in an ultrahigh vacuum apparatus the formation of CH_4 ice in two separate co-deposition experiments: C + H on a 10 K surface to mimic CH_4 formation right before H_2O ice is formed on the dust grain, and C + H + H_2O on a 10 K surface to mimic CH_4 formed simultaneously with H_2O ice. We confirm that CH_4 can be formed by the reaction of atomic C and H, and that the CH_4 formation rate is 2 times greater when CH_4 is formed within a H_2O-rich ice. This is in agreement with the observational finding that interstellar CH_4 and H_2O form together in the polar ice phase, i.e., when C- and H-atoms simultaneously accrete with O-atoms on dust grains. For the first time, the conditions that lead to interstellar CH_4 (and CD_4) ice formation are reported, and can be incorporated into astrochemical models to further constrain CH_4 chemistry in the interstellar medium and in other regions where CH_4 is inherited.

3.1 Introduction

Interstellar methane (CH_4) ice has been detected towards low- and high-mass young stellar objects (YSOs), where it has an abundance relative to H_2O ice of 1-11% (Boogert et al. 2015), and is observationally constrained to be formed primarily from the reaction of H-atoms and solid C at the onset of the H_2O-rich ice phase of molecular clouds (Öberg et al. 2008). This primary pathway to

CH_4 ice formation is also accounted for in astrochemical models (Aikawa et al. 2008). Such a constraint is complemented by the fact that the sequential solid-state reactions, $C + H \rightarrow CH$, $CH + H \rightarrow CH_2$, $CH_2 + H \rightarrow CH_3$, $CH_3 + H \rightarrow CH_4$, are likely to be barrierless (Cuppen et al. 2017) and exothermic (Nuth III et al. 2006), whereas the gas-phase CH_4 formation pathway includes rate-limiting steps (Smith 1989). CH_4 has been detected on comets (Mumma et al. 1996; Gibb et al. 2003), which are thought to have delivered interstellar CH_4 to planetary bodies, particularly during the early phases of our Solar System. Indeed, CH_4 has been detected in a number of planetary systems (Formisano et al. 2004; Swain et al. 2008; Stern et al. 2015), where its origin may be from the interstellar medium (ISM), as reported for the CH_4 found in Titan's atmosphere (Mousis et al. 2002, 2009). In essence, CH_4 is a ubiquitous species within the star formation cycle, with partial origin from the ISM.

To date, the solid-state formation of CH_4 by atomic C and H under conditions relevant to the H_2O-rich ice phase in interstellar clouds has not been confirmed in the laboratory, which causes ambiguity to the idea of the origin and interstellar formation of CH_4. Experimental investigations have been limited to the hydrogenation of graphite surfaces (Bar-Nun et al. 1980) and H_2O-poor conditions (Hiraoka et al. 1998), where the reported formation pathways of CH_4 are still under debate. The work by Hiraoka et al. (1998), which the experimental conditions are closest to the study presented here, consisted of plasma-activated CO gas as the atomic carbon source and did not include a H_2O ice matrix. The present work shows CH_4 formation starting directly from atomic C in a H_2O-rich ice, which is a more realistic interstellar scenario. The lack of experimental evidence on this topic is due to the technical challenges that are associated with the coupling of an atomic carbon source with an ultrahigh vacuum (UHV) setup that is designed to study atom-induced surface reactions under molecular cloud conditions. In this study, we investigate two interstellar relevant reactions for CH_4 ice formation: the simultaneous deposition of C + H and C + H + H_2O on a 10 K surface. This first experimental investigation of CH_4 ice by the reaction of C- and H-atoms under conditions mimicking those of interstellar molecular cloud environments is essential to understanding the distribution of CH_4 in the star formation cycle. Such work also provides formation yields, rates, temperature and reactant dependencies – values which were not previously available in the literature.

3.2 Results

Figure 3.1 provides a visual of the two investigated experiments, whereas more details are found in the Methods section. Product identification is unambiguously shown by the *in situ* detection technique, reflection-absorption infrared spectroscopy (RAIRS). A list of the experiments performed and the following formation yields are provided in Table 3.1. The flux of H_2O ($\sim 6 \times 10^{12}$ molecules cm^{-2} s^{-1}) was chosen to create a CH_4:H_2O ratio of 10% for experiments 2.1-2.3 in order to reflect the composition of interstellar ices (Boogert et al. 2015). It is important to note that H_2O is simultaneously deposited with C and H to create a mixed CH_4 and H_2O ice, as would be found in cold interstellar clouds, and is not meant to represent the accretion of gas-phase H_2O in such environ-

ments. The flux of H-atoms used was $\sim 9 \times 10^{12}$ atoms cm^{-2} s^{-1}, in comparison to $\sim 5 \times 10^{11}$ atoms cm^{-2} s^{-1} for that of C-atoms, which is representative of the dominance of H-atoms over C-atoms in the ISM. Each experimental set has the purpose of disentangling other possible CH_4 formation routes. Additionally, the table provides information on how various experimental conditions influence the formation of CH_4 (CD_4) when H_2O is present and/or absent. The results from each experiment are discussed below.
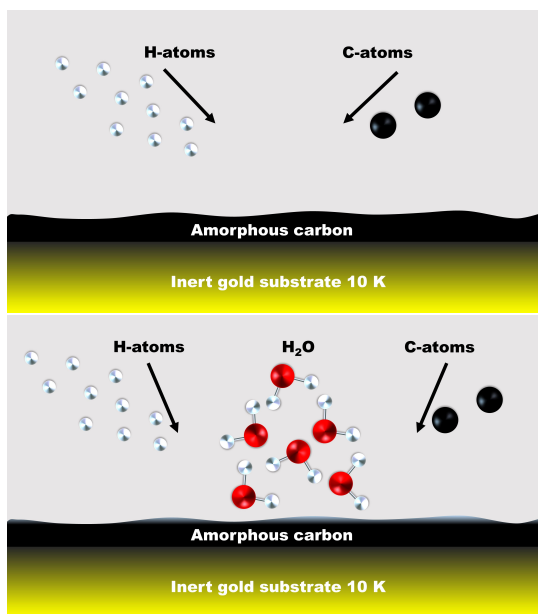

Figure 3.1: Visualization of the two experiments highlighted in this study. (Left) The simultaneous deposition of C- and H-atoms on a 10 K carbonaceous surface is shown. (Right) The addition of H_2O molecules is illustrated. Note that the formation of carbonaceous layers is due to the high sticking of C-atoms and available flux. The angles of deposition are arbitrarily displayed.

The RAIR spectra reflecting the experiments of 1.1-1.3 and 2.1-2.3 in Table 3.1 are displayed in Figure 3.2. The left and right panels unambiguously confirm CH_4 formation by featuring the very strong ν_4 mode of CH_4 (Chapados & Cabana 1972) at various deposition times. Extra confirmation of CH_4 formation by D-isotope substitution and appearance of the ν_3 mode are provided in the Supporting Information, Figure S2. In both, C + H and C + H + H_2O experimental sets, CH_4 formation is observed within minutes, in addition to no detection of CH_n radicals or their recombination products such as C_2H_2, C_2H_4, and C_2H_6. This is consistent with the efficient recombinations between CH_n radicals and H-atoms, and that the lifetime of such radicals is relatively short under our experimental conditions. This also implies that the competing H-abstraction reactions do not dominate in either case. The abstraction reactions, $CH + H \rightarrow C + H_2$ and $CH_2 + H \rightarrow CH + H_2$, are reported to be essentially barrierless (Baulch et al. 1992; Harding et al. 1993), whereas the barrier for $CH_3 + H \rightarrow CH_2 + H_2$ is reported to have a high value of $\sim$7600-7700 K (Baulch et al. 1992). $CH_4 + H \rightarrow CH_3 + H_2$ also has a high barrier height of $\sim$7450-7750

Table 3.1: A list of experiments, along with the experimental parameters and subsequent product yields. Note that experiments 1.1-1.3 represent the same experiment, but with varying fluences (also with experiments 2.1-2.3). (-) and (<) refer to not applicable and non-detections, respectively. (*) Cannot directly compare to CH_4 column densities. See main text for more details. Details on band strength determination for column density calculations are found in the Methods section. The reported CH_4 column densities are overestimated by $< 25\%$, as C can possibly react with H_2/D_2 in the H_2O/D_2O experiments to form CH_4/CD_4, but not with H_2O/D_2O, as further discussed in the Supporting Information (see Figures S1 and S3).

No.	Experiments	T_{sample}	Column density$_{CH_4/CD_4}$	Column density$_{H_2O}$	Ratio$_{CH_4:H_2O}$	Time
		(K)	(molecules cm^{-2})	(molecules cm^{-2})	(%)	(s)
1.1	C + H	10	2.8×10^{14}	-	-	1440
1.2	C + H	10	2.5×10^{14}	-	-	1080
1.3	C + H	10	2.1×10^{14}	-	-	720
2.1	C + H + H$_2$O	10	8.1×10^{14}	8.0×10^{15}	10	1440
2.2	C + H + H$_2$O	10	6.4×10^{14}	6.4×10^{15}	10	1080
2.3	C + H + H$_2$O	10	4.3×10^{14}	4.2×10^{15}	10	720
2.4	C + H$_2$ + H$_2$O	10	2.0×10^{14}	4.1×10^{15}	5	1440
3	C + D + H$_2$O	10	7.7×10^{14}*	7.6×10^{15}	10	1440
4	C + H + H$_2$O	25	$< 4.2 \times 10^{13}$	7.2×10^{15}	< 0.6	1440

K (Corchado et al. 2009), and thus may explain why CH_4 continues to form despite some abstraction reactions competing with addition reactions.
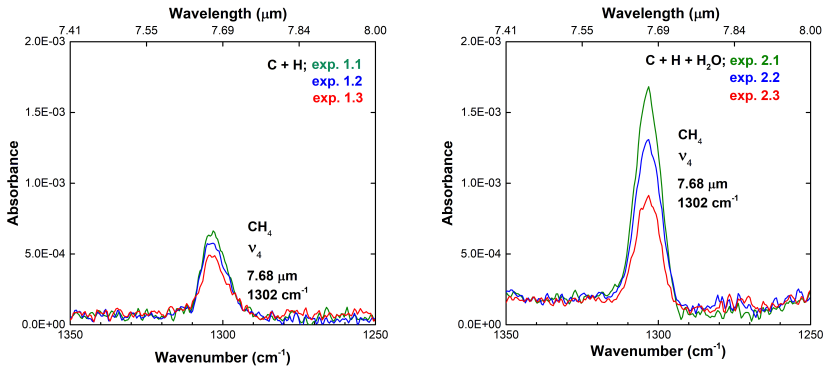
Figure 3.2: (Left) RAIR spectra, in which only the selected feature of interest is shown (i.e., CH_4 ν_4 mode), were acquired after co-deposition of C + H on a 10 K surface in 360 second intervals (exps. 1.1-1.3), and (right) after co-deposition of C + H + H$_2$O on a 10 K surface in 360 second intervals (exps. 2.1-2.3). RAIR spectra are offset for clarity.

It is apparent from Table 3.1 and the panels of Figure 3.2 that CH_4 formation is more efficient in the C + H + H$_2$O experiment. The formation rate of CH_4 in the C + H experiment is no greater than 3.5×10^{11} molecules cm^{-2} s^{-1}, and in the C + H + H$_2$O experiment, it is 5.6×10^{11} molecules cm^{-2} s^{-1}. Note that the total C + H kinetic curve (until CH_4 saturation) is non-linear. After

1440 s of deposition, the total column density of CH_4 amounts to 2.8×10^{14} molecules cm^{-2} and 8.1×10^{14} molecules cm^{-2} for the C + H and C + H + H_2O experiments, respectively. Thus, despite the H_2O-ice matrix, which could potentially block C- and H-atoms from meeting each other, formation of CH_4 is actually enhanced when H_2O is included. This phenomenon is likely, in part, due to the increase in the sticking coefficient of atomic H when H is in the presence of amorphous solid water (ASW) (Öberg et al. 2010; Veeraghattam et al. 2014), and the increase in the surface area that atoms can stick to (Mayer & Pletzer 1986). The sticking probability of H-atoms with an incident energy of 300 K on a 10 K ASW ice is 0.4 (Veeraghattam et al. 2014), in comparison to the lower value of ~0.02 for that of graphite (Lepetit et al. 2011). Note that the carbon allotrope formed from the atomic source is determined to be amorphous (Albar et al. 2017), and thus the sticking coefficient of H on our carbon surface is likely higher than ~0.02.

The surface formation mechanism is probed in the C + H + H_2O experiment at 25 K (exp. 4, Figure S4 of the Supporting Information). The formation of CH_4 at a deposition temperature of 25 K is negligible in comparison to the formation of CH_4 in exp. 2.1, and additionally the CH_4 feature is within the level of the noise. This finding indicates that the temperature of the surface largely influences the reaction probability, as the residence time of H-atoms drastically drops above ~15 K (Fuchs et al. 2009; Ioppolo et al. 2010; Chuang et al. 2016). Thus, the Langmuir-Hinshelwood mechanism, which is temperature dependent, is predominant in the formation of CH_4 at 10 K.

3.3 Astrochemical implications and conclusions

With the utilization of a UHV setup designed, in part, to investigate the simultaneous accretion of C- and H-atoms in two interstellar relevant ices, we experimentally confirm that CH_4 formation proceeds and is more favored when H_2O is added to the C + H reaction at 10 K. This supports the conclusions of the observational survey of CH_4 ice by Öberg et al. (2008) that much of the detected CH_4 is found in the polar phase of ice evolution and formed by atomic C and H. The main route to CH_4 formation in our experiments is H-atom addition to C-atoms in a H_2O ice:

$$C + H \underset{H_2O}{\rightarrow} CH, CH + H \underset{H_2O}{\rightarrow} CH_2, CH_2 + H \underset{H_2O}{\rightarrow} CH_3, CH_3 + H \underset{H_2O}{\rightarrow} CH_4$$
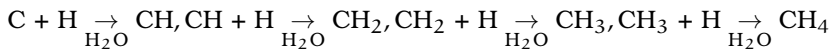
which predominantly follows a Langmuir-Hinshelwood mechanism at 10 K.

The findings presented here parallel the assumption used in models that the sequential hydrogenation of C is barrierless. It is suggested that astrochemical models take into account that the formation of interstellar CH_4 should still proceed when C and H accrete onto the growing polar ice, as it is experimentally shown that H_2O enhances the probability for C and H to react. Whether the CH_4 abundance will substantially increase due to the presence of H_2O on an interstellar dust grain needs to be tested in a model. As the astronomically observed CH_4-H_2O correlation towards YSOs is predominantly set by the availability of the simultaneous accretion of C, O, and H, the CH_4 formation rate factor of 2 in a H_2O-rich ice experiment is not expected to directly lead to a

CH_4 formation rate factor of 2 in an astrochemical model. Additionally, in an interstellar ice, C will compete with other species to react with H. Thus, it is also suggested that the assumed rate of 2×10^{11} s^{-1} used in models for barrierless reactions (*private communication, H. Cuppen*) should be multiplied by 1 < x < 2 for CH_4 formation in a H_2O-rich ice by the sequential hydrogenation of C.

This work shows that CH_4 can be formed in the solid-state under conditions relevant to interstellar clouds, without the need for extra heat or 'energetic' particles. On the other hand, UV photons (or enhanced cosmic rays) are needed to maintain a high abundance of atomic C and O in the gas-phase, which can accrete onto grains to make CH_4 and H_2O ices. Thus, the early low density translucent cloud phase is optimally suited to make both ices simultaneously and abundantly. In the later denser cloud phases, most gaseous carbon has been transformed into CO, which – after freeze-out onto the grains – can be transformed into complex organic ices, and, under cold protoplanetary disk conditions, ultimately to CH_4 and hydrocarbon ices (Bosman et al. 2018). It is clear that the reaction proceeds effectively at lower versus higher temperatures, and is enhanced in a H_2O matrix, both of which are in-line with astronomical observations. Astrochemical modeling is necessary to take into account the available C-atom fluxes in the ISM in order to place the present findings into a cosmochemical picture. Such dedicated models can then be used to aid in the interpretation of CH_4 ice observations with the upcoming James Webb Space Telescope (JWST), as CH_4 is best observed with space-based observatories. The increase in sensitivity of the JWST Mid-Infrared Instrument is expected to allow observations of CH_4 ice towards numerous background stars to probe more quiescent environments, in addition to observations towards YSOs. The work presented here is the first experimental proof of solid-state CH_4 formed in a polar ice. The incorporation of a pure C-atom channel in interstellar networks is as important as including the N-atom channel for the formation of NH_3 (Fedoseev et al. 2014) and the O-atom channel for the formation of H_2O (Ioppolo et al. 2008). As molecular clouds are the universal starting point in the star and planet formation process, this also means that much of the chemical inventory in protoplanetary disks and possibly planets is due to the chemical processes that take place on icy dust grains in molecular clouds prior to collapse.

The present approach also has applications beyond the formation of CH_4. It becomes possible to focus on COM formation through C-atom addition (Charnley 1997a, 2001a; Charnley & Rodgers 2005, 2009). The carbon backbone of COMs has already been proven to be formed by the reaction between C-bearing radicals, such as between HCO and CH_2OH (Chuang et al. 2016). This new experimental way of forming COMs by adding atomic C will aid in better understanding the origin of detected COMs, as astrochemical models will be able to take into account the relevance of C-atom addition reactions by including data from experimental simulations, such as those found here.

3.4 Methods

The experiments presented in this article were performed with SURFRESIDE^2, which is an ultrahigh vacuum (UHV) apparatus that allows qualitative and quantitative investigations of the ice chemistry of molecular clouds. The initial design is discussed in the work by Ioppolo et al. (2013), and details on the recent modifications are provided by Qasim et al. (2019). The apparatus partially consists of three atomic beam line chambers that are connected to a main chamber, which reaches a base pressure of $2-3 \times 10^{-10}$ mbar prior to co-deposition. Within the middle of the chamber is a closed-cycle helium cryostat that has a gold-plated copper sample used to grow ices. On top of the sample lies a coating of carbon that is visible to the naked eye, and has been characterized to be amorphous when originating from the atomic carbon source (Albar et al. 2017). Due to the high sticking coefficient of atomic carbon, formation of these carbonaceous layers is difficult to avoid. Resistive heating of a cartridge heater was applied to heat the sample. With the incorporation of a sapphire rod, the sample is able to be cooled to a low temperature of 7 K and heated to a high temperature of 450 K. Such temperatures were measured by a silicon diode sensor that has an absolute accuracy of 0.5 K.

In this study, two of the three atomic beam lines were used to create atoms, where the base pressure of both atomic chambers was $2-3 \times 10^{-9}$ mbar. A Microwave Atom Source (MWAS; Oxford Scientific Ltd.), which consists of a 2.45 GHz microwave power supply (Sairem) that was operated at 200 W, was employed to produce H- and D-atoms from H_2 and D_2, respectively, with a dissociation rate that is less than unity. A nose-shaped quartz tube is attached at the exit of the source so that atoms can depart energy through collisions with the tube before reaching the cooled sample. An atomic carbon sublimation source (SUKO-A 40; Dr. Eberl MBE-Komponenten GmbH), which uses a power supply (Delta Elektronika, SM 15-100) to induce carbon sublimation, was exploited to create ground state C-atoms. Graphite powder was packed within a tantalum tube that was heated to around 2300 K, which leads to a reaction between molecular carbon and tantalum to form TaC_x. This process ultimately breaks apart molecular carbon into atomic carbon. Due to the high sticking coefficient of atomic carbon, a quartz pipe was not incorporated to cool the atoms prior to deposition. However, the heat of the C-atoms involved in the initial step of CH_4 formation is not expected to qualitatively affect the results, as C + H is expected to be barrierless, and $C + H_2 \rightarrow CH + H$ is highly endothermic (Harding et al. 1993; Guadagnini & Schatz 1996). The third atomic beam line, a Hydrogen Atom Beam Source (HABS) (Tschersich & Von Bonin 1998; Tschersich 2000; Tschersich et al. 2008), was not used as a source of H-atoms in this work.

Details on the preparation of gases and liquids used to create the interstellar ice analogues are described below. H_2 (Linde 5.0) and D_2 (Sigma-Aldrich 99.96%) gases were transferred into the MWAS vacuum chamber. A H_2O sample was connected to the HABS chamber, where the H_2O was cleaned before every experiment by one freeze-pump-thaw cycle. Note that H_2O was not formed on the surface but instead deposited, as the focus is to disentangle the formation routes to CH_4. All prepared gases and liquids were released into the main chamber by leak valves.

The reflection-absorption infrared spectroscopy (RAIRS) technique was performed to probe product formation *in situ*, as well as obtain quantitative information about the products formed through analysis of their vibrational modes. A Fourier Transform Infrared Spectrometer (FTIR), with a fixed scan range of 4000 - 700 cm^{-1} and resolution of 1 cm^{-1}, was applied in the RAIRS study. To measure the abundances of CH_4/CD_4 formed and the CH_4/CD_4:H_2O ice abundance ratios, a modified Lambert-Beer equation was used. Band strength values of 4.40×10^{-17} cm molecule^{-1}, 2.20×10^{-17} cm molecule^{-1}, and 4.95×10^{-17} cm molecule^{-1} were used to calculate the column densities of CH_4 (v_4 mode; 1302 cm^{-1}), CD_4 (v_4 mode; 993 cm^{-1}), and H_2O (v_2 mode; 1665 cm^{-1}), respectively. The initial values were obtained from Bouilloud et al. (2015) for CH_4 and H_2O, and from Addepalli & Rao (1976) for CD_4. A transmission-to-RAIR setup determined proportionality factor of 5.5 was then applied. The proportionality factor was calculated using the band strength of CO (2142 cm^{-1}) measured on our setup through the laser interference technique, where the band strength is reported in Chuang et al. (2018).

To secure that the CH_4 formation rate is higher in the H_2O-rich experiment, the repeatability of the C + H and C + H + H_2O experiments was evaluated. As the formation rates are determined by plotting the CH_4 column densities as a function of time, the uncertainty in the formation rates and column densities can be assessed by measuring the relative standard deviation (RSD) between data points of the same experiment that was performed on different days. For the C + H and C + H + H_2O experiments, average RSD values of 10% and 2% were measured, respectively. Such values further secure the claim that the CH_4 formation rate is larger in a H_2O-rich ice. The higher repeatability of the C + H + H_2O experiment is predominantly due to the more accurate column density measurement of CH_4, as the S/N of the 1302 cm^{-1} feature is greater.

S1　Supporting Information

Figure S1 shows RAIR spectra in the range of 1350 - 1250 cm^{-1} in order to compare the control experiment of C + H_2 + H_2O with C + H(H_2) + H_2O, as not all of the H_2 is converted into H in the MW source. Thus, atomic C may participate in a sequence of reactions involving H_2 to ultimately form CH_4. As both experiments were performed under the same parameters (flux, deposition time, and temperature), the abundances of CH_4 formed can be compared. The column densities of CH_4 in the C + H(H_2) + H_2O and C + H_2 + H_2O experiments are 8.1×10^{14} molecules cm^{-2} and 2.0×10^{14} molecules cm^{-2}, respectively. This implies that the upper limit for the C + H_2 reaction route contribution towards the total CH_4 abundance is 25%. It is less because the more dominant reaction route, C + H, is omitted in the C + H_2 + H_2O experiment (i.e., the reaction efficiency is at least a factor of 4 less and likely much more). It is reported that C + H_2 barrierlessly leads to CH + H through the intermediate, CH_2, although it is endothermic by ∼13,450 K (Harding et al. 1993; Guadagnini & Schatz 1996), and therefore considered negligible in the presented experiments. Thus, it is expected that the minor amount of CH_4 formed starting from H_2 is at least due to the barrierless reaction of C + H_2 to form the intermediate, CH_2, followed by two H-atom additions. CH_2 is stabilized due to the presence of the surface

third body. The barrier for the $CH_2 + H_2 \rightarrow CH_3 + H$ reaction is ambiguous (Gesser & Steacie 1956; Lu et al. 2010).
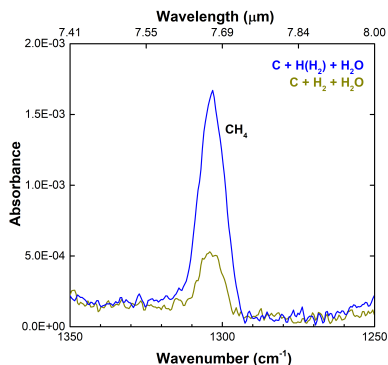

Figure S1: RAIR spectrum acquired after co-deposition of $C + H(H_2) + H_2O$ (exp. 2.1; blue) and $C + H_2 + H_2O$ (exp. 2.4; green) on a 10 K surface, which shows the minor formation of CH_4 starting from H_2 versus H. RAIR spectra are offset for clarity.

Figure S2 provides additional proof for CH_4 formation in the $C + H + H_2O$ experiments. The left panel shows the isotopic shift of the deformation mode when H-atoms are substituted by D-atoms in the co-deposition experiment. This additionally shows that CD_4 can also be formed in a H_2O-rich ice via atom-atom reactions, if D-atoms are available for reaction. A CD_4 column density of 7.7×10^{14} molecules cm^{-2} was measured, which is close to the CH_4 column density. However, the abundances cannot be directly compared, as the D-atom flux used was approximately twice less in comparison to that of H-atoms. The right panel shows the strong C-H stretching vibrational mode of CH_4.
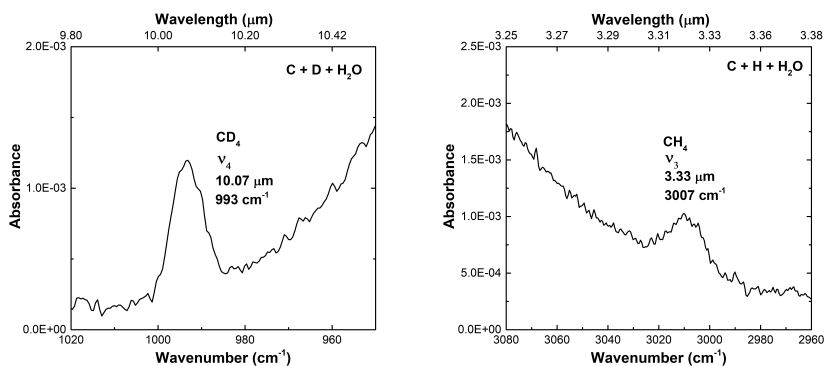

Figure S2: The two panels display proof of methane formation. (Left) The ν_4 mode in the $C + D + H_2O$ experiment (exp. 3), which is intrinsic to that of CD_4 (Chapados & Cabana 1972). This is evidence for CH_4 formation in the C + H + H_2O experiment by observation of the isotopic shift. (Right) Evidence of CH_4 formation in the $C + H + H_2O$ experiment (exp. 2.1) by observation of the CH_4 ν_3 mode on the H_2O wing. RAIR spectra are offset for clarity.

The absence of the CH_4 signature at ~1300 cm^{-1} in the C + D + H_2O experiment (exp. 3) is shown in Figure S3. This indicates that C and H_2O do not react to form CH_4 in exp. 3, and therefore should not contribute to form CH_4 by abstraction of H-atoms from H_2O. This is expected, as the competing reaction of atomic C and H(D) addition is likely barrierless. CD_3H, CD_2H_2, and CDH_3 were also not identified. Whether C reacts with the O-atom of H_2O will be investigated in a separate dedicated study. Figure S4 clearly shows that CH_4 formation is negligible at a deposition temperature of 25 K due to the drop in the H-atom residence time on the surface. This extended residence time required for CH_4 formation is an indication that both, H-atoms and CH_n intermediates have a period of time available to thermalize with the surface prior to reaction in the 10 K experiments.
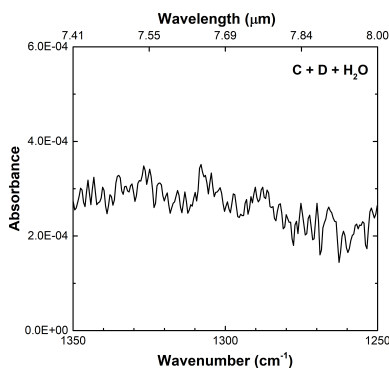

Figure S3: Lack of the C-H bending vibrational signal in the C + D + H_2O experiment (exp. 3), which shows that C does not react with H_2O to form CH_4. RAIR spectrum is offset for clarity.
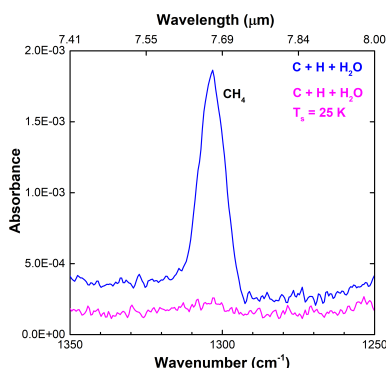

Figure S4: RAIR spectra acquired after co-deposition of C + H + H_2O on a 10 K surface (exp. 2.1; blue) and co-deposition of C + H + H_2O on a 25 K surface (exp. 4; pink), which shows the negligible formation of CH_4 at 25 K. RAIR spectra are offset for clarity.

Bibliography

Addepalli, V. & Rao, N. R. 1976, Indian J. Pure Appl. Phys., 14, 117

Aikawa, Y., Wakelam, V., Garrod, R. T., & Herbst, E. 2008, Astrophys. J., 674, 984

Albar, J., Summerfield, A., Cheng, T. S., et al. 2017, Sci. Rep., 7, 6598

Bar-Nun, A., Litman, M., & Rappaport, M. 1980, Astron. Astrophys., 85, 197

Baulch, D., Cobos, C., Cox, R., et al. 1992, J. Phys. Chem. Ref. Data, 21, 411

Boogert, A., Gerakines, P. A., & Whittet, D. C. 2015, Annu. Rev. Astron. Astrophys., 53, 541

Bosman, A. D., Walsh, C., & van Dishoeck, E. F. 2018, Astron. Astrophys., 618, A182

Bouilloud, M., Fray, N., Bénilan, Y., et al. 2015, Mon. Not. R. Astron. Soc., 451, 2145

Chapados, C. & Cabana, A. 1972, Can. J. Chem., 50, 3521

Charnley, S. 1997a, in IAU Colloq. 161: Astronomical and Biochemical Origins and the Search for Life in the Universe, ed. C. Cosmovici, S. Bowyer, & D. Werthimer, Vol. 161, 89–96

Charnley, S. 2001a, in The bridge between the Big Bang and Biology: Stars, Planetary Systems, Atmospheres, Volcanoes: their Link to Life, ed. F. Giovannelli, 139–149

Charnley, S. & Rodgers, S. 2005, Proceedings of the International Astronomical Union, 1, 237

Charnley, S. & Rodgers, S. 2009, in Bioastronomy 2007: Molecules, Microbes and Extraterrestrial Life, ed. K. Meech, J. Keane, M. Mumma, J. Siefert, & D. Werthimer, Vol. 420, 29–34

Chuang, K.-J., Fedoseev, G., Ioppolo, S., van Dishoeck, E. F., & Linnartz, H. 2016, Mon. Not. R. Astron. Soc., 455, 1702

Chuang, K.-J., Fedoseev, G., Qasim, D., et al. 2018, Astrophys. J., 853, 1

Corchado, J. C., Bravo, J. L., & Espinosa-Garcia, J. 2009, J. Chem. Phys., 130, 184314

Cuppen, H., Walsh, C., Lamberts, T., et al. 2017, Space Sci. Rev., 212, 1

Fedoseev, G., Ioppolo, S., Zhao, D., Lamberts, T., & Linnartz, H. 2014, Mon. Not. R. Astron. Soc, 446, 439

Formisano, V., Atreya, S., Encrenaz, T., Ignatiev, N., & Giuranna, M. 2004, Science, 306, 1758

Fuchs, G., Cuppen, H., Ioppolo, S., et al. 2009, Astron. Astrophys., 505, 629

Gesser, H. & Steacie, E. 1956, Can. J. Chem., 34, 113

Gibb, E., Mumma, M., Russo, N. D., DiSanti, M., & Magee-Sauer, K. 2003, Icarus, 165, 391

Guadagnini, R. & Schatz, G. C. 1996, J. Phys. Chem., 100, 18944

Harding, L. B., Guadagnini, R., & Schatz, G. C. 1993, J. Phys. Chem., 97, 5472

Hiraoka, K., Miyagoshi, T., Takayama, T., Yamamoto, K., & Kihara, Y. 1998, Astrophys. J., 498, 710

Ioppolo, S., Cuppen, H., Romanzin, C., van Dishoeck, E. F., & Linnartz, H. 2008, Astrophys. J., 686, 1474

Ioppolo, S., Cuppen, H., Romanzin, C., van Dishoeck, E. F., & Linnartz, H. 2010, Phys. Chem. Chem. Phys., 12, 12065

Ioppolo, S., Fedoseev, G., Lamberts, T., Romanzin, C., & Linnartz, H. 2013, Rev. Sci. Instrum., 84, 1

Lepetit, B., Lemoine, D., Medina, Z., & Jackson, B. 2011, J. Chem. Phys., 134, 114705

Lu, K.-W., Matsui, H., Huang, C.-L., et al. 2010, J. Phys. Chem. A, 114, 5493

Mayer, E. & Pletzer, R. 1986, Nature, 319, 298

Mousis, O., Gautier, D., & Coustenis, A. 2002, Icarus, 159, 156

Mousis, O., Lunine, J. I., Pasek, M., et al. 2009, Icarus, 204, 749

Mumma, M. J., DiSanti, M. A., Russo, N. D., et al. 1996, Science, 272, 1310

Nuth III, J. A., Charnley, S. B., & Johnson, N. M. 2006, in Meteorites and the Early Solar System II, ed. D. Lauretta & H. McSween (this volume. Univ. of Arizona, Tucson), 147–167

Öberg, K. I., Boogert, A., Pontoppidan, K. M., et al. 2008, Astrophys. J., 678, 1032

Öberg, K. I., van Dishoeck, E. F., Linnartz, H., & Andersson, S. 2010, Astrophys. J., 718, 832

Qasim, D., Fedoseev, G., Lamberts, T., et al. 2019, ACS Earth Space Chem., 3, 986

Smith, I. W. 1989, Astrophys. J., 347, 282

Stern, S., Bagenal, F., Ennico, K., et al. 2015, Science, 350, aad1815

Swain, M. R., Vasisht, G., & Tinetti, G. 2008, Nature, 452, 329

Tschersich, K. 2000, J. Appl. Phys., 87, 2565

Tschersich, K., Fleischhauer, J., & Schuler, H. 2008, J. Appl. Phys., 104, 1

Tschersich, K. & Von Bonin, V. 1998, J. Appl. Phys., 84, 4065

Veeraghattam, V. K., Manrodt, K., Lewis, S. P., & Stancil, P. 2014, Astrophys. J., 790, 4

Methanol ice prior to heavy CO freeze–out

The formation of methanol (CH$_3$OH) on icy grain mantles during the star formation cycle is mainly associated with the CO freeze–out stage. Yet there are reasons to believe that CH$_3$OH also can form at an earlier period of interstellar ice evolution in CO–poor and H$_2$O–rich ices. This work focuses on CH$_3$OH formation in a H$_2$O–rich interstellar ice environment following the OH–mediated H–abstraction in the reaction, CH$_4$ + OH. Experimental conditions are systematically varied to constrain the CH$_3$OH formation yield at astronomically relevant temperatures. CH$_4$, O$_2$, and hydrogen atoms are co–deposited in an ultrahigh vacuum chamber at 10–20 K. OH radicals are generated by the H + O$_2$ surface reaction. Temperature programmed desorption – quadrupole mass spectrometry (TPD–QMS) is used to characterize CH$_3$OH formation, and is complemented with reflection-absorption infrared spectroscopy (RAIRS) for CH$_3$OH characterization and quantitation. CH$_3$OH formation is shown to be possible by the sequential surface reaction chain, CH$_4$ + OH $\rightarrow$ CH$_3$ + H$_2$O and CH$_3$ + OH $\rightarrow$ CH$_3$OH at 10–20 K. This reaction is enhanced by tunneling, as noted in a recent theoretical investigation (Lamberts et al. 2017). The CH$_3$OH formation yield via the CH$_4$ + OH route versus the CO + H route is approximately 20 times smaller for the laboratory settings studied. The astronomical relevance of the new formation channel investigated here is discussed.

4.1 Introduction

Methanol (CH$_3$OH) is an important interstellar molecule. CH$_3$OH has been observed abundantly in both the gas phase (Friberg et al. 1988; Turner 1998; Parise et al. 2002; Bergman et al. 2011; Wirström et al. 2011; Guzmán et al. 2013; Öberg et al. 2014; Taquet et al. 2015) and the solid state (Grim et al. 1991; Allamandola et al. 1992; Skinner et al. 1992; Chiar et al. 1996; Dartois et al. 1999; Gibb et al. 2000; Pontoppidan et al. 2003; Taban et al. 2003; Gibb et al. 2004; Boogert et al. 2008; Bottinelli et al. 2010; Boogert et al. 2011). It is generally accepted that CH$_3$OH formation is most efficient by solid state interactions

on icy grain mantles. Models, supported by experiments, of gas phase synthesis of CH_3OH provide abundances orders of magnitude below the observed fractional abundance of CH_3OH (Garrod et al. 2006; Geppert et al. 2006), while solid state laboratory studies show that CH_3OH is efficiently formed in CO–rich ices through sequential hydrogenation of CO (Hiraoka et al. 1994; Watanabe & Kouchi 2002; Fuchs et al. 2009). This is further supported by computational models (Cuppen et al. 2009; Fuchs et al. 2009; Garrod et al. 2006) that show that hydrogenation of CO ice leads to the production of CH_3OH. Indeed, these findings are in line with the spectroscopic interpretation of observational data; CO and CH_3OH are found to coexist in CO–rich and H_2O–poor interstellar ices (Cuppen et al. 2011; Boogert et al. 2015; Penteado et al. 2015). Not only is it a prevalent interstellar molecule, but CH_3OH is also an important precursor in the formation of larger species. Öberg et al. (2009) illustrated that upon vacuum UV irradiation, CH_3OH can break apart into fragments that can recombine to form complex organic molecules (COMs). In UV–rich environments in the interstellar medium, the formation of CH_3OH may thus be crucial to the formation of larger COMs. The studies by Chuang et al. (2016, 2017) and Fedoseev et al. (2017) show that CH_3OH may be a key player in the formation of larger COMs, also for cold prestellar core conditions. The authors show that radicals derived from CH_3OH via an abstraction process can recombine or combine with other radicals, resulting in the formation of COMs as large as glycerol, even at temperatures below 20 K and without the need for UV–induced radiation.

Recent theoretical and experimental efforts (Lamberts et al. 2017) have provided results that have sparked the idea of H_2O and CH_3OH coexisting in a CO–poor and H_2O–rich interstellar ice. Such ices are thought to form before the "heavy" CO freeze–out stage, which starts to occur at a cloud extinction (A_V) of $A_V > 3$ and dust temperatures < 20 K, and that is followed by the "catastrophic" CO freeze–out stage at $A_V > 9$ and dust temperatures also < 20 K. Prior to the heavy CO freeze–out stage, a $CO:H_2O$ ice ratio of < 5% is expected due to some CO freezing out as well as atom–addition reactions (C, O, H, etc.). Due to the relatively low gas densities at this stage, only a relatively low amount of CO is able to accrete onto dust grains, as examined in Pontoppidan (2006) and discussed in Öberg et al. (2011), Boogert et al. (2015), and van Dishoeck (2017). This time period is known as the "H_2O–rich ice phase" or "polar ice phase" (i.e., the phase that lacks CO ice). CH_3OH formation through this reaction, $CH_4 + OH$, can take place in this phase. However, this does not exclude this reaction to also take place during the CO freeze–out stage, where CH_3OH formation is normally dominated by CO hydrogenation. During this time, O_2 might be intimately mixed with CO (Vandenbussche et al. 1999) and can be hydrogenated to form OH radicals. Gas phase CH_4 becomes more dominant relative to atomic carbon (van Dishoeck 1998) and could freeze out with CO. The importance of the present study is that it focuses on a phase in which CH_3OH is only formed through $CH_4 + OH$, as CO is not frozen out yet, and an identification of CH_3OH in corresponding environments, therefore, directly relates to this alternative reaction pathway.

The study by Lamberts et al. (2017) was done to provide reaction rates at cryogenic temperatures of the reaction between methane (CH_4) and OH as CH_4 has been observed in the H_2O–rich ice phase (Boogert et al. 1997; Öberg et al.

2008), and OH radicals are expected to be abundant in that phase (Cuppen & Herbst 2007; Ioppolo et al. 2008; Cuppen et al. 2010; Oba et al. 2012; Lamberts et al. 2013). These authors, as well as others (Wada et al. 2006; Hodyss et al. 2009; Weber et al. 2009; Zins et al. 2012; Bossa et al. 2015), showed that CH_4 hydrogen abstraction by an OH radical results in the efficient formation of CH_3 radicals; a process that can be induced by tunneling (Lamberts et al. 2017). Thus, these findings can be taken one step further by postulation that the OH–induced abstraction reaction of CH_4 may result in the formation of CH_3OH by the sequential reaction chains: $CH_4 + OH \rightarrow CH_3 + H_2O$ and $CH_3 + OH \rightarrow CH_3OH$. There are already a number of laboratory experiments that exhibit CH_3OH formation via energetic processing of ice mixtures containing CH_4 and H_2O (Schutte 1988; d'Hendecourt et al. 1996; Moore & Hudson 1998; Wada et al. 2006; Hodyss et al. 2009; Martín-Doménech et al. 2016). In addition, Bergner et al. (2017) have explored the formation of CH_3OH via O–atom insertion in CH_4 molecules upon photodissociation of O_2 in binary mixtures. In our paper, the reaction $CH_4 + OH$ leading to the formation of CH_3OH under relevant cold cloud conditions is discussed. The OH radicals are already present at the earliest stages of ice formation via photodissociation of H_2O molecules and by atomic H– and O–rich accreting gas (see, e.g., Boogert et al. 2015). Therefore, this formation mechanism could work even under non–energetic conditions, and can be extended to the formation of COMs that contain the hydroxyl functional group (–OH). Furthermore, CH_3 radical formation is constrained to abstraction reactions only, whereas in the energetic processing studies, it is unclear whether CH_3 radicals are formed by energetic and/or non–energetic pathways.

Data from astronomical observations also provide an incentive to explore CH_3OH ice formation before the heavy CO freeze–out stage (i.e., in the H_2O–rich ice phase). In the review published by Boogert et al. (2015), Figure 7 displays the observed ice column densities of CH_3OH and H_2O, as well as other species, as a function of (A_V). Consistent with the current model of interstellar ice evolution, H_2O is concentrated at a lower A_V with respect to CH_3OH. However, taking a closer look at the figure reveals that CH_3OH upper limit values can be found at a lower A_V and at lower column densities than CH_3OH detections. Such upper limits do not prove that CH_3OH can be formed at lower A_V, but they also do not exclude the idea. A possible explanation for the relatively low A_V and column densities for the CH_3OH upper limits may be due to other reaction pathways expected to take place before the CO freeze–out phase. It is also possible that at such low A_V, the sensitivity of the telescopes used may not have been high enough. In the dawn of the James Webb Space Telescope (JWST) era, it is expected that soon it will be possible to extend on the formation schemes in which solid CH_3OH is formed or consumed.

In this paper, the formation of CH_3OH ice by $CH_4 + OH$ under relevant cold cloud conditions is discussed. Section 4.2 provides an overview of the experimental conditions and methods. Section 4.3 details how CH_3OH was identified, formed in the ice, and quantified. Section 4.4 provides insights into how the laboratory results presented here can be used to constrain the ice chemistry in the H_2O–rich ice phase of cold prestellar core environments, as well as a discussion of Figure 7 from Boogert et al. (2015). Section 4.5 summarizes the findings from this paper.

4.2 Experimental setup and methods

The experiments described here are performed with SURFRESIDE^2. This is a double atom beam line, ultrahigh vacuum (UHV) setup with a base pressure of ~10^{-10} mbar in the main chamber. An in–depth description of the setup and experimental procedures can be found in Ioppolo et al. (2013) and Linnartz et al. (2015). Ices are grown on a gold–plated copper substrate (2.5×2.5 cm^2) that is attached to the cold–finger of a closed–cycle helium cooled cryostat (ColdEdge CH–204 SF). Temperatures as low as 7 K can be realized. The temperature settings are controlled by a LakeShore 340 temperature controller. The substrate temperature is measured by a silicon diode sensor (DT–670) with an absolute accuracy of 1 K. The substrate temperature is changed by resistive heating of a tungsten filament. Incorporation of a sapphire rod within the cryocooler allows substrate temperatures as high as 450 K.

The processes taking place in the ice can be studied through infrared (IR) spectroscopy and mass spectrometry. Species formed in the ice are probed by their IR signatures with a Fourier transform infrared spectrometer (FTIR; Agilent Cary 640/660) applying the reflection-absorption infrared spectroscopy (RAIRS) technique. The FTIR permits a coverage of 6000–700 cm^{-1} with a resolution of 1 cm^{-1}. To further constrain species present in the ice, a quadrupole mass spectrometer (QMS; Spectra Microvision Plus LM76) is used to measure the desorption temperature of ice species during a temperature programmed desorption (TPD) run, as well as the mass spectrum of the desorbing species upon electron impact ionization. A commonly used electron impact ionization energy of 70 eV is chosen. All TPD experiments involve a linear ramp rate of 2 K min^{-1}.

In order to simulate cold cloud conditions, all ices are grown on a substrate surface with a temperature between 10–20 K. CH$_4$, H, and O$_2$ are admitted into the main vacuum chamber following the *co–deposition* technique (i.e., different molecular species deposited simultaneously), which reproduces interstellar conditions better than with previously used pre–deposition techniques (i.e., different molecular species deposited sequentially) (Linnartz et al. 2015). Additionally, this technique allows all deposited species to react with one another, regardless of the ice thickness, which is advantageous when trying to probe trace species. The OH radicals are formed by H–atom addition to O$_2$ (Cuppen et al. 2010) and the CH$_3$ radicals are formed by OH–mediated H–abstraction of CH$_4$ (i.e., radicals are formed *in situ*). A series of control experiments performed by Lamberts et al. (2017) showed that the produced OH radicals are solely responsible for the H–abstraction of CH$_4$ (i.e., formation of CH$_3$ radicals directly through reaction with H–atoms is not efficient, as proved in Lamberts et al. (2017)). We note that the formation of OH radicals from O$_2$ is not necessarily representative of the formation of OH radicals in low A_V (low density) environments, where the O + H route dominates, as well as photodissociation of H$_2$O. Since the OH and CH$_3$ radicals are formed in the ice, they are expected to be thermalized before further reactions occur.

To perform H–atom addition reactions, H–atoms are produced by a Hydrogen Atom Beam Source (HABS) (Tschersich & Von Bonin 1998; Tschersich 2000; Tschersich et al. 2008), and the H–atom beam line has an angle of 45° to surface normal of the gold–plated sample. Hydrogen molecules (H$_2$; Praxair 99.8%)

Table 4.1: Experiments performed in this study. All fluxes, except the H flux, are derived from the Hertz–Knudsen equation.

No.	Experiments	Ratio $CH_4:H:O_2$	T_{sample}* (K)	$Flux_{CH_4}$ $cm^{-2}s^{-1}$	$Flux_H$ $cm^{-2}s^{-1}$	$Flux_{O_2}$ $cm^{-2}s^{-1}$	$Flux_{CH_3OH}$ $cm^{-2}s^{-1}$	$Flux_{H_2O}$ $cm^{-2}s^{-1}$	$Flux_{CO}$ $cm^{-2}s^{-1}$	Time (s)
1.0	$CH_4 + H + O_2$	1:2:1	10	3E12	6E12	4E12	–	–	–	43200
2.0	$CH_4 + H + O_2$	1:2:1	10	3E12	6E12	4E12	–	–	–	21600
2.1	$^{13}CH_4 + H + O_2$	1:2:1	10	3E12	6E12	4E12	–	–	–	21600
2.2	$CH_4 + H + {}^{18}O_2$	1:2:1	10	3E12	6E12	4E12	–	–	–	21600
2.3	$^{13}CH_4 + H + {}^{18}O_2$	1:2:1	10	3E12	6E12	4E12	–	–	–	21600
3.0	CH_3OH	–	10	–	–	–	4E13	–	–	100
4.0	CH_3OH	–	10	–	–	–	1E13	–	–	1200
4.1	$CH_3OH + O_2$ (MWAS)$^\diamond$	–	10	–	–	4E13	1E11	–	–	9000
4.2	$CH_3OH + CH_4$	–	10	6E13	–	–	1E11	–	–	9000
4.3	$CH_3OH + H_2O$	–	10	–	–	–	1E11	6E13	–	9000
4.4	$CH_3OH + H_2O$ (MWAS)$^\diamond$	–	10	–	–	–	1E11	6E13	–	9000
4.5	$CH_3OH + H_2O$ (MWAS)$^\diamond$ + CH_4	–	10	6E13	–	–	1E11	6E13	–	9000
4.6	$CH_3OH + CO$	–	15	–	–	–	2E10	–	7E10	3600
5.0	$^{13}CH_4 + H + {}^{18}O_2$	1:2:1♣	20	3E12♣	6E12	4E12	–	–	–	21600
6.0	$CH_4 + H + O_2$	1:2:1	10	3E12	6E12	1E13	–	–	–	21600

*Temperature of the sample at which the ices are grown. ♣The CH_4 flux is lower than the listed value in order to have the same $CH_4:H_2O$ ice ratio as found in exp. 2.0. Thus, a constant CH_4 flux is not carried out in this particular experiment. $\diamond$"(MWAS)" denotes species that were placed in the MWAS chamber. See also Section 4.3.2.

flow into the HABS chamber via a leak valve and are thermally cracked by a tungsten filament. The gas deposition lines of O_2 (Linde Gas 99.999%) and CH_4 (Linde Gas 99.995%) are angled at $135°$ and $68°$, respectively, to the plane of the sample's surface. Gas isotopologues, $^{18}O_2$ (Campro Scientific 97%) and $^{13}CH_4$ (Sigma–Aldrich 99%), are used as controls to aid in identification of the formed ice products.

Fluxes and column densities are characterized as follows. An absolute D–atom flux was measured by Ioppolo et al. (2013), and the O_2 and CH_4 fluxes are calculated using the Hertz–Knudsen equation (Kolasinski 2012). Column densities are determined by the relation between absorbance and column density, as described in Hudgins et al. (1993). As discussed previously by Ioppolo et al. (2013), Teolis et al. (2007), and Loeffler et al. (2006), such measurements must be done with caution. Therefore in this work, only the relative column densities of CH_4, H_2O, and CH_3OH are given (i.e., absolute column densities are not listed). Care is taken to use integrated absorbances that do not deviate from the linear trend of the column density over time. The band strength used to determine the CH_3OH column density is 7.1×10^{-17} cm molecule^{-1} (1030 cm^{-1}) and is obtained by performance of a He–Ne laser interference experiment in SURFRESIDE^2 (Chuang et al. in prep). The underlying experimental procedure is described in detail in Paardekooper et al. (2016). CH_4 (1302 cm^{-1}) and H_2O (1659 cm^{-1}) band strengths of 8.0×10^{-18} cm molecule^{-1} and 9.0×10^{-18} cm molecule^{-1}, respectively, are extracted from Bouilloud et al. (2015). Since the band strengths from Bouilloud et al. (2015) are obtained from transmission IR experiments, a proportionality factor between the CH_3OH band strengths from Bouilloud et al. (2015) and our laser interference experiment is used as a correction factor. It should be noted that literature transmission band strength values cannot be used with optical depth values obtained from a RAIRS experiment partly due to surface–enhanced dipole coupling that occurs in RAIRS. Setup specific values have to be determined for specified conditions. All experiments discussed in this paper are listed in Table 4.1.

4.3 Results and discussion

4.3.1 Identification and analysis of CH_3OH formation

In the next sections, three different ways to confirm the formation of CH_3OH ice by the reaction, CH_4 + OH, are presented.

4.3.1.1 TPD

Figure 4.1 (top) shows the TPD spectra of pure CH_3OH compared to the TPD spectra of the CH_4 + H + $^{18}O_2$ reaction (bottom) for m/z = 31, 32 and 33, 34, respectively. We note that m/z = 32 also represents the $O_2^{·+}$ ion in the CH_4 + H + O_2 reaction, and therefore TPD data from the $^{18}O_2$ isotope experiment are used instead. Because m/z = 31 (CH_3O^+) and 32 ($CH_3OH^{·+}$) represent the most intense ions for the CH_3OH cracking pattern found in our experimental setup and because their isotopically–induced shifted m/z values in the isotope–enriched experiments can be tracked for most experiments (i.e., the m/z values remain characteristic of CH_3OH and not of other species), we use the m/z
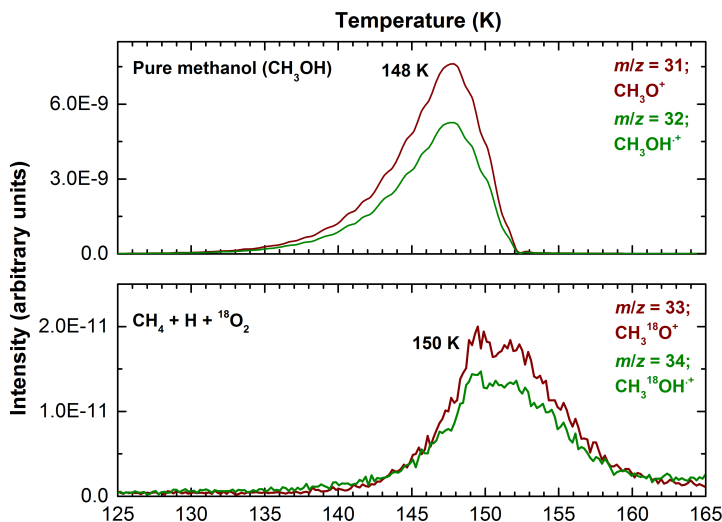
Figure 4.1: TPD of pure CH_3OH (top; exp. 3.0) and TPD of the $CH_4 + H + {}^{18}O_2$ reaction (bottom; exp. 2.2).

values representing CH_3O^+ and $CH_3OH^{·+}$ to confirm the formation of CH_3OH. As seen in Figure 4.1 (top), the signals for m/z = 31 and 32 peak at 148 K for pure CH_3OH. The same m/z signals peak at 150 K in the $CH_4 + H + {}^{18}O_2$ experiment, as seen in Figure 4.1 (bottom). This slight increase in the CH_3OH desorption temperature is expected since the binding energy of CH_3OH will be influenced by the presence of H_2O. It should be noted that H_2O, along with H_2O_2, are formed during the experiments and are not initial reactants of the ice mixture. The similar peak positions and profiles for the CH_3O^+ ($CH_3{}^{18}O^+$) and $CH_3OH^{·+}$ ($CH_3{}^{18}OH^{·+}$) ion signals between the two experiments allows to assign the observed desorption as originating from CH_3OH.

This assignment is further constrained by quantitatively comparing the fragmentation pattern of CH_3OH upon 70 eV electron impact ionization with values available from the NIST database[1]. Figure 4.2 presents a column chart of the relative integrated intensities of the CH_3O^+ and $CH_3OH^{·+}$ ion signals observed in a pure CH_3OH experiment and in isotopically–enriched ${}^{13}CH_4 + H + {}^{18}O_2$ experiments. As seen in Figure 4.2, the relative integrated intensities of pure CH_3OH for m/z = 31 (CH_3O^+) and 32 ($CH_3OH^{·+}$) are 100 and 69, respectively. In the $CH_4 + H + {}^{18}O_2$ experiment, the intensities for m/z = 33 ($CH_3{}^{18}O^+$) and 34 ($CH_3{}^{18}OH^{·+}$) are 100 and 71, respectively. In the ${}^{13}CH_4 + H + {}^{18}O_2$ experiment, the values for m/z = 34 (${}^{13}CH_3{}^{18}O^+$) and 35 (${}^{13}CH_3{}^{18}OH^{·+}$) are 100 and 69, respectively. In the NIST database, the relative integrated intensities for m/z = 31 (CH_3O^+) and 32 ($CH_3OH^{·+}$) are 100 and 74, respectively.

1 NIST Mass Spec Data Center, S.E. Stein, director, "Mass Spectra" in NIST Chemistry WebBook, NIST Standard Reference Database Number 69, Eds. P.J. Linstrom and W.G. Mallard, National Institute of Standards and Technology, Gaithersburg MD, 20899, doi:10.18434/T4D303, (retrieved November 7, 2017)
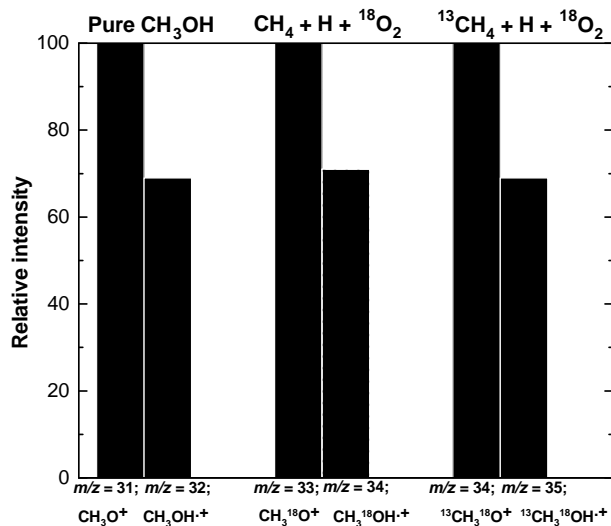
Figure 4.2: Integrated QMS signals normalized to the integrated QMS signals of the $CH_3O^{.+}$, $CH_3^{18}O^{.+}$, and $^{13}CH_3^{18}O^{.+}$ ions from the CH_3OH (exp. 3.0), $CH_4 + H + {}^{18}O_2$ (exp. 2.2), and $^{13}CH_4 + H + {}^{18}O_2$ (exp. 2.3) experiments, respectively. Ratios of the integrated intensities between the isotopes are in agreement with each other and with NIST values representing CH_3OH.

The relative integrated intensities in the three experiments are nearly identical and are close to the values from NIST, fully in line with CH_3OH formation in the ice.

4.3.1.2 RAIRS

Figure 4.3 shows the resulting 4000–700 cm^{-1} (2.5–14.3 μm) spectrum for CH_4 + H + O_2 interacting on a 10 K substrate. Table 4.2 lists the frequencies measured, as well as the identification of species observed and the corresponding vibrational modes. The assignment of the peaks are constrained by considering literature values, isotope experiments, ice desorption temperatures, and varying flux ratios of the reactants. The inset in Figure 4.3 shows a band at 1001 cm^{-1} that is assigned to the C–O stretching mode of CH_3OH. This assignment is based on experiments performed in Section 4.3.2. Literature values for this band (Wada et al. 2006; Hodyss et al. 2009; Martín-Doménech et al. 2016) are normally somewhat higher; around 1015 cm^{-1} when CH_3OH is mixed with H_2O. Even though this band is rather weak, it offers a tool to unambiguously link to CH_3OH as it has no overlap with bands of other species formed in these experiments and actually provides a nicely isolated feature.

A series of additional experiments are performed in order to further prove that the band at 1001 cm^{-1} is indeed due to the C–O stretching frequency of CH_3OH. This is realized in a set of isotope substitution experiments. Figure 4.4 shows spectra of three experiments that involve CH_4, $^{13}CH_4$, O_2, and $^{18}O_2$

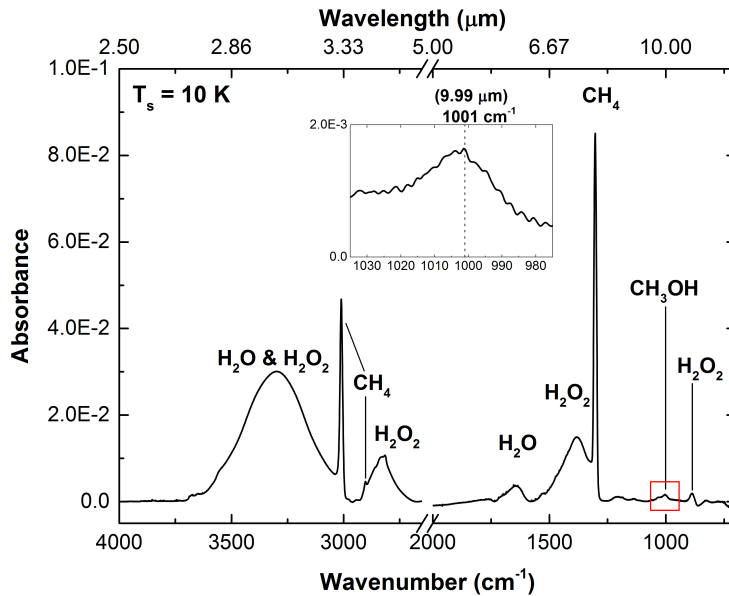Figure 4.3: RAIR spectrum of the reaction, $CH_4 + H + O_2$, on a 10 K substrate surface after 12 hours (exp. 1.0). The relative column density of CH_4:CH_3OH is 100:1, and the relative column density of H_2O:CH_3OH is 100:4. Spectra of the resulting species are shown (see Table 4.2), most noticeably a weaker band around 1000 cm^{-1} (inset) highlighting the C–O stretch of the CH_3OH feature.

Table 4.2: Infrared ice signatures from the $CH_4 + H + O_2$ reaction and the corresponding vibrational modes.

Peak position (cm^{-1})	Peak position (μm)	Molecule	Mode*	Reference
884	11.3	H_2O_2	v_3	1, 2, 3
1001	9.99	CH_3OH	v_8	this work
1302	7.68	CH_4	v_4	4, 5, 7, 8, 9
1381	7.24	H_2O_2	v_2	1, 2, 3
1637	6.11	H_2O	v_2	6
2815	3.55	CH_4	$v_2 + v_4$	4, 5, 7, 8, 9
2836	3.53	H_2O_2	$2v_2$	1, 2, 3
2902	3.45	CH_4	v_1	7, 8, 9
3010	3.32	CH_4	v_3	4, 5, 7, 8, 9
3295	3.0	$H_2O_2 + H_2O$	O–H stretch	10, 11
3675	2.7	H_2O	dangling bonds	7

*The vibrational mode numbers are obtained from NIST.
(1) Giguere & Harvey (1959); (2) Lannon et al. (1971); (3) Romanzin et al. (2011); (4) Hagen et al. (1981); (5) Gerakines et al. (2005); (6) Hodyss et al. (2009); (7) Gálvez et al. (2009); (8) Herrero et al. (2010); (9) Ennis et al. (2011); (10) Cuppen et al. (2010); (11) Ioppolo et al. (2010).

isotopes. By the simple harmonic oscillator approach, a heavier isotope should result in a redshift in the stretching frequency. As seen in Figure 4.4, the 1001 cm^{-1} feature redshifts to 984 cm^{-1} and 973 cm^{-1} for the reactions involving $^{13}CH_4$ and $^{18}O_2$, respectively. This leads to differences of 17 cm^{-1} and 28 cm^{-1} from the 1001 cm^{-1} feature, respectively, comparable to the differences found in CH_3OH isotope experiments performed by Maity et al. (2014). These findings are consistent with isotopically enriched C–O bonds in newly formed CH_3OH.
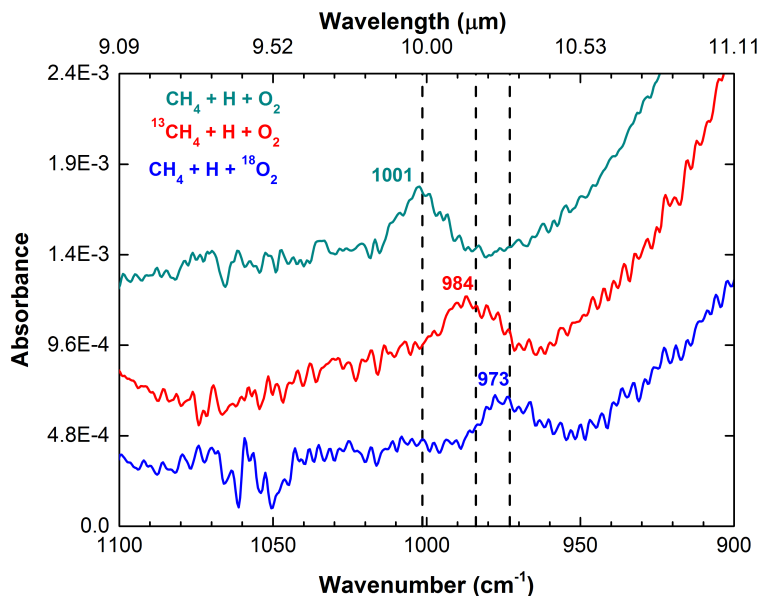
Figure 4.4: RAIR spectra of the reactions, CH_4 + H + O_2 (exp. 2.0), $^{13}CH_4$ + H + O_2 (exp. 2.1), and CH_4 + H + $^{18}O_2$ (exp. 2.2) on a 10 K substrate surface after 6 hours each.

4.3.1.3 Temperature–dependent RAIR difference spectra

The TPD and RAIRS data can be correlated to one another to match IR features with desorption temperatures to further identify species that are initially made in the ice (i.e., before thermal processing via the TPD technique). Figure 4.5 shows the change in the IR features as a function of the substrate temperature (i.e., RAIR difference spectra) for the CH_4 + H + O_2 reaction. In Section 4.3.1.1 the desorption of CH_3OH is observed at 150 K, and in Section 4.3.1.2 the IR feature at 1001 cm^{-1} is shown to be due to CH_3OH formation. The combination of these two pieces of data tells us that below 150 K, CH_3OH should be present in the ice, and above 150 K a majority of the CH_3OH should desorb. In Figure 4.5, the C–O bond feature remains present at a substrate temperature of 145 K and is absent at a substrate temperature of 155 K. This correlates well with the desorption temperature of CH_3OH observed in Figure 4.1 (bottom). Thus, the experiments discussed in Sections 4.3.1.1, 4.3.1.2, and 4.3.1.3 make a consistent case that CH_3OH is formed in the ice.
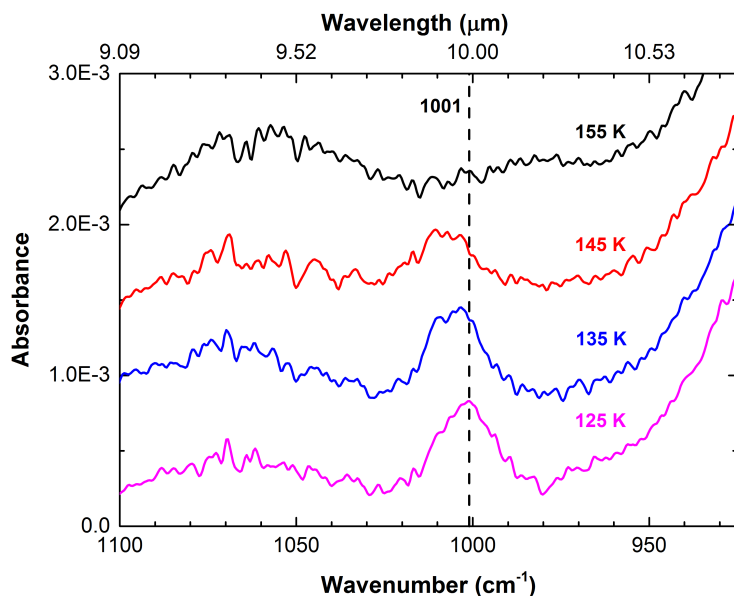
Figure 4.5: RAIR difference spectra of the CH_4 + H + O_2 reaction (exp. 2.0). The 1001 cm^{-1} feature blueshifts between 125 K and 145 K, and could be due to CH_3OH segregating in a H_2O–ice environment (Martín-Doménech et al. 2014), and disappears upon further heating to 155 K.

4.3.2 Spectral signature of CH_3OH in a H_2O–rich ice

Because the C–O bond of CH_3OH is known to be sensitive to its surrounding environment, it holds a potential as a diagnostic tool to provide a deeper insight to the interactions of CH_3OH with other species in the H_2O–rich interstellar ice analogue. Figure 4.6 (left) shows a RAIR spectrum of the C–O stretching frequency of pure CH_3OH (a) in comparison to CH_3OH embedded in an environment originating from the CH_4 + H + O_2 reaction (f), in addition to CH_3OH mixed with other species (b–e, g). Figure 4.6 (right) shows a RAIR spectrum of the C–H stretch of pure CH_3OH; a mode that is a useful tracer of CH_3OH ice and can be probed by observational facilities (e.g., JWST NIRSpec). The experiments are performed using both the previously described HABS and a microwave atom source (MWAS), which dissociates a fraction of the incoming molecules into fragments. The fragments can recombine with each other and form products in the ice that would be found in, for example, the CH_4 + H + O_2 reaction (OH, H, O_2, O, H_2, H_2O_2, etc.). The C–O stretching frequency of pure CH_3OH is found at 1043 cm^{-1} and redshifts to 1015 cm^{-1} in the ice where CH_4 and fragments from dissociated H_2O are co–deposited. We note that the peak does not redshift to 1001 cm^{-1}, and there is a logical explanation for this. As illustrated in Figure 7 in the study by Dawes et al. (2016), an increase in the H_2O concentration in a CH_3OH + H_2O mixture does not necessarily correlate to a more redshifted C–O stretching frequency. Thus, it is expected that a specific ratio of the ice products in the CH_4 + H + O_2 reaction is needed in order to recreate the 1001 cm^{-1} feature. From the spectra presented in Figure 4.6,

it is clear that the largest redshift for the C–O stretch takes place in a H_2O–rich ice matrix that contains CH_4, H_2O, and H_2O dissociation products (i.e., the mixture in the actual CH_4 + H + O_2 experiment; exp. 4.5), as expected. When CH_3OH is mixed with a single species, such as H_2O or CH_4, the C–O stretching frequency does not redshift as much. In conclusion, it is proposed that many, rather than one or two molecular species, interact simultaneously with CH_3OH in the CH_4 + H + O_2 reaction.
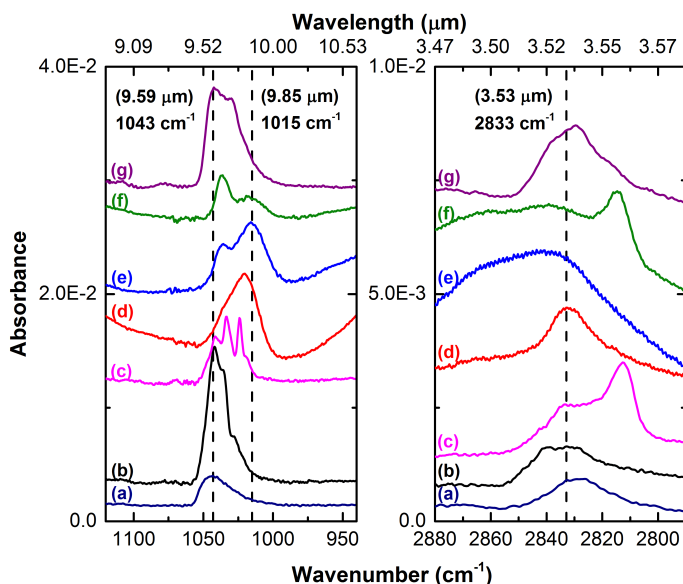

Figure 4.6: (Left) RAIR spectra of the C–O stretch of CH_3OH when CH_3OH is mixed with different species. (a) Pure CH_3OH (exp. 4.0), (b) CH_3OH + O_2 (exp. 4.1), (c) CH_3OH + CH_4 (exp. 4.2), (d) CH_3OH + H_2O (exp. 4.3), (e) CH_3OH + H_2O (exp 4.4), (f) CH_3OH + H_2O + CH_4 (exp 4.5), and (g) CH_3OH + CO (exp 4.6). (Right) RAIR spectra of the symmetric C–H stretch of CH_3OH.

4.3.3 CH_3OH formation at 10 and 20 K

As mentioned in Section 4.2, an absolute value for the CH_3OH column density is not obtained in this study. Thus, in order to provide information on the formation yield of CH_3OH formed at 10–20 K, a relative yield is obtained by comparing the amount of CH_3OH formed at 10 K (exp. 2.0) to the amount of CH_3OH formed at 20 K (exp. 5.0). Since it is expected in interstellar space that CH_4 and H_2O ice are initially formed by hydrogenation reactions (Tielens & Hagen 1982; Öberg et al. 2008; Ioppolo et al. 2008; Cuppen et al. 2010; van Dishoeck et al. 2013), the CH_4:H_2O ice ratio should not be drastically different between surface temperatures of 10 and 20 K. Therefore, the CH_4:H_2O ice ratio is kept the same in this temperature range. At 20 K, a 65% decrease in the CH_3OH abundance is observed compared to the amount of CH_3OH formed at 10 K. This decrease in abundance is expected to be due to the decrease in the H–atom lifetime on the surface (Fuchs et al. 2009; Cuppen et al. 2010), as expected if CH_3OH is being formed by the OH radical. Although, it should

be noted that the reaction steps for CH_3OH formation may also be affected by the temperature change, which can influence the change in the CH_3OH abundance.

4.3.4 Constraining the formation of CH_3OH in the reaction network

The experiments discussed here show that it is possible to form CH_3OH in a H_2O–rich environment along the low temperature pathway:

$$CH_4 + OH \rightarrow CH_3 + H_2O \tag{10a}$$

$$CH_3 + OH \rightarrow CH_3OH \tag{10b}$$

To observe how these channels fit into the overall reaction network ongoing in H_2O–rich ice, the change in abundances of CH_3OH and other ice species needs to be tracked (Öberg et al. 2010). Figure 4.7 shows two RAIR spectra of the reaction, $CH_4 + H + O_2$, and the subsequent infrared features pertaining to newly formed CH_3OH, H_2O, H_2O_2, and O_3. With an enhancement of the O_2 flux (dashed line in Figure 4.7), the CH_3OH abundance decreases and the H_2O_2 and O_3 abundances clearly increase. The decrease in the CH_3OH abundance at the expense of the H_2O_2 and O_3 abundances gives an indication that the formation channel of CH_3OH at least crosses with the formation channels of H_2O_2 and O_3.

The link between the formation of CH_3OH, H_2O_2, and O_3 in the H_2O–rich ice can be better understood when looking at the reaction network presented by Cuppen et al. (2010). In this study, the $H + O_2$ reaction is extensively discussed, and it is found that the O atom used to react with O_2 to form O_3 is most likely created by two reactions,

$$H + HO_2 \rightarrow H_2O + O \tag{11}$$

and

$$OH + O_2 \rightarrow HO_2 + O, \tag{12a}$$
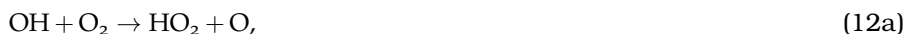
where OH is mainly formed by the following reaction:

$$H + HO_2 \rightarrow 2OH \tag{12b}$$

We note that only the relevant steps are discussed here, and the full reaction scheme can be found in Cuppen et al. (2010). The RAIR spectra shown in Figure 4.7 suggest that the latter reactions are dominant in the $CH_4 + H + O_2$ reaction. As observed in Figure 4.7, a threefold increase in the O_2 flux (exp. 2.0 has a threefold increase in the O_2 flux compared to exp. 6.0) results in a substantial increase in the H_2O_2 abundance compared to the change in the H_2O abundance. This is consistent with reactions 12a and 12b as HO_2 is an intermediate of the H_2O_2 product; HO_2 is also an intermediate of H_2O formation, as shown in reaction 11. However, comparison of the two spectra in
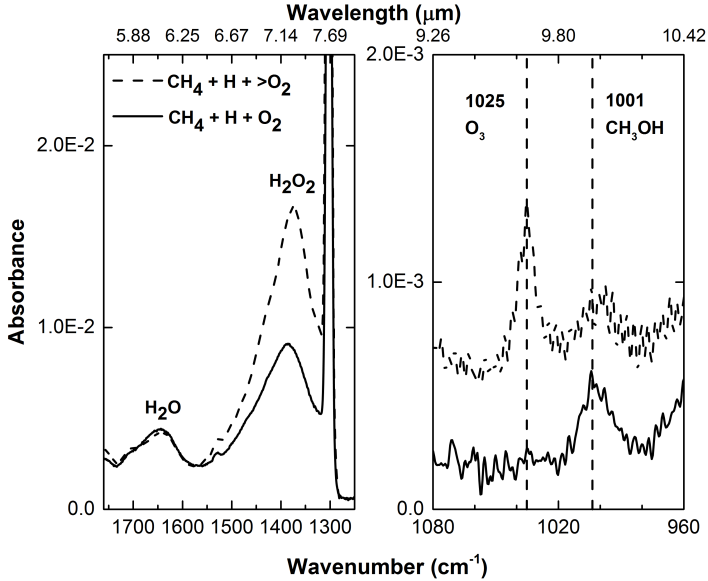
Figure 4.7: RAIR spectra of the reactions, $CH_4 + H + O_2$, where $>O_2$ indicates a threefold increase in the O_2 flux. The dashed–line spectrum corresponds to exp. 2.0, and the solid–line spectrum corresponds to exp. 6.0.

Figure 4.7 shows that an increase in the O_3 abundance is followed by a significant difference in the H_2O_2 abundance and a relatively minor change in the H_2O abundance, suggesting that reactions 12a and 12b are carried out more efficiently than reaction 11 in the $CH_4 + H + O_2$ experiment. Decreasing the CH_4 abundance by 20% shows a 10% decrease in the CH_3OH abundance and no change in the H_2O abundance, which further supports that reaction 11 is not the dominating channel. In addition, reactions 12a and 12b show that O_3 is formed by an OH–induced process, and this is expected since CH_3OH is formed by an OH–mediated reaction. These insights piece together to demonstrate that reactions 12a and 12b are the likely pathways that connect the formation channel of CH_3OH to other formation channels in a H_2O–rich ice reaction network. In Figure 4.8, the laboratory experiments and the astrochemical proposed reactions are summarized in one figure. The main difference between the two is how OH radicals are inserted into the reaction scheme, but this does not change the conclusions derived here for the presented pre–CO freeze–out formation scheme.
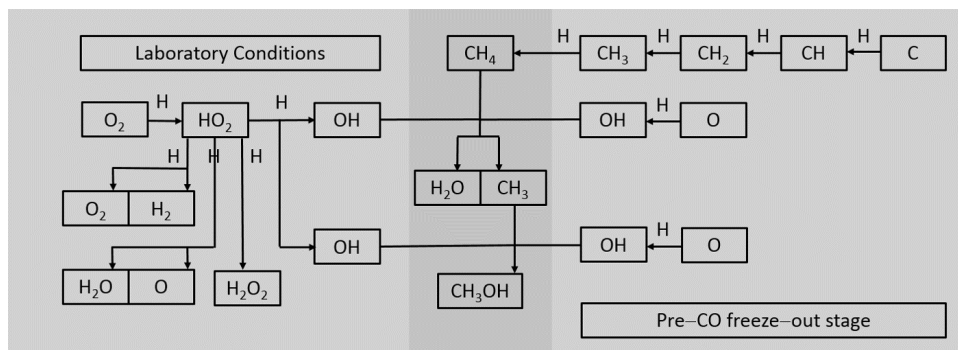
Figure 4.8: Comparison of the laboratory work discussed here and the astrochemical network, resulting in the formation of CH_3OH in the pre–CO freeze–out stage. Only the relevant steps are shown.

4.4 Astrophysical implications

The experimental work presented here calls into question the A_V at which CH_3OH ice starts to grow (i.e., the CH_3OH ice formation threshold). If an observational search for the CH_3OH ice formation threshold in low extinction (i.e., H_2O–rich) environments is to be performed, it would be useful to know beforehand an approximation of the CH_3OH abundance in these H_2O–rich ices. That way, the amount of CH_3OH formed before and after the CO freeze–out stage can be distinguished. A laboratory experiment of CO + H performed under similar conditions to exp. 2.0 shows that the CO:CH_3OH ratio is 100:20. In the parallel CH_4 + OH experiment, the CH_4:CH_3OH ratio is 100:1. A comparison of these two experiments leads to the conclusion that the CH_4 + OH reaction is 20 times less efficient at producing CH_3OH than the CO + H reaction in the laboratory setting. Making the simple assumption that CH_3OH is primarily formed by CH_4 + OH and CO + H in interstellar ices around the CO freeze–out stage, laboratory data can be combined with observational data to determine the amount of CH_3OH in the two different ice phases. According to Boogert et al. (2015), the H_2O:CH_4 and H_2O:CO median ice ratios around low mass young stellar objects (LYSOs) are 100:4.5 and 100:21, respectively. Incorporation of the laboratory results shows that 0.045% of the interstellar ice should contain CH_3OH that derives from CH_4, and 4.2% of the ice should contain CH_3OH that derives from CO. Thus, of the total observed abundance of CH_3OH, about 1% of the total amount is the abundance of CH_3OH from the CH_4 + OH reaction that is expected to be ongoing in the H_2O–rich ice phase. Although a CH_3OH:H_2O percentage of 0.045% may appear insignificant, multiplying this value by the typical H_2O ice to H ratio of 2E–5 yields a CH_3OH ice to H ratio of 9E–9, which is greater than the abundance of gas–phase CH_3OH and other gas–phase species detected in cold cores relative to H_2 (Herbst & van Dishoeck 2009). Using values from the 20 K experiment (exp. 5.0), the CH_3OH ice to H ratio results in a value of 3E–9, which is similar to the abundance of gas–phase CH_3OH in these particular astrophysical environments. We note that the median ice ratios contain sources that also have a relatively high amount of CO ice, so the calculated values are not entirely representative of low extinction

(i.e., H_2O–rich ice) scenarios. See Figure 4.9 for a better approximation of the possible CH_3OH abundance in the H_2O–rich ice layer at various extinctions.
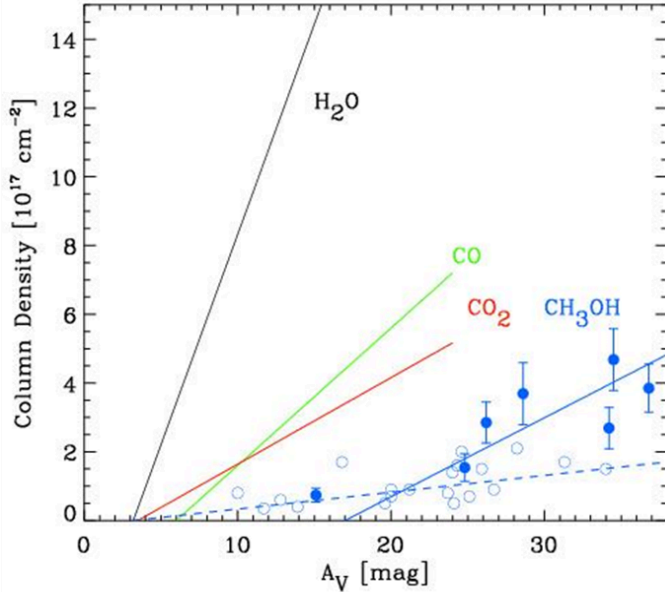

Figure 4.9: Relationships between ice column density and visual extinction (A_V) as observed toward stars behind dense clouds and cores for H_2O (black), CO (green), CO_2 (red), and CH_3OH (blue). For clarity, for H_2O, CO, and CO_2, the least–squares linear fits are shown and not the actual data points. For CH_3OH, blue bullets indicate detections with 1σ error bars and open circles indicate 3σ upper limits. The solid blue line is a fit to the detections, and the dashed blue line (from exp. 1.0) indicates the scenario in which CH_3OH has the same ice formation threshold as H_2O at a maximum abundance of $CH_3OH{:}H_2O$ = 4%, as found in the listed experiments. The 3σ upper limits prove in principle that $CH_3OH{:}H_2O$ is less than 4% in the observed sight lines. This figure was adapted from Figure 7 in Boogert et al. (2015).

Figure 4.9, which is adapted from Boogert et al. (2015), shows that CH_3OH detections have an ice formation threshold at an A_V value higher than H_2O and CO (the ice formation threshold in this figure is the x–axis cut–off divided by 2 because the background stars trace both the front and back sides of the clouds). This is in line with the currently accepted model that CH_3OH ice is mainly formed in prestellar cores at $A_V > 9$ via hydrogenation of accreted CO molecules. However, what is puzzling is that the upper limit sight lines are all below the detections and at similar A_V values to that of the detections. The $CH_3OH{:}H_2O$ ratio of 4:100 derived from the laboratory work presented here (from exp. 1.0) is represented by the dashed blue line and is at the level of 3σ upper limits. Thus, the current observations are consistent with a $CH_3OH{:}H_2O$ ratio of at most a few percent, though likely not as high as 4%, the value seen in our optimized experiments, since H_2O is a by–product in the $CH_4 + H + O_2$ reaction and is not the main source of H_2O in interstellar ices. At this level, a formation threshold as low as that of H_2O (1.6 mag) as a result of chemical

reactions in H_2O–rich ices cannot be excluded. More sensitive observations are needed to further constrain this scenario and with the upcoming launch of the JWST, this soon will be within range.

The insights gained here also link to the formation of larger COMs. Reaction 10 gives rise to the possibility that such a mechanism could lead to the formation of more complex species in H_2O–rich ices. It has been shown that COMs such as glycolaldehyde, ethylene glycol, and glycerol can be successfully formed by hydrogenation of CO (Fedoseev et al. 2015, 2017), thus providing a promising reaction scheme for COM formation in CO–rich interstellar ices. Formation of COMs in H_2O–rich ices has been less studied, and the mechanism described in this paper could be a potential source of molecular complexity in cold H_2O–dominated ice matrices, although formation efficiencies will be lower.

4.5 Conclusions

The formation of CH_3OH by CH_4 + OH shown in this laboratory study suggests that CH_3OH ice can also be formed before the heavy CO freeze–out stage in prestellar cores, i.e., at A_V < 3 and grain temperatures of 20 K. The main findings from this work are summarized below:

◆ The formation of CH_3OH in H_2O–rich ices occurs by the sequential reactions, $CH_4 + OH \rightarrow CH_3 + H_2O$ and $CH_3 + OH \rightarrow CH_3OH$.

◆ Since CH_4 and OH radicals are expected to be found in the H_2O–rich ice phase of cold interstellar clouds, CH_3OH is also expected to be found in those ices, suggesting that the CH_3OH formation threshold is below A_V = 9.

◆ Raising the sample temperature to 20 K results in a 65% decrease in the CH_3OH abundance compared to CH_3OH formed on a 10 K surface, showing that the formation pathway of CH_3OH in this study is relevant to the period of the cold interstellar cloud stage at which ice species are formed primarily by atom–induced reactions (i.e., before gas–phase molecules, like CO, accrete onto the grain surface).

◆ Under similar experimental parameters, the CO + H channel is about 20 times more efficient to forming CH_3OH than the CH_4 + OH channel at temperatures around 10 K.

◆ More sensitive astronomical observations are warranted to determine the CH_3OH:H_2O ratio in H_2O–rich interstellar ices, which is likely to be a few percent at most, as derived from Figure 4.9.

◆ The formation of COMs under cold dense cloud conditions is mainly linked to the CO freeze–out stage. The reactions studied here carry the potential to lead to the formation of COMs at an earlier astrochemical evolution stage.

Bibliography

Allamandola, L., Sandford, S., Tielens, A., et al. 1992, Astrophys. J., 399, 134

Bergman, P., Parise, B., Liseau, R., & Larsson, B. 2011, Astron. Astrophys., 527, A39

Bergner, J. B., Öberg, K. I., & Rajappan, M. 2017, Astrophys. J., 845, 29

Boogert, A., Gerakines, P. A., & Whittet, D. C. 2015, Annu. Rev. Astron. Astrophys., 53, 541

Boogert, A., Huard, T., Cook, A., et al. 2011, Astrophys. J., 729, 1

Boogert, A., Pontoppidan, K. M., Knez, C., et al. 2008, Astrophys. J., 678, 985

Boogert, A., Schutte, W., Helmich, F., et al. 1997, Astron. Astrophys., 317, 929

Bossa, J.-B., Paardekooper, D., Isokoski, K., & Linnartz, H. 2015, Phys. Chem. Chem. Phys., 17, 17346

Bottinelli, S., Boogert, A., Bouwman, J., et al. 2010, Astrophys. J., 718, 1100

Bouilloud, M., Fray, N., Bénilan, Y., et al. 2015, Mon. Not. R. Astron. Soc., 451, 2145

Chiar, J., Adamson, A., & Whittet, D. 1996, Astrophys. J., 472, 665

Chuang, K.-J., Fedoseev, G., Ioppolo, S., van Dishoeck, E. F., & Linnartz, H. 2016, Mon. Not. R. Astron. Soc., 455, 1702

Chuang, K.-J., Fedoseev, G., Qasim, D., et al. 2017, Mon. Not. R. Astron. Soc., 467, 2552

Cuppen, H. & Herbst, E. 2007, Astrophys. J., 668, 294

Cuppen, H., Ioppolo, S., Romanzin, C., & Linnartz, H. 2010, Phys. Chem. Chem. Phys., 12, 12077

Cuppen, H., Penteado, E., Isokoski, K., et al. 2011, Mon. Not. R. Astron. Soc., 417, 2809

Cuppen, H., van Dishoeck, E. F., Herbst, E., & Tielens, A. 2009, Astron. Astrophys., 508, 275

Dartois, E., Schutte, W., Geballe, T., et al. 1999, Astron. Astrophys., 342, L32

Dawes, A., Mason, N. J., & Fraser, H. J. 2016, Phys. Chem. Chem. Phys., 18, 1245

d'Hendecourt, L., Jourdain de Muizon, M., Dartois, E., et al. 1996, Astron. Astrophys., 315, L365

Ennis, C., Yuan, H., Sibener, S., et al. 2011, Phys. Chem. Chem. Phys., 13, 17870

Fedoseev, G., Chuang, K.-J., Ioppolo, S., et al. 2017, Astrophys. J., 842, 1

Fedoseev, G., Cuppen, H. M., Ioppolo, S., Lamberts, T., & Linnartz, H. 2015, Mon. Not. R. Astron. Soc., 448, 1288

Friberg, P., Madden, S., Hjalmarson, A., & Irvine, W. M. 1988, Astron. Astrophys., 195, 281

Fuchs, G., Cuppen, H., Ioppolo, S., et al. 2009, Astron. Astrophys., 505, 629

Gálvez, Ó., Maté, B., Herrero, V. J., et al. 2009, Astrophys. J., 703, 2101

Garrod, R., Park, I. H., Caselli, P., & Herbst, E. 2006, Faraday Discuss., 133, 51

Geppert, W. D., Hamberg, M., Thomas, R. D., et al. 2006, Faraday Discuss., 133, 177

Gerakines, P. A., Bray, J., Davis, A., et al. 2005, Astrophys. J., 620, 1140

Gibb, E., Whittet, D., Boogert, A., & Tielens, A. 2004, Astrophys. J. Suppl. Ser., 151, 35

Gibb, E., Whittet, D., Schutte, W. a., et al. 2000, Astrophys. J., 536, 347

Giguere, P. & Harvey, K. 1959, J. Mol. Spectrosc., 3, 36

Grim, R., Baas, F., Greenberg, J., et al. 1991, Astron. Astrophys., 243, 473

Guzmán, V., Goicoechea, J., Pety, J., et al. 2013, Astron. Astrophys., 560, A73

Hagen, W., Tielens, A., & Greenberg, J. 1981, J. Chem. Phys., 56, 367

Herbst, E. & van Dishoeck, E. F. 2009, Annu. Rev. Astron. Astrophys., 47, 427

Herrero, V. J., Gálvez, Ó., Maté, B., et al. 2010, Phys. Chem. Chem. Phys., 12, 3164

Hiraoka, K., Ohashi, N., Kihara, Y., et al. 1994, Chem. Phys. Lett., 229, 408

Hodyss, R., Johnson, P. V., Stern, J. V., et al. 2009, Icarus, 200, 338

Hudgins, D., Sandford, S., Allamandola, L., & Tielens, A. 1993, Astrophys. J. Suppl. Ser., 86, 713

Ioppolo, S., Cuppen, H., Romanzin, C., van Dishoeck, E. F., & Linnartz, H. 2008, Astrophys. J., 686, 1474

Ioppolo, S., Cuppen, H., Romanzin, C., van Dishoeck, E. F., & Linnartz, H. 2010, Phys. Chem. Chem. Phys., 12, 12065

Ioppolo, S., Fedoseev, G., Lamberts, T., Romanzin, C., & Linnartz, H. 2013, Rev. Sci. Instrum., 84, 1

Kolasinski, K. W. 2012, Surface science: foundations of catalysis and nanoscience (West Chester, PA: John Wiley & Sons)

Lamberts, T., Cuppen, H. M., Ioppolo, S., et al. 2013, Phys. Chem. Chem. Phys., 15, 8287

Lamberts, T., Fedoseev, G., Kästner, J., et al. 2017, Astron. Astrophys., 599, A132

Lannon, J. A., Verderame, F. D., & Anderson Jr, R. W. 1971, J. Chem. Phys., 54, 2212

Linnartz, H., Ioppolo, S., & Fedoseev, G. 2015, Int. Rev. Phys. Chem., 34, 205

Loeffler, M., Raut, U., Vidal, R., et al. 2006, Icarus, 180, 265

Maity, S., Kaiser, R. I., & Jones, B. M. 2014, Faraday Discuss., 168, 485

Martín-Doménech, R., Caro, G. M., Bueno, J., & Goesmann, F. 2014, Astron. Astrophys., 564, A8

Martín-Doménech, R., Caro, G. M., & Cruz-Díaz, G. 2016, Astron. Astrophys., 589, A107

Moore, M. & Hudson, R. 1998, Icarus, 135, 518

Oba, Y., Watanabe, N., Hama, T., et al. 2012, Astrophys. J., 749, 67

Öberg, K. I., Boogert, A., Pontoppidan, K. M., et al. 2008, Astrophys. J., 678, 1032

Öberg, K. I., Boogert, A., Pontoppidan, K. M., et al. 2011, Astrophys. J., 740, 109

Öberg, K. I., Fayolle, E. C., Reiter, J. B., & Cyganowski, C. 2014, Faraday Discuss., 168, 81

Öberg, K. I., Garrod, R. T., van Dishoeck, E. F., & Linnartz, H. 2009, Astron. Astrophys., 504, 891

Öberg, K. I., van Dishoeck, E. F., Linnartz, H., & Andersson, S. 2010, Astrophys. J., 718, 832

Paardekooper, D., Fedoseev, G., Riedo, A., et al. 2016, Astron. Astrophys., 596, A72

Parise, B., Ceccarelli, C., Tielens, A., et al. 2002, Astron. Astrophys., 393, L49

Penteado, E., Boogert, A., Pontoppidan, K., et al. 2015, Mon. Not. R. Astron. Soc., 454, 531

Pontoppidan, K. M. 2006, Astron. Astrophys., 453, L47

Pontoppidan, K. M., Dartois, E., van Dishoeck, E. F., Thi, W.-F., & d'Hendecourt, L. 2003, Astron. Astrophys., 404, L17

Romanzin, C., Ioppolo, S., Cuppen, H., van Dishoeck, E. F., & Linnartz, H. 2011, J. Chem. Phys., 134, 1

Schutte, W. 1988, PhD thesis

Skinner, C., Tielens, A., Barlow, M., et al. 1992, Astrophys. J., 399, L79

Taban, I., Schutte, W., Pontoppidan, K., et al. 2003, Astron. Astrophys., 399, 169

Taquet, V., López-Sepulcre, A., Ceccarelli, C., et al. 2015, Astrophys. J., 804, 1

Teolis, B., Loeffler, M., Raut, U., et al. 2007, Icarus, 190, 274

Tielens, A. & Hagen, W. 1982, Astron. Astrophys., 114, 245

Tschersich, K. 2000, J. Appl. Phys., 87, 2565

Tschersich, K., Fleischhauer, J., & Schuler, H. 2008, J. Appl. Phys., 104, 1

Tschersich, K. & Von Bonin, V. 1998, J. Appl. Phys., 84, 4065

Turner, B. 1998, Astrophys. J., 501, 731

van Dishoeck, E. F. 1998, in The Molecular Astrophysics of Stars and Galaxies, ed. T. Hartquist & D. Williams (Oxford: Clarendon Press), 53

van Dishoeck, E. F. 2017, Proceedings of the International Astronomical Union, 13, 3

van Dishoeck, E. F., Herbst, E., & Neufeld, D. A. 2013, Chem. Rev., 113, 9043

Vandenbussche, B., Ehrenfreund, P., Boogert, A., et al. 1999, Astron. Astrophys., 346, L57

Wada, A., Mochizuki, N., & Hiraoka, K. 2006, Astrophys. J., 644, 300

Watanabe, N. & Kouchi, A. 2002, Astrophys. J. Lett., 571, L173

Weber, A. S., Hodyss, R., Johnson, P. V., et al. 2009, Astrophys. J., 703, 1030

Wirström, E., Geppert, W. D., Hjalmarson, Å., et al. 2011, Astron. Astrophys., 533, A24

Zins, E.-L., Pirim, C., Joshi, P. R., et al. 2012, J. Phys. Chem. A, 116, 12357

Methanol ice formation threshold in dense clouds and dark cores revisited

CH$_3$OH is a central molecule for interstellar complex organic molecule formation. Theoretical, experimental, and observational studies have shown that it is formed abundantly by the hydrogenation of CO-rich ice, deep inside cold, dark cores (formation threshold of $A_V > 9$ mag). This scenario does not seem uniformly applicable, however, because observations have shown a deficiency of the CH$_3$OH ice abundance, by at least a factor of 3, in a significant number of dark core and dense cloud sight-lines tracing depths well above 9 mag. Also, at shallower depths, CH$_3$OH may still be formed, but at lower abundances, via, e.g., CH$_4$ abstraction reactions (Qasim et al. 2018).

In this study, we aim to help address these questions by re-analyzing previously published data (Boogert et al. 2011), as well as new L$-$band spectra of a sample of dense cloud and dark core sight-lines toward background stars. Focus was put into increasing the sensitivity to CH$_3$OH abundances, enabling an improved study of abundance variations as a function of cloud/core depth. The detection and absorption profile analysis of weak ice features in dense clouds and dark cores, such as those of CH$_3$OH, are limited by the contamination with photospheric absorption lines of the background stars. We demonstrate a method to reduce photospheric contamination by dividing over the spectra of un-reddened stars from the NASA Infrared Telescope Facility database.

In a sample of 41 stars behind quiescent dense cloud material and isolated dense cores we report 1 new CH$_3$OH ice detection, bringing the total to 8. The CH$_3$OH ice abundances are 3.4-21% relative to H$_2$O, corresponding to $1.6 \times 10^{-6} - 8.8 \times 10^{-6}$ relative to H$_2$. A linear fit to these detections yields a CH$_3$OH ice detection threshold of only 13.5 ± 7.8 mag. This is within the uncertainty range from Boogert et al. (2011).

Significant non-detections are reported in 34 sight-lines. After correction for the photospheric lines, and at sufficiently high S/N, the CH$_3$OH ice abundances are limited by the contamination with the 3.47 μm ice feature (likely due to NH$_3$.H$_2$O hydrates). Still, the CH$_3$OH ice abundance upper limits (rel-

ative to A_V and H_2O) are low across the entire observed detection threshold A_V range of 5.1–46.0 mag: <0.34% relative to H_2O at A_V = 5.1-16.8 mag, and <0.21% relative to H_2O at A_V = 19.6-46.0 mag.

These results put strict observational constraints on the formation efficiency of CH_3OH ice. A full understanding requires the measurement of the CO ice abundance, as well as ice maps to trace the CO freeze out and CH_3OH formation rate in individual clouds and cores. This will be possible with the upcoming James Webb Space Telescope (JWST). Our method of the photospheric line correction of background star spectra can be applied to the JWST observations.

5.1 Introduction

Grain surface ice chemistry is initiated in the translucent phase of interstellar clouds (density of $\sim 10^3$ H_2 molecules cm^{-3}), and is further accelerated at densities of $\sim 10^4$ - 10^5 cm^{-3} in dense clouds and dark cores (Pontoppidan 2006; Boogert et al. 2015). At a cloud depth corresponding to a visual extinction (A_V) of $\sim$ 1.6 mag, a H_2O-rich ice is present, in which the ice matrix is composed of simple species such as NH_3, CO_2, and CH_4 (Boogert et al. 2015). At $\sim$ 3 mag, some CO ice grows to form an apolar layer (Chiar et al. 1995). At greater depths of $A_V \sim$ 9 mag (10^5 cm^{-3}), CO freezes out nearly completely (Jørgensen et al. 2005; Pontoppidan 2006; Boogert et al. 2015), and is hydrogenated to form methanol (CH_3OH), as confirmed by a number of laboratory, modeling, and observational studies (Watanabe & Kouchi 2002; Fuchs et al. 2009; Cuppen et al. 2009; Boogert et al. 2011; Wirström et al. 2011). A list of the physical parameters of translucent, dense clouds, and dark cores is provided in Table 5.1.

Table 5.1: Physical conditions of the different regions of interstellar clouds, as noted in Table II of van Dishoeck et al. (1993). (a) Dust temperatures are much lower for all noted regions.

ISM region	Density (cm^{-3})	Gas temperature[a] (K)	A_V (mag)
Translucent	500-5000	15-50	1-5
Dense cloud	10^2 - 10^4	$\gtrsim$ 10	$\gtrsim$2
Cold, dark core	10^4 - 10^5	$\approx$ 10	5-25

Hydrogen addition and abstractions reactions in the pathway to CH_3OH also lead to an assortment of complex organic molecules (COMs), such as glycolaldehyde, ethylene glycol, and methyl formate (Chuang et al. 2016), in addition to glycerol (Fedoseev et al. 2017), propanal and 1-propanol (Qasim et al. 2019b). During the dispersal of the envelopes of the Young Stellar Objects (YSOs), the temperature rises, which increases the mobility of ice species and molecular complexity (e.g., Herbst & van Dishoeck 2009). At reduced dust extinctions, enhanced UV-irradiation of CH_3OH ice leads to various COMs as well (Öberg et al. 2009). COMs formed in the ice are released into the gas-phase, however COMs may also be formed in the gas-phase starting from simple molecules that were liberated from the ice (Charnley et al. 1992). Low abundances of

gas phase COMs are also detected in cold (T = 10 K) molecular clouds, where CH_3OH ice is a likely precursor (Soma et al. 2018).

CH_3OH is a key interstellar molecule to complex chemistry, so understanding its prevalence and formation conditions are important. Observations have not provided a consistent formation model. At similar A_V, the CH_3OH ice abundance relative to H_2O varies between detections of 10% and 3σ upper limits of 3% (Boogert et al. 2011, 2015). Perhaps the CO freeze out is limited in certain clouds and cores. For background star observations of dense clouds, a sight-line with a high A_V may have a long pathlength at low density. Lower densities result in higher dust temperatures, which would then decrease the freeze-out and hydrogenation rates of CO (Cuppen et al. 2009). However, this lack of CH_3OH at high A_V has been observed in numerous dark cores (Boogert et al. 2011), and dark cores have high A_V and high densities. Alternatively, CO may be consumed into other reactions, as also proposed in Shimonishi et al. (2016). The CO hydrogenation chain includes many other products besides CH_3OH, as illustrated in Figure 1 of Fedoseev et al. (2017). The low CH_3OH abundance deep in some clouds and cores could also be due to destruction either by internal UV-photons (Öberg et al. 2009) and/or H-abstraction reactions (Goumans & Kästner 2011; Chuang et al. 2016). On the other hand, CH_3OH formation should not be limited to the formation threshold of ~ 9 mag (Boogert et al. 2015), as other formation routes should be relevant at shallower cloud depths. For example, in the laboratory investigation by Qasim et al. (2018), it was found that the CH_4 + OH formation route to CH_3OH should proceed on grain mantles, although at a factor of 20 lower efficiency compared to H addition in CO ices. CH_4 is formed at low extinctions, and there is tentative observational evidence that it is enhanced at cloud edges where not all C has been included in CO yet (Öberg et al. 2008).

Observational constraints on CH_3OH formation models are only based on a handful of detections in dark cores (with and without embedded YSOs) (Boogert et al. 2011; Chiar et al. 2011; Pontoppidan et al. 2003). This limited sample size is in part due to the low sensitivity that is available from current observational facilities, as well as the lack of ice mapping capabilities. The James Webb Space Telescope (JWST), which is expected to be launched in 2021, will significantly improve on both aspects.

Ices in dense clouds and dark cores are typically observed in spectra of background field stars, which are typically cool stars (K- and M-giants). The detection of the ice bands, as well as their absorption profile analysis, is often limited by photospheric line contamination. Here, we present a method to increase the sensitivity of previously published and new observations of the C-H symmetric stretching mode of CH_3OH ice at 3.537 μm by dividing out photospheric lines using spectra of un-reddened stars from the NASA Infrared Telescope Facility (IRTF) database (Rayner et al. 2009). Section 5.2 overviews the parameters of the dust/ice observations and data reduction. All observations were taken towards *background stars*. Section 5.3 details the steps involved in reducing the photospheric lines and measuring the CH_3OH column densities. Sections 5.4 and 5.5 show the application of the method to increase the sensitivity of the data and accuracy of the data analysis in order to better constrain the formation parameters of CH_3OH. Section 5.6 outlines the main findings and proposed work for future studies.

5.2 Observations and data reduction

41 different background stars were observed in the atmospheric L—band with the NASA IRTF/SpeX (Rayner et al. 2003) and Keck 2/NIRSPEC (McLean et al. 1998) spectrometers, tracing the quiescent material in 12 different dense clouds and isolated dense cores (Table 5.2). Some cores contain embedded YSOs, and it is also not certain whether the dense cloud sight-lines trace high densities ($\sim 10^4$), or low densities in long pathlengths. Note that some targets were observed with both SpeX and NIRSPEC. The targets were selected to trace molecular material at a wide range of detection threshold extinctions A_V= 5.1-48.0 mag, as determined from model fits to 1-5 μm broad-band photometry and spectroscopy (Boogert et al. 2011, and in preparation). The spectra of 25 targets were previously published in Boogert et al. (2011).

Table 5.2 also lists the observational parameters, including the spectrometer used, wavelength range covered, the standard star used to reduce telluric contamination, the date of the observation, and the signal-to-noise (S/N) of the continuum emission near the wavelength of the CH_3OH ice band at 3.537 μm (3.460 - 3.530 μm; a region with relatively few telluric lines).

The SpeX instrument was used in the LongXD(1.9) mode, with a slit width of 0.8 arcseconds, resulting in a resolving power R $= \lambda/\Delta\lambda$ = 938. Data reduction was performed using the software package SpeXtool (Cushing et al. 2004) and Xtellcor (Vacca et al. 2003). Keck/NIRSPEC was used in the long-slit mode with a slit width of 0.57 arcseconds, resulting in a resolving power of ~1600. The data reduction procedure for these observations is discussed in Boogert et al. (2011). The wavelength calibration for both SpeX and NIRSPEC is based on telluric emission lines. The radial velocity of the targets was not corrected for.

5.3 Photospheric line correction and column determination

A Python script was created to reduce contamination by photospheric absorption lines from the interstellar dust and ice spectra by fitting un-reddened template spectra from the IRTF spectral library (Rayner et al. 2009). The best-fitting templates for each source, $\chi_\nu{}^2$ (reduced-χ^2), and the CH_3OH column densities derived from the photosphere-corrected spectra are presented in Table 5.3. The following steps were used in this procedure:

1) The spectral resolution of the template spectra (R = 2500 in the L—band; slit width of 0.3 arcseconds) was matched to those of the observed spectra by applying boxcar smoothing. Typically, a boxcar value of 3 was found to be sufficient for the lower resolution SpeX spectra, and no smoothing was needed for the NIRSPEC spectra.

2) A cross-correlation was applied to detect differences of the central wavelengths of the photospheric lines between the template and background star spectra. A wavelength shift was subsequently applied to the science spectrum, correcting for small wavelength calibration errors as well as differences in the radial velocity. In the wavelength range relevant for this work (~3.34-3.71 μm), shifts of < 70 km/s were typically applied, but sometimes as large as 170 km/s.

Table 5.2: Observational parameters. Extinction A_V calculated assuming $A_V/A_K = 8$ (Cardelli et al. 1989). B2011: published in Boogert et al. (2011).

Source 2MASS J	Cloud/Core	Instrument	λ μm	Standard star (SPT)	Date yyyy/mm/dd	Continuum S/N	Notes 3.537μm
04215402+1530299	IRAM 04191	NIRSPEC	2.82-4.14	HR 1251 (A0.5V)	2006/10/09	45	B2011
17111501-2726180	B 59	NIRSPEC	2.41-4.14	HR 6141 (B3V)	2005/06/28	54	B2011
17111538-2727144	B 59	NIRSPEC	2.41-4.14	HR 6141 (B3V)	2005/06/28	55	B2011
17112005-2727131	B 59	NIRSPEC	2.38-4.14	HR 5993 (B1V)	2006/07/07	52	B2011
17155573-2055312	L 100	NIRSPEC	2.38-4.14	HR 5993 (B1V)	2006/07/06	54	B2011
17160467-2057072	L 100	NIRSPEC	2.39-4.14	HR 6946 (B2II)	2005/06/29	41	B2011
17160860-2058142	L 100	NIRSPEC	2.38-4.14	HR 5993 (B1V)	2006/07/06	76	B2011
18140712-0708413	L 438	NIRSPEC	2.82-4.14	HR 7141 (A5V)	2006/10/09	79	B2011
18160600-0225539	CB 130-3	NIRSPEC	2.82-4.14	HR 7141 (A5V)	2006/10/09	65	B2011
18165296-1801287	L 328	NIRSPEC	2.41-4.14	HR 6946 (B2II)	2005/06/28	64	B2011
18165917-1801158	L 328	NIRSPEC	2.41-4.14	HR 6946 (B2II)	2005/06/28	50	B2011
18170376-0815070	L 429-C	NIRSPEC	3.00-3.87	HR 6963 (B9V)	2018/06/01	43	
18170426-1802408	L 328	NIRSPEC	2.06-4.14	HR 6946 (B2II)	2005/06/29	52	B2011
18170429-1802540	L 328	NIRSPEC	2.39-4.09	HR 6946 (B2II)	2005/06/29	56	B2011
18170470-0814495	L 429-C	NIRSPEC	2.38-4.14	HR 7141 (A5V)	2006/07/07	62	B2011
18170957-0814136	L 429-C	NIRSPEC	2.38-4.14	HR 7141 (A5V)	2006/07/07	63	B2011
18171181-0814012	L 429-C	NIRSPEC	2.06-4.14	HR 7141 (A5V)	2006/10/09	43	B2011
18171366-0813188	L 429-C	NIRSPEC	2.06-4.14	HR 7141 (A5V)	2006/10/09	39	B2011
18171700-0813504	L 429-C	NIRSPEC	3.00-3.87	HR 6963 (B9V)	2018/06/01	54	
18172690-0438406	L 483	NIRSPEC	2.38-4.14	HR 7141 (A5V)	2006/10/09	59	B2011
18275901+0002337	Serpens MC	IRTF	1.92-4.19	HR 7141 (A5V)	2010/05/22	50	
		NIRSPEC	2.77-4.23	HR 7141 (A5V)	2009/10/12	62	
18282010+0029141	Serpens MC	IRTF	1.92-4.19	HR 7141 (A5V)	2010/05/24	28	
		NIRSPEC	2.77-4.23	HR 6744 (A5E)	2009/10/12	37	
18282631+0052133	Serpens MC	IRTF	1.92-4.19	HD 163336 (A0V)	2010/05/20	89	
		NIRSPEC	2.77-4.23	HR 7141 (A5V)	2009/10/12	116	
18284038+0044503	Serpens MC	IRTF	1.92-4.19	HD 161868 (A1V)	2010/05/21	34	
		NIRSPEC	2.77-4.23	HR 7141 (A5V)	2009/10/12	49	
18284797+0037431	Serpens MC	IRTF	1.92-4.19	HR 7141 (A5V)	2010/05/24	32	
		NIRSPEC	2.77-4.23	HR 7141 (A5V)	2009/10/12	50	
18285266+0028242	Serpens MC	NIRSPEC	2.75-4.21	HR 7141 (A5V)	2007/07/05	31	
18290316+0023090	Serpens MC	IRTF	1.92-4.19	HD 161868 (A1V)	2010/05/2	34	
		NIRSPEC	2.77-4.23	HR 7141 (A5V)	2009/10/12	63	
18290436+0116207	Serpens MC	IRTF	1.92-4.19	HR 7141 (A5V)	2010/05/20	41	
		NIRSPEC	2.77-4.23	HR 7141 (A5V)	2009/10/12	71	
18291619+0045143	Serpens MC	NIRSPEC	2.77-4.23	HR 7141 (A5V)	2009/10/12	55	
18291699+0037191	Serpens MC	IRTF	1.92-4.19	HR 6629 (A1V)	2010/05/23	19	
		NIRSPEC	2.77-4.23	HR 7141 (A5V)	2009/10/12	41	
18292528+0003141	Serpens MC	IRTF	1.92-4.19	HR 7141 (A5V)	2010/05/20	53	
		NIRSPEC	2.77-4.23	HR 7141 (A5V)	2009/10/12	62	
18294108+0127449	Serpens MC	IRTF	1.92-4.19	HR 7141 (A5V)	2010/05/23	26	
		NIRSPEC	2.77-4.22	HR 7141 (A5V)	2009/10/12	72	
18300061+0115201	Serpens MC	IRTF	1.92-4.19	HR 6744 (A0V)	2010/05/22	41	
		NIRSPEC	2.77-4.23	HR 7141 (A5V)	2011/04/18	47	
		NIRSPEC	2.82-4.14	HR 7141 (A5V)	2009/10/12	47	B2011
18300085+0017069	Serpens MC	IRTF	1.92-4.19	HR 7141 (A5V)	2010/05/23	110	
		NIRSPEC	2.77-4.23	HR 7141 (A5V)	2009/10/12	51	
18300896+0114441	Serpens MC	IRTF	1.92-4.19	HD 163336 (A0V)	2010/05/22	38	
		NIRSPEC	2.77-4.22	HR 7141 (A5V)	2009/10/12	64	
19201597+1135146	CB 188	NIRSPEC	2.41-4.14	HR 7724 (A1V)	2005/09/20	54	B2011
19201622+1136292	CB 188	NIRSPEC	2.06-4.14	HR 7724 (A1V)	2005/09/20	56	B2011
19214480+1121203	L 673-7	NIRSPEC	2.06-4.14	HR 7141 (A5V)	2006/07/07	62	B2011
21240517+4959100	L 1014	NIRSPEC	1.49-4.14	HR 7929 (B2V)	2005/06/28	65	B2011
21240614+4958310	L 1014	NIRSPEC	1.49-4.14	HR 7929 (B2V)	2005/06/28	72	B2011
22063773+5904520	L 1165	NIRSPEC	1.49-4.14	HR 8585 (A1V)	2006/10/09	117	B2011

3) After interpolating the modified template spectrum to the source spectrum, the source spectrum was divided by the template to produce a "residual" spectrum.

4) The "residual" spectrum was divided by a smooth baseline, constructed by applying a Savitzky-Golay filter. Subsequently, the standard deviation was measured in the range of 3.6 - 4.0 μm (i.e., the range at which photospheric lines are strongly present, and telluric and ice features are relatively weak).

The best-fitting template was selected to be the one resulting in the lowest standard deviation in the "residual" spectrum divided by a smooth baseline. Also, a range of best-fitting spectral types was determined by selecting those with χ^2_ν values within a factor of 2 of the minimum, although a precise spectral classification of the background stars is not the primary goal of this work.

After the division of the observed background star spectrum over the best fitting template spectrum, the ice features were analyzed. The well known 3.47 μm ice absorption feature, which overlaps with the 3.53 μm CH_3OH ice feature, is readily visible in many spectra. The 3.47 μm absorption feature is usually attributed to the $\nu(O–H\cdots N)$ mode of ammonia hydrates, $NH_3 \cdot H_2O$ (Dartois & d'Hendecourt 2001), although this is still open to interpretation (Shimonishi et al. 2016). A second or third order polynomial was fitted to the continuum surrounding this feature, in the wavelength ranges 3.34-3.36 and 3.60-3.70 μm (see Appendix 5.7).The photospheric line-corrected background star spectrum F was converted into optical depth (τ) scale using this baseline F_0 as follows:

$$\tau = -\ln(F/F_0) \tag{13}$$

Subsequently, two gaussians were fitted simultanesously to the overlapping 3.537 μm and 3.47 μm features. This decomposition method is similar to what was used for YSO spectra in Brooke et al. (1999). Instead of using a laboratory spectrum of CH_3OH, we applied a gaussian with a similar peak position and width (FWHM) as the main peak of the CH_3OH laboratory spectrum: 3.537 and 0.04 μm, respectively. For the second gaussian, we used values of 3.47 and 0.1 μm. The fitting procedure was performed in Python, using the GaussianModel class within the package, LmFit. An example of the decomposition of the two peaks is shown in Figure 5.1.

The CH_3OH column, $N(CH_3OH)$, was then derived following

$$N(CH_3OH) = \frac{\tau_0 \times FWHM}{A} \tag{14}$$

where the full width at half maximum (FWHM) was fixed at 32 cm^{-1} (0.04 μm) and the peak optical depth (τ_0) was derived with the Gaussian fits. The integrated band strength (A) of 5.6×10^{-18} cm molecule $^{-1}$ for the C-H symmetric stretching mode of solid CH_3OH was obtained from Kerkhof et al. (1999).

5.4 Results

The CH_3OH ice column densities and 3σ upper limits are presented in Table 5.3, along with the best-fitting templates for each source spectrum and

Table 5.3: CH$_3$OH column densities in cm^{-2} and relative to H$_2$O ice for all observed dense cloud and dark core lines of sight after correction for the photospheric absorption lines. The upper limits have 3σ significance and are indicated by ($<$). The uncertainties of the detections are 1σ and are indicated by parentheses. The uncertainty range for the spectral types is based on the template stars that have χ_ν^2 values within a factor 2 of the minimum. A_V and the H$_2$O column densities are obtained from Boogert et al. (2011) and Boogert et al. (in preparation). (*) indicates CH$_3$OH detected in this sight-line in Boogert et al. (2011). B2011: published in Boogert et al. (2011).

| Source 2MASS J	Instrument	A_V	Template star[1] mag	$\chi_\nu{}^2$	N(H$_2$O) 10^{18} cm^{-2}	N(CH$_3$OH) 10^{17} cm^{-2}	%H$_2$O	Notes
04215402+1530299	NIRSPEC	24.3	HD6903/F9 (F5-G2)	0.0021	1.84 (0.20)	<0.097	<0.53	B2011
17111501-2726180	NIRSPEC	31.3	HD94705/M5.5 (M0-M5)	0.00051	2.35 (0.26)	<0.084	<0.36	B2011
17111538-2727144	NIRSPEC	28.2	HD120052/M2 (M0-M3)	0.0018	2.01 (0.22)	<0.081	<0.40	B2011
17112005-2727131	NIRSPEC	48.0	HD124897/K1.5 (G8-K5)	0.0027	3.79 (0.42)	<0.081	<0.21	B2011
17155573-2055312	NIRSPEC	21.2	HD19058/M4 (K2-M4)	0.0013	1.63 (0.18)	<0.91	<5.58	B2011
17160467-2057072	NIRSPEC	25.9	Gl268AB/M4.5 (M2-M4.5)	0.0027	2.13 (0.23)	<1.08	<5.07	B2011
17160860-2058142	NIRSPEC	19.6	Gl381/M2.5 (K1-M2.5)	0.0029	1.53 (0.17)	<0.69	<4.51	B2011
18140712-0708413*	NIRSPEC	15.1	HD9852/K0.5 (K0-K1)	0.0026	1.40(0.15)	<0.59	<4.21	B2011
18160600-0225539	NIRSPEC	10.0	HD216946/K5 (K1-K5)	0.0028	1.06 (0.19)	<0.71	<6.70	B2011
18165296-1801287	NIRSPEC	24.0	HD204724/M1 (K5-M3)	0.00094	1.62 (0.22)	<0.72	<4.44	B2011
18165917-1801158	NIRSPEC	26.7	HD94705/M5.5 (M2-M5.5)	0.00044	1.85 (0.20)	<0.96	<5.19	B2011
18170376-0815070	NIRSPEC	16.0	HD108849/M7 (M1-M7)	0.00052	0.99 (0.12)	<0.48	<4.85	
18170426-1802408	NIRSPEC	20.0	HD6903/F9 (F6-F9)	0.0014	1.09 (0.12)	<0.069	<0.63	B2011
18170429-1802540	NIRSPEC	23.7	HD28487/M3.5 (M1-M5.5)	0.00058	1.43 (0.20)	<0.069	<0.48	B2011
18170470-0814495	NIRSPEC	34.2	HD108849/M7 (M2-M7)	0.0014	3.93 (0.44)	2.77 (0.016)	7.05	B2011
18170957-0814136	NIRSPEC	26.2	HD39045/M3 (M3-M7)	0.00071	2.85 (0.31)	2.91 (0.015)	10.21	B2011
18171181-0814012	NIRSPEC	34.5	HD124897/K1.5 (K1.5-K2)	0.0012	3.81 (0.42)	5.37 (0.014)	14.10	B2011
18171366-0813188	NIRSPEC	28.6	HD76151/G2 (G2-M0)	0.0044	3.40 (0.38)	3.85 (0.49)	11.32	B2011
18171700-0813504	NIRSPEC	14.0	HD207076/M7 (M2-M7)	0.0023	0.68 (0.12)	<0.26	<3.82	
18172690-0438406	NIRSPEC	36.8	HD108849/M7 (M3-M7)	0.00084	4.31 (0.48)	3.48 (0.020)	8.07	B2011
18275901+0002337	IRTF	7.2	HD214665/M4 (M3-M4)	0.00043	<0.08	<0.23	...	
			HD194193/K7 (K4-M0)	0.00063		<0.083	...	
18282010+0029141	IRTF	10.6	HD94705/M5.5 (M2-M6)	0.00023	<0.17	<0.42	...	
	NIRSPEC		HD194193/K7 (K5-M3)	0.00059		<0.082	...	
18282631+0052133	IRTF	5.1	HD132935/K2 (G9-K2)	0.0012	<0.08	<0.16	...	
	NIRSPEC		HD2901/K2 (K1-K7)	0.00092		<0.044	...	
18284038+0044503	IRTF	12.5	HD214665/M4 (K3-M4)	0.0022	0.38 (0.13)	<0.47	<12.37	
	NIRSPEC		HD94705/M5.5 (K3-M5)	0.00060		<0.079	<2.08	
18284797+0037431	IRTF	10.6	HD214665/M4 (K5-M4)	0.00032	0.40 (0.08)	<0.32	<8.00	
	NIRSPEC		HD39801/M1-M2 (M0-M3)	0.00049		<0.073	<1.83	
18285266+0028242	NIRSPEC	36.0	HD28487/M3.5 (M3-M6)	0.0017	2.9 (0.2)	6.14 (0.48)	21.17	
18290316+0023090	IRTF	8.1	HD213893/M0 (M0-M5)	0.00030	0.23 (0.07)	<0.29	<12.61	
	NIRSPEC		HD194193/K7 (K4-M1)	0.00075		<0.060	<2.61	
18290436+0116207	IRTF	10.3	HD207991/K4 (K2-K4)	0.0035	0.18 (0.05)	<0.58	<32.22	
	NIRSPEC		HD187238/K3 (K2-M1)	0.0010		<0.040	<2.22	
18291619+0045143	NIRSPEC	6.1	HD124897/K1.5 (K1.5-K4)	0.00051	<0.10	<0.052	...	
18291699+0037191	IRTF	19.8	HD213893/M0 (M0-M4)	0.00084	1.06 (0.12)	<0.66	<6.23	
	NIRSPEC		HD95735/M2 (M0-M3)	0.0013		<0.071	<0.67	
18292528+0003141	IRTF	7.0	HD28487/M3.5 (M1-M3.5)	0.00022	<0.12	<0.15	...	
	NIRSPEC		HD39801/M1-M2 (K7-M3)	0.00061		<0.065	...	
18294108+0127449	IRTF	8.6	HD27598/M4 (K1.5-M4)	0.00023	<0.08	<0.066	...	
	NIRSPEC		HD91810/K1 (K1-K2)	0.00095		<0.066	...	
18300061+0115201	IRTF	46.0	HD236697/M0.5 (M0.5-M5.5)	0.010	3.04 (0.34)	<0.18	<0.59	
	NIRSPEC		HD108849/M7 (M3-M7)	0.00059		<0.090	<0.30	
	NIRSPEC		HD108849/M7 (M3-M7)	0.00059		<0.095	<0.31	B2011
18300085+0017069	IRTF	5.9	HD2901/K2 (G9-K2)	0.00040	<0.10	<0.17	...	
	NIRSPEC		HD132935/K2 (K0-K2)	0.0014		<0.035	...	
18300896+0114441	IRTF	13.1	HD207991/K4 (K4-M2)	0.00033	0.50 (0.17)	<0.32	<6.40	
	NIRSPEC		HD14469/M3-M4 (K2-M3)	0.00068		<0.063	<1.26	
19201597+1135146	NIRSPEC	25.1	HD39045/M3 (K5-M3)	0.00057	1.34 (0.14)	<0.87	<6.49	B2011
19201622+1136292	NIRSPEC	20.0	HD120477/K5.5 (K1.5-K5.5)	0.0013	1.01(0.11)	<0.062	<0.61	B2011
19214480+1121203	NIRSPEC	16.8	HD39045/M3 (M2-M3)	0.00063	1.43 (0.16)	<0.048	<0.34	B2011
21240517+4959100	NIRSPEC	24.8	HD28487/M3.5 (M0-M3.5)	0.00052	2.19 (0.24)	0.74 (0.21)	3.38	B2011
21240614+4958310	NIRSPEC	12.8	HD124897/K1.5 (K1.5-K3)	0.0011	0.98 (0.11)	<0.058	<0.59	B2011
22063773+5904520	NIRSPEC	13.9	HD10307/G1 (F5-G1)	0.0030	1.13 (0.12)	<0.044	<0.39	B2011
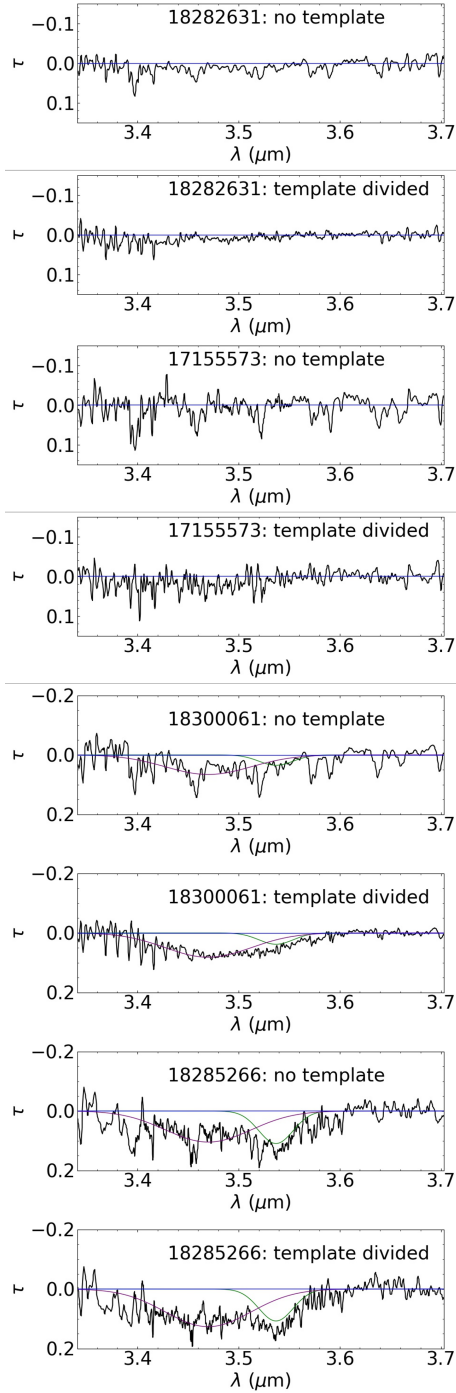
Figure 5.1: Optical depth spectra taken towards four background stars at varying visual extinctions: 2MASS J18282631 (A_V=5.1 mag), 2MASS J17155573 (A_V=10.6 mag), 2MASS J18300061 (A_V=46.0 mag), 2MASS J18285266 (A_V=36.0 mag). For each target, the two panels give the spectrum before (top) and after (bottom) template division, respectively. The blue line represents τ=0. The green and purple lines are Gaussian fits to the (tentative) 3.537 μm and 3.47 μm features, respectively.

corresponding reduced χ^2 values. The photosphere-corrected flux spectra and the final optical depth spectra are found in appendix 5.7.

To demonstrate the effect of the photospheric line correction, optical depth spectra with and without the correction are shown for four sources with A_V values in the range of 5.1-46.0 mag in Figure 5.1. Clearly, the reduction of photospheric lines allows for a more sensitive search for interstellar ice features. Blended photospheric lines could mimic narrow ice features, such as those of the CH_3OH band at 3.537 µm. Reduction of the photospheric lines also improves the fitting of the baseline. And for secure detections (e.g., 2MASS J18285266), a more reliable band profile is derived, as well as a more secure separation from the 3.47 µm feature.

When both the S/N and the photospheric line reduction are excellent, the CH_3OH ice abundance determination is limited by the decomposition of the 3.537 µm band from the broad ammonia hydrate feature at 3.47 µm. Unless a distinct dip at 3.537 µm is observed, the Gaussian decomposition (section 5.3) is uncertain.

For one of the targets in Boogert et al. (2011) we obtain different results. We do not confirm the CH_3OH ice detection toward 2MASS J18140712 ($7\pm2\times10^{16}$ cm^{-2} versus $< 6\times10^{16}$ cm^{-2} (3σ) in this work). Figure 5.2 shows that significant photospheric lines are still present after the division over the template. Perhaps our disagreement with Boogert et al. (2011) is due to the baseline choice.
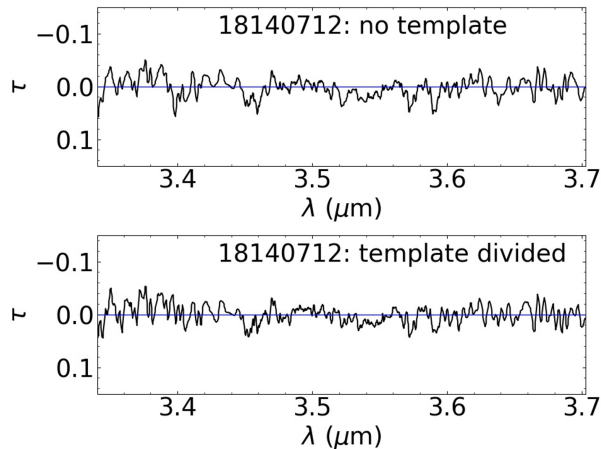
Figure 5.2: Optical depth spectra taken towards the field star, 18140712 (Boogert et al. 2011). No observable 3.537 µm CH_3OH feature is present in either panel, whereas the feature was present in Boogert et al. (2011). The choice of baseline may be the cause of such discrepancy. The blue line indicates τ=0.

5.4.1 CH_3OH column density relative to A_V and H_2O

Figure 5.3 shows the CH_3OH ice detections with 1σ error bars and 3σ upper limit values from Table 5.3 plotted as a function of the A_V. For upper limits of the same source, the lowest upper limit is plotted. Table 5.3 also shows the CH_3OH abundance relative to the H_2O ice column density. The A_V and N(H_2O)

values were taken from Boogert et al. (2011) and Boogert et al. (in preparation), and were determined by fitting observed 1-5 μm broad band photometry and spectra with a model consisting of spectra from the IRTF spectral database, the infrared interstellar extinction curve, an optical reddening of $A_V/A_K = 8$, and an H_2O ice spectrum for small spherical grains.

A fit is only made to the detections (closed blue circles). They apparently trace a distint environment particularly conducive to CH_3OH formation. As shown in the figure, the fit crosses the y-axis at A_V=13.5 ± 7.8 mag (i.e., the detection threshold). Taking into account the front and back of the cloud/core, the extinction as measured from the edge to the middle of the cloud/core along the line of sight is the observed value divided by 2, which results in a CH_3OH formation threshold of 6.8 ± 3.9 mag.
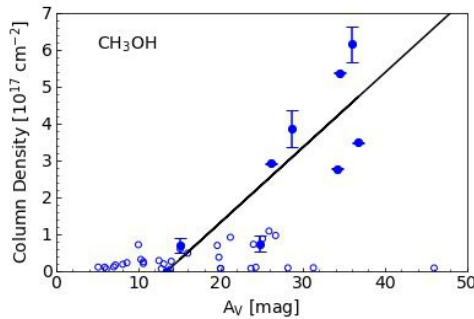
Figure 5.3: CH_3OH ice detections (solid blue circles; 1σ error bars) and upper limits (open blue circles; 3σ) plotted as a function of the visual extinction. A CH_3OH detection threshold of 13.5 ± 7.8 mag is found.

5.4.2 Averaging spectra in A_V bins

Spectra that do not show a secure CH_3OH feature at 3.537 μm are averaged into various A_V bins to increase the sensitivity (Figure 5.4). The averaging is weighed by $1/\sigma^2$, with σ the typical value used to determine the S/N column of Table 5.2. Three bins exist: an average over the lines of sight below the CH_3OH detection threshold, at and above the CH_3OH detection threshold, and with CH_3OH detections. The noise level in the $A_V < 18$ mag bin is 0.16, with a 3σ upper limit of 7.68×10^{17} cm^{-2} for the 3.537 μm feature. For the $A_V \geqslant 18$ mag bin, the noise level is 0.15, with a 3σ upper limit of 5.26×10^{16} cm^{-2} for the 3.537 μm feature. A noise level of 0.056 and a CH_3OH column density of 2.58×10^{18} cm^{-2} are measured for the bin containing CH_3OH detections. The A_V range of < 18 mag in Figure 5.4 does not show any observable CH_3OH feature. The 3.47 μm $NH_3 \cdot H_2O$ feature is clearly present at $A_V \geqslant 18$ mag, however there is no distinct feature at 3.537 μm.
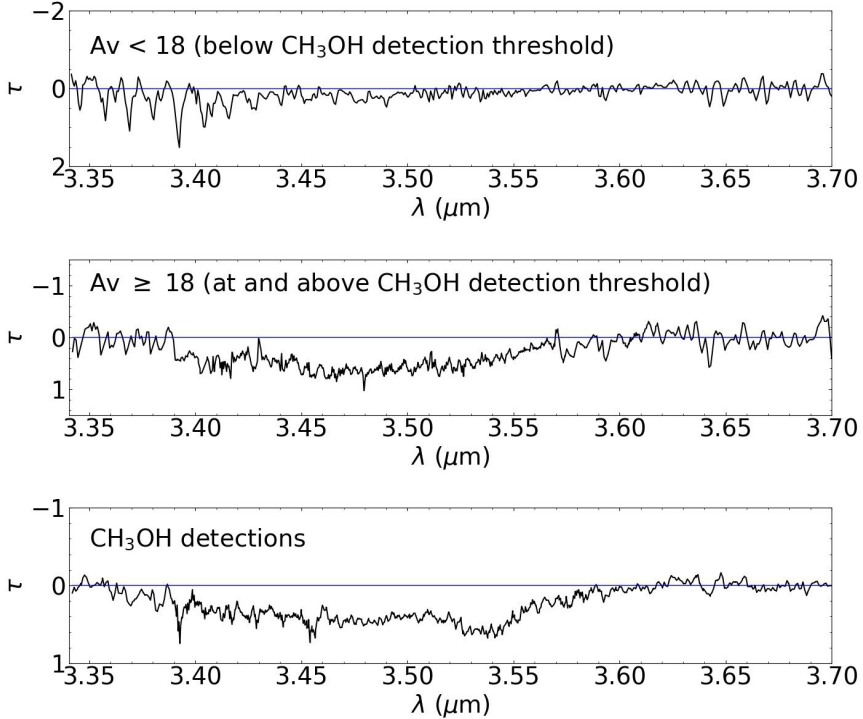
Figure 5.4: Optical depth spectra averaged across the indicated A_V bins, for targets without a CH$_3$OH ice detection, as probed by the 3.537 µm feature (see Table 5.3). For reference, a spectrum averaged over sight-lines with CH$_3$OH detections is shown in the bottom panel. The blue line shows τ=0. The number of targets in each bin is 30, 18, and 7 for $A_V < 18$, $A_V \geqslant$ 18, and CH$_3$OH detections averaged, respectively. Note that the detection for sight-line 2MASS J18140712 is not included.

5.5 Discussion

The extinction threshold for ice formation is a direct observational indicator of the chemical evolution of molecular clouds. The observed A_V values mentioned above sample both, the front and back of the clouds/cores. And thus, the maximum depth into the clouds/cores that is traced by these observations is $A_V/2$ (i.e., the formation threshold), which we will use in the remainder of this discussion.

The threshold value for abundant CH$_3$OH formation of A_V=6.8 $\pm$ 3.9 mag as derived from the linear fit is of low significance (1.7σ), reflecting the large spread in the CH$_3$OH abundances, while the uncertainties on the individual abundances are small.

Also, for many high extinction sight-lines, tight CH$_3$OH abundance upper limits were derived (Table 5.3), well below the detections at similar A_V (Figure 5.3). This strengthens the trend observed in Boogert et al. (2015). We speculate that CO has not sufficiently frozen out in these sight-lines, limiting the CH$_3$OH formation in some of these dense clouds and dark cores. CO

freeze out could have been suppressed by lower densities at the same A_V, by higher dust temperatures or radiation fields. Alternatively, CH_3OH may have been consumed or destroyed. Other formation channels that overlap with the CH_3OH formation route, such as those of HCOOH (Qasim et al. 2019a), may also be contributing factors.

Below A_V=7.6 mag, only upper limits are available, but they are tight (<0.39% H_2O), supporting that the threshold for abundant CH_3OH formation is indeed well above that for H_2O (~ 1.6) and CO (~ 3). CH_3OH formation below these limits is expected, however. As reported in the laboratory investigations by Bergner et al. (2017) and Qasim et al. (2018), CH_4 is a precursor to CH_3OH formation under low temperature molecular cloud conditions. The formation efficiency is a factor of ~20 below that of the high density CO ice hydrogenation route (Qasim et al. 2018). CH_4 is formed at low extinctions (A_V ~ 2 mag), similar to H_2O. At this stage, CO formation in the gas phase is not complete, and could enhance the CH_4 abundance in the first grain mantle layers. There is indeed a hint of enhanced CH_4 ice abundances at low extinctions (Öberg et al. 2008). Consequently, CH_3OH is expected to be present in the ices well below the threshold for enhanced formation via the CO ice hydrogenation route discussed above.

5.6 Conclusions and future work

Observations targeting the 3.537 μm feature of CH_3OH ice in dense molecular clouds and dark cores to constrain the CH_3OH ice formation threshold were pursued. A method to increase the sensitivity to weak ice absorption features and thus to the accuracy of the CH_3OH column density is presented. The following conclusions can be drawn from this work:

1) The method of fitting template spectra of unreddened stars to reduce photospheric lines from dense cloud and dark core background spectra increases the sensitivity to detect ice features. It also improves the accuracy of the baseline determination. With respect to the study of (Boogert et al. 2011), one new CH_3OH ice detection was made and one was not found. The total number of CH_3OH ice detections in quiescent molecular cloud and core material is now 8.

2) This photospheric correction method will be applicable to the analysis of future JWST spectra. Multi-object spectroscopy with JWST will make it possible to observe large sample sizes for both, background and template stars.

3) For high S/N spectra that are well corrected for photospheric lines, the limiting factor for accurate CH_3OH ice abundances is the decomposition of the 3.537 μm band from the 3.47 μm band of ammonia hydrates.

4) The CH_3OH formation threshold is constrained to be A_V=6.8 ± 3.9 mag. The error bars on the individual measurements are much smaller than the scatter in the column densities. No detections have been made below a formation threshold of A_V=7.6 mag. The abundance upper limits obtained in many sightlines both below and above the 13.5 mag detection threshold are significant.

6) The large scatter at high A_V values is puzzling. Perhaps CO is not an abundant resource for CH_3OH formation in some of these clouds and cores. Alternatively, CH_3OH may have been effectively destroyed.

7) The threshold for the efficient formation of CH_3OH via the CO ice hydrogenation route does not preclude the formation via less efficient pathways. Such pathways may well include CH_4 and/or CH_4 precursors (C, CH, etc.), as supported from recent laboratory experiments.

8) The sample size of CH_3OH detections is small and more observations are warranted to further investigate the origin of the large scatter in the CH_3OH abundance variations as well as the formation threshold.

9) Tracing the columns of CO and CH_4 alongside CH_3OH in the same clouds and cores will help understand how and when CH_3OH is formed. Whether CO is actually depleted in regions where CH_3OH is not detected, and if CH_4 could be a precursor for less abundant CH_3OH, can be better understood by mapping these ices simultaneously. JWST is ideally suited for this, because of its large wavelength coverage, high sensitivity, and mapping capabilities.
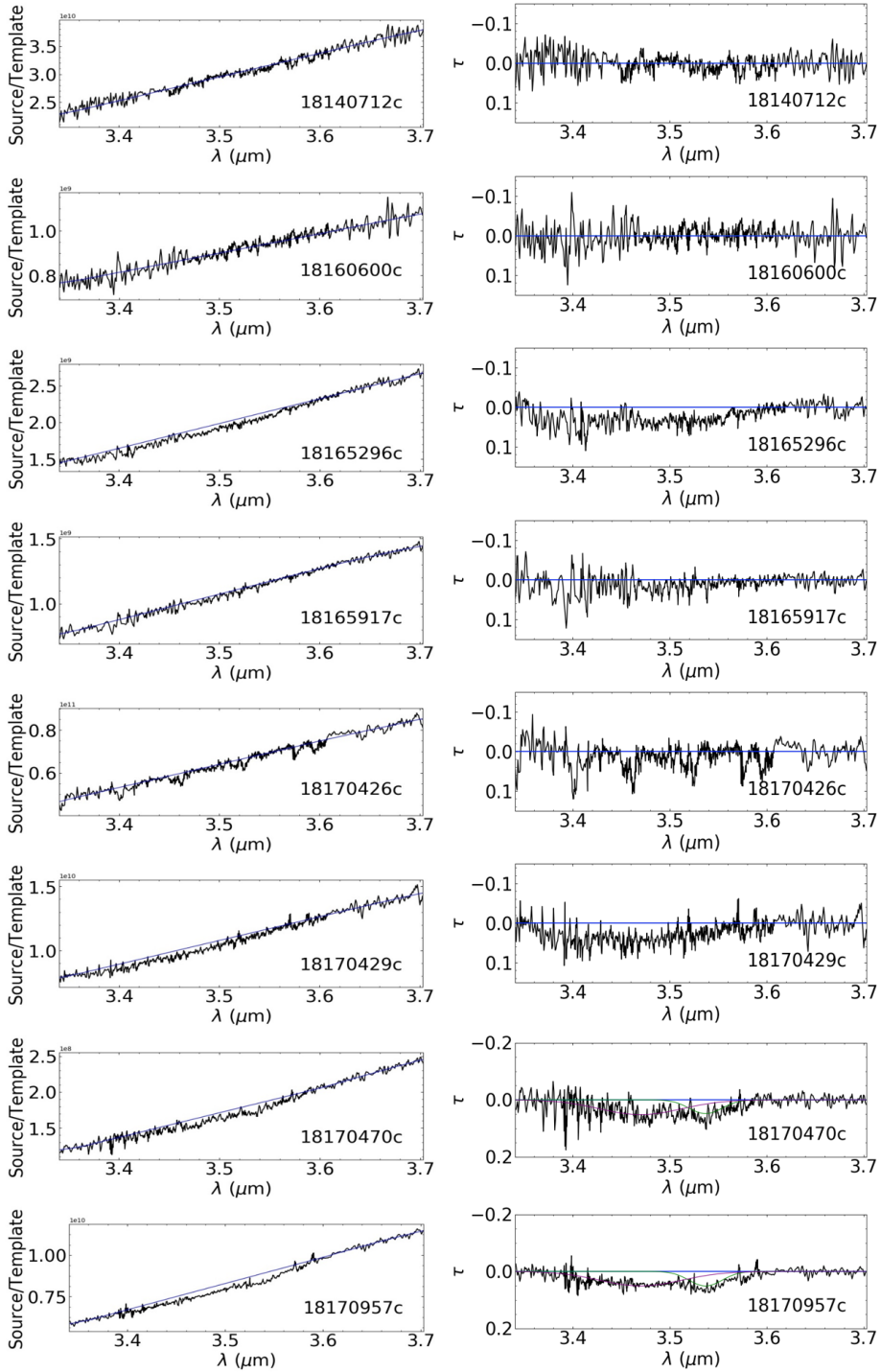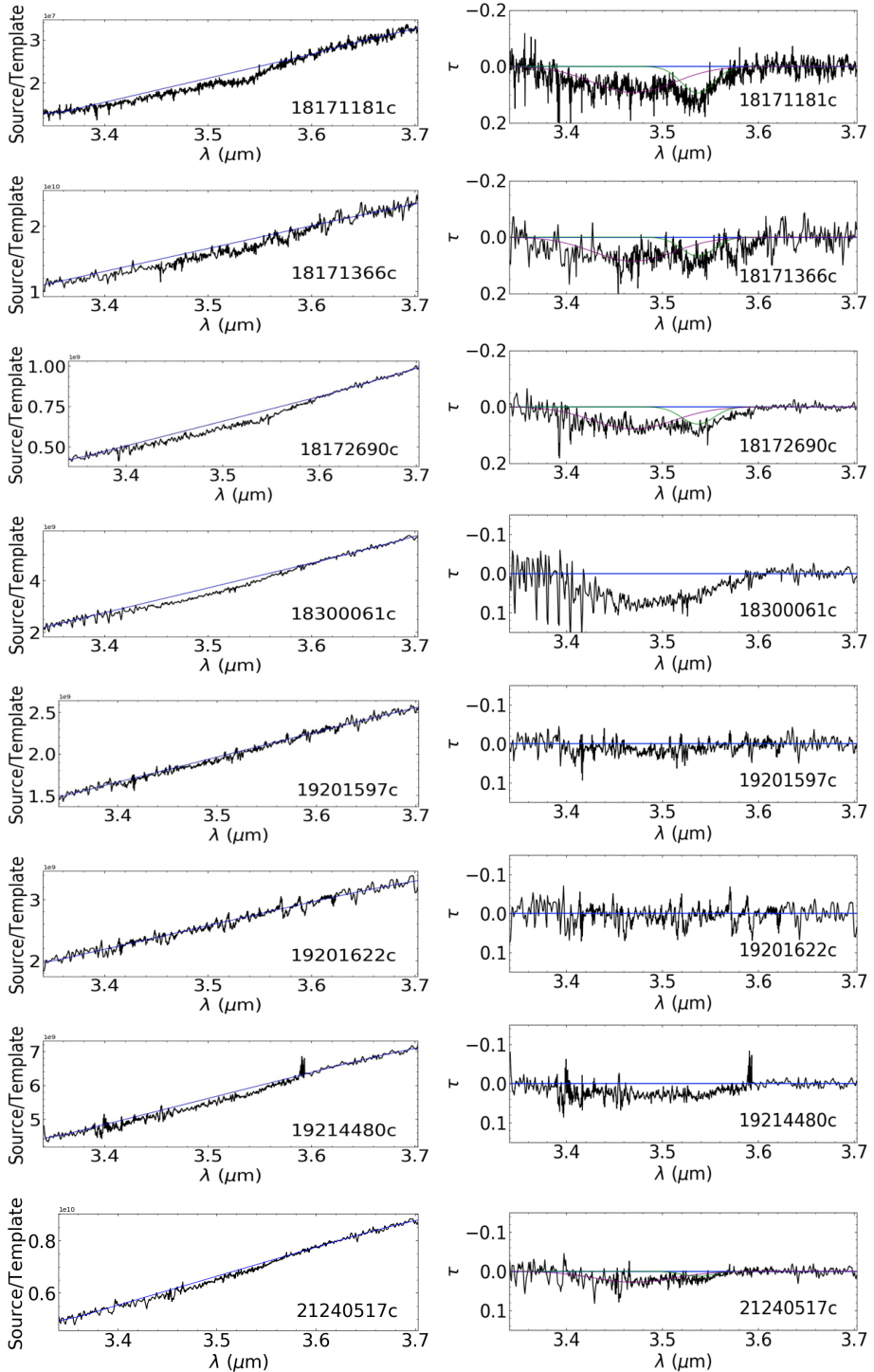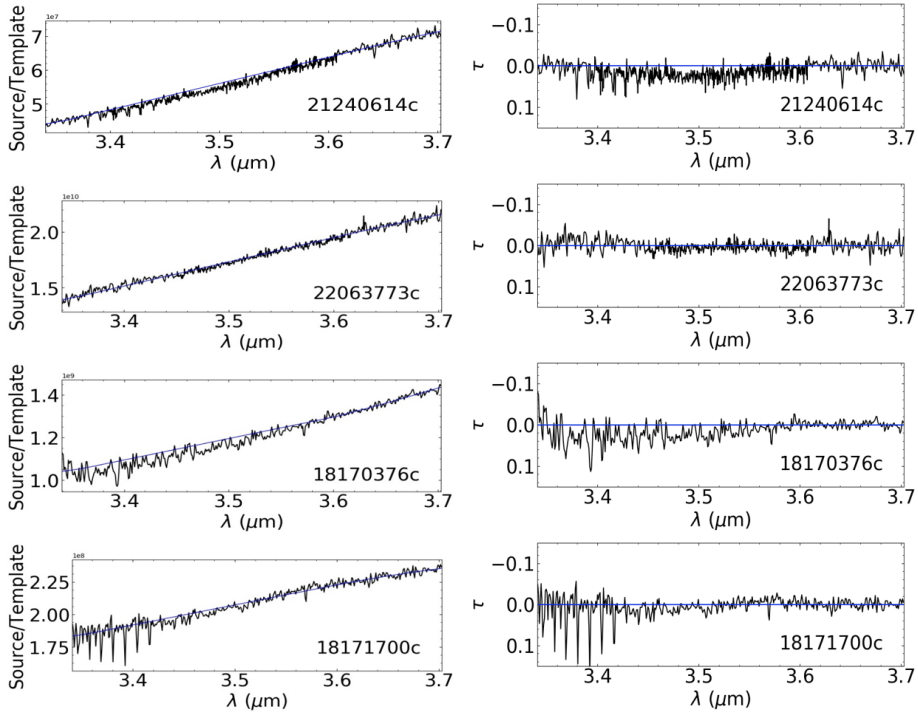
5.7 Appendix information
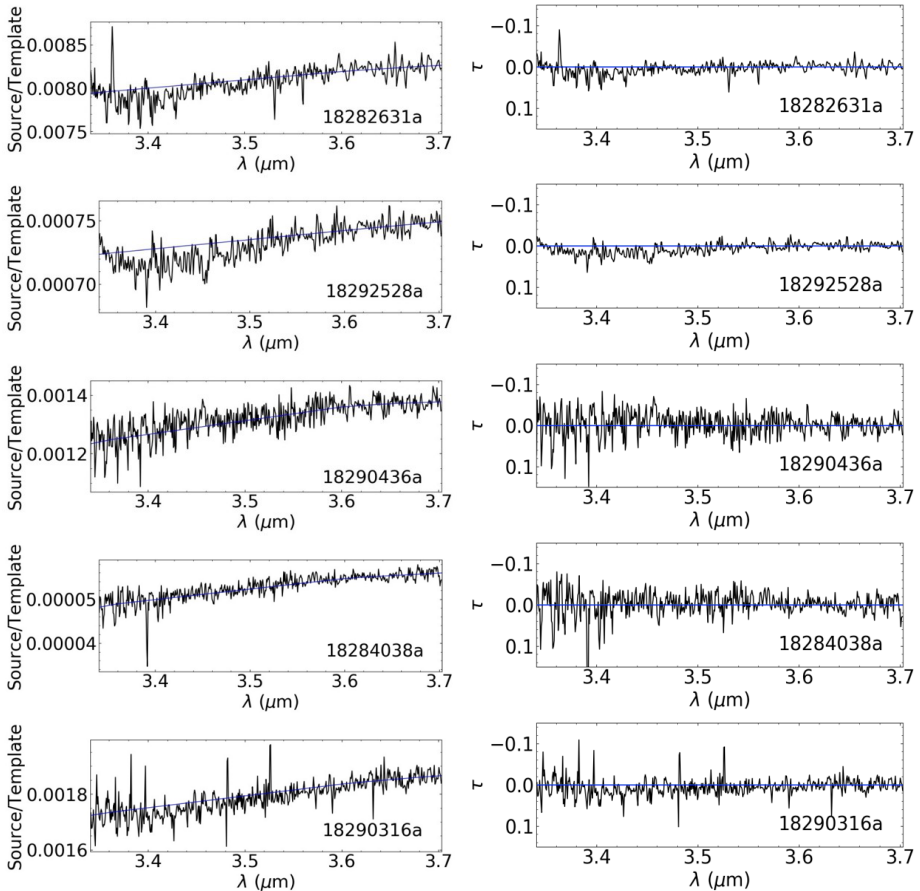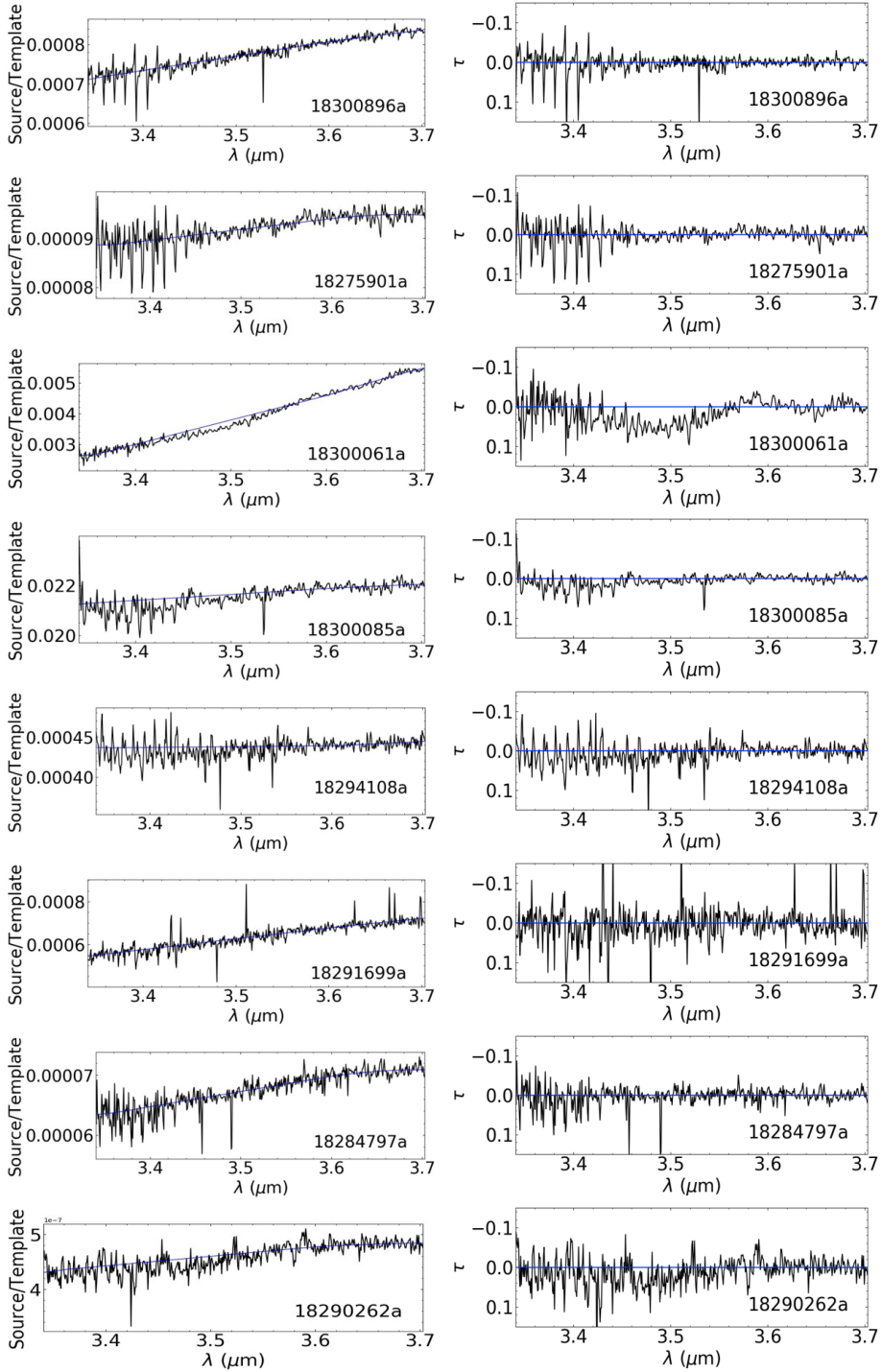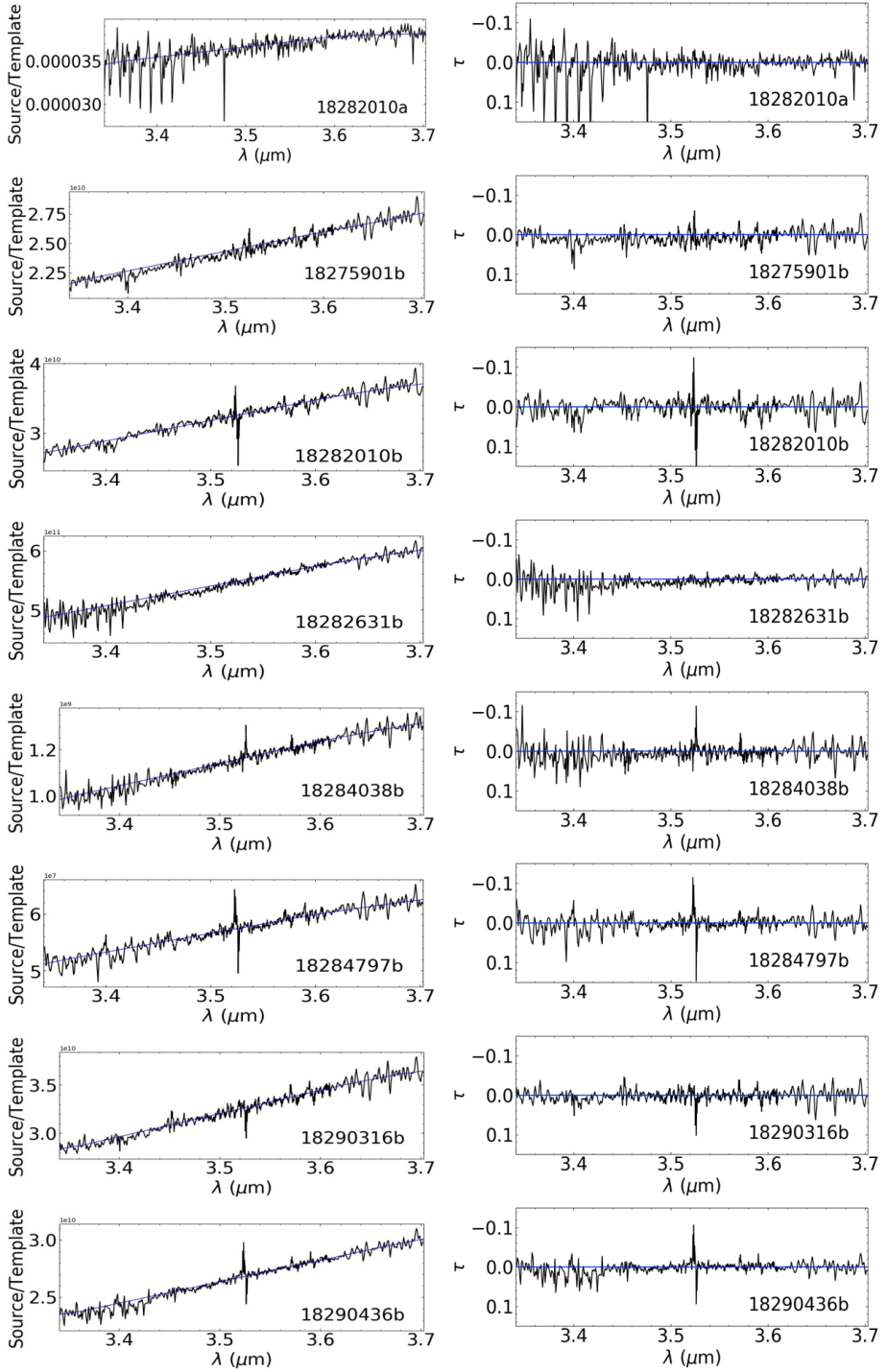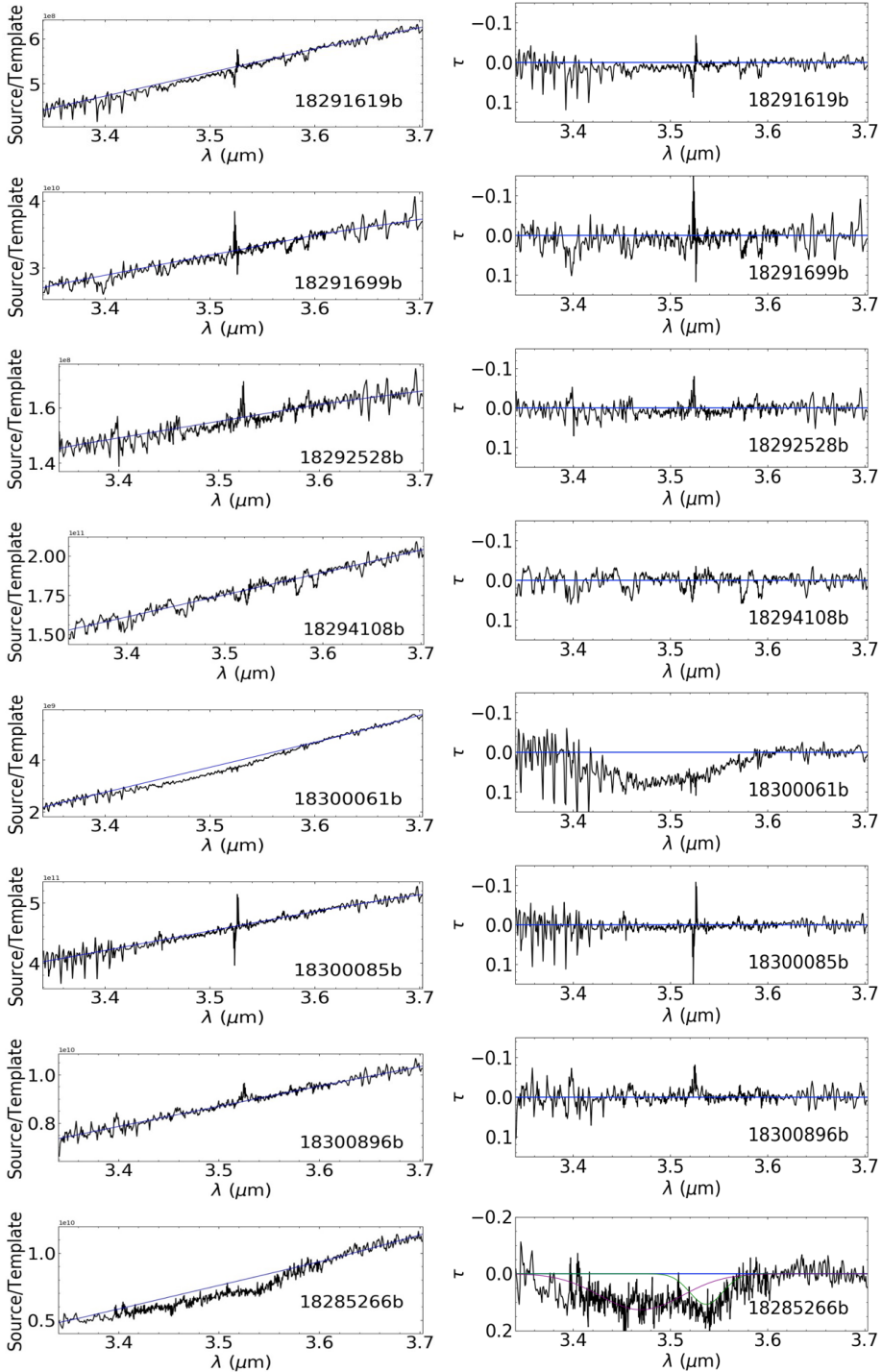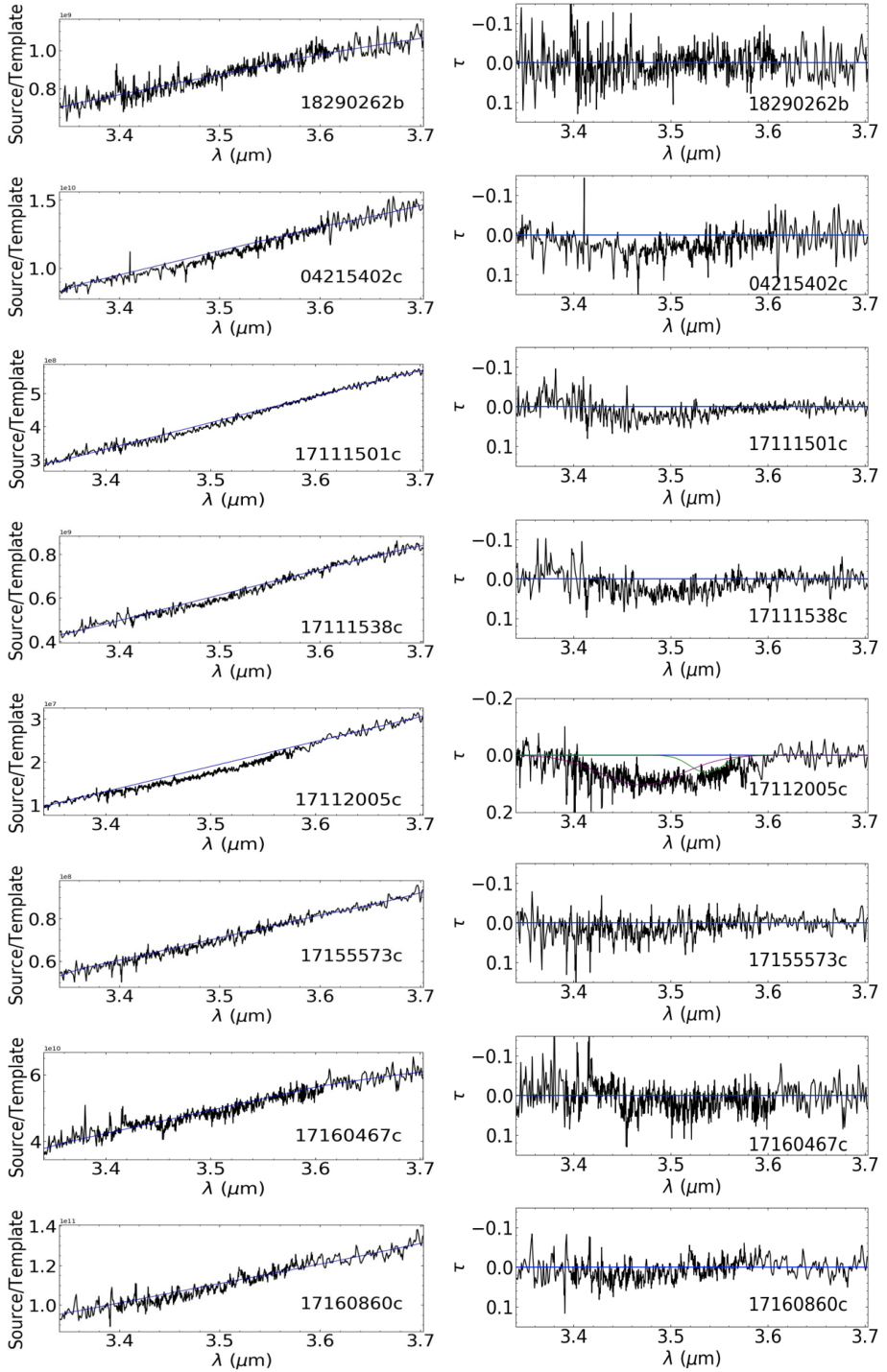
Figure 5.5: Flux and optical depth spectra of the 3.3-3.7 μm wavelength ragion towards the entire sample. The blue line in each left panel is the local continuum, and in the right panel is τ=0. The green and purple lines are Gaussian fits for the 3.537 μm and 3.47 μm absorption features, respectively.

Bibliography

Bergner, J. B., Öberg, K. I., & Rajappan, M. 2017, Astrophys. J., 845, 29

Boogert, A., Gerakines, P. A., & Whittet, D. C. 2015, Annu. Rev. Astron. Astrophys., 53, 541

Boogert, A., Huard, T., Cook, A., et al. 2011, Astrophys. J., 729, 1

Brooke, T., Sellgren, K., & Geballe, T. 1999, Astrophys. J., 517, 883

Cardelli, J. A., Clayton, G. C., & Mathis, J. S. 1989, Astrophys. J., 345, 245

Charnley, S., Tielens, A., & Millar, T. 1992, Astrophys. J., 399, L71

Chiar, J., Adamson, A., Kerr, T., & Whittet, D. 1995, Astrophys. J., 455, 234

Chiar, J., Pendleton, Y., Allamandola, L., et al. 2011, Astrophys. J., 731, 9

Chuang, K.-J., Fedoseev, G., Ioppolo, S., van Dishoeck, E. F., & Linnartz, H. 2016, Mon. Not. R. Astron. Soc., 455, 1702

Cuppen, H., van Dishoeck, E. F., Herbst, E., & Tielens, A. 2009, Astron. Astrophys., 508, 275

Cushing, M., Vacca, W., & Rayner, J. 2004, Publ. Astron. Soc. Pac., 116, 362

Dartois, E., & d'Hendecourt, L. 2001, Astron. Astrophys., 365, 144

Fedoseev, G., Chuang, K.-J., Ioppolo, S., et al. 2017, Astrophys. J., 842, 1

Fuchs, G., Cuppen, H., Ioppolo, S., et al. 2009, Astron. Astrophys., 505, 629

Goumans, T., & Kästner, J. 2011, J. Phys. Chem. A, 115, 10767

Jørgensen, J., Schöier, F., & van Dishoeck, E. F. 2005, Astron. Astrophys., 435, 177

Kerkhof, O., Schutte, W., Ehrenfreund, P., et al. 1999, Astron. Astrophys., 346, 990

McLean, I. S., Becklin, E. E., Bendiksen, O., et al. 1998, 3354, 566

Öberg, K. I., Boogert, A., Pontoppidan, K. M., et al. 2008, Astrophys. J., 678, 1032

Öberg, K. I., Garrod, R. T., van Dishoeck, E. F., & Linnartz, H. 2009, Astron. Astrophys., 504, 891

Pontoppidan, K. M. 2006, Astron. Astrophys., 453, L47

Pontoppidan, K. M., Dartois, E., van Dishoeck, E. F., Thi, W.-F., & d'Hendecourt, L. 2003, Astron. Astrophys., 404, L17

Qasim, D., Chuang, K.-J., Fedoseev, G., et al. 2018, Astron. Astrophys., 612, 1

Qasim, D., Lamberts, T., He, J., et al. 2019a, Astron. Astrophys., 626, A118

Qasim, D., Fedoseev, G., Chuang, K.-J., et al. 2019b, Astron. Astrophys., 627, A1

Rayner, J., Cushing, M., & Vacca, W. 2009, Astrophys. J. Suppl. Ser., 185, 289

Rayner, J., Toomey, D., Onaka, P., et al. 2003, Publ. Astron. Soc. Pac., 115, 362

Shimonishi, T., Dartois, E., Onaka, T., & Boulanger, F. 2016, Astron. Astrophys., 585, A107

Soma, T., Sakai, N., Watanabe, Y., & Yamamoto, S. 2018, Astrophys. J., 854, 116

Vacca, W., Cushing, M., & Rayner, J. 2003, Publ. Astron. Soc. Pac., 115, 389

van Dishoeck, E. F., Blake, G. A., Draine, B. T., & Lunine, J. 1993, in Protostars and Planets III, 163–241

Watanabe, N., & Kouchi, A. 2002, Astrophys. J. Lett., 571, L173

Wirström, E., Geppert, W. D., Hjalmarson, Å., et al. 2011, Astron. Astrophys., 533, A24

Extension of the HCOOH and CO$_2$ ice network

Formic acid (HCOOH) and carbon dioxide (CO$_2$) are simple species that have been detected in the interstellar medium. The solid-state formation pathways of these species under experimental conditions relevant to prestellar cores are primarily based off of weak infrared transitions of the HOCO complex and usually pertain to the H$_2$O-rich ice phase, and therefore more experimental data are desired. Here, we present a new and additional solid-state reaction pathway that can form HCOOH and CO$_2$ ice at 10 K 'non-energetically' in the laboratory under conditions related to the "heavy" CO freeze-out stage in dense interstellar clouds, i.e., by the hydrogenation of an H$_2$CO:O$_2$ ice mixture. This pathway is used to piece together the HCOOH and CO$_2$ formation routes when H$_2$CO or CO reacts with H and OH radicals. Temperature programmed desorption - quadrupole mass spectrometry (TPD-QMS) is used to confirm the formation and pathways of newly synthesized ice species as well as to provide information on relative molecular abundances. Reflection-absorption infrared spectroscopy (RAIRS) is additionally employed to characterize reaction products and determine relative molecular abundances. We find that for the conditions investigated in conjunction with theoretical results from the literature, H + HOCO and HCO + OH lead to the formation of HCOOH ice in our experiments. Which reaction is more dominant can be determined if the H + HOCO branching ratio is more constrained by computational simulations, as the HCOOH:CO$_2$ abundance ratio is experimentally measured to be around 1.8:1. H + HOCO is more likely than OH + CO (without HOCO formation) to form CO$_2$. Isotope experiments presented here further validate that H + HOCO is the dominant route for HCOOH ice formation in a CO-rich CO:O$_2$ ice mixture that is hydrogenated. These data will help in the search and positive identification of HCOOH ice in prestellar cores.
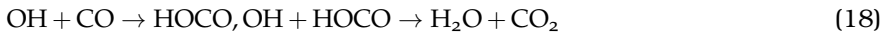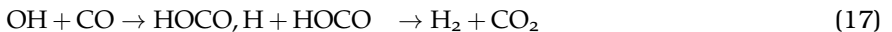
6.1 Introduction

HCOOH and CO$_2$ have been detected across various environments in space. HCOOH has been confirmed in the gas-phase (Zuckerman et al. 1971; Winnewisser & Churchwell 1975; Irvine et al. 1990; Turner et al. 1999; Liu et al. 2001; Ikeda et al. 2001; Liu et al. 2002; Requena-Torres et al. 2006; Bottinelli et al. 2007; Taquet et al. 2017; Favre et al. 2018), but its identification in the solid-state is uncertain (Boogert et al. 2015). Abundances relative to H$_2$O ice of less than 0.5 to up to 6 percent towards dense clouds, and low and high mass Young Stellar Objects have been derived (Schutte et al. 1999; Gibb et al. 2004; Bisschop et al. 2007a; Öberg et al. 2011; Boogert et al. 2015), providing the identification of HCOOH is indeed correct. CO$_2$ has been detected in the gas-phase (Dartois et al. 1998; van Dishoeck 1998; Boonman et al. 2003) and abundantly in the solid-state (d'Hendecourt & Jourdain de Muizon 1989; van Dishoeck et al. 1996; De Graauw et al. 1996; Whittet et al. 1998; Gerakines et al. 1999; Pontoppidan et al. 2008; Cook et al. 2011; Kim et al. 2012; Poteet et al. 2013; Ioppolo et al. 2013b; Boogert et al. 2015; Suhasaria et al. 2017, and references therein), and is one of the most ubiquitous ice constituents in the interstellar medium. Here, the observed CO$_2$:H$_2$O ice ratios are 15-35%.

At astrochemically relevant temperatures of $\leqslant$ 20 K, HCOOH ice has been shown to be formed by proton irradiation of H$_2$O and CO (Hudson & Moore 1999), electron irradiation of H$_2$O and CO (Bennett et al. 2010), UV irradiation of H$_2$O and CO (Watanabe et al. 2007), hydrogenation of CO and O$_2$ (Ioppolo et al. 2010), and a combined UV irradiation and hydrogenation of H$_2$O and CO (Watanabe et al. 2007). Upper limit values or tentative identification of HCOOH formation in UV-induced experiments containing CH$_3$OH (Öberg et al. 2009; Paardekooper et al. 2016) and H$_2$CO (Butscher et al. 2016) have also been reported. CO$_2$ ice can also be produced by both, 'energetic' and 'non-energetic' processes, where 'non-energetic' refers to a radical-induced process without the involvement of UV, cosmic rays, and/or other 'energetic' particles. For 'energetic' processes, CO$_2$ has been observed and formed experimentally by UV-irradiation of CO-containing ices (Gerakines et al. 1996; Ehrenfreund et al. 1997; Cottin et al. 2003; Loeffler et al. 2005), electron-induced radiation (Jamieson et al. 2006; Martin et al. 2008; Bennett et al. 2009b), as well as through ion bombardment (Moore et al. 1996; Palumbo et al. 1998; Satorre et al. 2000; Trottier & Brooks 2004). As relevant to this study, CO$_2$ has also been shown to be formed from the irradiation of CO:O$_2$ ices (Satorre et al. 2000; Strazzulla et al. 1997; Bennett et al. 2009a).

Solid-state laboratory experiments suggest that interstellar HCOOH and CO$_2$ may have an icy origin and with common formation pathways. CO$_2$ is typically formed alongside HCOOH (Hudson & Moore 1999; Ioppolo et al. 2010; Bennett et al. 2010; Butscher et al. 2016) or from HCOOH (Andrade et al. 2013; Bergantini et al. 2013; Ryazantsev & Feldman 2015). It has also been formed without co-detection of HCOOH (Oba et al. 2010a,b; Raut & Baragiola 2011; Ioppolo et al. 2011, 2013b,a; Raut et al. 2012; Minissale et al. 2015; Suhasaria et al. 2017), although not all the studies explicitly state a non-detection of HCOOH or involve hydrogen. And in the case of the HOCO intermediate, it can dissociate upon hydrogenation to form CO$_2$ rather than hydrogenate to form HCOOH (Ioppolo et al. 2011; Linnartz et al. 2015).

While the bulk of CO_2 and probably HCOOH is formed early in the cloud evolution, alongside with H_2O, the aforementioned laboratory experiments indicate that some HCOOH and CO_2 formation may occur during the heavy CO freeze-out stage as well. This is additionally supported by observations of CO_2 ice in a CO environment (Pontoppidan et al. 2008), where the fraction of CO_2 in a CO environment is 15-40%. The authors suggest that a quiescent formation mechanism could be at play for CO_2 formation, in addition to cosmic-ray induced chemistry. Such a mechanism may arise from the hydrogenation of a $CO:O_2$ ice mixture, as some O_2 is likely mixed with CO at greater cloud depths (Tielens & Hagen 1982; Vandenbussche et al. 1999; Qasim et al. 2018). Additionally, OH radicals near the top of the H_2O-rich ice may interact with incoming CO molecules. During the heavy CO freeze-out stage, a considerable amount of CO freezes out (Pontoppidan 2006; Boogert et al. 2015; Qasim et al. 2018) and can be hydrogenated to form H_2CO, CH_3OH, and more complex organics (Chuang et al. 2016; Fedoseev et al. 2017). The solid-state chemistry during the CO freeze-out stage is primarily driven by atom addition and abstraction reactions (Linnartz et al. 2015).

The experimentally and/or theoretically investigated 'non-energetic' formation pathways for HCOOH and CO_2 ice that are reported in the literature are:

$$HCO + OH \rightarrow HCOOH \tag{15}$$
$$OH + CO \rightarrow HOCO, H + HOCO \quad \rightarrow HCOOH \tag{16}$$
$$OH + CO \rightarrow HOCO, H + HOCO \quad \rightarrow H_2 + CO_2 \tag{17}$$
$$OH + CO \rightarrow HOCO, OH + HOCO \rightarrow H_2O + CO_2 \tag{18}$$
$$OH + CO \rightarrow H + CO_2 \tag{19}$$
$$CO + O \rightarrow CO_2 \tag{20}$$
$$H_2CO + O \rightarrow CO_2 + H_2 \tag{21}$$

Although investigated in detail before, many of the listed routes to HCOOH and CO_2 formation are yet to have tight experimental constraints. To our knowledge, only one study showed the formation of HCOOH under 'non-energetic' conditions (Ioppolo et al. 2010), and within this study, the reaction pathway involving the HOCO complex was considered. HCO + OH was reported to be unlikely since the HCO derivatives, H_2CO and CH_3OH, went undetected in the RAIR experiments under their experimental conditions. However, models suggest that HCO + OH is relevant to the solid-state chemistry of the prestellar core phase (Garrod & Herbst 2006). Oba et al. (2010a) also studied the reaction of OH and CO at low temperatures under different experimental conditions than those used by Ioppolo et al. (2010), and did not positively identify HCOOH formation. For the formation routes of CO_2, particularly reactions 17, 18, and 19 are of concern as it is uncertain which route dominates within an experiment, and thus which one is expected to be relevant to the interstellar medium (ISM). The reactant HOCO was considered an ingredient for CO_2 formation due to the reported weak IR band(s) of the HOCO complex (Oba et al. 2010a; Ioppolo et al. 2011). In the work by Noble et al. (2011), formation of CO_2 + H by solid-state OH + CO was reported to occur under their experimental conditions.

In this paper, we propose an additional way to form HCOOH and CO_2 under conditions relevant to the heavy CO freeze-out stage, and that is through the

hydrogenation of an H$_2$CO:O$_2$ ice mixture, where O$_2$ is used as a tool to produce an abundant amount of OH radicals in the ice (Cuppen et al. 2010). It is stressed that the focus of this work is not to mimic a realistic interstellar ice, but to identify potential interstellar ice reaction channels. We use this new experimental finding, deuterated experiments, theoretical results available from the literature, and revisit previous experimentally studied reactions to provide greater constraints on the HCOOH and CO$_2$ 'non-energetic' formation pathways. Section 6.2 overviews the current state of the experimental apparatus and details the experimental parameters and methods used. Section 6.3 discusses the formation pathways of HCOOH and CO$_2$. Section 6.4 outlines in particular how this study can contribute to the search for HCOOH ice in dense clouds. Section 6.5 lists the concluding remarks of this work.

6.2 Methodology

6.2.1 Experimental setup

The experiments described here are performed with SURFRESIDE^2; an ultra-high vacuum (UHV) system designed to investigate the atom-induced reaction dynamics that take place in interstellar ices found in translucent and dense clouds/dark cores. Within the main chamber, a closed cycle helium cryostat is connected to a gold-plated copper sample, which acts as a platform for solid-state reactions. More details on the design of the setup can be found in Ioppolo et al. (2013a), and recent modifications to the setup are included in Chuang et al. (2018).

To date, atoms including H, D, N, and O can be formed by the combination of two atom beam lines. Each line is placed in its own vacuum chamber and connected to the main chamber through a shutter valve, which has a base pressure of ~10^{-10} mbar. Ample hydrogen and deuterium atoms are formed by a Hydrogen Atom Beam Source (HABS) (Tschersich & Von Bonin 1998; Tschersich 2000; Tschersich et al. 2008) and a Microwave Atom Source (MWAS; Oxford Scientific Ltd.). For the HABS, atoms are formed by the thermal cracking of hydrogen molecules. Because the filament within the HABS reaches a temperature of 2065 K in this study, a nose-shaped quartz tube is placed at the end of the HABS in order to collisionally cool the H-atoms. Such a tube is also placed at the end of the MWAS, since the atoms are created by the bombardment of 'energetic' electrons that are stimulated by a 2.45 GHz microwave power supply (Sairem) at 275 W. Both sources are utilized for two series of experiments (see Table 6.1), where the HABS is exploited for most of the experiments. The MWAS was used when the HABS became unavailable due to maintenance.

Gases, liquids, and solids are used to make the necessary ice mixtures. H$_2$ (Linde 5.0) gas goes through the HABS and MWAS, while D$_2$ (Praxair 99.8%) is only fragmented by the MWAS. O$_2$ (Linde Gas 99.999%) and ^{18}O$_2$ gases (Campro Scientific 97%) flow through the vacuum chamber of the MWAS (microwave source off) and into the main chamber. HCOOH and H$_2$O liquids are connected to turbomolecular-pumped dosing lines and undergo freeze-pump-thaw cycles in order to get rid of volatile impurities. Paraformaldehyde (Sigma-Aldrich 95%) and paraformaldehyde-^{13}C (Sigma-Aldrich 99%) powders are also connected to

Table 6.1: A detailed list of the experiments described in this study. Fluxes are calculated by the Hertz-Knudsen equation except for the H/D flux.

No.	Experiments	T_{sample} (K)	$Flux_{H_2CO/CO}$ ($cm^{-2}s^{-1}$)	$Flux_{H/D}$ ($cm^{-2}s^{-1}$)	$Flux_{O_2}$ ($cm^{-2}s^{-1}$)	$Flux_{H_2O}$ ($cm^{-2}s^{-1}$)	$Flux_{HCOOH}$ ($cm^{-2}s^{-1}$)	Time (s)
1	$H_2CO + H + O_2$	10	3×10^{12}	5×10^{12}	4×10^{12}	-	-	43200
2	$H_2CO + H + O_2$	10	3×10^{12}	5×10^{12}	4×10^{12}	-	-	14400
3	$H_2{}^{13}CO + H + O_2$	10	3×10^{12}	5×10^{12}	4×10^{12}	-	-	14400
4	$H_2CO + H + {}^{18}O_2$	10	3×10^{12}	5×10^{12}	4×10^{12}	-	-	14400
5	$H_2{}^{13}CO + H + {}^{18}O_2$	10	3×10^{12}	5×10^{12}	4×10^{12}	-	-	14400
6	HCOOH	10	-	-	-	-	7×10^{11}	14400
7	$H_2CO + O_2 + H_2O$	10	$3 \times 10^{12}*$	-	4×10^{12}	$4 \times 10^{11}*$	-	4800
8	H_2O	15	-	-	-	2×10^{13}	-	2160
9	$H + O_2$	15	-	2×10^{12}	3×10^{12}	-	-	9120
10‡	$CO + D + O_2$	10	3×10^{12}	7×10^{12}	4×10^{12}	-	-	14400
11‡	$CO + H + O_2$	10	3×10^{12}	7×10^{12}	4×10^{12}	-	-	14400

*Fluxes adjusted during deposition in order to achieve the desired RAIR integrated band area ratio between H_2CO and H_2O.

‡H and D atoms are produced by the MWAS. Experiments 1-5 and 9 utilize the HABS.

the pre-pumped dosing lines, and are thermally decomposed by a bath of hot water in order to form H_2CO and $H_2{}^{13}CO$ vapours, respectively. CO gas (Linde Gas 99.997%) is also introduced through one of the dosing lines. Both dosing lines terminate with manually-operated leak valves. All isotopes are used for the purpose of constraining the newly formed ice species, HCOOH and CO_2, and their reaction pathways.

The techniques employed to investigate the ice composition, reaction pathways, and relative chemical abundances are temperature programmed desorption - quadrupole mass spectrometry (TPD-QMS) and reflection-absorption infrared spectroscopy (RAIRS). For TPD-QMS, a quadrupole mass spectrometer (Spectra Microvision Plus LM76) is used to probe the mass-to-charge (m/z) values of the sublimated ice reactants and products as a function of temperature. Resistive heating is used to heat the sample, which has a temperature range of 7-450 K. A silicon diode sensor placed at the back of the sample is used to measure the temperature and has an absolute accuracy of 0.5 K. An electron impact ionization energy of 70 eV is set for all experiments, while a TPD-QMS ramp rate of 2 or 5 K/min is chosen. It has been found that this small change in the ramp rate does not affect the main conclusions of this study. For RAIRS, a Fourier transform infrared spectrometer (FTIR; Agilent Cary 640/660) with a used wavenumber range of 4000-700 cm^{-1} and a resolution of 1 cm^{-1} is utilized to probe solid-state species through their molecular vibrations in the ice.The QMS detection limit is around 0.005 monolayers (equivalent to the amount in the solid-state), and for the FTIR, it is around an order of magnitude less for species with relatively high band strengths.

6.2.2 Experimental methods

Details of the experiments used for this study are outlined in Table 6.1. The H and D-atom fluxes are derived from an absolute D-atom flux that was determined by a QMS (Ioppolo et al. 2013a). All other fluxes are calculated by the

Hertz-Knudsen equation. The rationale for the set of experiments is discussed in the following paragraphs.

Experiments 1-11 are, in part, used to show the results of HCOOH and CO$_2$ ice formation at 10 K. The OH radicals needed for the formation of HCOOH and CO$_2$ are formed by H + O$_2$ (Cuppen et al. 2010). All experiments involve the co-deposition technique (i.e., reactants are deposited simultaneously). Co-deposition is more representative of interstellar conditions and enhances the possibility of radical recombination reactions. The purpose of the lengthy experiment, 1, is to increase the product abundance in order to probe the formed ice species via RAIRS, which is a less sensitive technique compared to TPD-QMS under our specific experimental settings. The isotopes used in experiments 3-5 are applied to observe the m/z and infrared band shifts in the TPD-QMS and RAIR data, respectively. These shifts are compared to the spectra of experiment 2, which represents the principal reaction of this study. Experiments 6-9 are used to confirm the HCOOH infrared signature in the RAIR data of experiment 1. Experiments 10-11 are used to validate the H + HOCO pathway in CO-rich ices, and thus provide additional insight into the formation of HCOOH and CO$_2$ in the H$_2$CO + H + O$_2$ experiment.

RAIR data are exploited to determine the HCOOH:CO$_2$ relative abundance using a modified Lambert-Beer equation. Band strength values of 5.4×10^{-17} and 7.6×10^{-17} cm molecule^{-1} are used to determine the column densities of HCOOH and CO$_2$, respectively, and are obtained from Bouilloud et al. (2015). Note that the values are multiplied by a transmission-to-RAIR proportionality factor, and the procedure to obtain this factor is discussed in Qasim et al. (2018). A HCOOH:CO$_2$ ice abundance ratio of 1.9:1 is measured. To check the validity of using RAIR data to measure abundances, the abundances are additionally determined from TPD-QMS data. For the TPD measurements of H^{13}COOH and ^{13}CO$_2$, the peak heights are measured at 157 K for H^{13}COOH desorption (m/z = 47), and 79 and 150 K for ^{13}CO$_2$ desorption (m/z = 45). The formula to determine the column density from TPD data is found in Martín-Doménech et al. (2015) and references therein. The total ionization cross sections used are 5.09×10^{-16} cm^2 for H^{13}COOH (Możejko 2007) and 2.74×10^{-16} cm^2 for ^{13}CO$_2$ (Orient & Strivastava 1987). The sensitivity values are 0.162 and 0.176 for m/z = 47 and 45, respectively, and are collected from SURFRESIDE^2 (Chuang 2018, Univ. Leiden). A H^{13}COOH:^{13}CO$_2$ ice abundance ratio of 1.6:1 is determined. The discrepancy is within range for the uncertainties that are associated with each method. Particularly with RAIRS, the accuracy maybe less than that of TPD-QMS since RAIRS is more sensitive to surface features than by the bulk of the ice.

The relative abundances of other formed products are determined by RAIR data solely, since the TPD-QMS data has overlapping m/z values (e.g., the CO$^+$ signal is completely dominated by the signal of the CO$^+$ fragment of H$_2$CO$^+$). Band strength values of 2.1×10^{-17} cm molecule^{-1} for H$_2$O$_2$, 7.6×10^{-18} cm molecule^{-1} for H$_2$O, and 5.2×10^{-17} cm molecule^{-1} for CO are used to determine the column densities of the three species, where the band strength values for H$_2$O$_2$ and H$_2$O are determined from Loeffler et al. (2006), and the value for CO is from Chuang et al. (2018). An H$_2$O$_2$:H$_2$O:CO abundance ratio of 1:0.7:0.02 is measured.

6.3 Results and discussion

6.3.1 Formation of HCOOH ice by $H_2CO + H + O_2$

The top panel of Figure 6.1 shows the TPD-QMS spectra of newly formed HCOOH obtained after the co-deposition of $H_2CO + H + O_2$, as well as pure HCOOH taken after deposition of pure HCOOH. Additional TPD-QMS spectra obtained after the formation of HCOOH isotopologues in correlated isotope-substituted reactions are shown in the bottom panel. Although HCOOH desorbs at 142 K in its pure form (top right panel), the literature shows that HCOOH typically desorbs at a higher temperature when mixed with less volatile compounds (Ioppolo et al. 2010; Bennett et al. 2010), in line with the present experiments. The m/z values displayed in the bottom panel of Figure 6.1 clearly represent the formation of HCOOH involving oxygen atoms that originate from two different molecules, H_2CO and O_2. If the oxygen atoms of newly formed HCOOH were to solely originate from H_2CO, then there would be no desorption signals at 157 K for m/z values of 48 and 47 in exp. 4, and for m/z values of 49 and 48 in exp. 5. Instead, the signals for m/z values of 46 and 45 in exp. 4 and 47 and 46 in exp. 5 would rise, which is not the case. Following this, the m/z values presented in the bottom panel of Figure 6.1 line-up with the formation of a species that contains an oxygen atom from H_2CO and an oxygen atom from O_2, with m/z values that are the same as that of the expected HCOOH isotopologues. Additionally, the desorption peak at 157 K is consistently present among the exps. 2, 4 and 5, and the profiles are nearly identical. This indicates that the desorption peaks should represent the same species and are thus assigned to HCOOH. This assignment is further supported by the QMS fragmentation pattern shown in Figure 6.2. HCOOH partially fragments to $COOH^+$ upon 70 eV electron impact ionization with a $COOH^+$:$HCOOH^+$ relative intensity of 78:100 in the pure HCOOH experiment (exp. 6). This relative intensity is similar to the values of 79:100, 79:100, and 82:100 found in the $H_2CO + H$ + O_2, $H_2CO + H + {}^{18}O_2$, and $H_2{}^{13}CO + H + {}^{18}O_2$ experiments, respectively.

Constraining the formation of HCOOH at 10 K by RAIR data is discussed below. In Figure 6.3, a spectrum of $H_2CO + H + O_2$ taken after deposition at 10 K is shown. The products formed in the $H_2CO + H + O_2$ experiment are listed in Table 6.2 along with the corresponding IR signatures that are labeled in Figure 6.3. Note that the two peaks around 1000 cm^{-1} are within the frequency range of the C-O stretch of CH_3OH (Dawes et al. 2016). However, these peaks disappear between 195 and 205 K (not shown here), which is a temperature range that is higher than the desorption temperature of CH_3OH or any species that are positively identified in this study. Therefore those peaks, although pronounced, are not attributed to a particular species at this time. Yet CH_3OH, an expected product, is detected in the TPD-QMS experiments (not shown here). The specific features in Table 6.2 arise from precursor species, intermediates, and reaction products. Some of these species, although formed abundantly in the experiment, are yet to be observed in space. However, certain conditions in the laboratory are vastly different from the conditions in the ISM, and therefore comparison of even relative product abundances from the laboratory must be taken with caution to the relative abundances found in space. For example, H_2O_2, which is a side product from the $H + O_2$ reaction, has yet to be detected
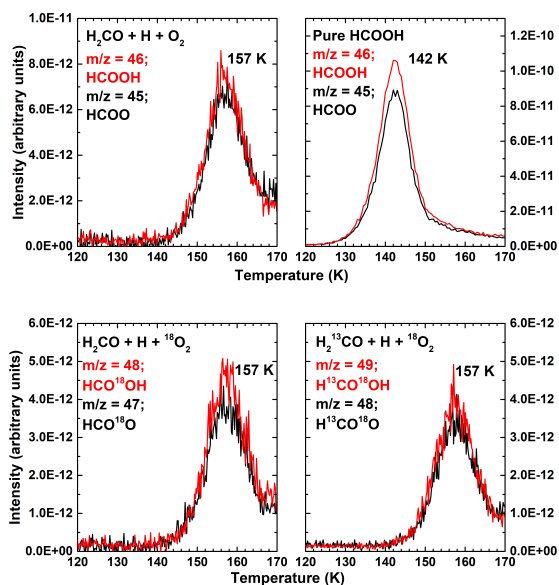
Figure 6.1: TPD-QMS spectra of H$_2$CO + H + O$_2$ (top left; exp. 2) and HCOOH (top right; exp. 6). TPD-QMS spectra of H$_2$CO + H + ^{18}O$_2$ (bottom left; exp. 4) and H$_2$^{13}CO + H + ^{18}O$_2$ (bottom right; exp. 5). All spectra are recorded after ice growth at 10 K.
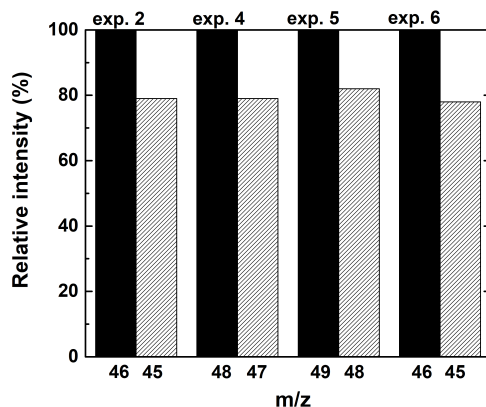

Figure 6.2: The QMS cracking pattern of the desorption feature peaking at 157 K in the H$_2$CO + H + O$_2$ experiment (exp. 2), H$_2$CO + H + ^{18}O$_2$ experiment (exp. 4), H$_2$^{13}CO + H + ^{18}O$_2$ experiment (exp. 5), and deposited HCOOH (exp. 6). The patterns are measured for temperatures at 157 K for exps. 2, 4, and 5, and 142 K for exp. 6. m/z = 46 and 45 are the masses of the HCOOH$^+$ and COOH$^+$ ions, respectively.
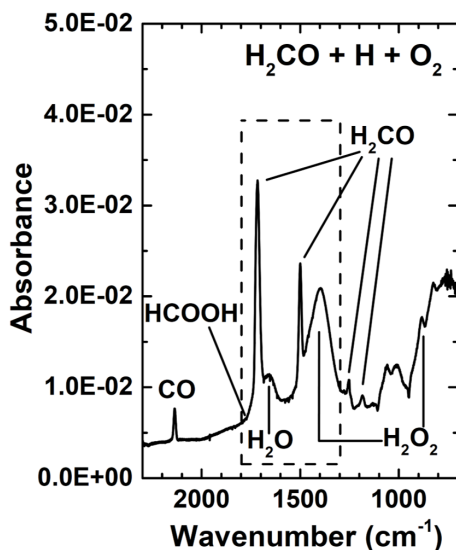
Figure 6.3: RAIR spectrum of $H_2CO + H + O_2$ (exp. 1). Spectra are recorded after deposition at 10 K. The dashed-line box is a zoom-in of the spectrum shown in Figure 6.4.

in interstellar ices. It could be efficiently destroyed by a mechanism that does not take place in our experiments, for example.

Although not straightforward, it is possible to show that HCOOH can be identified spectroscopically. For this, the spectrum is interpreted in a multiple linear regression (MLR) analysis. Figure 6.4 shows a zoom-in of the spectrum along with spectra of the independent variables. The dependent variable is the original spectrum from Figure 6.3. The independent variables represent the expected spectral components of the $H_2CO + H + O_2$ experiment. The differences between the components (e.g., HCOOH, H_2O, etc.) and the original spectrum (i.e., $H_2CO + H + O_2$), as well as the choice of the selected components, are discussed.

It is evident in Figure 6.4 that the H_2CO C=O stretching feature at 1717 cm^{-1} in the original spectrum (a) is shifted from that of the MLR spectrum (b), but this is not the case for the C-O stretching feature at 1499 cm^{-1}. This indicates that the 1717 cm^{-1} band is more sensitive to the ice mixture ratio and content than the 1499 cm^{-1} band. Therefore, the choice of using $H_2CO + O_2 + H_2O$ (c) versus pure H_2CO is to witness how O_2 and H_2O contribute to broadening and shifting of the C=O peak. The pure H_2O component (e) is relatively small, as the majority of H_2O is already in the $H_2CO + O_2 + H_2O$ component. The $H + O_2$ component (f) is used to contribute pure H_2O_2 (i.e., no H_2O formed) into the analysis, which is a molecule that is not possible to deposit under our experimental conditions. The contribution of pure H_2O_2 can probably explain why there is a difference in the profile shapes of the $\sim 1400 \text{ cm}^{-1}$ feature between the $H + O_2$ component and the original spectrum. Finally, the contribution of HCOOH (d) can reproduce the $\sim 1750 \text{ cm}^{-1}$ shoulder of the original spectrum,

Table 6.2: List of assigned species in the H$_2$CO + H + O$_2$ (exp. 1) experiment.

Peak position (cm^{-1})	Peak position (μm)	Literature values (cm^{-1})	Molecule	Mode
880	14.64	888[a], 880[b], 882[c], 884[d]	H$_2$O$_2$	ν_3
1184	8.446	1175[e], 1175[f], 1178[g]	H$_2$CO	ν_6
1251	7.994	1250[e], 1253[f], 1249[g]	H$_2$CO	ν_5
1396	7.163	1390[a], 1368[b], 1376[c], 1381[d]	H$_2$O$_2$	ν_2
1499	6.671	1499[e], 1499[f], 1499[g]	H$_2$CO	ν_3
1652	6.053	1650[h], 1653[i]	H$_2$O	ν_2
1717	5.824	1718[e], 1727[f], 1722[g]	H$_2$CO	ν_2
~1750 shoulder	~5.714	1690[e], ~1750[j], ~1750[k]	HCOOH	ν_2
2137	4.679	2141[e], 2138[l]	CO	ν_1
2343	4.268	2345[e], 2344[l]	CO$_2$	ν_3

[a]Romanzin et al. (2011) [b]Giguere & Harvey (1959) [c]Lannon et al. (1971) [d]Qasim et al. (2018) [e]Bennett et al. (2010) [f]Chuang et al. (2016) [g]Watanabe & Kouchi (2002) [h]Ioppolo et al. (2008) [i]Hodyss et al. (2009) [j]Ioppolo et al. (2010) [k]Bisschop et al. (2007b) [l]Ioppolo et al. (2011)
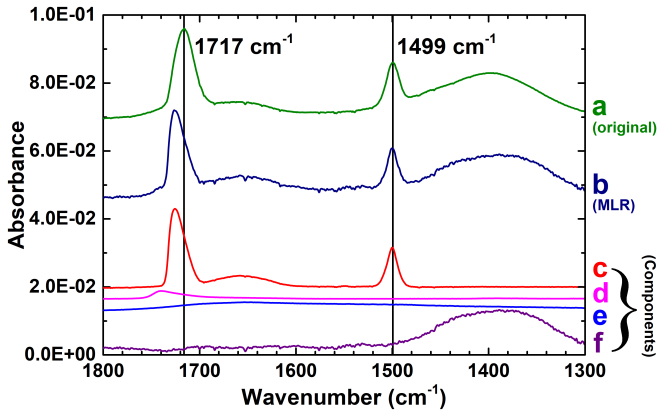
Figure 6.4: RAIR spectra of H$_2$CO + H + O$_2$ (a; exp. 1), the H$_2$CO + H + O$_2$ MLR spectrum (b), and its components multiplied by the coefficients derived from the MLR analysis: H$_2$CO + O$_2$ + H$_2$O (c; exp. 7; 1.2 coefficient), HCOOH (d; exp. 6; 0.3 coefficient), H$_2$O (e; exp. 8; 0.7 coefficient), and H + O$_2$ (f; exp. 9; 9.7 coefficient). Spectra are recorded after deposition at 10 K and are offset for clarity.
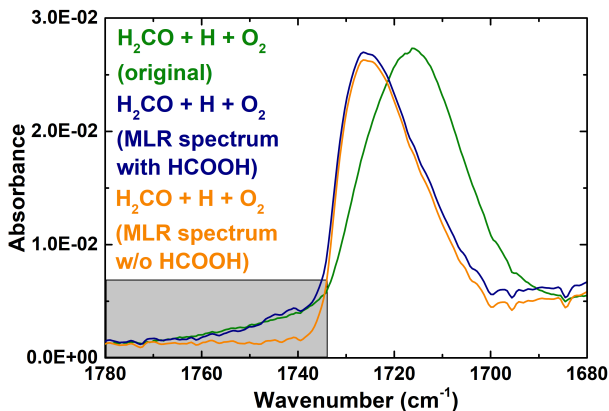
Figure 6.5: RAIR spectra of $H_2CO + H + O_2$ (exp. 1) and $H_2CO + H + O_2$ MLR spectra with and without HCOOH inclusion (i.e., component d from Figure 6.4). The grey box shows the shoulder found in the RAIR spectrum of exp. 1 that is assigned to the C=O stretching mode of HCOOH. Spectra are recorded after deposition at 10 K and are offset for clarity.

as shown in Figure 6.5. Note that the HCOOH out-of-phase C=O stretching feature is also sensitive to its surrounding environment (Bisschop et al. 2007a), and can range from ~1700 cm^{-1} (Bisschop et al. 2007a; Bennett et al. 2010) to ~1750 cm^{-1} (Bisschop et al. 2007b; Ioppolo et al. 2010). The figure provides zoom-in spectra of the original and MLR spectra from Figure 6.4, as well as the MLR spectrum that does not include the HCOOH component. The grey box highlights the shoulder of the C=O stretching feature in the $H_2CO + H + O_2$ experiment. When HCOOH is not included, the shoulder disappears. This infers that the shoulder is not solely due to intramolecular broadening effects, and that the inclusion of HCOOH allows to reproduce this feature. This shoulder may also be explained by glycolaldehyde ($HCOCH_2OH$), as the molecule has a signature at ~1750 cm^{-1} and can be formed from the hydrogenation of H_2CO (Chuang et al. 2016). Yet, its signal does not appear in the TPD-QMS data and therefore is not expected to appear in the correlating RAIR data. Thus, the RAIR data is fully consistent with the conclusion from the TPD-QMS experiments that HCOOH is formed at 10 K.

6.3.2 Formation of CO_2 ice by $H_2CO + H + O_2$

The formation of CO_2 ice is confirmed by RAIR and TPD-QMS data presented in Figure 6.6. The experiments, $H_2^{13}CO + H + O_2$ and $H_2^{13}CO + H + {}^{18}O_2$, are purposefully displayed in order to not confuse the newly formed CO_2 with residual CO_2 that is omnipresent as a background pollutant, even under UHV conditions. The RAIR spectra (left panel) clearly show the asymmetric stretching modes of $^{13}CO_2$ and $^{13}CO^{18}O$ at 2276 cm^{-1} and 2259 cm^{-1}, respectively (Maity et al. 2014). The TPD-QMS data (right panel) also clearly illustrate the desorption of both species at the CO_2 desorption temperature of 79 K (Fayolle et al. 2011). We also find that CO_2 desorbs at higher temperatures via 'volcano'

desorption at 150 K (prior to H$_2$O desorption) and co-desorption with H$_2$O$_2$ at 175 K (not shown here).
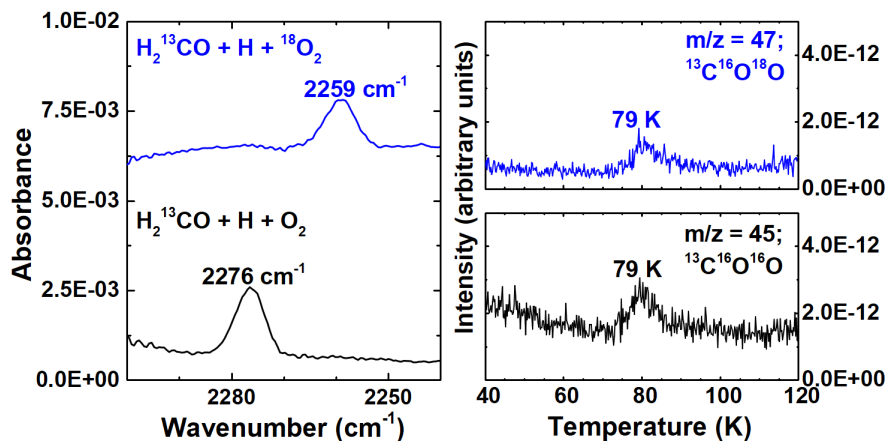

Figure 6.6: (Left) RAIR and (right) TPD-QMS signals that illustrate the characteristic features of ^{13}COO and ^{13}CO^{18}O found in the H$_2$^{13}CO + H + O$_2$ (exp. 3) and H$_2$^{13}CO + H + ^{18}O$_2$ (exp. 5) experiments, respectively. Both take place at a substrate temperature of 10 K. RAIR spectra are offset for clarity.

6.3.3 Pathways to HCOOH and CO$_2$ formed in the experiments

In order to tightly constrain the formation routes of HCOOH and CO$_2$ in our experiments, knowledge of the possible reactions taking place along with the activation barriers and branching ratios are needed. Table 6.3 lists reactions that are expected to occur in the H$_2$CO + H + O$_2$ experiment. Note that the values in the table are from predominantly theoretical studies, as shown in the footnotes.

6.3.3.1 HCOOH formation pathway

HCOOH can be formed by reactions 15 and/or 16 in the presented experiments: HCO + OH and/or H + HOCO. The formation of HCO occurs by H-atom addition of CO and H-atom abstraction from H$_2$CO; both which contain activation barriers (Andersson et al. 2011; Song & Kästner 2017). This was demonstrated experimentally by Hidaka et al. (2004) and Chuang et al. (2016). The OH radical is formed by H + HO$_2$, which is a barrierless reaction that occurs early within the H + O$_2$ reaction chain (Lamberts et al. 2013). It is also formed by the H + H$_2$O$_2$ reaction (Lamberts & Kästner 2017), which however involves barriers. The activation energy of HOCO formed by OH + CO is calculated to be nearly zero (Nguyen et al. 2012; Masunov et al. 2016; Tachikawa & Kawabata 2016), and since H + HOCO is barrierless, one may expect that H + HOCO dominates HCOOH formation. Yet, the pathway also requires two extra steps (i.e., H-abstraction from HCO and formation of HOCO) in comparison to the HCO +

Table 6.3: List of possible reactions taking place in the $H_2CO + H + O_2$ experiment.

Reaction	Product(s)	Branching ratio (%)	Activation energy (kJ mol^{-1})	Rate constant (s^{-1})	Reference
$H + H_2CO \rightarrow$	CH_3O	-	16-18	6×10^5 - 2×10^6	a
	CH_2OH	-	43-47	4×10^1 - 9×10^1	a
	$H_2 + HCO$	-	21-25	4×10^5 - 1×10^6	a
$H + HCO \rightarrow$	H_2CO	50	0	-	zeroth-order approximation[♠]
	$H_2 + CO$	50	0	-	zeroth-order approximation
$H + CO \rightarrow$	HCO	-	$12.4^b + 3^c$	2×10^5	b, c
$H + O_2 \rightarrow$	HO_2	100	~0	-	d
$H + HO_2 \rightarrow$	2 OH	50	0	-	e, zeroth-order approximation
	H_2O_2	50	0	-	e, zeroth-order approximation
2 OH $\rightarrow$	H_2O_2	90	0	-	d
	$H_2O + O$	10	0	-	d
$H + H_2O_2 \rightarrow$	$H_2O + OH$	-	21-27	2×10^3 - 1×10^6	f
	$H_2 + HO_2$	-	39	◇	g
$OH + HCO \rightarrow$	HCOOH	50	0	-	zeroth-order approximation
	$H_2O + CO$	50	0	-	zeroth-order approximation
$OH + H_2CO \rightarrow$	$H_2O + HCO$	-	2.64	◇	h
$OH + CO \rightarrow$	$H + CO_2$	-	*	*	i, j, k
	HOCO	~100	~0	-	i, j, k
$H + HOCO \rightarrow$	$H_2 + CO_2$	50	0	-	zeroth-order approximation
	HCOOH	50	0	-	zeroth-order approximation
$OH + H \rightarrow$	H_2O	100	0	-	-
$OH + H_2 \rightarrow$	$H_2O + H$	-	22.4-24.3	2×10^5 - 5×10^5	l
$H + CH_3O \rightarrow$	CH_3OH	50	0	-	zeroth-order approximation
	$H_2CO + H_2$	50	0	-	zeroth-order approximation

[a]Song & Kästner (2017) [b]Andersson et al. (2011) [c]Álvarez-Barcia et al. (2018); zero-point energy contribution [d]Lamberts et al. (2013) [e]Lamberts et al. (2014) [f]Lamberts & Kästner (2017) [g]Lamberts et al. (2016) [h]Zanchet et al. (2018) [i]Nguyen et al. (2012) [j]Masunov et al. (2016) [k]Tachikawa & Kawabata (2016) [l]Meisner et al. (2017)

(-) indicates values that are not the defining parameters.

(*) indicates multi-step reaction; values cannot be trivially obtained.

(◇) indicates that unimolecular rate constants are not available.
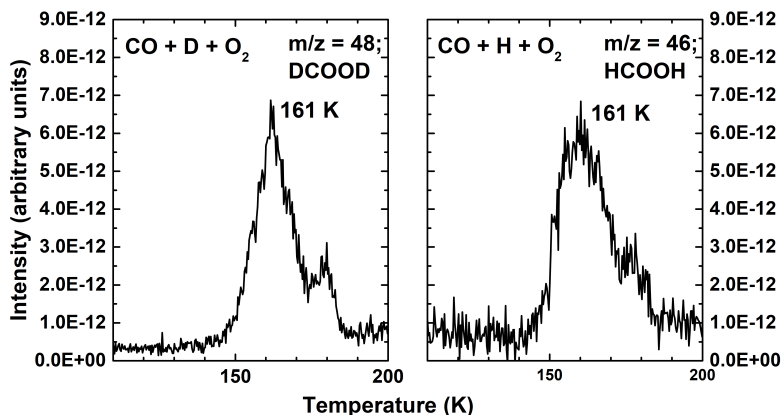
(♠) indicates first educated guess.

Figure 6.7: TPD-QMS spectra of CO + D + O$_2$ (exp. 10) and CO + H + O$_2$ (exp. 11) recorded after ice growth at 10 K.

OH route. To determine the relevance of the two pathways, experimental and theoretical data are combined and the outcomes are discussed below.

The formation of CO ice is shown in Figure 6.3 at 2137 cm^{-1}. This occurs by the hydrogen abstraction from H$_2$CO to produce HCO, and subsequently the hydrogen abstraction from HCO to produce CO. This HCO radical can react with a nearby OH radical barrierlessly to form HCOOH. Next, the contribution from the H + HOCO pathway is discussed. The HOCO intermediate is not observed in the RAIR spectra, as it was in other studies (Oba et al. 2010a; Ioppolo et al. 2010). However, HOCO is an unstable species, and can be stabilized depending on the polarity of the ice matrix (Ioppolo et al. 2011) and whether HOCO is embedded in the ice (Arasa et al. 2013). Therefore, HOCO can still be relevant to HCOOH formation in the H$_2$CO + H + O$_2$ experiment, even though it is undetected in our RAIR data. According to Ioppolo et al. (2010), in a CO-rich ice, H + HOCO is found to be the dominant pathway to HCOOH formation. Thus, with the sight of CO in our RAIR data as shown in Figure 6.3, it cannot be excluded that H + HOCO is a contributing route for HCOOH formation. As the dominance of the H + HOCO pathway was determined by one weak transition of HOCO in Ioppolo et al. (2010), we performed isotope experiments with CO to further confirm this.

Figure 6.7 shows TPD-QMS spectra of m/z = 48 (representative of DCOOD) from the CO + D + O$_2$ experiment and m/z = 46 (representative of HCOOH) from the CO + H + O$_2$ experiment. In essence, the relative abundance of DCOOD to HCOOH shows which pathway dominates formic acid formation starting from a CO-rich ice. This can be explained by discussion of the following reactions:

$$OD + CO \rightarrow DOCO \overset{+D}{\rightarrow} DCOOD \tag{22}$$

$$OH + CO \rightarrow HOCO \overset{+H}{\rightarrow} HCOOH \tag{23}$$

OD/OH + CO is essentially barrierless, and D/H + DOCO/HOCO is barrierless. Thus, the reaction rates of reactions 22 and 23 are similar. However, for the reactions below:

$$D + CO \rightarrow DCO \xrightarrow{+OD} DCOOD \qquad (24)$$

$$H + CO \rightarrow HCO \xrightarrow{+OH} HCOOH \qquad (25)$$

D + CO is more than two orders of magnitude slower than H + CO (Andersson et al. 2011). Thus, if the abundance of HCOOH is much greater than the abundance of DCOOD, then HCO + OH would be considered the more dominant pathway.

The TPD-QMS results from Figure 6.7 show that the integrated areas of DCOOD and HCOOH are essentially the same (i.e., they are not different by orders of magnitude). Therefore, it cannot be claimed from the presented results that HCO + OH is dominating in the $CO + H + O_2$ experiment. Rather, H + HOCO dominates a CO-rich ice, which is in agreement with the findings from Ioppolo et al. (2010). However, which pathway contributes more or less to the formation of HCOOH in the $H_2CO + H + O_2$ experiment cannot be extracted here. We restrict our conclusion to the finding that both pathways occur and contribute to the formation of HCOOH. This is for the conditions investigated in our setup. To extrapolate these to interstellar ices, it is important to use astrochemical simulations in order to compare the relative contributions of each of the suggested reaction pathways under dense cloud conditions.

6.3.3.2 CO_2 formation pathway

The formation of CO_2 is also via two pathways, as shown in Table 6.3. Note that OH + HOCO is not considered, as OH + HOCO should yield carbonic acid (H_2CO_3) (Oba et al. 2010b; Ioppolo et al. 2010), in addition to CO_2 (Yu et al. 2005; Francisco et al. 2010), and H_2CO_3 is not detected in our experiments. OH + CO $\rightarrow$ HOCO has an activation barrier of nearly zero, whereas OH + CO $\rightarrow$ CO_2 + H has barriers, making the HOCO product a more likely outcome. HOCO can then react with an H-atom to form $H_2 + CO_2$ and HCOOH without a barrier. In section 6.3.3.1, we discuss that H + HOCO must be a route to HCOOH formation in the $H_2CO + H + O_2$ experiment. According to Table 6.3, CO_2 is then also expected to be formed alongside HCOOH via H + HOCO. By combination of the experimental results in section 6.3.3.1 with the theoretical values from Table 6.3, we propose that H + HOCO is the dominating pathway to CO_2 formation in our experiments. Our experimental condition of co-deposition is also suitable for forming the HOCO complex, as the HOCO complex survives when it is able to dissipate its energy throughout the ice (Arasa et al. 2013). This excess energy is lost to the ice matrix within picoseconds (Arasa et al. 2010; Fredon et al. 2017), making it less likely that there is enough time for OH + CO $\rightarrow$ CO_2 + H to be attempted. Note that the H_2CO + O pathway is unlikely in the presented experiments, since H-atoms will actively compete with H_2CO to react with O-atoms. CO + O is also not listed, as the barrier of this reaction (Roser et al. 2001) makes it a relatively minor reaction channel (Goumans & Andersson 2010; Ioppolo et al. 2013a). The reaction of H + CO_2 has a very high

barrier of > ~15,000 K (Bisschop et al. 2007b; McCarthy et al. 2016), which is too high to allow for tunneling to speed up the reaction considerably.

Since CO_2 is predominantly formed by H + HOCO, the H + HOCO branching ratio can be used, in combination with the HCOOH:CO_2 ice abundance ratio of around 1.8:1, to determine the contributions of HCO + OH and H + HOCO to HCOOH formation in our experiments. Yet, as shown in Table 6.3, the H + HOCO branching ratio is based off an approximation. Thus, a more well-defined branching ratio is desired in order to perform such a quantitative analysis.

6.3.3.3 Surface reaction mechanism

The dominating reaction mechanism in our experiments is discussed. Typically, interstellar ice analogues are formed by three mechanisms: Langmuir-Hinshelwood (L-H), Eley-Rideal (E-R), and hot-atom (H-A) (Linnartz et al. 2015; He et al. 2017). At the low temperature of 10 K, H-atoms have a high enough sticking coefficient to diffuse through the ice and react with other ice constituents. However, as the surface temperature increases, the H-atom residence time dramatically decreases. This phenomenon has been demonstrated in a number of laboratory works (Watanabe & Kouchi 2002; Watanabe et al. 2003; Cuppen & Herbst 2007; Fuchs et al. 2009; Chuang et al. 2016; Qasim et al. 2018), where hydrogenation product abundances significantly decrease as the substrate temperature rises beneath the initial desorption point of the reactant molecule(s). These observations show that the product abundance is governed by the substrate temperature, which is in favor of the L-H mechanism as the dominating mechanism in these studies. This then also concludes that the majority of H-atoms are thermally equilibrated to the 10 K surface prior to reaction.

We also find that tunneling is essential to product formation in this study. As shown in Table 6.3, H + H_2CO has high activation barriers that range from 16-47 kJ mol^{-1}. However it is shown here, and also in Chuang et al. (2016), that the H-induced abstraction of two H-atoms from H_2CO to form CO occurs. With such high barrier values, the H-atom would not have sufficient energy to hop over the barrier, and therefore must undergo tunneling. The importance of tunneling in these type of reactions is discussed in more detail in Lamberts et al. (2017).

6.4 Astrophysical implications

Grain surface chemistry is a strong function of cloud depth, as the increasing density into the cloud enhances the gas-grain interaction. With the interstellar radiation field decreasing at larger extinctions (A_V) by dust particles, photo-induced processes become less relevant in comparison to 'non-energetic' processes, such as hydrogenation (Chuang et al. 2017). Thus, we expect the 'non-energetic' solid-state HCOOH formation route(s) investigated in our experiments, as well as their efficiencies, to depend strongly on cloud depth. The processes involved are complex and require detailed models in order to quantify their contribution to HCOOH and CO_2 ice formation in the CO freeze-out stage. However, such processes are roughly expected to take place as follows.

Following Cuppen et al. (2009) and Tielens & Hagen (1982), the gas-phase CO:H and O:H ratios are critical parameters in grain surface chemistry. Initially, at cloud depths corresponding to A_V values of less than a few magnitudes, the O-rich gas rapidly becomes hydrogenated on grain surfaces. Subsequently, a polar ice that is rich in H_2O is formed, and the abundantly formed intermediate product, OH, will also react with CO. Our study points to the conclusion that in this environment, this reaction is more likely to form the intermediate HOCO than directly CO_2. Competition by the reaction of CO with H is low at this stage because of the high abundance of OH on the grains and the relatively high gas-phase CO:H ratio, as CO is not yet frozen out. With the presence of HOCO, both CO_2 and HCOOH are then expected to be formed. Indeed, the observed CO_2 abundance is very high (~20% of H_2O Bergin et al. (2005)). The identification of HCOOH at low extinctions is tentative at best (< 5% (Boogert et al. 2011)), because its strongest mode (~6.0 µm) overlaps with that of the H_2O bending mode.

At visual extinctions above ~3 magnitude, the gas-phase CO:H ratio decreases as more CO freezes out. Also, most of the O is locked up in H_2O, reducing the OH abundance on the grain surface. This promotes CO hydrogenation (H + CO). The formation of HOCO becomes less relevant, as the barrierless HCO + OH reaction will contribute to the formation of HCOOH. The formation of CO_2 is then expected to be less important, although our experiments show that CO_2 is formed in the ice. At ever increasing extinctions and densities into the cloud, HCO preferably hydrogenates to H_2CO. H_2CO ice has indeed likely been detected towards Young Stellar Objects at the 2-7% level with respect to H_2O ice (Keane et al. 2001; Boogert et al. 2015). The observations are currently of insufficient quality to determine if H_2CO is present in the polar (H_2O-rich) or apolar (CO-rich) ice phases, but the latter is most likely (Cuppen et al. 2009). H-abstraction reactions will maintain an HCO reservoir and thus the HCO + OH route to HCOOH will continue. From the presented experiments, it is also observed that H + HOCO takes place in the H_2CO + H + O_2 experiment to form HCOOH. With two formation routes involving H_2CO to form HCOOH, it is expected that the HCOOH:CO_2 ratio is highest at A_V > 3. Nevertheless, due to the low OH abundance, the absolute HCOOH abundance (with respect to dust) in the CO-rich layer is probably still less than that at lower extinctions in the H_2O-rich layer. An illustration of the relevance of these reactions to the H_2O-rich and heavy CO freeze-out stages are schematically shown in Figure 6.8. Note that the figure only includes the formation mechanisms found in this work and does not provide an overview of all expected/studied mechanisms. Observations have shown that at A_V > 9, where the "catastrophic" CO freeze-out takes place, CH_3OH becomes dominant (Boogert et al. 2011), and this is expected to be a less favorable environment for HCOOH formation due to the lack of HCO radicals. An important caveat is that the CH_3OH formation threshold of 9 mag is very uncertain. In fact, in some molecular cores, no CH_3OH ice is observed well above this threshold (Boogert et al. 2011). Following the discussion above, this could enhance HCOOH abundances.
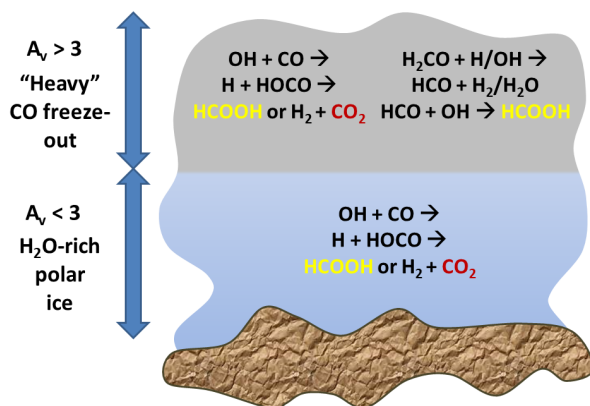
Figure 6.8: Illustration of the formation pathways of HCOOH (highlighted in yellow) and CO$_2$ (highlighted in red) ice in the H$_2$O-rich and heavy CO freeze-out stages, as proposed only from the findings from this study (i.e., not all possible reactions are included). Note that an extra pathway to HCOOH formation is found in the heavy CO freeze-out stage due to the presence of H$_2$CO.

A search for HCOOH at extinctions across the entire extinction range is warranted. The best band to detect HCOOH is at 7.25 μm (Schutte et al. 1999) and has been seen only toward a few YSO envelopes (Öberg et al. 2011; Boogert et al. 2015). In a few years, however sensitive searches in prestellar sightlines across a wide A_V range will be possible with the James Webb Space Telescope (JWST). Studies of the absorption band profiles (peak positions and widths) for a range of sightlines are needed to secure the identification of HCOOH in H$_2$O and CO-rich sightlines.

6.5 Conclusions

The primary findings of this study are listed below:

◆ The hydrogenation of an H$_2$CO:O$_2$ ice mixture to study the H$_2$CO + OH reaction at 10 K adds another 'non-energetic' formation route to the solid-state formation of HCOOH and CO$_2$ in cold interstellar clouds. Astrochemical modeling is desired to know to what extent the new reactions added here contribute.

◆ The formation of HCOOH in the H$_2$CO + H + O$_2$ experiment occurs by both, H + HOCO and HCO + OH. The exact value of their relative contributions can be determined once a more well-defined branching ratio of H + HOCO becomes available.

◆ The formation of HCOOH in the CO + H + O$_2$ experiment occurs predominantly by H + HOCO, as shown here and in Ioppolo et al. (2010).

◆ The formation of CO_2 in both, H_2CO + H + O_2 and CO + H + O_2 experiments, is predominantly through H + HOCO rather than OH + CO for the conditions studied here.

◆ A search for HCOOH ice in the ISM is expected to be promising at extinctions where HCO and H_2CO are formed, but before H_2CO is sufficiently hydrogenated to form CH_3OH, which albeit has an uncertain formation threshold of 9 mag.

Bibliography

Álvarez-Barcia, S., Russ, P., Kästner, J., & Lamberts, T. 2018, Mon. Not. R. Astron. Soc., 479, 2007

Andersson, S., Goumans, T., & Arnaldsson, A. 2011, Chem. Phys. Lett., 513, 31

Andrade, D. P., de Barros, A. L., Pilling, S., et al. 2013, Mon. Not. R. Astron. Soc., 430, 787

Arasa, C., Andersson, S., Cuppen, H., van Dishoeck, E. F., & Kroes, G.-J. 2010, J. Chem. Phys., 132, 1

Arasa, C., van Hemert, M. C., van Dishoeck, E. F., & Kroes, G.-J. 2013, J. Phys. Chem. A, 117, 7064

Bennett, C. J., Hama, T., Kim, Y. S., Kawasaki, M., & Kaiser, R. I. 2010, Astrophys. J., 727, 27

Bennett, C. J., Jamieson, C. S., & Kaiser, R. I. 2009a, Astrophys. J. Suppl. Ser., 182, 1

Bennett, C. J., Jamieson, C. S., & Kaiser, R. I. 2009b, Phys. Chem. Chem. Phys., 11, 4210

Bergantini, A., Pilling, S., Rothard, H., Boduch, P., & Andrade, D. 2013, Mon. Not. R. Astron. Soc., 437, 2720

Bergin, E. A., Melnick, G. J., Gerakines, P. A., Neufeld, D. A., & Whittet, D. C. 2005, Astrophys. J. Lett., 627, L33

Bisschop, S., Fuchs, G., Boogert, A., van Dishoeck, E. F., & Linnartz, H. 2007a, Astron. Astrophys., 470, 749

Bisschop, S., Fuchs, G., van Dishoeck, E. F., & Linnartz, H. 2007b, Astron. Astrophys., 474, 1061

Boogert, A., Gerakines, P. A., & Whittet, D. C. 2015, Annu. Rev. Astron. Astrophys., 53, 541

Boogert, A., Huard, T., Cook, A., et al. 2011, Astrophys. J., 729, 1

Boonman, A., van Dishoeck, E. F., Lahuis, F. v., & Doty, S. 2003, Astron. Astrophys., 399, 1063

Bottinelli, S., Ceccarelli, C., Williams, J. P., & Lefloch, B. 2007, Astron. Astrophys., 463, 601

Bouilloud, M., Fray, N., Bénilan, Y., et al. 2015, Mon. Not. R. Astron. Soc., 451, 2145

Butscher, T., Duvernay, F., Danger, G., & Chiavassa, T. 2016, Astron. Astrophys., 593, A60

Chuang, K. 2018, Univ. Leiden, PhD thesis

Chuang, K.-J., Fedoseev, G., Ioppolo, S., van Dishoeck, E. F., & Linnartz, H. 2016, Mon. Not. R. Astron. Soc., 455, 1702

Chuang, K.-J., Fedoseev, G., Qasim, D., et al. 2017, Mon. Not. R. Astron. Soc., 467, 2552

Chuang, K.-J., Fedoseev, G., Qasim, D., et al. 2018, Astrophys. J., 853, 1

Cook, A., Whittet, D., Shenoy, S., et al. 2011, Astrophys. J., 730, 124

Cottin, H., Moore, M. H., & Bénilan, Y. 2003, Astrophys. J., 590, 874

Cuppen, H. & Herbst, E. 2007, Astrophys. J., 668, 294

Cuppen, H., Ioppolo, S., Romanzin, C., & Linnartz, H. 2010, Phys. Chem. Chem. Phys., 12, 12077

Cuppen, H., van Dishoeck, E. F., Herbst, E., & Tielens, A. 2009, Astron. Astrophys., 508, 275

Dartois, E., d'Hendecourt, L., Boulanger, F., et al. 1998, Astron. Astrophys., 331, 651

Dawes, A., Mason, N. J., & Fraser, H. J. 2016, Phys. Chem. Chem. Phys., 18, 1245

De Graauw, T., Whittet, D., Gerakines, P. a., et al. 1996, Astron. Astrophys., 315, L345

d'Hendecourt, L. & Jourdain de Muizon, M. 1989, Astron. Astrophys., 223, L5

Ehrenfreund, P., Boogert, A., Gerakines, P., et al. 1997, Astron. Astrophys., 328, 649

Favre, C., Fedele, D., Semenov, D., et al. 2018, Astrophys. J. Lett., 862, L2

Fayolle, E. C., Öberg, K., Cuppen, H. M., Visser, R., & Linnartz, H. 2011, Astron. Astrophys., 529, A74

Fedoseev, G., Chuang, K.-J., Ioppolo, S., et al. 2017, Astrophys. J., 842, 1

Francisco, J. S., Muckerman, J. T., & Yu, H.-G. 2010, Acc. Chem. Res., 43, 1519

Fredon, A., Lamberts, T., & Cuppen, H. 2017, Astrophys. J., 849, 1

Fuchs, G., Cuppen, H., Ioppolo, S., et al. 2009, Astron. Astrophys., 505, 629

Garrod, R. T. & Herbst, E. 2006, Astron. Astrophys., 457, 927

Gerakines, P., Schutte, W., & Ehrenfreund, P. 1996, Astron. Astrophys., 312, 289

Gerakines, P., Whittet, D., Ehrenfreund, P., et al. 1999, Astrophys. J., 522, 357

Gibb, E., Whittet, D., Boogert, A., & Tielens, A. 2004, Astrophys. J. Suppl. Ser., 151, 35

Giguere, P. & Harvey, K. 1959, J. Mol. Spectrosc., 3, 36

Goumans, T. & Andersson, S. 2010, Mon. Not. R. Astron. Soc., 406, 2213

He, J., Emtiaz, S. M., & Vidali, G. 2017, Astrophys. J., 851, 104

Hidaka, H., Watanabe, N., Shiraki, T., Nagaoka, A., & Kouchi, A. 2004, Astrophys. J., 614, 1124

Hodyss, R., Johnson, P. V., Stern, J. V., et al. 2009, Icarus, 200, 338

Hudson, R. & Moore, M. 1999, Icarus, 140, 451

Ikeda, M., Ohishi, M., Nummelin, A., et al. 2001, Astrophys. J., 560, 792

Ioppolo, S., Cuppen, H., Romanzin, C., van Dishoeck, E. F., & Linnartz, H. 2008, Astrophys. J., 686, 1474

Ioppolo, S., Cuppen, H., van Dishoeck, E. F., & Linnartz, H. 2010, Mon. Not. R. Astron. Soc., 410, 1089

Ioppolo, S., Fedoseev, G., Lamberts, T., Romanzin, C., & Linnartz, H. 2013a, Rev. Sci. Instrum., 84, 1

Ioppolo, S., Sangiorgio, I., Baratta, G., & Palumbo, M. 2013b, Astron. Astrophys., 554, A34

Ioppolo, S., Van Boheemen, Y., Cuppen, H., van Dishoeck, E. F., & Linnartz, H. 2011, Mon. Not. R. Astron. Soc., 413, 2281

Irvine, W. M., Friberg, P., Kaifu, N., et al. 1990, Astron. Astrophys., 229, L9

Jamieson, C. S., Mebel, A. M., & Kaiser, R. I. 2006, Astrophys. J. Suppl. Ser., 163, 184

Keane, J., Tielens, A., Boogert, A., Schutte, W., & Whittet, D. 2001, Astron. Astrophys., 376, 254

Kim, H. J., Evans II, N. J., Dunham, M. M., Lee, J.-E., & Pontoppidan, K. M. 2012, Astrophys. J., 758, 38

Lamberts, T., Cuppen, H. M., Ioppolo, S., et al. 2013, Phys. Chem. Chem. Phys., 15, 8287

Lamberts, T., de Vries, X., & Cuppen, H. 2014, Faraday Discuss., 168, 327

Lamberts, T., Fedoseev, G., Kästner, J., et al. 2017, Astron. Astrophys., 599, A132

Lamberts, T. & Kästner, J. 2017, Astrophys. J., 846, 43

Lamberts, T., Samanta, P. K., Köhn, A., & Kästner, J. 2016, Phys. Chem. Chem. Phys., 18, 33021

Lannon, J. A., Verderame, F. D., & Anderson Jr, R. W. 1971, J. Chem. Phys., 54, 2212

Linnartz, H., Ioppolo, S., & Fedoseev, G. 2015, Int. Rev. Phys. Chem., 34, 205

Liu, S.-Y., Girart, J., Remijan, A., & Snyder, L. 2002, Astrophys. J., 576, 255

Liu, S.-Y., Mehringer, D. M., & Snyder, L. E. 2001, Astrophys. J., 552, 654

Loeffler, M., Baratta, G., Palumbo, M., Strazzulla, G., & Baragiola, R. 2005, Astron. Astrophys., 435, 587

Loeffler, M. J., Teolis, B. D., & Baragiola, R. A. 2006, J. Chem. Phys., 124, 104702

Maity, S., Kaiser, R. I., & Jones, B. M. 2014, Faraday Discuss., 168, 485

Martin, I., Bertin, M., Domaracka, A., et al. 2008, Int. J. Mass Spectrom., 277, 262

Martín-Doménech, R., Manzano-Santamaría, J., Caro, G. M., et al. 2015, Astron. Astrophys., 584, 1

Masunov, A. E., Wait, E., & Vasu, S. S. 2016, J. Phys. Chem. A, 120, 6023

McCarthy, M. C., Martinez Jr, O., McGuire, B. A., et al. 2016, J. Chem. Phys., 144, 124304

Meisner, J., Lamberts, T., & Kästner, J. 2017, ACS Earth Space Chem., 1, 399

Minissale, M., Loison, J.-C., Baouche, S., et al. 2015, Astron. Astrophys., 577, A2

Moore, M., Ferrante, R., & Nuth III, J. 1996, Planet. Space Sci., 44, 927

Możejko, P. 2007, Eur. Phys. J. Spec. Top., 144, 233

Nguyen, T. L., Xue, B. C., Weston Jr, R. E., Barker, J. R., & Stanton, J. F. 2012, J. Phys. Chem. Lett., 3, 1549

Noble, J. A., Dulieu, F., Congiu, E., & Fraser, H. J. 2011, Astrophys. J., 735, 121

Oba, Y., Watanabe, N., Kouchi, A., Hama, T., & Pirronello, V. 2010a, Astrophys. J. Lett., 712, L174

Oba, Y., Watanabe, N., Kouchi, A., Hama, T., & Pirronello, V. 2010b, Astrophys. J., 722, 1598

Öberg, K. I., Boogert, A., Pontoppidan, K. M., et al. 2011, Astrophys. J., 740, 109

Öberg, K. I., Garrod, R. T., van Dishoeck, E. F., & Linnartz, H. 2009, Astron. Astrophys., 504, 891

Orient, O. & Strivastava, S. 1987, J. Phys. B, 20, 3923

Paardekooper, D., Bossa, J.-B., & Linnartz, H. 2016, Astron. Astrophys., 592, 1

Palumbo, M., Baratta, G., Brucato, J., et al. 1998, Astron. Astrophys., 334, 247

Pontoppidan, K. M. 2006, Astron. Astrophys., 453, L47

Pontoppidan, K. M., Boogert, A., Fraser, H. J., et al. 2008, Astrophys. J., 678, 1005

Poteet, C. A., Pontoppidan, K. M., Megeath, S. T., et al. 2013, Astrophys. J., 766, 117

Qasim, D., Chuang, K.-J., Fedoseev, G., et al. 2018, Astron. Astrophys., 612, 1

Raut, U. & Baragiola, R. 2011, Astrophys. J. Lett., 737, L14

Raut, U., Fulvio, D., Loeffler, M., & Baragiola, R. 2012, Astrophys. J., 752, 159

Requena-Torres, M. A., Martín-Pintado, J., Rodríguez-Franco, A., et al. 2006, Astron. Astrophys., 455, 971

Romanzin, C., Ioppolo, S., Cuppen, H., van Dishoeck, E. F., & Linnartz, H. 2011, J. Chem. Phys., 134, 1

Roser, J. E., Vidali, G., Manicò, G., & Pirronello, V. 2001, Astrophys. J. Lett., 555, L61

Ryazantsev, S. V. & Feldman, V. I. 2015, Phys. Chem. Chem. Phys., 17, 30648

Satorre, M., Palumbo, M., & Strazzulla, G. 2000, Astrophys. Space Sci., 274, 643

Schutte, W., Boogert, A., Tielens, A., et al. 1999, Astron. Astrophys., 343, 966

Song, L. & Kästner, J. 2017, Astrophys. J., 850, 1

Strazzulla, G., Brucato, J., Palumbo, M., & Satorre, M. 1997, Astron. Astrophys., 321, 618

Suhasaria, T., Baratta, G., Ioppolo, S., Zacharias, H., & Palumbo, M. 2017, Astron. Astrophys., 608, A12

Tachikawa, H. & Kawabata, H. 2016, J. Phys. Chem. A, 120, 6596

Taquet, V., Wirström, E., Charnley, S. B., et al. 2017, Astron. Astrophys., 607, A20

Tielens, A. & Hagen, W. 1982, Astron. Astrophys., 114, 245

Trottier, A. & Brooks, R. L. 2004, Astrophys. J., 612, 1214

Tschersich, K. 2000, J. Appl. Phys., 87, 2565

Tschersich, K., Fleischhauer, J., & Schuler, H. 2008, J. Appl. Phys., 104, 1

Tschersich, K. & Von Bonin, V. 1998, J. Appl. Phys., 84, 4065

Turner, B., Terzieva, R., & Herbst, E. 1999, Astrophys. J., 518, 699

van Dishoeck, E. F. 1998, Faraday Discuss., 109, 31

van Dishoeck, E. F., Helmich, F., de Graauw, T., et al. 1996, Astron. Astrophys., 315, L349

Vandenbussche, B., Ehrenfreund, P., Boogert, A., et al. 1999, Astron. Astrophys., 346, L57

Watanabe, N. & Kouchi, A. 2002, Astrophys. J. Lett., 571, L173

Watanabe, N., Mouri, O., Nagaoka, A., et al. 2007, Astrophys. J., 668, 1001

Watanabe, N., Shiraki, T., & Kouchi, A. 2003, Astrophys. J. Lett., 588, L121

Whittet, D., Gerakines, P., Tielens, A., et al. 1998, Astrophys. J. Lett., 498, L159

Winnewisser, G. & Churchwell, E. 1975, Astrophys. J., 200, L33

Yu, H.-G., Muckerman, J. T., & Francisco, J. S. 2005, J. Phys. Chem. A, 109, 5230

Zanchet, A., del Mazo, P., Aguado, A., et al. 2018, Phys. Chem. Chem. Phys., 20, 5415

Zuckerman, B., Ball, J. A., & Gottlieb, C. A. 1971, Astrophys. J., 163, L41

Formation of interstellar propanal and 1-propanol ice

1-propanol ($CH_3CH_2CH_2OH$) is a three carbon-bearing representative of the primary linear alcohols that may have its origin in the cold dark cores in interstellar space. To test this, we investigated in the laboratory whether 1-propanol ice can be formed along pathways possibly relevant to the prestellar core phase. We aim to show in a two-step approach that 1-propanol can be formed through reaction steps that are expected to take place during the heavy CO freeze-out stage by adding C_2H_2 into the CO + H hydrogenation network via the formation of propanal (CH_3CH_2CHO) as an intermediate and its subsequent hydrogenation. Temperature programmed desorption-quadrupole mass spectrometry (TPD-QMS) was used to identify the newly formed propanal and 1-propanol. Reflection-absorption infrared spectroscopy (RAIRS) was used as a complementary diagnostic tool. The mechanisms that can contribute to the formation of solid-state propanal and 1-propanol, as well as other organic compounds, during the heavy CO freeze-out stage are constrained by both laboratory experiments and theoretical calculations. Here it is shown that recombination of HCO radicals formed upon CO hydrogenation with radicals formed via C_2H_2 processing – H_2CCH and H_3CCH_2 – offers possible reaction pathways to solid-state propanal and 1-propanol formation. This extends the already important role of the CO hydrogenation chain to the formation of larger complex organic molecules (COMs). The results are compared with ALMA observations. The resulting 1-propanol:propanal ratio concludes an upper limit of $< 0.35 - 0.55$, which is complemented by computationally derived activation barriers in addition to the experimental results.

7.1 Introduction

The search for three carbon-bearing aldehydes and alcohols has been the subject of a number of devoted observational studies. An example of recent observations of such species is the work by Lykke et al. (2017), where propanal (an aldehyde), among other organics, was detected towards the low-mass protostar

IRAS 16293-2422B. In addition to these observations, propanal has also been identified in the Sagittarius B2 North (Sgr B2(N)) molecular cloud (Hollis et al. 2004; McGuire et al. 2016) and within the Central Molecular Zone of the Milky Way (Requena-Torres et al. 2008). Its detection on comet 67P/Churyumov-Gerasimenko was claimed by Goesmann et al. (2015) but is still under debate (Altwegg et al. 2017). Given the chemical link between aldehydes and alcohols, it is expected that propanol will be formed alongside propanal. Yet in comparison to propanal, the number of reported detections of 1-propanol in observational projects is very limited. Observations towards Sgr B2(N2), the northern hot molecular core within Sgr B2(N), only lead to an upper limit value of < 2.6×10^{17} cm^{-2} for 1-propanol (Müller et al. 2016). Tercero et al. (2015) discussed the identification of 1-propanol towards Orion KL, but their claim has been questioned by others (Müller et al. 2016). The detection of propanol (without isomeric details) on comet 67P/Churyumov-Gerasimenko was reported by Altwegg et al. (2017).

In the laboratory, both propanal and propanol have been synthesized in astrophysical ice analogue experiments that require 'energetic' processing for product formation. 'Energetic' refers here to a radical-induced process that requires the involvement of UV, cosmic rays, and/or other 'energetic' particles. Kaiser et al. (2014) and Abplanalp et al. (2016) showed that propanal can be formed by the electron-induced radiation of $CO:CH_4$ or $CO:C_2H_6$. Hudson et al. (2017) were able to form propanal by proton irradiation of a $CO_2:C_3H_6$ ice mixture at 10 K. $H_2O:^{13}CH_3OH:NH_3$ 78 K ice exposed to UV photons and heated to room temperature also yielded propanal (de Marcellus et al. 2015). Propanol was reported to be formed by electron irradiation of a $^{13}CO:^{13}CD_4$ ice mixture at 5 K in experiments that did not allow to discriminate between 1- and 2-propanol (Abplanalp et al. 2018).

In both the laboratory and observational work, propanal has been detected in conjunction with other organics such as acetone, propylene oxide, acetaldehyde, and so on. This demonstrates that propanal may be a reaction product in a number of astrochemical formation networks and its presence in the ISM may therefore be linked to the formation of a range of organic species. In this article, we focus solely on the formation of propanal and its direct derivative, 1-propanol, focusing on pathways relevant to the prestellar core, that is low temperature of ~10 K and predominantly 'non-energetic' processing. 'Non-energetic' is used to refer to radical-induced processes that do not involve external energy input such as UV, cosmic rays, and/or electrons.

The particular focus on 1-propanol is strongly motivated by the astrobiological relevance of this compound. 1-propanol is a primary alcohol, and it is hypothesized that primary alcohols may have been the constituents of cell membranes during abiogenesis. Cell membranes are currently and commonly composed of glycerophospholipids (Moran et al. 2012), but whether such complex amphiphiles could be available on the early Earth is debated (Deamer et al. 2002). More simple and thus more likely lipids would be those composed of primary alcohols, such as prenol lipids. Additionally, the cell membranes of archaea (i.e., domain of ancient prokaryotic unicellular organisms) are known to be composed of primary alcohols (De Rosa et al. 1986), providing extra motivation to investigate formation routes of primary alcohols, including propanol.

In this study we investigate whether propanal and 1-propanol can be formed by adding acetylene (C_2H_2) to the CO + H surface reaction chain. That is, we focus on the 'non-energetic' (dense cloud relevant) processing of the ice. It has been experimentally demonstrated that complex organic molecules (COMs) – as large as glycerol (a polyol compound) and/or glyceraldehyde (an aldose) – can be formed below 20 K and without 'energetic' input via the solid-state CO hydrogenation network (Fedoseev et al. 2015, 2017; Butscher et al. 2015, 2017; Chuang et al. 2016). This aligns with the observationally constrained heavy CO freeze-out stage (Pontoppidan 2006; Boogert et al. 2015; Qasim et al. 2018). It has been shown that the CO + H reaction product, formaldehyde (H_2CO), can be hydrogenated to form methanol (CH_3OH) (Watanabe & Kouchi 2002; Fuchs et al. 2009). In a somewhat related way, glycolaldehyde ($HCOCH_2OH$) and ethylene glycol (H_2COHCH_2OH) are proposed to be linked through sequential H-addition reactions (Fedoseev et al. 2017). Additionally, acetaldehyde (CH_3CHO) can be hydrogenated to form ethanol (CH_3CH_2OH) (Bisschop et al. 2007). Thus we expect propanal to be hydrogenated to form 1-propanol.

The hydrogenation of C_2H_2 has a barrier (Kobayashi et al. 2017) and it is expected that in space, hydrocarbon radicals formed by atom-addition are good candidates to combine with reactive CO + H intermediates to form COMs. For these reasons, in this study, the CO and C_2H_2 solid-state hydrogenation chains are connected to investigate the formation of reaction products that cannot be formed along the individual hydrogenation schemes. It should be noted that C_2H_2 has not yet been observed in interstellar ices. In the experiments discussed below, C_2H_2 was used both as a likely interstellar precursor species, and as a tool to form hydrocarbon radicals, in a comparable way to how O_2 was used to generate OH radicals (Cuppen et al. 2010).

This paper is organised in the following way. Section 7.2 is an overview of the experimental setup and performed experiments. Section 7.3 contains results that show how propanal and possibly 1-propanol are formed by the simultaneous hydrogenation of CO and C_2H_2, and how propanal hydrogenation unambiguously results in the formation of 1-propanol. In Sect. 7.4, we discuss the identification and formation pathways of a variety of organic compounds. Section 7.5 is a discussion on how this combined laboratory work and theoretical calculations connect to the chemical inventory during the heavy CO freeze-out stage, and compares the outcomes with recent observations from the Atacama Large Millimeter/submillimeter Array (ALMA). Section 7.6 is a summary of the findings presented in this paper.

7.2 Experimental procedure

7.2.1 Description of the setup

All experiments described in this study took place in the ultrahigh vacuum (UHV) setup, SURFRESIDE[2]. The design of the setup is described by Ioppolo et al. (2013), and details on the recent modifications are given by Fedoseev et al. (2017), Chuang et al. (2018), and Qasim et al. (2018). Below, only the relevant settings are summarised. Ices were formed on a gold-plated copper substrate that is positioned in the centre of the main chamber (base pressure of low ~10^{-10} mbar range) and can be cooled to 7 K by a closed-cycle helium

cryostat and heated to 450 K by resistive heating. Substrate temperatures were measured by a silicon diode sensor with a 0.5 K absolute accuracy.

Connected to the central vacuum chamber are two atomic beam lines. Hydrogenation of the ice was possible by a Hydrogen Atom Beam Source (HABS) (Tschersich & Von Bonin 1998; Tschersich 2000; Tschersich et al. 2008). H-atoms were formed by the thermal cracking of hydrogen molecules (H_2; Linde 5.0) within the HABS chamber. As the atoms and undissociated H_2 molecules exited the HABS chamber, they were collisionally cooled by a nose-shaped quartz pipe before landing on the icy substrate, where they were thermalized instantly to the temperature of the substrate. The second atomic beam line, a microwave plasma atom source, was not used in the present study.

Gases and vapours were prepared as follows. Acetylene (5% of C_2H_2 in He; Linde 2.6) and carbon monoxide (CO; Linde 4.7) entered the main chamber via two separate pre-pumped dosing lines equipped with two leak valves. ^{13}CO (Sigma-Aldrich 99%) and $^{13}C^{18}O$ (Sigma-Aldrich 99%) isotopologues were used as tools to confirm the identification of the formed products. Propanal (Sigma-Aldrich $\geqslant$ 98%) and 1-propanol (Honeywell $\geqslant$ 99.9%) solutions, which were placed in individual glass tubes connected to the gas manifold by ultra-torr fittings, underwent freeze-pump-thaw cycles in order to remove gas impurities and were subsequently bled into the main chamber through the aforementioned dosing lines.

Two complementary diagnostic tools were used to monitor ice processing. Reflection-absorption infrared spectroscopy (RAIRS) simultaneously samples the consumption of precursor material and the formation of reaction products by visualizing the intensity decrease or increase, respectively, of molecule specific vibrational modes. In our setup, a Fourier Transform Infrared Spectrometer (FTIR) was used to cover the 4000-750 cm^{-1} region with a spectral resolution of 1 cm^{-1}. In total, 512 scans were averaged over 230 seconds to obtain one spectrum. Temperature programmed desorption-quadrupole mass spectrometry (TPD-QMS) was used to investigate the thermally desorbed ice constituents as a function of desorption temperature. A typical ramp rate of 5 K/min was applied. The QMS electron impact source was operated at 70 eV, which induces well characterised and molecule specific fragment patterns. RAIRS is less sensitive than TPD-QMS, but has the advantage that it does not destroy the ice. The latter probes two molecule-specific parameters: the desorption temperature and the electron impact induced fragmentation pattern. In general, this combination allows unambiguous molecule identifications, particularly when isotopic species are also used as a cross-check. For an overview of the positives and negatives of both methods, see the work by Ioppolo et al. (2014).

7.2.2 Overview of experiments

Table 7.1 lists the experiments that were performed in this study. All fluxes were determined via the Hertz-Knudsen equation (Kolasinski 2012) except for the H-atom flux, which was based on an absolute D-atom flux measured by Ioppolo et al. (2013). The purpose of the experiments is described below.

Experiments 1.0-1.4 were used to verify the formation of propanal by the radical–radical recombination reaction between the radicals formed from hy-

Table 7.1: A list of the selected experiments and experimental conditions. Molecular fluxes were determined by the Hertz-Knudsen equation.

No.	Experiments	Ratio C_2H_2:CO:H	T_{sample} K	$Flux_{C_2H_2}$ $cm^{-2}s^{-1}$	$Flux_{CO}$ $cm^{-2}s^{-1}$	$Flux_H$ $cm^{-2}s^{-1}$	$Flux_{propanal}$ $cm^{-2}s^{-1}$	$Flux_{1-propanol}$ $cm^{-2}s^{-1}$	Time s
1.0	$C_2H_2 + CO + H$	1:2:10	10	5×10^{11}	1×10^{12}	5×10^{12}	-	-	21600
1.1	$C_2H_2 + CO$	-	10	5×10^{11}	1×10^{12}	-	-	-	21600
1.2	$C_2H_2 + H$	-	10	5×10^{11}	-	5×10^{12}	-	-	21600
1.3	$C_2H_2 + C^{18}O + H$	1:2:10	10	5×10^{11}	1×10^{12}	5×10^{12}	-	-	21600
1.4	$C_2H_2 + {}^{13}C^{18}O + H$	1:2:10	10	5×10^{11}	1×10^{12}	5×10^{12}	-	-	21600
2.0	1-propanol	-	10	-	-	-	-	1×10^{12}	3600
2.1	propanal + H	-	10	-	-	5×10^{12}	3×10^{12}	-	28800
2.2	propanal + H	-	10	-	-	5×10^{12}	2×10^{11}	-	7200
2.3	propanal	-	10	-	-	-	2×10^{12}	-	3600
2.4	propanal	-	10	-	-	-	3×10^{14}	-	100

drogenation of CO and C_2H_2. Experiment 1.0 was compared to experiments 1.1 and 1.2 to demonstrate that product formation requires radical species to be formed in the ice. We note that the listed C_2H_2:CO:H ratio in Table 7.1 was experimentally found to be the most favourable ratio for product formation among our set of performed ratios (not discussed here). Carbon monoxide (CO) isotopologues were exploited in experiments 1.3 and 1.4 to witness the mass-to-charge (m/z) shift in the TPD experiments that must occur if propanal (and 1-propanol) is formed.

Experiments 2.0-2.4 were used to verify the formation of 1-propanol ice via the surface hydrogenation of propanal at 10 K. Experiment 2.0 provides a 1-propanol reference. The TPD spectra of experiments 2.0, 2.2, and 2.3 were analysed to verify 1-propanol formation. Experiments 2.3 and 2.4 were used as controls to verify that the IR feature at 969 cm^{-1} in experiment 2.1 does not overlap with the features of propanal. The feature was additionally compared to the IR spectrum of experiment 2.0.

It should be noted that in all experiments, the precursor species listed in Table 7.1 were used in co-deposition experiments. These result in a higher product abundance compared to experiments in which pre-deposited precursor species are bombarded. Moreover, co-deposition is more representative for the actual processes taking place in space (Linnartz et al. 2015).

7.2.3 Formation of propanal from C_2H_2:CO hydrogenation

Figure 7.1 shows the RAIR spectrum obtained after the co-deposition of C_2H_2 + CO + H at 10 K. A list of the identified RAIR bands for this experiment is found in Table 7.2. The solid-state hydrogenation of an ice containing C_2H_2 leads to the formation of C_2H_4 and C_2H_6, which was also reported by Kobayashi et al. (2017). The reaction of CO and H, which has been extensively investigated by Watanabe & Kouchi (2002) and Fuchs et al. (2009), yields H_2CO and CH_3OH. There is no clear spectral proof of propanal or 1-propanol.
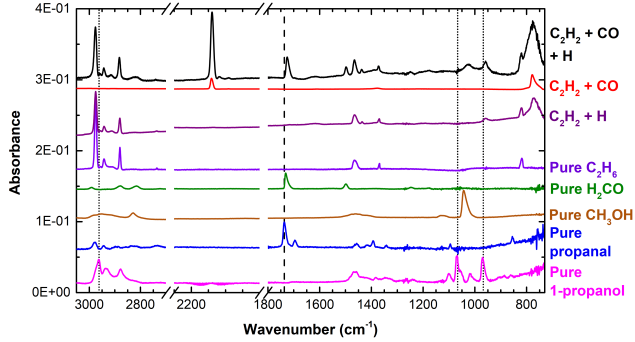
Figure 7.1: RAIR spectra obtained after the deposition of C_2H_2 + CO + H (exp. 1.0), C_2H_2 + H (exp. 1.2), 1-propanol (exp. 2.0), CH_3OH (5×10^{15} cm^{-2}), propanal (exp. 2.3), H_2CO (5×10^{15} cm^{-2}), C_2H_6 (5×10^{15} cm^{-2}), and C_2H_2 + CO (exp. 1.1) on a 10 K surface. The spectrum of C_2H_6 is adapted from the work by Öberg et al. (2009). The dashed and dotted lines highlight the frequencies that correlate to the strongest features of propanal and 1-propanol, respectively. Spectra are scaled to highlight the IR features of interest, and are offset for clarity.

Table 7.2: List of assigned IR absorption features in the co-deposition of C_2H_2 + CO + H (exp. 1.0).

Peak position (cm^{-1})	Peak position (μm)	Molecule	Mode	Reference
776	12.887	C_2H_2	v_5	This work
820	12.195	C_2H_6 and C_2H_4	v_{12} and v_{10}	a,b,c,d,e,f,g,h,i
959	10.428	C_2H_4	v_7	a,b,c,e,f,g,h,i,j
1025	9.756	CH_3OH	v_8	k,l
1371	7.294	C_2H_6	v_6	a,b,d,e,f,g,h,i
1438	6.954	C_2H_4	v_{12}	a,b,c,d,f,g,h,i
1466	6.821	C_2H_6	v_{11} or v_8	a,b,c,d,e,f,g,h,i
1498	6.676	H_2CO	v_3	k,l
1726	5.794	H_2CO	v_2	k,l
2138	4.677	CO	v_1	k,l
2882	3.470	C_2H_6	v_5	a,b,c,e,f,g,h,i
2915	3.431	C_2H_6	$v_8 + v_{11}$	e,c
2943	3.398	C_2H_6	$v_8 + v_{11}$	a,b,c,d,e,f,g,h
2958	3.381	C_2H_6	v_1	e,g
2976	3.360	C_2H_6 and C_2H_4	v_{10} and v_{11}	a,c,d,e,f,g,h,i

[a]Kim et al. (2010) [b]Zhou et al. (2014) [c]abp (2018) [d]Gerakines et al. (1996) [e]Abplanalp & Kaiser (2016) [f]Moore & Hudson (1998) [g]Bennett et al. (2006) [h]Moore & Hudson (2003) [i]Hudson et al. (2014) [j]Kobayashi et al. (2017) [k]Watanabe & Kouchi (2002) [l]Chuang et al. (2016)

7.3 Results

Besides the resulting RAIR spectrum of C_2H_2 + CO + H in Figure 7.1, also RAIR spectra of several control experiments are shown. The C_2H_2 + CO RAIR spectrum shows two features that belong to C_2H_2 and CO, but does not show the signatures of the other CH- and HCO-bearing species that are seen in the RAIR spectrum when H is present. As expected, this implies that H-atoms, and subsequently radicals, are required for the formation of C_2H_4, C_2H_6, H_2CO, and CH_3OH in the C_2H_2 + CO + H experiment. Some of the spectra of these reaction products are shown in Figure 7.1 to point out their IR features in the C_2H_2 + CO + H experiment. The RAIR spectra of pure propanal and 1-propanol in Figure 7.1 illustrate the obstacle of detecting these species as reaction products in the RAIRS data of the C_2H_2 + CO + H experiment. The strongest band of propanal overlaps with the feature of H_2CO ($\sim$1750 cm^{-1}), whereas the strongest bands of 1-propanol overlap with the features of C_2H_4 ($\sim$950 and $\sim$2950 cm^{-1}), C_2H_6 ($\sim$2950 cm^{-1}), and CH_3OH ($\sim$1050 cm^{-1}), as shown in Figure 7.1 by the dashed and dotted lines. With such closely overlapping features, even the incorporation of propanal and 1-propanol in a matrix containing relevant reactant species, which would affect the peak positions and profiles, would likely not lead to the explicit detection of propanal and 1-propanol IR signatures. Due to the lack of distinguishable IR peaks of propanal and 1-propanol in the C_2H_2 + CO + H spectrum, it is necessary to resort to an alternative detection method, such as TPD.

TPD spectra along with the QMS cracking pattern of synthesized and deposited propanal are compared in Figure 7.2. In the TPD spectra obtained after the co-deposition of C_2H_2 + CO + H (top left), the m/z signals of 58 and 57 peak at 125 K, which is what is observed in the TPD spectra of a pure propanal ice (bottom left). We note that there is a shoulder around 115 K in the pure propanal experiment that is not observed in the C_2H_2 + CO + H experiment. This is believed to be caused by the phase transition of propanal, which occurs during the desorption of propanal, as verified by the sharpening of the IR peaks in the RAIR spectra that are recorded at different temperatures (not shown here). Because propanal is mixed with other species in the C_2H_2 + CO + H experiment, it is much harder for these molecules to rearrange into the crystalline form, hence the lack of the phase transition shoulder in the top left figure. The fragmentation pattern involving the $C_3H_6O^+$ (m/z = 58) and $C_3H_5O^+$ (m/z = 57) ions that derive from propanal is shown (Fig. 7.2, (right)) to complement the TPD findings. A fragmentation pattern of 33:100, 32:100, 36:100, and 30:100 is measured for the two ions from experiments 2.3, 1.0, 1.3, and 1.4, respectively. It is clear that the fragmentation pattern between the isotopically enhanced reactions is consistent and additionally their average value matches that of the pattern seen in the pure propanal experiment. The information from the discussed TPD experiments supports the hypothesis that propanal is formed in the C_2H_2 + CO + H experiment.
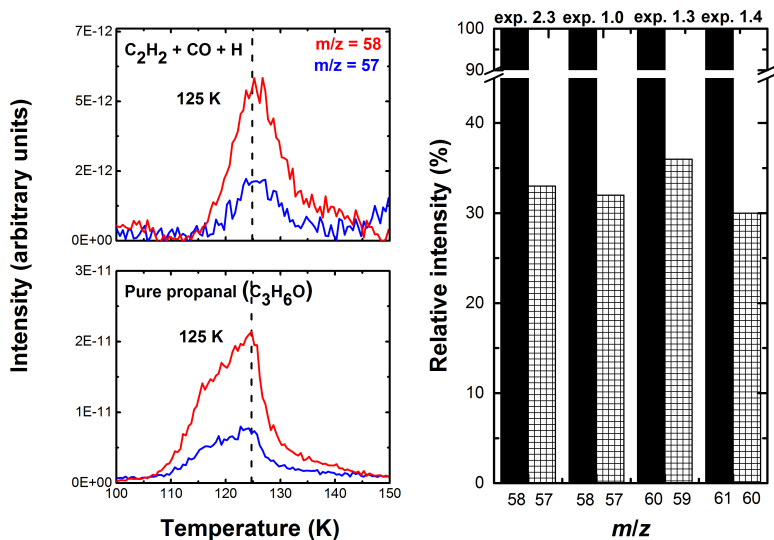
Figure 7.2: (Left) TPD spectra of C_2H_2 + CO + H (top; exp. 1.0) and propanal (bottom; exp. 2.3) taken after deposition at 10 K. (Right) QMS fragmentation pattern of two m/z values that are normalized to the QMS signal of the $C_3H_6O^+$ ion (or the corresponding isotopologue) found in the propanal (exp. 2.3), C_2H_2 + CO + H (exp. 1.0), C_2H_2 + $C^{18}O$ + H (exp. 1.3), and C_2H_2 + $^{13}C^{18}O$ + H (exp. 1.4) experiments.

Due to the limited abundance of the formed propanal starting from C_2H_2 + CO + H and the desorption of side products that appear around the desorption of pure 1-propanol (e.g., glycolaldehyde), the detection of 1-propanol starting from a propanal-poor sample is just around the limit of our detection capabilities. Figure 7.3 shows TPD spectra of m/z values that are tentatively identified as the $C_3H_7O^+$ and $C_3H_7^{18}O^+$ ions of 1-propanol. These m/z values (59 and 61) are selected as they should not appear for glycolaldehyde desorption, which occurs already around 160 K. The peak desorptions at 165 K are shifted +10 K from the peak desorption temperature of pure 1-propanol (155 K), which can be explained by the desorption of 1-propanol from the bare substrate surface and/or sub-monolayer regime. In this case, molecules occupy spots with higher binding energies. Although the signal intensities between the two desorption peaks are similar and both m/z values peak at the same temperature, more information (i.e., more m/z channels) is needed to conclusively prove that 1-propanol formation can also be directly detected in the C_2H_2 + CO + H experiment. For this reason, we present results for the hydrogenation of propanal, which is shown in the following section. A similar two-step approach was used in a previous study to confirm the formation of glycerol from CO + H (Fedoseev et al. 2017).
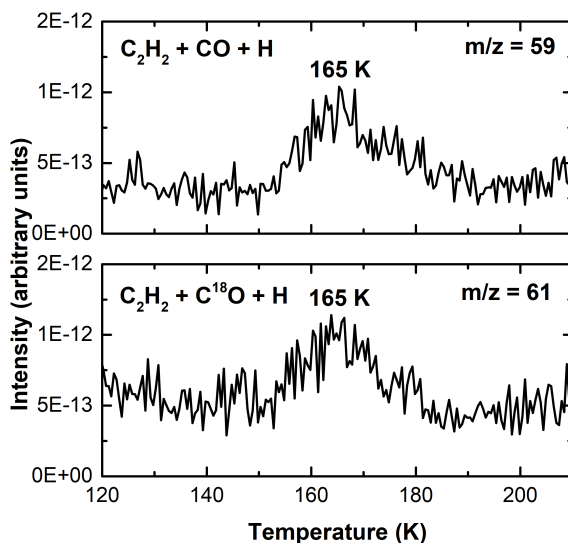
Figure 7.3: TPD spectra that include m/z values that may represent the desorption of 1-propanol. TPD of the reactions, $C_2H_2 + CO + H$ (top; exp. 1.0) and $C_2H_2 + C^{18}O + H$ (bottom; exp. 1.3), taken after deposition at 10 K.

7.3.1 Formation of 1-propanol from propanal

To confirm the formation of 1-propanol by solid-state hydrogenation of propanal ice, TPD spectra were collected and are presented in Fig. 7.4. The TPD spectra of propanal + H, propanal, and 1-propanol for $m/z = 29$, 31, 59, and 60 are displayed top-down in the left panel, as these m/z values are representative of the ions produced when propanal and 1-propanol are fragmented by the QMS ionization source. For a pure propanal ice, the desorption peaks of $m/z = 29$, 31, and 59 appear at 125 K, and are also found in the propanal + H experiment, as expected. In the propanal + H experiment, desorption peaks of $m/z = 29$, 31, 59, and 60 appear also at 155 K, which are observed in the 1-propanol experiment. To confirm that the signals at 155 K in the propanal + H experiment are due to the desorption of 1-propanol ice, the fragmentation patterns of the m/z values found in the propanal + H and pure 1-propanol experiments were compared (right panel). The relative intensities in the propanal + H experiment are 19:100, 3:100, and 2:100 for $m/z = 29{:}31$, $m/z = 59{:}31$, and $m/z = 60{:}31$, respectively. These relative intensity values are almost identical to those found in the 1-propanol reference experiment, which are 15:100, 4:100, and 2:100 for these three m/z values. This confirms that 1-propanol is derived from the hydrogenation of propanal at 10 K.
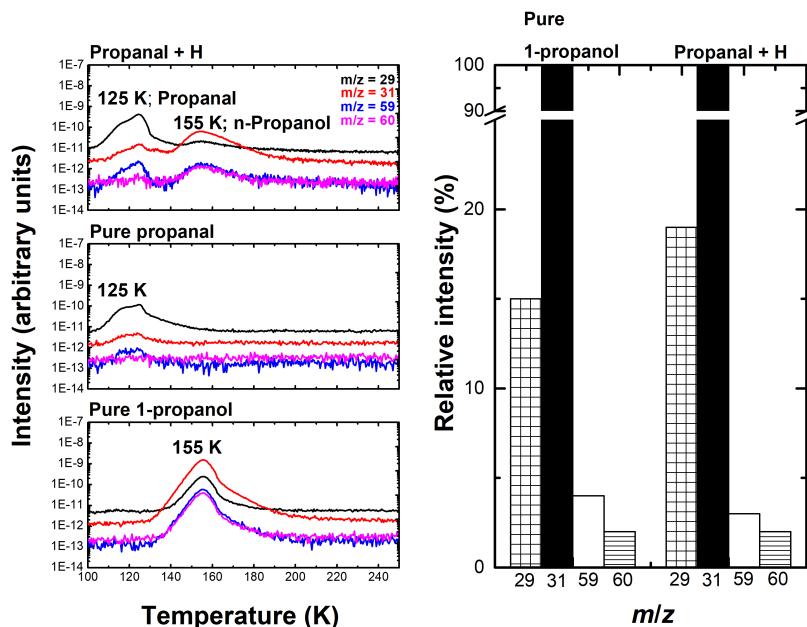
Figure 7.4: (Left) TPD of propanal + H (top; exp. 2.2), propanal (middle; exp. 2.3), and 1-propanol (bottom; exp. 2.0) taken after deposition at 10 K. (Right) QMS fragmentation pattern of four m/z values that are normalized to the QMS signal of $m/z = 31$ found in the 1-propanol (exp. 2.0) and propanal + H (exp. 2.2) experiments for a temperature of 125 K.

To further complement the results from Fig. 7.4, the formation of 1-propanol from the hydrogenation of propanal can be tentatively identified from the RAIRS annealing series (RAIR spectra recorded at different temperatures) presented in Fig. 7.5. The feature at 860 cm^{-1} is assigned to the CH$_3$ rocking mode of propanal (Köroğlu et al. 2015) and the band at 969 cm^{-1} overlaps nicely with the C-O stretching frequency of 1-propanol (Max et al. 2002). As seen in the figure, the propanal band disappears at 125 K, which is in-line with the peak desorption temperature of 125 K for propanal, as demonstrated in Fig. 7.4. The 969 cm^{-1} feature disappears at 155 K, which is also the peak desorption temperature of 1-propanol. The results from Fig. 7.5 provide additional evidence of 1-propanol formation from propanal + H, even though the figure only shows one potential band of 1-propanol. Other RAIR bands of 1-propanol cannot be positively identified or probed largely due to the low signal-to-noise ratio of the new bands in experiment 2.1. The data shown in Fig. 7.5 support the results from the TPD experiments that are presented in Fig. 7.4.
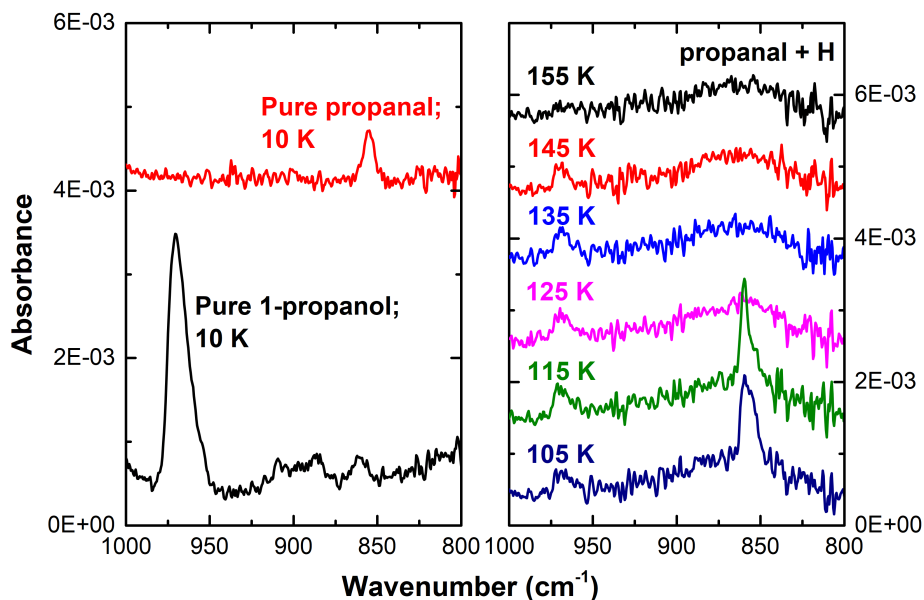
Figure 7.5: (Left) Infrared features of pure propanal (exp. 2.3) and 1-propanol (exp. 2.0). (Right) RAIRS annealing series of propanal + H (exp. 2.1), taken after deposition at 10 K. We note that the features at 860 cm^{-1} and 969 cm^{-1} are signatures of propanal and newly formed 1-propanol (tentative), as the signatures disappear by 125 K (propanal peak desorption temperature) and 155 K (1-propanol peak desorption temperature), respectively. RAIR spectra are offset for clarity.

7.4 Discussion

Figure 7.6 shows a list of possible pathways that hold the potential to form propanal and 1-propanol by the co-deposition of C_2H_2 + CO + H under our experimental conditions. These aim to mimic interstellar conditions as closely as possible, but one must bear in mind that mixed CO:C_2H_2 ices are likely not representative for interstellar ices. Here, we mainly aim at reproducing conditions that allow to study reaction pathways that will be at play in interstellar ices. The two left-most reaction chains in Fig. 7.6 show how the reacting radicals and stable molecules from the hydrogenation of CO (HCO, H_2CO, CH_3O, and CH_2OH) and C_2H_2 (H_2CCH, H_2CCH_2, and H_3CCH_2) are formed. We note that CO and C_2H_2 do not react with each other under our experimental conditions. From this set of radicals and molecules, the combination of which most likely leads to the formation of propanal and 1-propanol is discussed here first by process of elimination. The barrier value for H-abstraction from C_2H_2 is > 56,000 K (Zhou et al. 2008), which is very high for thermalized H-atoms to bypass at cryogenic temperatures used in our experiments. This H-abstraction is required for species – such as propynal – to be formed. Therefore, the pathways involving the formation of propynal are excluded from our reaction network. A

direct consequence of this is that the C≡C bond must be converted to a single C-C bond by H-atom addition, as demonstrated in the works of Hiraoka et al. (2000) and Kobayashi et al. (2017).
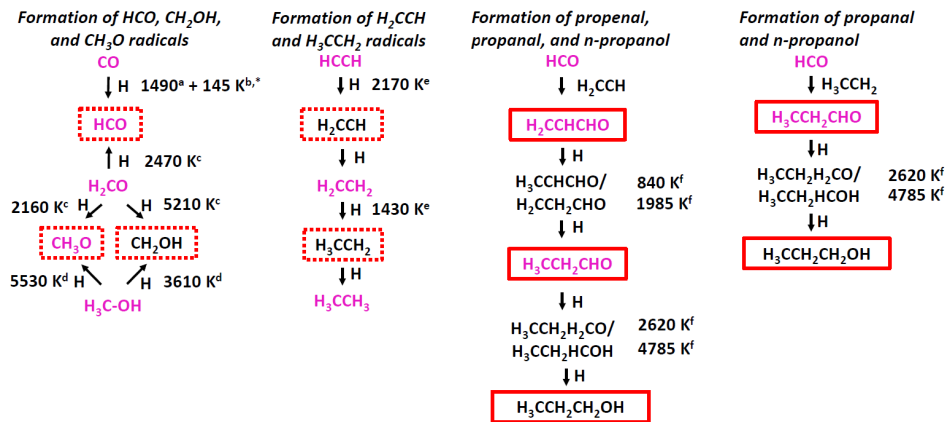
Figure 7.6: Proposed mechanisms for experiment 1.0. We note that all radical–radical reactions shown here are barrierless. Relevant species within each mechanism are boxed; solid-line boxes indicate stable species and dotted-line boxes indicate radicals. Species labelled with purple font are those that have been detected in space. Activation energies are by a) Andersson et al. (2011), b) Álvarez-Barcia et al. (2018), c) Song & Kästner (2017), d) Goumans & Kästner (2011), e) Kobayashi et al. (2017), and f) Zaverkin et al. (2018). An asterisk indicates the zero-point energy (ZPE) contribution.

Radical–molecule reactions, such as those between the HCO radical and C_2H_2 or C_2H_4 molecules, can also be excluded due to their high activation barriers. These activation energies are calculated following the method described by Kobayashi et al. (2017) and Zaverkin et al. (2018). Briefly, the electronic structure is described by density functional theory (DFT) with the MPWB1K functional (Zhao & Truhlar 2004) and the def2-TZVP basis set (Weigend et al. 1998). This combination has been shown to yield good results via benchmark studies. The activation energies are calculated including ZPE and with respect to the pre-reactive complex. Transition state geometries are listed in Table 7.3 in Appendix 7.8. These values are determined for the gas-phase, which will yield representative values as we expect the influence of the predominantly CO-rich environment to play a minor role in altering the reaction potential energy landscape. We find the activation energy for the reaction HCO + C_2H_2 → HCCHCHO to be 4290 K and that for the reaction HCO + C_2H_4 → H_2CCH_2CHO to be 3375 K. Such high barriers hint at a low overall efficiency, especially because, as indicated by Álvarez-Barcia et al. (2018), reactions where two heavy atoms are involved, for example formation of a carbon–carbon bond, are expected not to tunnel efficiently. Such barriers could be overcome if the HCO radical would have considerable leftover excess energy after formation.

With the exclusion of H-abstraction reactions involving stable hydrocarbon molecules and also radical–neutral reactions, the following reactions are left to consider: HCO + H_2CCH/H_3CCH_2, CH_3O + H_2CCH/H_3CCH_2, and CH_2OH

+ H_2CCH/H_3CCH_2. Of these, only HCO + H_2CCH/H_3CCH_2 leads to the formation of both – propanal and 1-propanol. As shown in Fig. 7.6, propenal can be formed by HCO + H_2CCH. Propenal was not detected in our experiments, and this is likely due to the low activation barrier of 842 K for propenal + H (Zaverkin et al. 2018), effectively converting propenal to further hydrogenation products. CH_3O and CH_2OH radicals may react with hydrocarbon radicals to form methoxyethene, methoxyethane, allyl alcohol, and 1-propanol. Yet, these radicals are further down the CO + H chain, and since H_2CO + H has a barrier of > 2000 K (Woon 2002; Song & Kästner 2017), reactions with CH_3O and CH_2OH radicals are less probable than with HCO under our experimental conditions. However, it should be noted that interstellar CH_3OH (ice and gas) is an abundant molecule that is primarily formed by the CO + H surface reaction, thus CH_3O and CH_2OH radicals must also be abundant in the ISM. Therefore other primary alcohols, aldehydes, and even ethers maybe formed with abundances that can be used to search for astrochemical links.

Comparison of the hydrogenation activation barriers of H_2CO and propanal shows that the values have a difference of < 500 K (with H_2CO + H having the smaller barrier), although the low-temperature rate constant is greater for the case of H_2CO. Since hydrogenation of H_2CO is the dominating pathway to CH_3OH formation in interstellar space, this means that also the hydrogenation of propanal resulting in the formation of interstellar 1-propanol maybe a notable pathway.

The work by Jonusas et al. (2017), in which propanal hydrogenation was not found to result in 1-propanol formation, seems to be in contradiction with our findings. A direct comparison is hard, since the hydrogen and propanal fluxes and fluences, and particularly the deposition methods, are different between the two studies. Jonusas et al. (2017) deposited propanal first, then bombarded the ice with hydrogen atoms. This is known as the pre-deposition method, which results in less product formation in comparison to the co-deposition method usually because of the limited penetration depth of hydrogen atoms in the ice, as discussed by Fuchs et al. (2009) in the case of CO + H. The theoretical work by Zaverkin et al. (2018) suggested that the non-detection of 1-propanol by Jonusas et al. (2017) could be due to the continuous H-abstraction and subsequent H-addition from and onto the carbonyl-C, respectively, since H-abstraction from the carbonyl-C of propanal was found to be five orders of magnitude faster than H-addition to O at 60 K (we note that the experiments presented here occur at 10 K). Another scenario could exist: after H-abstraction from the carbonyl-C, the resulting radical could be more prone to hydrogenation on the O, which would favour 1-propanol formation. However, there are no rate constants or branching ratios available for that process.

Finally, we address the dominant reaction mechanism. Reactions that take place on surfaces such as that studied here usually have three mechanisms: Langmuir-Hinshelwood (L-H), Eley-Rideal (E-R), and hot-atom (H-A) (He et al. 2017). In the presented experiments, the ice temperature is at 10 K during the deposition. This allows the residence time of H-atoms to be long enough for the atoms to rapidly scan the surface and have multiple chances of reaction with other ice reactants. Further, the rate of reaction via the L-H mechanism dominates over E-R and H-A mechanisms especially when the reaction possesses a significant activation barrier. As demonstrated by Watanabe & Kouchi (2002),

Watanabe et al. (2003), Cuppen & Herbst (2007), Fuchs et al. (2009), Chuang et al. (2016), and Qasim et al. (2018), the abundance of products that are formed from hydrogenation decreases substantially as the deposition temperature increases to temperatures that are below the initial desorption temperature of the reactant molecule(s). This is due to the rapid drop of the H-atom residence time on the surface. If the E-R or H-A mechanism were responsible for the formation of products, then no drastic drop in the amount of the formed products would be observed. This evidence in favour of the L-H mechanism also allows us to claim that the H-atoms involved in the reactions are in thermal equilibrium with the 10 K surface.

7.5 Astrophysical implications

The experimental conditions and chemical species studied aim to mimic reaction pathways that can take place on icy dust grains in a cold and dense prestellar core or the outer regions of protostellar envelopes (i.e., 10 K ices formed primarily by radical-induced reactions). Specifically, we have investigated how species formed along the well-studied CO hydrogenation chain can interact with radicals formed upon hydrogenation of other species expected to be present in an interstellar ice environment. Newly formed ice constituents can then be observed in the gas-phase after warm-up in the hot core region following thermal desorption. Following the outcome of our experiments, the detection of propanal in hot cores may be explained following the reaction scheme discussed in Fig. 7.6 and the formation of 1-propanol is a logical consequence, providing solid motivation for future surveys for this species. C_2H_2 was used in the experiments as a source for hydrocarbon radicals, which are species that can also be formed in different ways in the ISM. Strong lines of gaseous C_2H_2 have been detected in warm gas in protostellar envelopes (Lacy et al. 1989; Lahuis & van Dishoeck 2000; Rangwala et al. 2018) and in protoplanetary disks (Gibb et al. 2007; Carr & Najita 2008; Salyk 2011), with typical abundances of 10^{-7} - 10^{-6} with respect to H_2, or 10^{-3} - 10^{-2} with respect to gaseous H_2O or CO. However, there has not yet been a detection of interstellar solid C_2H_2. The limits on C_2H_2 ice are < 1.4% with respect to H_2O ice (Boudin et al. 1998), which is similar to or lower than the abundance of CH_4 ice (typical abundance of ~5%) (Gibb et al. 2004; Öberg et al. 2008, 2011; Boogert et al. 2015). Other models of gas-grain chemistry predict lower C_2H_2 abundances; a factor of 50 - 100 lower than that of CH_4 (Garrod 2013). In cometary ices, C_2H_2 is detected, at a level of 0.1 - 0.5% with respect to H_2O ice (Mumma & Charnley 2011). A logical explanation for such low abundances is that the bulk of the solid C_2H_2 is transformed to other species, through reactions such as those studied here.

As stated in Sect. 7.1, 1-propanol has not yet been identified in the ISM, but several surveys have attempted its detection. Here we put the laboratory and theoretical findings presented in the previous sections into an astrochemical context, using deep interferometric observations by ALMA with the aim to constrain the abundance of 1-propanol around the hot core of the low-mass protostar IRAS 16293-2422B. We use the 12m array ALMA data from the work by Taquet, V. et al. (2018) under Cycle 4 (program 2016.1.01150.S) in Band 6

at 233 - 236 GHz. These observations have a circular Gaussian beam fixed to 0.5" and with a 1σ rms sensitivity of 1.2 - 1.4 mJy beam^{-1} per 0.156 km s^{-1} channel. This provides one of the deepest ALMA datasets towards a low-mass protostar obtained so far. Spectra of the four spectral windows obtained towards a position located at 1 beam size offset in the southwest direction with respect to the source B dust continuum position are analysed, which gives the best compromise between intensity and opacity of the continuum and the molecular emission. The observed and predicted spectra of the four spectral windows towards the full-beam offset position are shown in the Appendix of Taquet, V. et al. (2018). As explained there, more than 250 spectroscopic entries mostly using the CDMS and JPL catalogues have been taken into account to identify all detected transitions. However, as discussed by Taquet, V. et al. (2018), ~70% of the ~670 transitions remain unidentified at a 5σ level. The full spectrum of 1-propanol over the entire frequency range is simulated (Fig. 7.9 in Appendix 7.9) and compared with observations. The spectroscopic data of the 1-propanol molecule are provided by Kisiel et al. (2010). About 60 "bright" transitions (i.e. $E_{up} < 500$ K, $A_{i,j} > 10^{-5}$ s^{-1}) from 1-propanol are located in the frequency range covered by the four spectral windows. The transition that gives the deepest constraint on the column density of 1-propanol is that at 236.138 GHz ($E_{up} = 160$ K, $A_{i,j} = 6.6 \times 10^{-5}$ s^{-1}) as seen in Fig. 7.9.

We derive the upper limit of the 1-propanol column density assuming conditions at the Local Thermal Equilibrium (LTE) and assuming optically thin emission and excitation temperatures of 300 and 125 K, following previous ALMA observations of other COMs towards this source (Jørgensen et al. 2018). Both panels in Fig. 7.7 show the spectrum around the targeted transition obtained after a baseline correction through a fit over the line-free regions around 236.138 GHz. We note that only the spectrum at $T_{ex} = 300$ K is shown, since the spectrum for $T_{ex} = 125$ K at around 236.138 GHz is the same. The 1-propanol transition is blended by two lines at 236.1376 and at 236.1390 GHz, which is clearly visible from the zoom-in shown in the right panel. The former transition (on the left) could be partially attributed to CH_2NH, recently detected toward IRAS 16293-2422B by Ligterink et al. (2018) using ALMA. The peak on the right is of unknown nature and may be due to a rotational transition starting from a vibrationally excited species. With an offset of 0.15 MHz with respect to the synthetic transition (red), it is unlikely that this peak is actually due to 1-propanol. Only a modification of the source velocity from 2.7 km/s – the source velocity of IRAS16293-B usually derived – to 2.5 km/s would result in a match. In that case, the next strongest transitions should be searched for. We verified that other "bright" 1-propanol lines are not detected in our observed spectrum for the two different upper limits and associated excitation temperatures. For the moment, we conclude that the transition to the right is not due to 1-propanol.
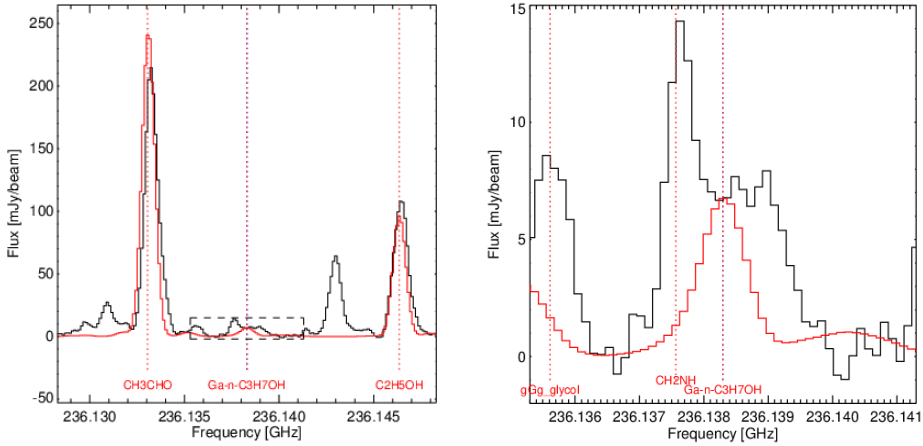
Figure 7.7: Extended (left) and zoomed-in (right) spectra around the 1-propanol transition. Observed spectrum (black) around the targeted 1-propanol transition at 236.138 GHz (purple dotted-line and black dashed-line box) towards the "full-beam" offset position located 0.5 arcseconds away from the continuum peak of IRAS 16293-2422B. Synthetic spectrum of the LTE model is shown in red. The predicted 1-propanol transition shown here is for N(1-propanol) = 1.2×10^{15} cm^{-2} and T_{ex} = 300 K (see text for more details). Red dotted-lines refer to the position of transitions of identified species detected above 5σ, with the associated species labelled below the spectrum.

In order to derive a conservative limit for the 1-propanol column density, we neglect the spectral contribution of the two peaks shown in Fig. 7.7 near the wavelength of the predicted 1-propanol transition and instead derive the column density using the synthetic transition. At 300 and 125 K, 1-propanol column densities of 1.2×10^{15} cm^{-2} and 7.6×10^{14} cm^{-2} are derived, respectively, which are the highest column densities that still result in a non-detection of 1-propanol. Comparing this value to the propanal column density of 2.2×10^{15} cm^{-2} found by Lykke et al. (2017) for 125 K with similar observational properties, this results in a 1-propanol:propanal upper limit of < 0.55 (T_{ex} = 300 K) and < 0.35 (T_{ex} = 125 K). This is consistent with the experiments in this work and also with the theoretical calculations by Zaverkin et al. (2018), which show that the hydrogenation of propanal to 1-propanol involves a barrier. From the perspective that only the activation barrier is considered, there should be less 1-propanol in space in comparison to propanal if 1-propanol originates from propanal.

The C_2H_2 + CO + H experiment shows the importance of introducing different molecules to the CO + H channel. The CO hydrogenation chain is generally taken as the way to explain the observed CH_3OH abundances in space under dense cloud conditions. In recent work, an extension of this network towards larger sugars and sugar alcohols was proven. Here we demonstrate that this reaction chain also holds potential for the formation of other species,

including radicals formed by other means. By adding C_2H_2, reaction pathways are realised in which 1-propanol can be formed. This is significant, as the molecule has astrobiological relevance and may already be formed during the dense cloud stage, for example when particularly 'non-energetic' processes are at play. It is clear from the detections and proposed list of mechanisms in this work that the extension of the CO + H channel is promising to explain the formation of potentially important interstellar species that have solid-state formation pathways that are not yet well understood.

From the studied reactions, it can be generalized that a whole set of various aldehydes and primary alcohols can be formed starting from CO and polyynes, where polyynes are composed of alkynes such as C_2H_2. Such molecules can directly participate in the formation of micelles, or serve as the analogues of fatty acids in the formation of glycerol esters (analogues of glycolipids). The latter is particularly intriguing since previous results indicate that glycerol is formed by hydrogenation of CO during the heavy CO freeze-out stage (Fedoseev et al. 2017).

7.6 Conclusions

This study focuses on the possible formation of the COMs, propanal and 1-propanol, that may take place when radicals formed in the hydrogenation of C_2H_2 and CO ice interact. For a temperature of 10 K and upon H-atom addition during a C_2H_2 and CO co-deposition experiment, our findings can be summarised as follows.

◆ We find the formation of propanal and possibly 1-propanol ice.

◆ We show that the hydrogenation of propanal ice leads to 1-propanol formation. Further theoretical investigations on the scenario that favours 1-propanol formation are desired.

◆ We conclude that the most likely formation scheme of these two COMs is through the radical–radical reactions of HCO + H_2CCH and HCO + H_3CCH$_2$.

◆ We derive 1-propanol upper limits of 1.2×10^{15} cm^{-2} (T_{ex} = 300 K) and 7.6×10^{14} cm^{-2} (T_{ex} = 125 K) from ALMA observations towards the IRAS 16293-2422B low-mass protostar. These values are compared to the propanal column density of 2.2×10^{15} cm^{-2} from Lykke et al. (2017). The 1-propanol to propanal abundance ratio of $< 0.35 - 0.55$ is complemented by activation barriers of propanal + 2H $\rightarrow$1-propanol found in the presented experiments and in theoretical works.

7.7 Appendix: Additional RAIR spectra
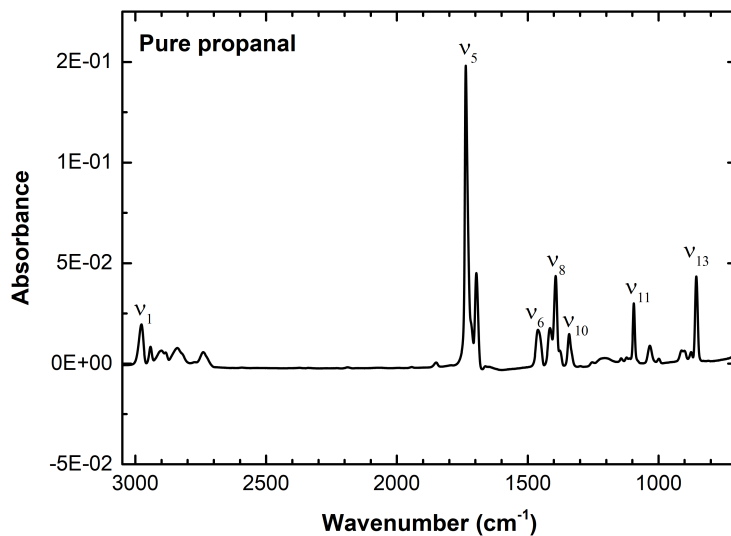
Figure 7.8: RAIR spectrum of propanal (exp. 2.4) taken at 10 K. Vibrational mode assignments are acquired from the work by Köroğlu et al. (2015).

7.8 Appendix: xyz coordinates of transition state structures

Table 7.3: Transition state (TS) geometries for HCO + C_2H_2 and HCO + C_2H_4 in the gas-phase.

		TS	
		R1: HCO + C_2H_2 → HCCHCHO	
C	2.457338	0.140746	0.005500
C	2.631181	-0.091562	1.180635
H	2.643330	-0.284788	2.221672
H	2.726948	0.284977	-1.012337
H	-0.004679	0.618071	0.718368
C	0.378597	0.141577	-0.202373
O	-0.111318	-0.735052	-0.794637
		R2: HCO + C_2H_4 → H_2CCH_2CHO	
C	2.503771	0.131055	-0.104025
C	2.587871	-0.106220	1.216301
H	2.638529	0.697532	1.930552
H	2.561540	-1.108352	1.607866
H	2.634615	1.125558	-0.495603
H	2.576039	-0.671720	-0.817177
H	0.014387	0.814221	0.535546
C	0.362966	0.096368	-0.230237
O	-0.158186	-0.904331	-0.528368

7.9 Appendix: 1-propanol spectra at T_{ex} = 125 and 300 K
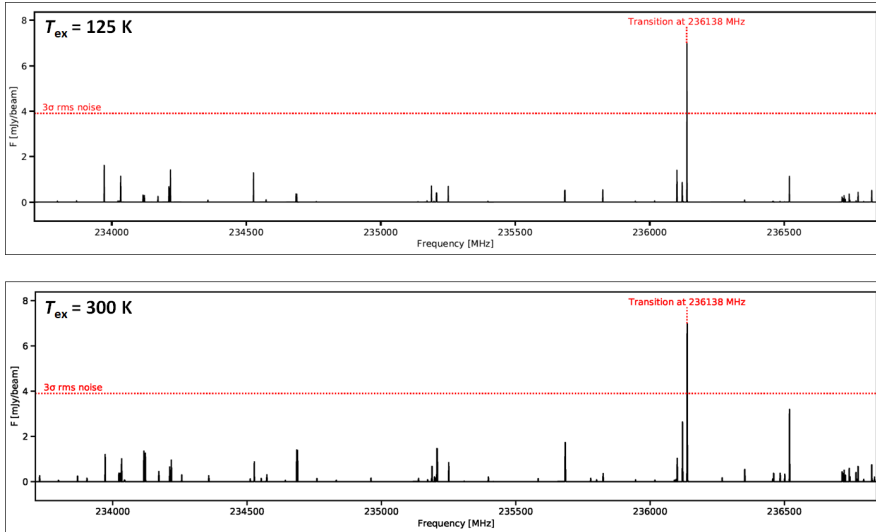
Figure 7.9: Synthetic spectra of the 1-propanol emission for excitation temperatures T_{ex} = 125 K (top) and 300 K (bottom) with associated 1-propanol column densities of 7.6×10^{14} cm^{-2} and 1.2×10^{15} cm^{-2}, respectively. These are the highest column densities that result in non-detection of the 1-propanol transition at 236.138 GHz (see text for more details).

Bibliography

2018, Phys. Chem. Chem. Phys., 20, 5435

Abplanalp, M. J., Góbi, S., Bergantini, A., Turner, A. M., & Kaiser, R. I. 2018, ChemPhysChem, 19, 556

Abplanalp, M. J., Gozem, S., Krylov, A. I., et al. 2016, Proc. Natl. Acad. Sci. U.S.A., 113, 7727

Abplanalp, M. J. & Kaiser, R. I. 2016, Astrophys. J., 827, 1

Altwegg, K., Balsiger, H., Berthelier, J.-J., et al. 2017, Mon. Not. R. Astron. Soc., 469, S130

Álvarez-Barcia, S., Russ, P., Kästner, J., & Lamberts, T. 2018, Mon. Not. R. Astron. Soc., 479, 2007

Andersson, S., Goumans, T., & Arnaldsson, A. 2011, Chem. Phys. Lett., 513, 31

Bennett, C. J., Jamieson, C. S., Osamura, Y., & Kaiser, R. I. 2006, Astrophys. J., 653, 792

Bisschop, S., Fuchs, G., van Dishoeck, E. F., & Linnartz, H. 2007, Astron. Astrophys., 474, 1061

Boogert, A., Gerakines, P. A., & Whittet, D. C. 2015, Annu. Rev. Astron. Astrophys., 53, 541

Boudin, N., Schutte, W. A., & Greenberg, J. M. 1998, Astron. Astrophys., 331, 749

Butscher, T., Duvernay, F., Rimola, A., Segado-Centellas, M., & Chiavassa, T. 2017, Phys. Chem. Chem. Phys., 19, 2857

Butscher, T., Duvernay, F., Theule, P., et al. 2015, Mon. Not. R. Astron. Soc., 453, 1587

Carr, J. S. & Najita, J. R. 2008, Science, 319, 1504

Chuang, K.-J., Fedoseev, G., Ioppolo, S., van Dishoeck, E. F., & Linnartz, H. 2016, Mon. Not. R. Astron. Soc., 455, 1702

Chuang, K.-J., Fedoseev, G., Qasim, D., et al. 2018, Astrophys. J., 853, 1

Cuppen, H. & Herbst, E. 2007, Astrophys. J., 668, 294

Cuppen, H., Ioppolo, S., Romanzin, C., & Linnartz, H. 2010, Phys. Chem. Chem. Phys., 12, 12077

de Marcellus, P., Meinert, C., Myrgorodska, I., et al. 2015, Proc. Natl. Acad. Sci. U.S.A., 112, 965

De Rosa, M., Gambacorta, A., & Gliozzi, A. 1986, Microbiol. Rev., 50, 70

Deamer, D., Dworkin, J. P., Sandford, S. A., Bernstein, M. P., & Allamandola, L. J. 2002, Astrobiology, 2, 371

Fedoseev, G., Chuang, K.-J., Ioppolo, S., et al. 2017, Astrophys. J., 842, 1

Fedoseev, G., Cuppen, H. M., Ioppolo, S., Lamberts, T., & Linnartz, H. 2015, Mon. Not. R. Astron. Soc., 448, 1288

Fuchs, G., Cuppen, H., Ioppolo, S., et al. 2009, Astron. Astrophys., 505, 629

Garrod, R. T. 2013, Astrophys. J., 765, 60

Gerakines, P., Schutte, W., & Ehrenfreund, P. 1996, Astron. Astrophys., 312, 289

Gibb, E., van Brunt, K., Brittain, S. D., & Rettig, T. 2007, Astrophys. J., 660, 1572

Gibb, E., Whittet, D., Boogert, A., & Tielens, A. 2004, Astrophys. J. Suppl. Ser., 151, 35

Goesmann, F., Rosenbauer, H., Bredehöft, J. H., et al. 2015, Science, 349, 1

Goumans, T. & Kästner, J. 2011, J. Phys. Chem. A, 115, 10767

He, J., Emtiaz, S. M., & Vidali, G. 2017, Astrophys. J., 851, 104

Hiraoka, K., Takayama, T., Euchi, A., Handa, H., & Sato, T. 2000, Astrophys. J., 532, 1029

Hollis, J. M., Jewell, P. R., Lovas, F. J., Remijan, A., & Møllendal, H. 2004, Astrophys. J. Lett., 610, L21

Hudson, R., Loeffler, M., & Yocum, K. 2017, Astrophys. J., 835, 1

Hudson, R. L., Gerakines, P. A., & Moore, M. 2014, Icarus, 243, 148

Ioppolo, S., Fedoseev, G., Lamberts, T., Romanzin, C., & Linnartz, H. 2013, Rev. Sci. Instrum., 84, 1

Ioppolo, S., Öberg, K., Linnartz, H., et al. 2014 (Wiley, 289, New York)

Jonusas, M., Guillemin, J.-C., & Krim, L. 2017, Mon. Not. R. Astron. Soc., 468, 4592

Jørgensen, J., Müller, H., Calcutt, H., et al. 2018, Astron. Astrophys., 620, A170

Kaiser, R. I., Maity, S., & Jones, B. M. 2014, Phys. Chem. Chem. Phys., 16, 3399

Kim, Y., Bennett, C., Chen, L.-H., O'Brien, K., & Kaiser, R. 2010, Astrophys. J., 711, 744

Kisiel, Z., Dorosh, O., Maeda, A., et al. 2010, Phys. Chem. Chem. Phys., 12, 8329

Kobayashi, H., Hidaka, H., Lamberts, T., et al. 2017, Astrophys. J., 837, 1

Kolasinski, K. W. 2012, Surface science: foundations of catalysis and nanoscience (West Chester, PA: John Wiley & Sons)

Köroğlu, B., Loparo, Z., Nath, J., Peale, R. E., & Vasu, S. S. 2015, J. Quant. Spectrosc. Radiat. Transf., 152, 107

Lacy, J., Evans, N. J., Achtermann, J., et al. 1989, Astrophys. J., 342, L43

Lahuis, F. & van Dishoeck, E. F. 2000, Astron. Astrophys., 355, 699

Ligterink, N., Calcutt, H., Coutens, A., et al. 2018, Astron. Astrophys., 619, A28

Linnartz, H., Ioppolo, S., & Fedoseev, G. 2015, Int. Rev. Phys. Chem., 34, 205

Lykke, J. M., Coutens, A., Jørgensen, J. K., et al. 2017, Astron. Astrophys., 597, 1

Max, J.-J., Daneault, S., & Chapados, C. 2002, Can. J. Chem., 80, 113

McGuire, B. A., Carroll, P. B., Loomis, R. A., et al. 2016, Science, 1449

Moore, M. & Hudson, R. 1998, Icarus, 135, 518

Moore, M. & Hudson, R. 2003, Icarus, 161, 486

Moran, L. A., Horton, H. R., Scrimgeour, G., & Perry, M. 2012, Principles of biochemistry (Upper Saddle River, NJ: Pearson Boston)

Müller, H. S., Belloche, A., Xu, L.-H., et al. 2016, Astron. Astrophys., 587, 1

Mumma, M. J. & Charnley, S. B. 2011, Annu. Rev. Astron. Astrophys., 49, 471

Öberg, K. I., Boogert, A., Pontoppidan, K. M., et al. 2008, Astrophys. J., 678, 1032

Öberg, K. I., Boogert, A., Pontoppidan, K. M., et al. 2011, Proc. IAU Symp. 280, 7, 65

Öberg, K. I., Garrod, R. T., van Dishoeck, E. F., & Linnartz, H. 2009, Astron. Astrophys., 504, 891

Pontoppidan, K. M. 2006, Astron. Astrophys., 453, L47

Qasim, D., Chuang, K.-J., Fedoseev, G., et al. 2018, Astron. Astrophys., 612, 1

Rangwala, N., Colgan, S. W. J., Gal, R. L., et al. 2018, Astrophys. J., 856, 1

Requena-Torres, M., Martín-Pintado, J., Martín, S., & Morris, M. 2008, Astrophys. J., 672, 352

Salyk, C. 2011, Proc. IAU Symp. 280, 7, 127

Song, L. & Kästner, J. 2017, Astrophys. J., 850, 1

Taquet, V., van Dishoeck, Ewine F, Swayne, M., et al. 2018, Astron. Astrophys., 618, 1

Tercero, B., Cernicharo, J., López, A., et al. 2015, Astron. Astrophys., 582, L1

Tschersich, K. 2000, J. Appl. Phys., 87, 2565

Tschersich, K., Fleischhauer, J., & Schuler, H. 2008, J. Appl. Phys., 104, 1

Tschersich, K. & Von Bonin, V. 1998, J. Appl. Phys., 84, 4065

Watanabe, N. & Kouchi, A. 2002, Astrophys. J. Lett., 571, L173

Watanabe, N., Shiraki, T., & Kouchi, A. 2003, Astrophys. J. Lett., 588, L121

Weigend, F., Häser, M., Patzelt, H., & Ahlrichs, R. 1998, Chem. Phys. Lett., 294, 143

Woon, D. E. 2002, Astrophys. J., 569, 541

Zaverkin, V., Lamberts, T., Markmeyer, M., & Kästner, J. 2018, Astron. Astrophys., 617, 1

Zhao, Y. & Truhlar, D. G. 2004, J. Phys. Chem. A, 108, 6908

Zhou, L., Kaiser, R. I., Gao, L. G., et al. 2008, Astrophys. J., 686, 1493

Zhou, L., Maity, S., Abplanalp, M., Turner, A., & Kaiser, R. I. 2014, Astrophys. J., 790, 38

Alcohols on the rocks: formed in a H$_3$CC≡CH + OH cocktail

A number of recent experimental studies have shown that solid-state complex organic molecules (COMs) can form under conditions that are relevant to the CO freeze-out stage in dense clouds. In this work, we show that alcohols can be formed well before the CO freeze-out stage (i.e., during the very early stage of the H$_2$O-rich ice phase). This joint experimental and computational investigation shows that the isomers, n- and i-propanol (H$_3$CCH$_2$CH$_2$OH and H$_3$CCHOHCH$_3$) and n- and i-propenol (H$_3$CCH=CHOH and H$_3$CCOH=CH$_2$), can be formed in radical-addition reactions starting from propyne (H$_3$CC≡CH) + OH at the low temperature of 10 K, where H$_3$CC≡CH is one of the simplest representatives of stable carbon chains already identified in the interstellar medium (ISM). The resulting average abundance ratio of 1:1 for n-propanol:i-propanol is aligned with the conclusions from the computational work that the geometric orientation of strongly interacting species is influential to the extent of which 'mechanism' is participating, and that an assortment of geometries leads to an averaged-out effect. Three isomers of propanediol are also tentatively identified in the experiments. It is also shown that propene and propane (H$_3$CCH=CH$_2$ and H$_3$CCH$_2$CH$_3$) are formed from the hydrogenation of H$_3$CC≡CH. This experimental finding falls in-line with the lower activation barrier of hydrogenation of a C=C bond in comparison to a C≡C bond. Reactants and products are probed by temperature programmed desorption-quadrupole mass spectrometry (TPD-QMS) and reflection-absorption infrared spectroscopy (RAIRS). Product relative abundances are determined from TPD-QMS data. Computationally-derived activation barriers give additional insight into what types of reactions and mechanisms are more likely to occur in the laboratory and in the ISM. Our findings not only suggest that the alcohols studied here share common chemical pathways and therefore can show up simultaneously in astronomical surveys, but also that their extended counterparts that derive from polyynes containing H$_3$C-(C≡C)$_n$-H structures may exist in the ISM. Such larger species, like fatty alcohols, are the possible constituents of simple lipids that primitive cell membranes on the early Earth are thought to be partially composed of.

8.1 Introduction

The origin of cosmic carbon lies in the outflows of carbon-rich stars (Cherchneff 2011; Contreras & Salama 2013). How carbon evolves into hydrocarbon species, from small molecules such as methane (CH_4) and acetylene (C_2H_2) to polycyclic aromatic hydrocarbons (PAHs), to carbon nanoparticles, or other carbon containing species like alcohols, is far from understood. In addition to "bottom-up" approaches, which merges smaller precursors into larger species (in the gas-phase or solid-state), also "top-down" approaches have been proposed. Both scenarios are considered as likely road maps towards molecular complexity in space, but as mentioned, many details are lacking (Tielens 2013; Castellanos 2018).

From a bottom-up perspective, simple species such as C_2H_2 can polymerize to form polyacetylene ($[C_2H_2]_n$) (Woods et al. 2003; Cuylle et al. 2014). The complexity can increase by addition of a methyl (–CH_3) group to form methylpolyacetylene. Such species can eventually accrete onto carbonaceous dust grains that were formed from nucleation of PAHs (Pascoli & Polleux 2000; Contreras & Salama 2013). An alternative is that these species form through surface reactions in the ice layers that are on top of dust grains. In this article, we focus on the simplest representative of the latter row of species: methylacetylene, also known as propyne ($H_3CC\equiv CH$). $H_3CC\equiv CH$ has been detected in space (Snyder & Buhl 1973; Irvine et al. 1981; Kuiper et al. 1984; Cernicharo et al. 2001; Kaifu et al. 2004; Agúndez et al. 2008; Muller et al. 2011; Malek et al. 2011; Qiu et al. 2018). Not only is it reported to be observed towards carbon-rich stars (Agúndez et al. 2008) as expected, but it is also reported to be detected towards cold and dense clouds/cores (Kaifu et al. 2004; Irvine et al. 1981), where it has a column density of $(4-8) \times 10^{13}$ cm^{-2} in TMC-1 (Irvine et al. 1981). Assuming an H_2 abundance of $\sim 10^{21}$ cm^{-2} (Tielens 2013), this leads to $< 1\%$ with respect to H_2O ice following the calculation from Herbst & van Dishoeck (2009).

H_2O ice is formed on dust grains (Miyauchi et al. 2008; Ioppolo et al. 2008, 2010; Matar et al. 2008; Cuppen et al. 2010; Romanzin et al. 2011). Laboratory experiments show that every formed H_2O molecule, in the solid-state and gas-phase, has an OH radical and/or ion as an intermediate (van Dishoeck et al. 2013). In the ice, OH radicals have the chance to react with other species that are in direct proximity prior to hydrogenation to yield H_2O, as the accretion of an H-atom onto a dust grain of radius 10^{-5} cm happens once a day (Hama & Watanabe 2013). An example of this is the formation of CO_2 from CO and OH in H_2O-rich ices (Chang & Herbst 2012). Thus, the interaction between OH radicals and $H_3CC\equiv CH$ is a valid topic to be addressed in astrochemical laboratories. This interaction may result in the formation of simple and polyalcohols.

The formation of alcohols is particularly intriguing as they may have a role in astrobiology, assuming that alcohols can be delivered to planetary bodies such as the early Earth (Chyba et al. 1990). Simple alcohols are amphiphilic molecules, i.e., both sides of the molecule have different affinities from each other (Moran et al. 2012). As they are composed of a polar head (–OH group) and a hydrophobic tale (aliphatic group), they can take part in the formation of micelles in primordial oceans. More complex alcohols (e.g., polyalcohols and

fatty alcohols), in turn, can play a role in the formation of primitive lipids. Like sugars in saccharolipids, sphingosines in sphingolipids, and glycerol in modern phospholipids, fatty alcohols can act as the backbone to which fatty acids are attached. Their presence during abiogenesis is supported by the idea that complex lipids may not have been available on the early Earth (Deamer et al. 2002; Budin & Szostak 2011), and also through the finding that primary alcohols are components of archaea cell membranes (De Rosa et al. 1986).

The mechanism proposed in this paper results in the formation of alcohols already in H_2O–rich ices. Meaning, the alcohols can be synthesized before the CO freeze-out stage, well below extinctions (A_V) of 9 in interstellar clouds (Boogert et al. 2015). In the literature, most solid-state laboratory experiments report the formation of simple alcohols (e.g., methanol (CH_3OH) and ethanol (H_3CCH_2OH)) and polyalcohols (e.g., ethylene glycol ($HOCH_2CH_2OH$), glycerol ($HOCH_2CHOHCH_2OH$), and methoxymethanol (H_3COCH_2OH)) in the context where much CO has already been frozen out (Bernstein et al. 1995; Chen et al. 2013; Abplanalp et al. 2016; Paardekooper et al. 2016; Fedoseev et al. 2015; Butscher et al. 2015; Chuang et al. 2016; Butscher et al. 2017). These experiments can be divided into two subgroups: 'energetic' and 'non-energetic' processing, where 'non-energetic' refers to a radical-induced process without the involvement of UV, cosmic rays, and/or other 'energetic' particles (Fuchs et al. 2009). In the 'energetic'-induced studies, CH_3OH and/or CO-containing ices are irradiated to form alcohols, and CH_3OH is either mixed with CO or explicitly stated to be a product of CO hydrogenation (Bernstein et al. 1995; Chen et al. 2013; Abplanalp et al. 2016; Paardekooper et al. 2016). In experiments that focus on 'non-energetic' processes, alcohols are formed by reactions that involve the hydrogenation of a CO-rich ice (Fedoseev et al. 2015; Butscher et al. 2015; Chuang et al. 2016; Butscher et al. 2017).

Many of the icy alcohols that have been formed in the laboratory have also been detected as gas-phase species in the ISM. This includes the detections of CH_3OH, H_3CCH_2OH, H_2CCHOH, $HOCH_2CH_2OH$, and H_3COCH_2OH, which were first reported by Ball et al. (1970), Zuckerman et al. (1975), Turner & Apponi (2001), Hollis et al. (2002), and McGuire et al. (2017), respectively. CH_3OH also has been detected in the solid-state (Boogert et al. 2011). Much effort has been recently put into explaining the transition from frozen to gas-phase CH_3OH to explain, for example, CH_3OH abundances observed in protoplanetary disks (van´t Hoff et al. 2018). Other alcohols are still elusive, such as n-propanol ($H_3CCH_2CH_2OH$) (Qasim et al. 2019).

This paper overviews the reaction of solid-state $H_3CC{\equiv}CH$ with H and OH under conditions relevant to the translucent cloud stage. Section 8.2 provides details on the experimental and computational parameters used for this study. Section 8.3 presents the findings from the laboratory experiments. Section 8.4 reports the computationally derived energies that are applicable to the reactions taking place in the experiments. These results are combined with the laboratory work to uncover the products formed and their formation pathways. Section 8.5 discusses how the formation of such icy alcohols can take place at the interface of astrochemical and astrobiological environments. Finally, the conclusions of this study are bulleted in Section 8.6.

Given the many different species that will be discussed in the next sections, Table 8.1 is added and summarizes the names and chemical structure formu-

Table 8.1: Chemical terminology used in this article.

IUPAC name	Referred to in this article
propan-1-ol (H$_3$CCH$_2$CH$_2$OH)	n-propanol
propen-1-ol (H$_3$CCH=CHOH)	n-propenol
propan-2-ol (H$_3$CCHOHCH$_3$)	i-propanol
propen-2-ol (H$_3$CCOH=CH$_2$)	i-propenol
propane-1,1-diol (H$_3$CCH$_2$CH(OH)$_2$)	propane-1,1-diol
propane-2,2-diol (H$_3$CC(OH)$_2$CH$_3$)	propane-2,2-diol
propane-1,2-diol (H$_3$CCHOHCH$_2$OH)	propane-1,2-diol
propan-2-one (H$_3$CCOCH$_3$)	acetone
propanal (H$_3$CCH$_2$CHO)	propanal
propanoic acid (H$_3$CCH$_2$COOH)	propanoic acid
propyne (H$_3$CC≡CH)	H$_3$CC≡CH
propene (H$_3$CCH=CH$_2$)	H$_3$CCH=CH$_2$
propane (H$_3$CCH$_2$CH$_3$)	H$_3$CCH$_2$CH$_3$

las of all relevant species. A majority of the listed chemicals are the expected products of solid-state H$_3$CC≡CH hydrogenation or hydroxylation.

8.2 Methodology

8.2.1 Experimental apparatus

The creation of ices and the subsequent measurements occur within an ultra-high vacuum (UHV) apparatus, SURFRESIDE^2. The main chamber reaches a base pressure of low 10^{-10} mbar. Near the center of the chamber, ices (typically tens of monolayers thick) are formed on a gold-plated copper substrate that is attached to a closed cycle helium cryostat. The inclusion of resistive heating and a sapphire rod allows the sample to have a temperature range of 7 - 450 K. The temperature is measured by a silicon diode sensor that has an absolute accuracy of 0.5 K. Further details of the initial design of SURFRESIDE^2 is found in Ioppolo et al. (2013), and recent upgrades are found in Qasim et al. (2018) and Chuang et al. (2018).

Two atomic beam lines are connected to the main chamber: a Hydrogen Atom Beam Source (HABS) and a Microwave Atom Source (MWAS). In this study, only the HABS is used, and more details about the design of the source is found in Tschersich & Von Bonin (1998), Tschersich (2000), and Tschersich et al. (2008). The HABS chamber is also under UHV conditions, where it reaches a base pressure of low 10^{-10} mbar. To form hydrogen atoms, hydrogen molecules (Linde 5.0) are thermally cracked by heated tungsten. This process also increases the kinetic energy of the H-atoms. To cool these atoms to room temperature, a nose-shaped quartz tube is positioned at the exit of the HABS source, which allows excess energy to be transferred via collisions with glass walls. Upon impact with

the icy surface, a fraction of the impinging H-atoms temporarily sticks to the ice that covers the surface and is thermalized. These H-atoms are then available for the reactions through the Langmuir-Hinshelwood mechanism. This mechanism was confirmed in several studies, where the intial step in the reaction chain initiated by H-atoms exhibits a significant activation barrier and requires quantum tunneling to proceed (Watanabe & Kouchi 2002; Watanabe et al. 2003; Cuppen & Herbst 2007; Fuchs et al. 2009; Chuang et al. 2016; Qasim et al. 2018).

All gases and vapors are prepared within a turbomolecularly-pumped gas manifold. $H_3CC{\equiv}CH$ (Sigma-Aldrich 97%), O_2 (Linde Gas 99.999%), and $^{18}O_2$ (Campro Scientific 97%) gases enter the main chamber through one of two dosing lines that are each connected to manually-operated leak valves. n-propanol (Honeywell 99.9%) and i-propanol (Sigma-Aldrich 99.8%) are placed in a tube and freeze-pump-thawed in order to rid of volatile impurities.

Two techniques are used to examine ice constituents and consequently the underlying ice chemistry: reflection-absorption infrared spectroscopy (RAIRS) and temperature programmed desorption quadrupole mass spectrometry (TPD-QMS). In this study, RAIRS is specifically exploited to identify the species formed at 10 K *in situ*. Spectra are recorded by a fourier transform infrared (FTIR) spectrometer that utilizes a wavenumber range of 4000-700 cm^{-1}, and can ultimately span to 6000 cm^{-1}. A resolution of 1 cm^{-1} is chosen. Vibrational mode assignments in the RAIR spectra originate from the NIST database.[1]

TPD-QMS is additionally utilized to probe newly formed ice species – particularly species that present a number of unresolved and/or overlapping infrared peaks. Employment of a QMS with an electron impact ionization energy of 70 eV allows comparison of the fragmentation (dissociative ionization) patterns from the experiments to fragmentation patterns found in the NIST database.[2] The relative abundances of $H_3CC{\equiv}CH$, $H_3CCH{=}CH_2$, and $H_3CCH_2CH_3$, as well as n- and i-propanol, are determined by a combination of the TPD-QMS data recorded at a molecule specific temperature and mass spectrometry data from NIST. The formula used to determine their relative abundances can be found in Martín-Doménech et al. (2015). $H_3CC{\equiv}CH$, $H_3CCH{=}CH_2$, and $H_3CCH_2CH_3$ have similar ionization cross sections of 7.66×10^{-16} cm^2, 8.74×10^{-16} cm^2, and 8.62×10^{-16} cm^2, respectively.[3] Additionally, the QMS sensitivity values of their correlating mass fragments, $m/z = 43$, $m/z = 42$, and $m/z = 41$, respectively, are similar. (Chuang 2018, Univ. Leiden) Therefore, only the fragmentation factors and relative intensities are taken into account, where the relative intensities are measured in the temperature range of 70 - 110 K. This method can also

---

1 T. Shimanouchi, "Molecular Vibrational Frequencies" in NIST Chemistry WebBook, NIST Standard Reference Database Number 69, Eds. P.J. Linstrom and W.G. Mallard, National Institute of Standards and Technology, Gaithersburg MD, 20899, https://doi.org/10.18434/T4D303, (retrieved December 4, 2018)

2 NIST Mass Spec Data Center, S.E. Stein, director, "Mass Spectra" in NIST Chemistry WebBook, NIST Standard Reference Database Number 69, Eds. P.J. Linstrom and W.G. Mallard, National Institute of Standards and Technology, Gaithersburg MD, 20899, https://doi.org/10.18434/T4D303, (retrieved December 4, 2018)

3 Kim, Y.-K., Irikura, K.K., Rudd, M.E., Ali, M.A., Stone, P.M., Chang, J., Coursey, J.S., Dragoset, R.A., Kishore, A.R., Olsen, K.J., Sansonetti, A.M., Wiersma, G.G., Zucker, D.S., and Zucker, M.A. (2004), Electron-Impact Ionization Cross Section for Ionization and Excitation Database (version 3.0). [Online] Available: http://physics.nist.gov/ionxsec [2019, March 16]. National Institute of Standards and Technology, Gaithersburg, MD.

be applied to determining the relative abundance of n- and i-propanol in the temperature range of 120 - 190 K, using m/z values of 31 for n-propanol, and 45 and 59 for i-propanol. However, their respective sensitivity values of 0.3179, 0.1762, and 0.0982 are taken into account, as their values will significantly influence the determined relative abundances. A TPD ramp rate of 5 K/min is applied to all experiments.

8.2.2 Experimental procedure

The experiments and experimental parameters used in this study are listed in Table 8.2. Fluxes are determined by the Hertz-Knudsen equation (Kolasinski 2012) except for the H-atom flux, which is based on an absolute D-atom flux measurement that is reported in Ioppolo et al. (2013). Motivation for the listed experiments is discussed below.

Experiments 1.0 - 1.2 are used to show what products are formed from the hydrogenation of H$_3$CC≡CH ice, as well as to determine the relative abundance of the newly formed products. The addition of oxygen in experiments 2.0 - 2.3 is used to study the products formed from H$_3$CC≡CH + OH and their subsequent relative abundance. Note that OH radicals are effectively formed from H + O$_2$ (Cuppen et al. 2010). ^{18}O$_2$ is used in experiments 2.1 and 2.3 in order to confirm the identity of species formed in experiments 2.0 and 2.2, respectively, by observation of the isotopic shift in the TPD-QMS data. To further confirm the identity of the species formed in experiments 2.0 - 2.3, the TPD-QMS data of experiments 3.0 - 3.2 are used as references.

8.2.3 Computational details

We calculate activation energies and reaction energies for the reactions of hydrogen atoms and hydroxyl radicals with both H$_3$CC≡CH and H$_3$CCH=CH$_2$ molecules. Benchmark calculations and additional supporting information are found in the Supporting Information Section S2. As radicals may attack either the center or exterior carbon atom, this results in a total of eight reactions. Additionally, two isomerization reactions are studied, namely the conversion from n-propenol to propanal (and vice versa) and i-propenol to acetone (and vice versa).

The potential energy surface (PES) or electronic structure is described by density functional theory (DFT). Following the benchmark calculations performed by Kobayashi et al. (2017), the MPWB1K functional (Zhao & Truhlar 2004) in combination with the basis set def2-TZVP (Weigend et al. 1998) is chosen. The energy and gradient calculations are carried out in NWChem version 6.6 (Valiev et al. 2010). An additional benchmark is performed for the activation energies with the M06-2X functional (Zhao & Truhlar 2008) with the same basis set (def2-TZVP). Furthermore, the interaction energies of the OH-C$_3$H$_n$ pre-reactive complexes calculated with MPWB1K/def2-TZVP are compared to single-point energies calculated with CCSD(T)-F12/cc-VDZ-F12 (Knowles et al. 1993, 2000; Deegan & Knowles 1994; Adler et al. 2007; Peterson et al. 2008; Knizia et al. 2009) in Molpro version 2012 (Werner et al. 2012).

Geometry optimizations are carried out for the separated reactant, product, and transition structures and verified by the appropriate number of imaginary

Table 8.2: A list of experiments performed and the corresponding experimental parameters. Fluxes are calculated by the Hertz-Knudsen equation, and the H-flux is derived from Ioppolo et al. (2013). "Other" refers to either n- or i-propanol.

No.	Experiments	T_{sample} K	$Flux_{HC\equiv CCH_3}$ $cm^{-2}s^{-1}$	$Flux_H$ $cm^{-2}s^{-1}$	$Flux_{O_2}$ $cm^{-2}s^{-1}$	$Flux_{other}$ $cm^{-2}s^{-1}$	Time s
				$H_3CC\equiv CH$ hydrogenation			
1.0	$H_3CC\equiv CH$	10	2×10^{12}	-	-	-	21600
1.1	$H_3CC\equiv CH + H$	10	2×10^{12}	5×10^{12}	-	-	21600
1.2	$H_3CC\equiv CH + H$	10	7×10^{12}	5×10^{12}	-	-	7200
				$H_3CC\equiv CH$ and $O_2/^{18}O_2$ hydrogenation			
2.0	$H_3CC\equiv CH + H + O_2$	10	7×10^{12}	5×10^{12}	1×10^{12}	-	21600
2.1	$H_3CC\equiv CH + H + {}^{18}O_2$	10	7×10^{12}	5×10^{12}	1×10^{12}	-	21600
2.2	$H_3CC\equiv CH + H + O_2$	10	2×10^{12}	5×10^{12}	4×10^{12}	-	21600
2.3	$H_3CC\equiv CH + H + {}^{18}O_2$	10	2×10^{12}	5×10^{12}	4×10^{12}	-	21600
				Reference experiments			
3.0	n-propanol	10	-	-	-	3×10^{12}	3600
3.1	i-propanol	10	-	-	-	3×10^{12}	3600
3.2	i-propanol + H + O_2	10	-	5×10^{12}	1×10^{12}	2×10^{10}	7200
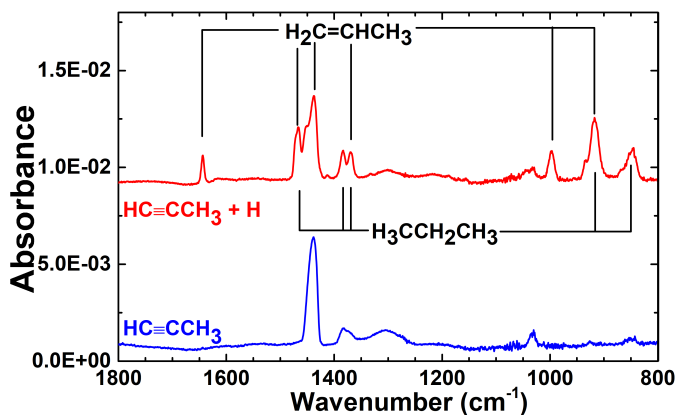
Figure 8.1: RAIR spectra acquired after deposition of HC≡CCH₃ (bottom spectrum; exp. 1.0) and HC≡CCH₃ + H (top spectrum; exp. 1.1) on a 10 K surface. The infrared peaks of newly formed H₃CCH=CH₂ and H₃CCH₂CH₃ are highlighted. RAIR spectra are offset for clarity.

frequencies. A transition structure is characterized by the Hessian bearing exactly one negative eigenvalue. To confirm that the found transition structure connects the desired reactant and product, an intrinsic reaction coordinate (IRC) search is conducted. From the end-point of the IRC, a re-optimization is performed to obtain the pre-reactive complex (PRC). All calculations are performed with DL-find (Kästner et al. 2009) within Chemshell (Sherwood et al. 2003; Metz et al. 2014). IRC searches are performed using the algorithm described by Meisner et al. (2017) and Hratchian & Schlegel (2004). Finally, for the reaction OH + H₃CCH=CH₂, transition states are only found through a nudged elastic band (NEB) approach.

All calculated energies include a zero-point energy (ZPE) correction that is listed separately. Note that these ZPE corrections can be quite sizable and are thus important to include due to their impact on the total activation energy. Finally, activation energies are calculated with respect to both separated reactants (SR) and the pre-reactive complex (PRC). Although the difference between these two approaches lies only in the considered starting point of the reaction, the effect on the activation energies again can be quite pronounced.

All calculations are performed in the gas-phase as we expect the influence of H_2O molecules in the neighborhood of unsaturated hydrocarbons to play a minor role in altering the reaction potential energy landscape (Kobayashi et al. 2017).

8.3 Experimental results and discussion

8.3.1 Hydrogenation of HC≡CCH₃

The formation of $H_3CCH=CH_2$ and $H_3CCH_2CH_3$ by the hydrogenation of $H_3CC≡CH$ at 10 K is visible from the RAIR data displayed in Figure 8.1 (upper panel), and

Table 8.3: The relevant normal vibrational modes detected in the $HC\equiv CCH_3$ + H (exp. 1.1) and $HC\equiv CCH_3$ + H + O_2 (exp. 2.0) experiments.

Peak position (cm^{-1})	Peak position (μm)	Molecule	Reference
851	11.75	$H_3CCH_2CH_3$	a, b
917	10.91	$H_3CCH=CH_2$ and $H_3CCH_2CH_3$	d; c, a, b
997	10.03	$H_3CCH=CH_2$	d
1030	9.71	$H_3CC\equiv CH$	this work
1370	7.30	$H_3CC\equiv CH$, $H_3CCH=CH_2$ and $H_3CCH_2CH_3$	this work; d; c, a, b
1384	7.23	$H_3CC\equiv CH$ and $H_3CCH_2CH_3$	this work; c, a, b
1439	6.95	$H_3CC\equiv CH$ and $H_3CCH=CH_2$	this work; d
1466	6.82	$H_3CCH=CH_2$ and $H_3CCH_2CH_3$	d; c, a, b
1644	6.08	$H_3CCH=CH_2$	d
1669	5.99	$H_3CCH=CHOH/H_3CCOH=CH_2$*	e

a(NIST) b(Comeford & Gould 1961) c(Ghosh et al. 2018) d(Abplanalp et al. 2018) e(Shaw et al. 2017)
* indicates tentative identification

the corresponding vibrational mode assignments are listed in Table 8.3. Despite the overlap of a number of vibrational bands between $H_3CCH=CH_2$ and $H_3CCH_2CH_3$, there are distinct peaks that are characteristic to these species and also do not overlap with the IR signatures of $H_3CC\equiv CH$. The C=C stretch of $H_3CCH=CH_2$ at 1644 cm^{-1} (Abplanalp et al. 2018) is conveniently isolated, and the C-C stretch of $H_3CCH_2CH_3$ at 851 cm^{-1} is clearly visible. The hydrogenation of $H_3CC\equiv CH$ to form $H_3CCH=CH_2$ and $H_3CCH_2CH_3$ parallels the hydrogenation of the two-carbon counterpart, acetylene (HCCH), which results in the formation of ethene ($H_2C=CH_2$) and ethane (H_3CCH_3) (Kobayashi et al. 2017).

TPD-QMS spectra provide additional proof for the newly formed $H_3CCH=CH_2$ and $H_3CCH_2CH_3$ from $H_3CC\equiv CH$ hydrogenation, and are presented in Figure 8.2. The m/z fragment values upon 70 eV electron impact ionization with the highest relative intensities for $H_3CCH=CH_2$ and $H_3CCH_2CH_3$ are 41 and 29, respectively (NIST). The desorption peak temperature of $H_3CCH_2CH_3$ from an amorphous solid H_2O surface is ~ 80 K (Smith et al. 2015), a peak that is also observed in Figure 8.2. Since $H_3CCH_2CH_3$ is composed of single bonds and $H_3CCH=CH_2$ has a double bond, $H_3CCH_2CH_3$ should have a lower desorption energy than $H_3CCH=CH_2$ (an effect of pi stacking) (Nykänen & Honkala 2011). Thus, the desorption at 81 K is assigned as the main desorption peak of $H_3CCH_2CH_3$, and the higher temperature signal at 86 K must be the main desorption peak of $H_3CCH=CH_2$. Additionally, it is observed that some $H_3CCH_2CH_3$ co-desorbs with $H_3CCH=CH_2$ at 86 K, which maybe due to the amorphous to crystalline phase transition of $H_3CC\equiv CH$, since m/z = 29 is not a fragment value of $H_3CCH=CH_2$ (or $H_3CC\equiv CH$), yet there is a desorption peak for m/z = 29 at 86 K. The desorption of the bulk of unreacted $H_3CC\equiv CH$ ice peaks around 104 K.

The abundance of $H_3CCH_2CH_3$ is measured to be 2-3 times greater than that of $H_3CCH=CH_2$. This infers that the hydrogenation of $H_3CCH=CH_2$ to form $H_3CCH_2CH_3$ is faster than hydrogenation of $HC\equiv CCH_3$ to yield $H_3CCH=CH_2$.
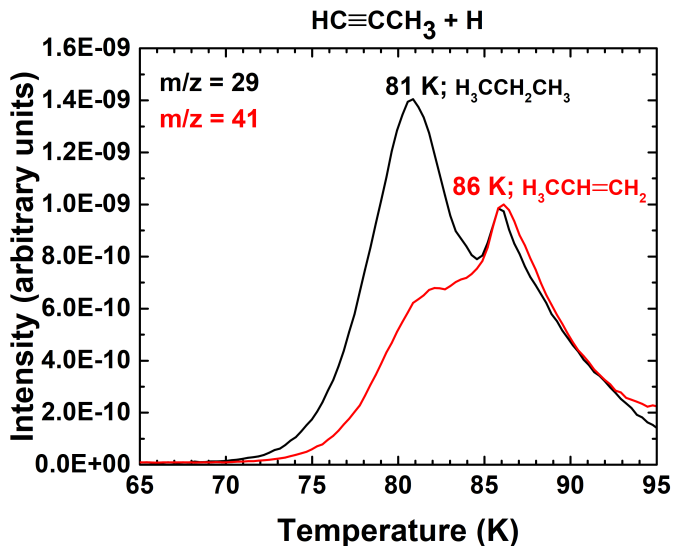
Figure 8.2: TPD-QMS fragment spectra acquired after deposition of HC≡CCH$_3$ + H (exp. 1.2) on a 10 K surface. The main desorption peaks of newly formed H$_3$CCH$_2$CH$_3$ and H$_3$CCH=CH$_2$ are shown at 81 and 86 K, respectively, by m/z = 29 (C$_2$H$_5^+$) and 41 (C$_3$H$_5^+$). A HC≡CCH$_3$:H$_3$CCH=CH$_2$:H$_3$CCH$_2$CH$_3$ abundance ratio of 9:1:2 is measured.

The work of Kobayashi et al. (2017) reported a similar result for the two-carbon equivalents, H$_2$C=CH$_2$ and H$_3$CCH$_3$, where the effective hydrogenation reaction rate constant was found to be ~ 3 times higher for H$_3$CCH$_3$ than for H$_2$C=CH$_2$.

8.3.2 Inclusion of OH into HC≡CCH$_3$ hydrogenation network

8.3.2.1 Experimental evidence of n- and i-propanol formation

As shown in Figure 8.1, the number of overlapping bands makes it difficult to discern between the RAIR features of H$_3$CCH=CH$_2$ and H$_3$CCH$_2$CH$_3$, with only two distinct bands apparent. The RAIR spectra become even more convoluted when O$_2$ is added to the mixture. Figure 8.3 displays the RAIR spectrum of H$_3$CC≡CH + H + O$_2$, in addition to four control RAIR spectra, to attempt characterization of the infrared bands in exp. 2.0. Spectra of n- and i-propanol are compared as they are expected products from the H$_3$CC≡CH + H + O$_2$ experiment, and are also commercially available and feasible for UHV conditions. Comparison of the n- and i-propanol spectra to the HC≡CCH$_3$ + H spectrum shows that many of the RAIR features overlap with each other. Additionally, some bands that arise in the H$_3$CC≡CH + H + O$_2$ experiments are difficult to identify (asterisked in Figure 8.3) as expected, since the hydrogenation of a three-carbon species with O$_2$ is a relatively complex molecular reaction. Thus, the overlapping infrared signals belonging to identified and unidentified molecules make it complicated to track the formation of n- and i-propanol in

the infrared at 10 K or even in temperature-dependent RAIR spectra. As discussed in Ioppolo et al. (2014), the formation of complex organic molecules at low temperatures can alternatively be shown by TPD-QMS experiments.
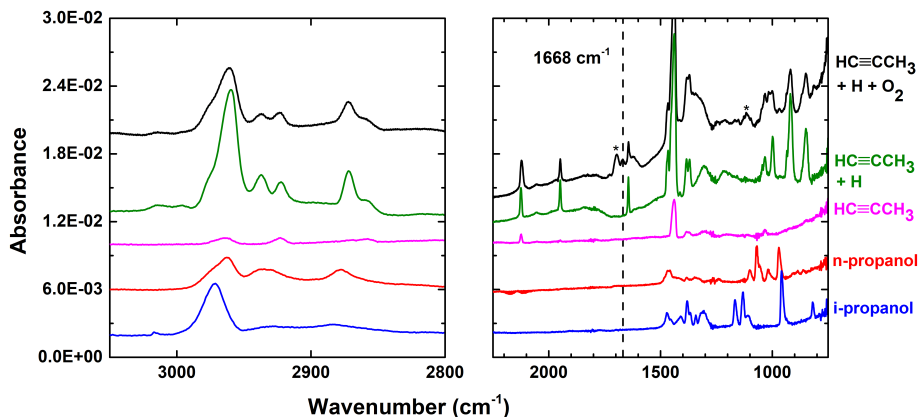

Figure 8.3: (Top to bottom) RAIR spectra acquired after deposition of HC≡CCH$_3$ + H + O$_2$ (exp. 2.0; column density of 1×10^{16} cm^{-2}), HC≡CCH$_3$ + H (exp. 1.1), HC≡CCH$_3$ (exp. 1.0), n-propanol (exp. 3.0; column density of 1×10^{16} cm^{-2}), and i-propanol (exp. 3.1; column density of 1×10^{16} cm^{-2}) on a 10 K surface. * indicates peaks that are unidentified, and the band highlighted with a dashed line in the top spectrum is likely due to n- or i-propenol. These are further discussed in Section 8.3.2.2. RAIR spectra are offset for clarity.

Figure 8.4 shows the desorption of newly formed n- and i-propanol (and their isotopic counterparts) in two different isotope experiments, where an average abundance ratio of 1:1 for n-propanol:i-propanol is measured. In the H$_3$CC≡CH + H + O$_2$ experiment, the m/z values with the highest intensities for n- and i-propanol are 31 and 45, respectively. Other fragments, such as m/z = 60 and 46, are also shown. In the H$_3$CC≡CH + H + ^{18}O$_2$ experiment, the m/z values bump up to 33 and 47, respectively, due to isotopically enhanced oxygen. The fragmentation patterns that represent the desorptions of n- and i-propanol are shown in Figure 8.5. For the desorption of n-propanol at 163 K, the measured relative intensities are 100:2 for m/z = 31:60, 100:3 for m/z = 33:62, and 100:2 for m/z = 31:60. Concerning the desorption of formed i-propanol at 160 K, the relative intensities are also consistent, with ratios of 100:3 for m/z = 45:46, 47:48, and 45:46. The consistency of the relative intensities found between the isotope experiments, and well as between the isotope experiments and the pure n- and i-propanol experiments, further supports the confirmation of solid-state formation of both propanols.

The desorption temperature acts as a further diagnostic, in that the desorption temperature of certain species can shift when they are trapped by relatively less volatile species (Collings et al. 2004). An example of this is demonstrated in the Supporting Information Figure S1, where the peak desorption of pure i-propanol is seen at 150 K, and shifts to 160 K upon addition of H and O$_2$, which
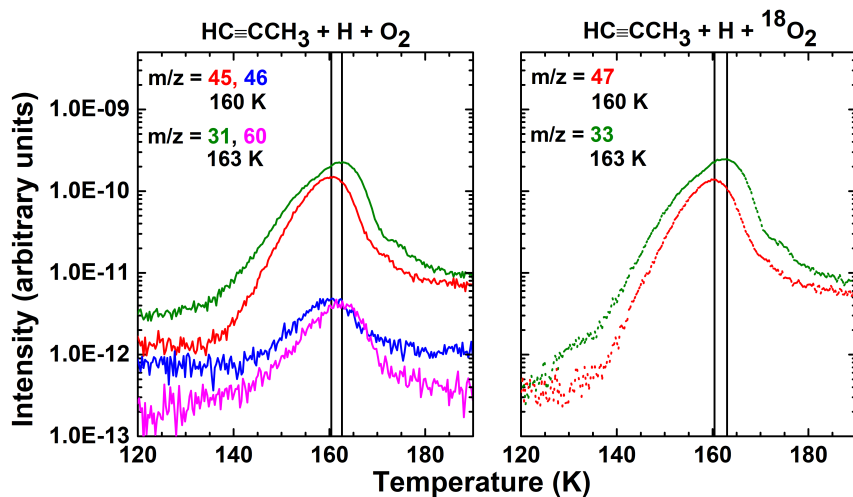
Figure 8.4: TPD-QMS fragment spectra acquired after deposition of $HC\equiv CCH_3$ + H + O_2 (left; exp. 2.0) and $HC\equiv CCH_3$ + H + $^{18}O_2$ (right; exp. 2.1) on a 10 K surface. The desorption peaks of newly formed i-propanol and n-propanol are shown at 160 and 163 K, respectively. An n-propanol:i-propanol average abundance ratio of 1:1 is measured.

is the desorption temperature observed for newly formed i-propanol shown in Figure 8.4.

8.3.2.2 Tentative experimental evidence of the formation of other oxygen-bearing COMs: n- and i-propenol

The $H_3CC\equiv CH$ + H + O_2 experiment is expected to generate a variety of COMs that unfortunately not only pushes the limits of the TPD-QMS technique in unambiguously distinguishing the different products formed, but also yields species that are not commercially available for control purposes or are challenging to use in a UHV setup. Example reaction products are n- and i-propenol, which are not commercially available as they undergo keto-enol tautomerism at room temperature to primarily form propanal and acetone, respectively (Shaw et al. 2017). However at lower temperatures, the enol form becomes more stabilized (Burdett & Rogers 1966), thus n- and i-propenol ices can be present under the applied experimental conditions following addition of OH to the triple bond of $H_3CC\equiv CH$. Tentative identifications in the RAIR and TPD-QMS data are discussed below. Note that although there is partial evidence for n- and i-propenol formation from the experimental data, the inclusion of computationally-derived results confirms their presence in the experiments, and is discussed in a later section.

The dashed line in Figure 8.3 shows the potential identification of n- or i-propenol marked at 1668 cm^{-1} in the $H_3CC\equiv CH$ + H + O_2 experiment. This feature is a likely candidate for the C=C stretching mode of propenols. This peak does not overlap with infrared signatures in the $H_3CC\equiv CH$ + H, $H_3CC\equiv CH$, n- or i-propanol experiments, meaning it does not represent a product or reactant
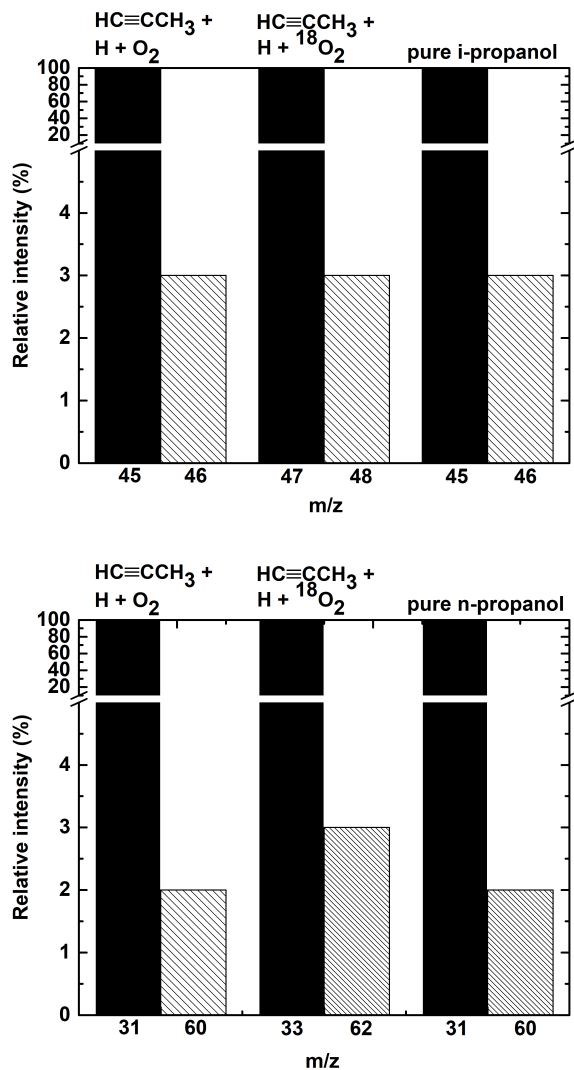
Figure 8.5: QMS fragmentation pattern of two m/z values that are normalized to the QMS signal of the $CHOHCH_3^+$ ion (top) and CH_2OH^+ ion (bottom) found in the $HC\equiv CCH_3 + H + O_2$ (exp. 2.0), $HC\equiv CCH_3 + H + {}^{18}O_2$ (exp. 2.1), and pure i- and n-propanol experiments (exps. 3.0 and 3.1 respectively) for a temperature of 160 K (top) and 163 K (bottom).

from those experiments. It also does not red-shift in the $H_3CC\equiv CH$ + H + $^{18}O_2$ experiment (not shown here), therefore the correlated functional group does not include oxygen. As shown in Shaw et al. (2017), n- and i-propenol have strong absorptions for the C=C stretch at 1684 cm^{-1} and 1678 cm^{-1}, respectively. Our value of 1668 cm^{-1} is expected, as solid-state infrared frequencies can be red-shifted from that of the gas-phase due to the ice matrix (e.g., CO_2) (Isokoski et al. 2013). The C=C stretching mode is also one of the strongest bands of propenol (Shaw et al. 2017), and thus has the highest probability to be visible in our data. The other propenol vibrational modes with relatively high band strengths (i.e., the COH bend at $\sim$ 1100 cm^{-1} and OH stretch at $\sim$ 3600 cm^{-1}) (Shaw et al. 2017) unfortunately overlap with modes of multiple products in the $H_3CC\equiv CH$ + H + O_2 experiment. As a direct consequence, an unambiguous identification of propenol in the RAIR data is currently not possible.

For TPD-QMS, since electron impact ionization fragmentation patterns of n- and i-propenol are not available, simple assumptions have to be used to theoretically derive the possible fragment m/z values. With an electron energy of 70 eV, single bonds can easily break upon dissociative ionization. For both propenols, this results in species with m/z pairs of 43 ($C_2H_2OH^+$) and 15 (CH_3^+), and 41 ($C_3H_5^+$) and 17 (OH^+). n- and i-propenol can also remain intact (non-dissociative ionization), which will result in a m/z = 58 signal. Removal of an H-atom from the O/C-atom of propenol results in a signal for m/z = 57. In the $H_3CC\equiv CH$ + H + $^{18}O_2$ experiment, these values bump up to 45 and 15; 41 and 19; 60; and 59; respectively. The signals for some of these m/z values are shown in Figure 8.6. Two desorption peaks are displayed with peak desorption temperatures of around $\sim$ 153 and $\sim$ 159 K in the regular and isotopically-enhanced experiments, which is in the range for which the desorption of propenols is expected. From our estimated propenol fragment results, it is not possible to conclude which desorption peak corresponds to which propenol desorption. It should be stressed that no positive identification for the tautomers, propanal and acetone, could be found at their corresponding desorption temperatures of 125 K (Qasim et al. 2019) and 133 K (Schaff & Roberts 1998), respectively. The signal of m/z = 43 from $\sim$ 130 - 170 K has some overlap with the signals of m/z = 57 and 58, and appears to contain other oxygen containing COMs due to its broad and bumpy desorption profile. Like that of n- and i-propanol, the desorption temperatures of tentatively assigned n- and i-propenol are not that far apart. However, the difference in desorption temperature between isomers also varies depending on the isomers involved. The peak desorption temperatures of around $\sim$ 153 and $\sim$ 159 K shown in Figure 8.6 are within the range of n-propenol desorption of 146 - 185 K (Abplanalp et al. 2016), and are also between the peak desorption temperatures of propanal (125 K) (Qasim et al. 2019) and n-propanol (160 K). This is expected when comparing the desorption temperature trend to that of the two-carbon counterparts, acetaldehyde (H_3CCHO), vinyl alcohol (H_2CCHOH), and ethanol (H_3CCH_2OH), which have peak desorption temperatures of 131 K, 146 K, and 164 K, respectively (Chuang et al. in prep). Yet, without mass spectra and information on the desorption temperatures and profiles of pure n- and i-propenol, the formation of both species in the $H_3CC\equiv CH$ + H + O_2 experiment can only be concluded as tentative.
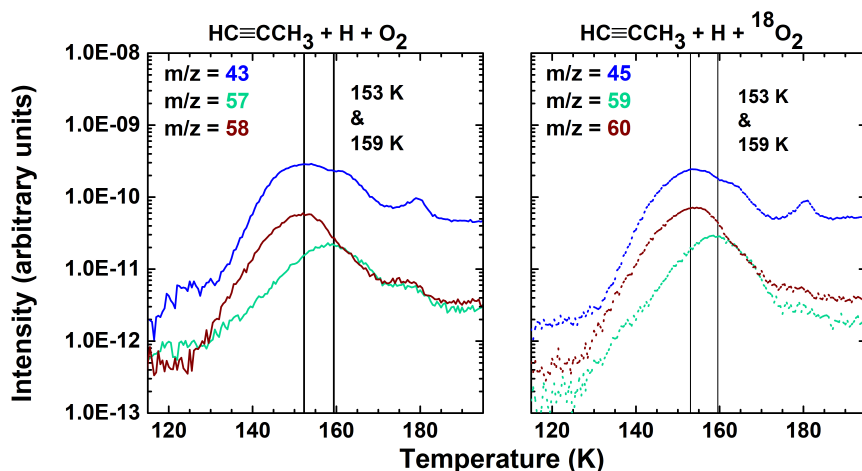
Figure 8.6: TPD-QMS fragment spectra acquired after deposition of HC≡CCH₃ + H + O₂ (left; exp. 2.2) and HC≡CCH₃ + H + ¹⁸O₂ (right; exp. 2.3) on a 10 K surface. n- and i-propenol are tentatively identified. It cannot be distinguished which of the two propenol isomers desorbs at 153 K and which desorbs at 159 K. The desorption features at ∼ 180 K are due to the co-desorption of both species with H_2O_2 (an abundant product of H + O₂), where both species were trapped in the H_2O_2 bulk ice.

8.3.2.3 Tentative experimental evidence of the formation of other oxygen-bearing COMs: three isomers of propanediol

The hydroxylation of n- and i-propenol can lead to the formation of COMs with two oxygens, such as propane-1,1-diol, propane-2,2-diol, and propane-1,2-diol. However, study of the pure samples is difficult due to their chemical instability and low vapor pressure under standard temperature and pressure conditions. Particularly, propane-1,1-diol and propane-2,2-diols are very unstable, and are therefore not commercially available. Upon desorption into the gas-phase, the geminal-diol equilibrium of propane-1,1-diol and propane-2,2-diol shifts greatly towards formation of the spontaneous decomposition products, propanal with H_2O and acetone with H_2O, respectively (Dewick 2006). Such chemical transformations can be used to tag the formation of propanediol isomers. If the geminal diols are formed in the solid-state, then upon their desorption into the gas-phase following spontaneous decomposition, QMS signatures of propanal, acetone, and H_2O would be observed at their non-characteristic desorption temperature of around 200 K, where propanal and acetone have characteristic peak desorption temperatures of 125 K (Qasim et al. 2019) and 133 K (Schaff & Roberts 1998), respectively. As shown in Figure 8.7, m/z = 43, 29, 31 and 45 represent the main m/z signals of acetone, propanal, and propane-1,2-diol, respectively, according to the NIST database. The peak intensity of these values is found around ∼ 207 K, which is in-line with the temperature of 203 K that was tentatively assigned for propane-1,2-diol and propane-1,3-diol desorption (Maity et al. 2015). The expected m/z shifts are also found in the H₃CC≡CH + H + ¹⁸O₂ experiment, as shown in the right panel of Figure 8.7. Yet, without confirmation of the desorption temperatures,

decomposition products, and fragmentation patterns of the pure samples, only a tentative identification of the isomers of propanediol is reported here.
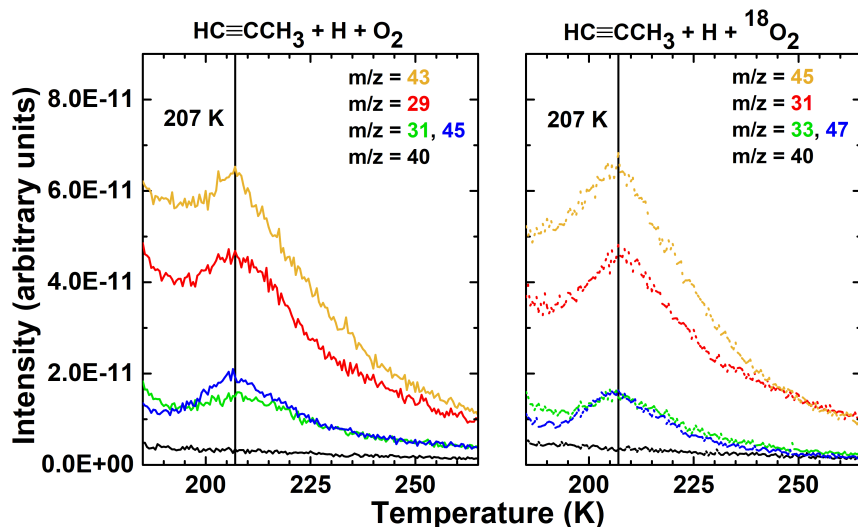

Figure 8.7: TPD-QMS fragment spectra acquired after deposition of HC≡CCH$_3$ + H + O$_2$ (left; exp. 2.2) and HC≡CCH$_3$ + H + ^{18}O$_2$ (right; exp. 2.3) on a 10 K surface. Tentatively identified peaks of propane-1,1-diol decomposition product (propanal; m/z = 31, 45), propane-2,2-diol decomposition product (acetone; m/z = 43), and propane-1,2-diol (m/z = 31, 45) are shown. "Blank" refers to the m/z value that does not have a peak desorption in the illustrated temperature range.

We summarize all the experimental results presented here. As shown in Section 8.3.1, H$_3$CCH=CH$_2$ and H$_3$CCH$_2$CH$_3$ are experimentally confirmed to form from the hydrogenation of H$_3$CC≡CH, with an abundance ratio of HC≡CCH$_3$:H$_3$CCH=CH$_2$:H$_3$CCH$_2$CH$_3$ 9:1:2. In Section 8.3.2, it is shown that inclusion of OH leads to the formation of n- and i-propanol, and the average abundance ratio of n-propanol:i-propanol is 1:1. Tentative detections of n- and i-propenol, propane-1,1-diol, propane-2,2-diol, and propane-1,2-diol are found. The tautomers of n-propenol (propanal) and i-propenol (acetone), as well as the acidic derivative propanoic acid, are not detected.

8.4 Energies and formation mechanisms

The experimental findings are joined by computationally derived energy barriers to draw the exact products formed and the correlated formation mechanisms. Computationally derived energies for eight different reactions that occur in the experiments are found in Table 8.4. The first column of the table lists three types of energies studied: interaction, activation, and reaction. The interaction energy is the energy gained when the pre-reactive complex (PRC) is formed. This complex is formed when the two reactants have enough time or energy to rearrange themselves in the ice before product formation. This is

Table 8.4: Interaction, activation, and reaction energies for $H_3CC\equiv CH + OH$, $H_3CCH=CH_2 + OH$, $H_3CC\equiv CH + H$, and $H_3CCH=CH_2 + H$ calculated at the MPWB1K/def2-TZVP level of theory. E and I refer to the exterior and interior carbon, respectively. SR and PRC refer to the separated reactants and pre-reactive complex, respectively. All values are in units of Kelvin.

Energy type	E or I carbon	SR or PRC	Total
$HC\equiv CCH_3 + OH$			
Activation	I	SR	636
Activation	E	SR	380
Activation	I	PRC	1387
Activation	E	PRC	1762
$H_2C=CHCH_3 + OH$			
Activation	I	SR	-691
Activation	E	SR	-671
Activation	I	PRC	47
Activation	E	PRC	221
$HC\equiv CCH_3 + H$			
Activation	I	SR	2866
Activation	E	SR	1742
Activation	I	PRC	2634
Activation	E	PRC	1591
$H_2C=CHCH_3 + H$			
Activation	I	SR	2136
Activation	E	SR	1109
Activation	I	PRC	1960
Activation	E	PRC	991

opposite to the situation of the separated reactants (SR), where the reactants immediately react to form the end product. The activation energy is with respect to both SR and with respect to the PRC, and the difference between these two values is equal to the interaction energy of the PRC. Finally, the reaction energy is defined by the exothermicity.

The main findings from Table 8.4 are discussed as follows. Comparing the reactivity towards H and OH, in all but one case the reaction of an unsaturated species with an OH radical is more favorable than with an H atom. However, it is important to keep in mind that the reaction with OH results in the formation of a C-O bond. This, contrary to the formation of a C-H bond, is not accelerated much by taking tunneling into account at low temeprature. Furthermore, in accordance with results from Kobayashi et al. (2017) and Zaverkin et al. (2018), we find that reaction with a double-bonded (C=C) species is easier than with a triple-bonded (C≡C) molecule. It is also confirmed that the exterior carbon is more reactive towards H than the interior carbon.

Whether the reactions proceed with or without a PRC is evaluated from the results from Table 8.4. When the activation energies for the reactions, $H_3CC\equiv CH$ + OH and $H_3CCH=CH_2$ + OH (where OH is derived from H + O_2 in the experiments), are considered with respect to the separated reactants, it is obvious that the reactions should be able to take place very easily as the reaction is either barrierless ($H_3CCH=CH_2$ + OH) or has a relatively low activation energy ($H_3CC\equiv CH$ + OH, 380 or 636 K). However, when the two reactants form a PRC, it is expected that the excess energy of the complex formation is dissipated into the ice mantle well before the reaction itself is attempted, as the energy dissipation in ices seems to take place on a picosecond timescale (Arasa et al. 2010; Fredon et al. 2017). Therefore, the effective activation energy to be overcome increases by the same amount of energy that is gained from the interaction of OH with $H_3CC\equiv CH$/$H_3CCH=CH_2$ (i.e., the interaction energy is added to determine the total activation energy). This significantly increases the activation energy, although for the reaction with $H_3CCH=CH_2$, it remains close to barrierless. Which of the two surface 'mechanisms' is the best description for these reactions in an ice (be it in the laboratory or in the interstellar medium) can be debated and it is quite likely that a variety of geometries exist that may lead to an averaged-out effect. For example, if OH is a neighboring species to $H_3CC\equiv CH$/$H_3CCH=CH_2$, the immediate surroundings may cause steric hindrance between the two species, and therefore mitigate a favorable orientation of the two species with respect to each other. On the other hand, OH could potentially use its excess energy to rearrange the position and thus obtain a more favorable orientation. Note that for the reaction of H with any molecule, the low diffusion barrier of the H-atom always allows for a mechanism that considers the PRC to take place. Therefore, the effect of the relative geometries on the reaction efficiency is less pronounced for species that have low diffusion barriers or high activation barriers.

The likelihood of constitutional isomerization (or tautomerization) for products formed in the experiments is assessed from the computationally-derived results in Table 8.5. From the results, it is immediately clear that direct isomerization reactions cannot take place efficiently in ices in cold interstellar clouds, as the typical activation energy is more than 25,000 K. If the reaction were to be actively catalyzed by another molecule that can simultaneously donate and accept an H-atom, such as H_2O or the OH-group of CH_3OH, the activation energy may drop considerably (Vöhringer-Martinez et al. 2007; Rimola et al. 2018). The value could then drop close to the values involved for H-hopping from an OH group to an OH radical, which is > 1800 K for the reaction CH_3OH + OH (Xu & Lin 2007), and between 2500 - 9000 K for the reaction OH + $(H_2O)_n$ (n = 1-3) (Gonzalez et al. 2011). This can only happen, however, if a suitable multi-species geometry can be established in the ice (i.e., if solvation is present).

The products formed and their formation mechanisms are finally discussed below. It is apparent from Table 8.4 that the activation barriers of $H_3CC\equiv CH$ + OH are primarily lower than that of $H_3CC\equiv CH$ + H and by a substantial amount. This is even more pronounced when comparing the activation barriers of $H_3CCH=CH_2$ + OH and $H_3CCH=CH_2$ + H. The formation of propanols in the experiments indicates that OH-addition is relatively efficient under our experimental conditions. However, H-atoms are more mobile and can effectively

Table 8.5: Activation barriers of the isomerization reactions of n- and i-propenol. All values are in units of Kelvin.

Reaction	PES	ZPE	Total
Acetone $\rightarrow$ i-propenol	34452	-1692	32760
i-propenol $\rightarrow$ acetone	28686	-2116	26569
Propanal $\rightarrow$ n-propenol	35132	-1892	33240
n-propenol $\rightarrow$ propanal	31209	-2100	29109

tunnel at low temperatures, making H-addition competitive to OH-addition. Therefore, from the combination of computationally-derived activation barriers and the unambiguous identification of propanol formation, it is found that $H_3CC\equiv CH$ is effectively attacked by OH radicals more so than by H-atoms only when both species neighbor $H_3CC\equiv CH$, and when OH is oriented in a favorable position for reaction. According to Table 8.4, this narrows the selection of activation energies to four values: 636 and 1387 K (OH attack on the interior carbon) and 380 and 1762 K (OH attack on the exterior carbon). The experimental results give an n-propanol:i-propanol average abundance ratio of 1:1, depending on which m/z values are used to determine the relative abundance. Therefore, it is likely that both species are formed with comparable abundances (i.e., attack to the exterior and interior carbons occurs equally under our experimental conditions). Moreover, this conclusion is fully in-line with the idea that for reactants that can strongly interact with each other, the efficiency of both 'mechanisms' is influenced by the geometric orientation of the formed OH radical with respect to the $H_3CC\equiv CH$ molecule (i.e., both 'mechanisms' are actively participating). If this was not the case, then it is expected that n-propanol would be distinctly more abundant in the experiments, as the lowest activation barrier of 380 K would favor n-propanol formation. The outcome of the experimental and theoretical results pieced together leads to the formation mechanisms that are most likely occurring in the $H_3CC\equiv CH$ + H + O_2 experiment, which are illustrated in Figure 8.8. The activation barriers for some of the displayed reaction steps are listed in Table 8.4. As shown, the formation pathways of n- and i-propanol include the formation of n- and i-propenol. Thus, n- and i-propenol are products formed in our experiments. Since the activation barriers of OH-addition to propenols are not investigated in this work, the propanediol isomers remain to be tentative reaction products, as noted in Figure 8.8. For the $H_3CC\equiv CH$ + H experiment, the relatively high barriers show that $H_3CC\equiv CH$ and H do not have a strong interaction with each other as that of $H_3CC\equiv CH$ and OH. Therefore, the geometric orientation of the two species has less of an effect on which 'mechanism' would proceed. H-attack on the exterior carbon of $H_3CC\equiv CH$ and $H_3CCH=CH_2$ results in the lower activation barrier in comparison to H-attack on the interior carbon, and thus is proposed to be the more likely scenario involved in $H_3CCH=CH_2$ and $H_3CCH_2CH_3$ formation.

Formation of propene ($H_2C=CHCH_3$) and propane ($H_3CCH_2CH_3$)

$H_3CC{\equiv}CH$
↓ H
$H_3CC=CH_2$
↓ H
$\boxed{H_3CCH=CH_2}$
↓ H
H_3CCHCH_3
↓ H
$\boxed{H_3CCH_2CH_3}$

Formation of n-propenol ($H_3CCH=CHOH$) and n-propanol ($H_3CCH_2CH_2OH$)

$H_3CC{\equiv}CH$
↓ OH
$H_3CC=CHOH$
↓ H
$\boxed{H_3CCH=CHOH}$
↓ H
$H_3CCHCH_2OH/$
H_3CCH_2CHOH
↓ H
$\boxed{H_3CCH_2CH_2OH}$

Formation of i-propenol ($H_3CCOH=CH_2$) and i-propanol ($H_3CCHOHCH_3$)

$H_3CC{\equiv}CH$
↓ OH
$H_3CCOH=CH$
↓ H
$\boxed{H_3CCOH=CH_2}$
↓ H
$H_3CCHOHCH_2/$
$H_3CCOHCH_3$
↓ H
$\boxed{H_3CCHOHCH_3}$

Formation of propane-1,1-diol ($H_3CCH_2CH(OH)_2$), propane-2,2-diol ($H_3CC(OH)_2CH_3$), and propane-1,2-diol ($H_3CCHOHCH_2OH$)

$H_3CC{\equiv}CH$
↓ OH
$H_3CC=CHOH/H_3CCOH=CH$
↓ H
$\boxed{H_3CCH=CHOH/H_3CCOH=CH_2}$
↓ OH   ↓ OH
$H_3CCHCH(OH)_2/$ $H_3CC(OH)_2CH_2/$
$H_3CCHOHCHOH$ $H_3CCOHCH_2OH$
↓ H   ↓ H
$H_3CCH_2CH(OH)_2/$ $H_3CC(OH)_2CH_3/$
$H_3CCHOHCH_2OH$ $H_3CCHOHCH_2OH$

Figure 8.8: Proposed mechanisms for exps. 2.0 and 2.2. Relevant species within each mechanism are boxed. Species labeled with green font are those that have been detected in space. Dotted-boxes indicate tentatively identified species in this study.

8.5 Astrochemical and astrobiological implications

The formation of three-carbon chains, alcohols, and to an extent, geminal diols, from $H_3CC{\equiv}CH$ + H/OH at the low temperature of 10 K can take place at the interface of carbonaceous grains and H_2O-rich ice in the cold cloud stage of stellar formation. At an $A_V < 1.5$, H_2O is just starting to coat interstellar grains partially by the accretion of H and O atoms (Boogert et al. 2015). These atoms combine on the grain surface to form OH radicals and have the potential to react with the carbon-rich constituents that are at the surface of the dust grain. As the visual extinction grows to 3, a H_2O-rich ice is formed on top of the mineral-ice interface. The icy grain is further coated by other molecules (e.g., CO) as it travels through various molecular freeze-out stages (Boogert et al. 2015).

The formation of n- and i-propanol and propenol shown in this combined experimental and theoretical study brings to light possible formation pathways for these species in astrochemical environments. Particularly, the formation of solid-state i-propanol and propenol is intriguing, as there are no experimentally-based studies on these molecules to our knowledge. It has been shown by Qasim et al. (2019) and Abplanalp et al. (2016) that n-propanol and propenol can be formed in a CO-rich ice, respectively. For the first time experimentally, it is shown here that all four alcohols can be formed before the heavy CO freeze-out stage (i.e., in the H_2O-rich ice phase) and along the same formation route. Thus, astronomical surveys may be able to identify all four species simultaneously.

This route can be extrapolated to polyynes containing H_3C-$(C{\equiv}C)_n$-H structures and therefore have an astrobiological context. As a $H_3CC{\equiv}CH$-containing ice yields n-propanol, similarly ices with H_3C-$(C{\equiv}C)_n$-H structures can lead to the formation of fatty alcohols (i.e., long-chain alcohols), which are found to

be constituents of simple lipids. For example, the incorporation of dodecanol to form primitive-like lipid bilayer membranes has been shown (Hargreaves & Deamer 1978). Moreover waxes, which are simple lipids, are composed of fatty alcohols which fatty acids are attached to. This includes the wax spermaceti, which contains hexadecan-1-ol ($H_3C(CH_2)_{14}CH_2OH$), and beeswax and carnuba, which both contain triacontan-1-ol ($H_3C(CH_2)_{28}CH_2OH$) (Alamgir 2018).

The hydroxylation of polyynes discussed in our study provides a valid mechanism for the formation of various linear alcohols starting from carbon chains. Such alcohols maybe present in the bottom layer (layer closest to the grain surface) of H_2O-rich interstellar ices. Such layering is advantageous to the preservation of such interface reaction products, in that bulk H_2O-ice can partially block UV-light (Gerakines et al. 2000; Cottin et al. 2003). From there, the possibility increases for such prebiotic material to be safely transferred to the early Earth and contribute to the formation of primitive cell membranes.

8.6 Conclusions

This combined experimental and computational study provides insights into what and how solid-state alcohols may be formed in the H_2O-rich ice phase of cold molecular cores. The main conclusions from the conjoined results are highlighted below:

- ◆ $H_3CC{\equiv}CH$ (propyne) + H forms $H_3CCH{=}CH_2$ (propene) and $H_3CCH_2CH_3$ (propane) efficiently, where the abundance ratio of the three species is 9:1:2, respectively. The experimental result is in-line with the computational results, in that the barrier to hydrogenate C=C is lower than to hydrogenate C≡C.

- ◆ The experimental investigation shows that $H_3CC{\equiv}CH$ + OH leads to the formation of n- and i-propanol at 10 K under 'non-energetic' (without UV, cosmic rays, etc. and/or other 'energetic' particles) conditions. The formation of n- and i-propenol in our experiments is confirmed from the combination of the experimental and theoretical results. Tentative identifications of propane-1,1-diol, propane-2,2-diol, and propane-1,2-diol are found from the experimental data.

- ◆ The formation yield of n-propanol (and thus n-propenol) in the experiments is observed to be comparable to that of i-propanol (and thus i-propenol), with an experimentally-measured n-propanol:i-propanol average abundance ratio of 1:1. This value is in-line with the computational calculations and the finding that both 'mechanisms' (PRC and SR) are equally influential due to the prominent role of how $H_3CC{\equiv}CH$ and OH are oriented towards each other.

- ◆ OH-addition to $H_3CC{\equiv}CH$ is observed to be more effective than H-addition when both radicals are in close vicinity to $H_3CC{\equiv}CH$, and when the OH radical is situated in a favorable orientation for reaction. This is supported by the relatively low computationally-derived activation barriers of $H_3CC{\equiv}CH$ + OH and the formation of propanols in the experiments.

◆ Propanols and propenols, and to an extent propanediols, are expected to form simultaneously in suitable ISM regions and may have an icy origin at the very beginning of interstellar clouds.

◆ The presented formation routes may be extended to polyynes with H_3C-$(C\equiv C)_n$-H structures. These structures can transform into fatty alcohols, which are the components of simple lipids which primitive cell membranes, were likely, in part, assembled by.
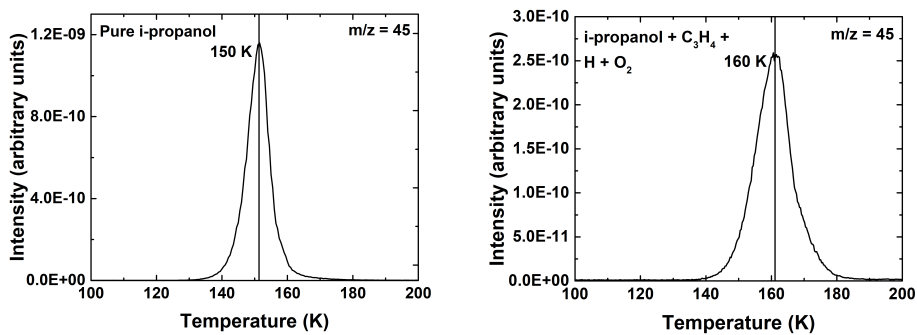
S1 Additional TPD-QMS spectra

Figure S1: TPD-QMS fragment spectra acquired after deposition of i-propanol (top; exp. 3.1) and i-propanol + H + O_2 (bottom; exp. 3.2) on a 10 K surface. Note the 10 K shift of the main desorption peak of i-propanol between the two experiments.

S2 Pathways and benchmark calculations

S2.1 IRC paths

For the reaction $H_3CC\equiv CH$ + OH, we perform IRC calculations to confirm that the found transition state structures connect the relevant pre-reactive complex and desired product. The resulting paths are presented in Figures S2 and S3. The pre-reactive complex energy is set to zero, acting as the reference value for the energy.

Examining Figure S3, it also becomes clear why the activation energy for the reaction $H_3CC\equiv CH$ + OH on the exterior carbon atom has such a high activation energy in comparison to that at the center carbon. This is because there is an extra rotation of the OH radical involved in order to reach the transition state structure. In other words, this only plays a role for a starting geometry where the OH and $H_3CC\equiv CH$ are fully relaxed.

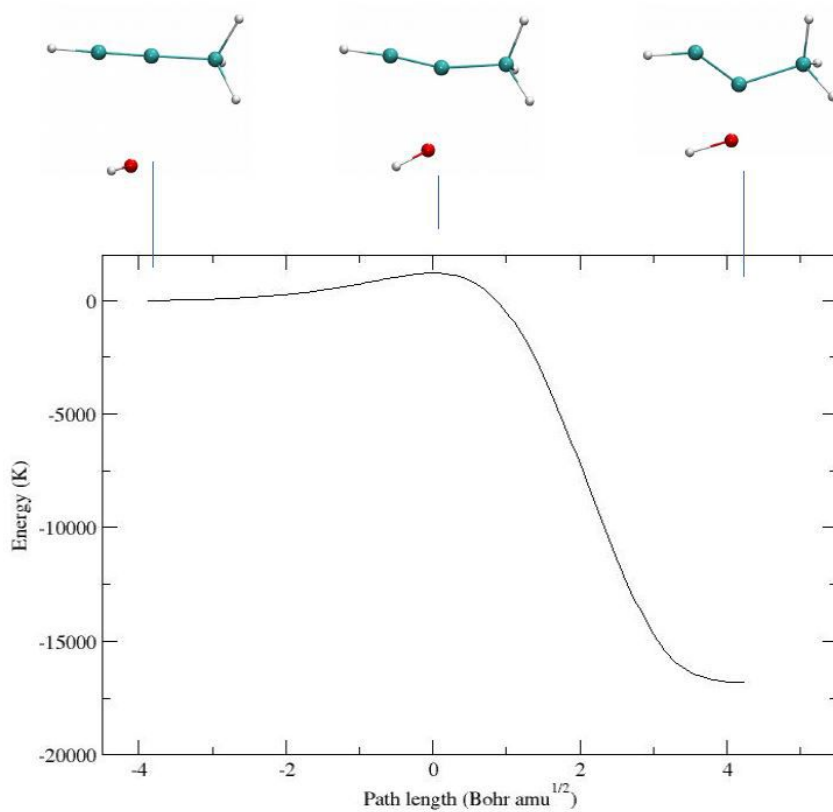Figure S2: Intrinsic reaction coordinate path for the reaction $H_3CC\equiv CH$ + OH on the centered carbon atom. The geometries corresponding to the pre-reactive complex, transition state, and product are displayed above.

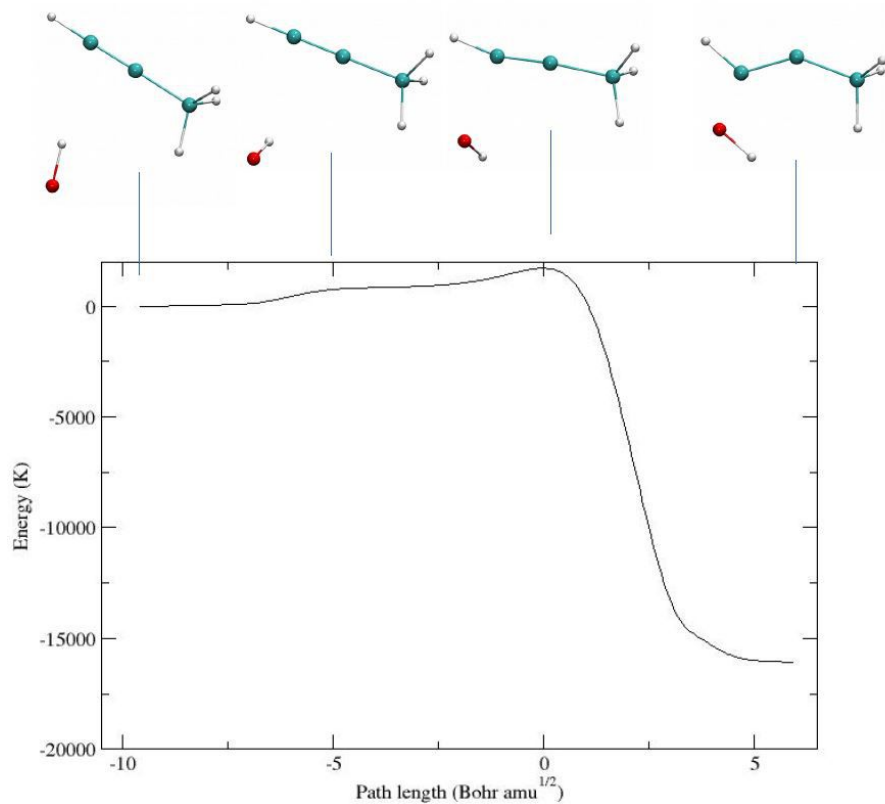Figure S3: Intrinsic reaction coordinate path for the reaction H$_3$CC≡CH + OH on the exterior carbon atom. The geometries corresponding to the pre-reactive complex, an intermediate state, the transition state, and product are displayed above.

S2.2 NEB paths
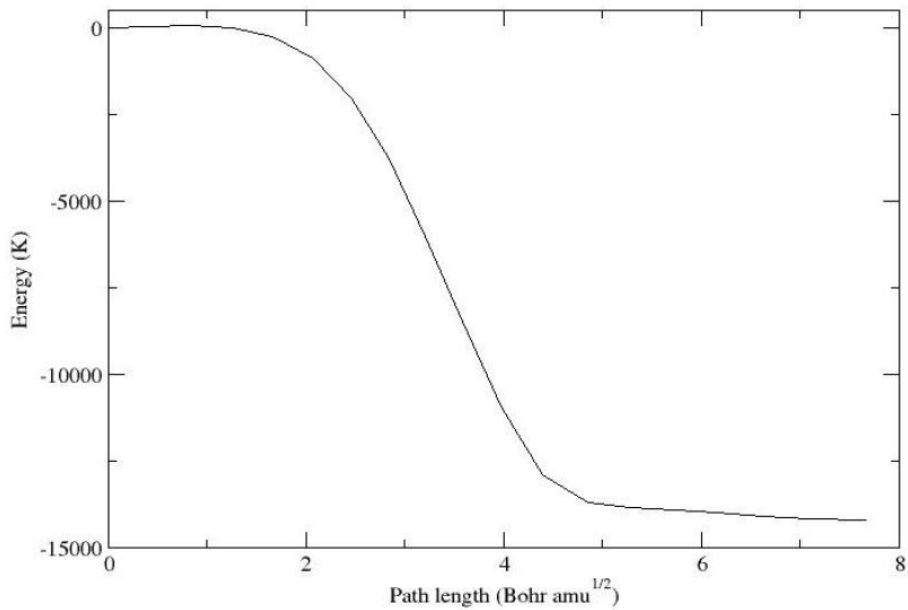
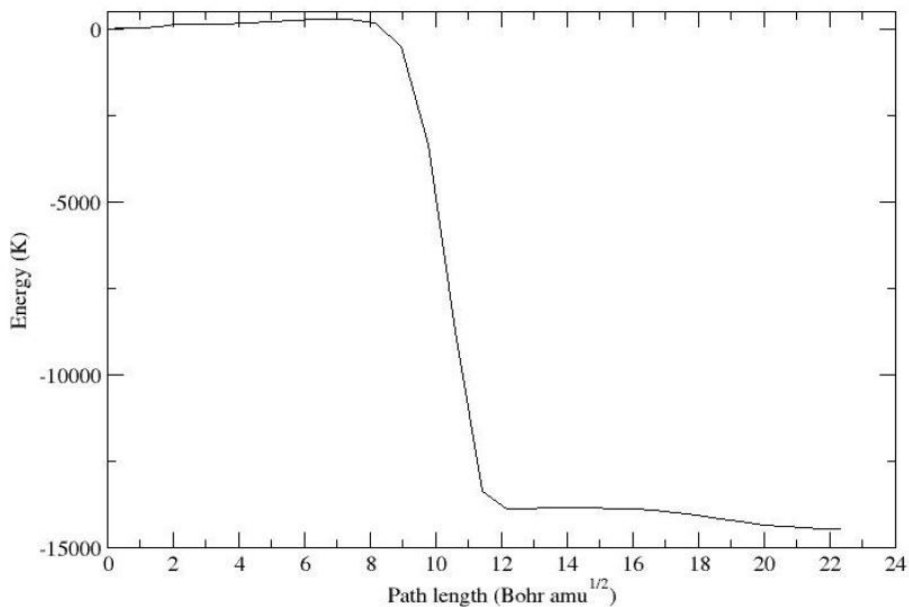Figure S4: Nudged-elastic band path for the reaction $H_3CCH=CH_2 + OH$ on the centered carbon atom.

Figure S5: Nudged-elastic band path for the reaction $H_3CCH{=}CH_2$ + OH on the exterior carbon atom.

S2.3 M06-2X validity check

In order to test if the use of the MPWB1K is valid, the activation energies have been recalculated with the M06-2X functional with the same basis set (def2-TZVP). This is a functional very commonly used for these types of reactions as well and is thought to be able to reasonably describe the reaction paths. Indeed, it is shown in Table S1 that the activation energies that are responsible for determining the reactivity differ by at most 240 K, indicating a proper choice of functional.

Table S1: Reaction of $H_3CC \equiv CH + OH$ and $H_3CCH=CH_2 + OH$, respectively. E and I refer to the exterior and interior carbon, respectively. All values are in units of Kelvin.

HC≡CCH$_3$ + OH				
MPWB1K				
Energy type	E or I carbon	PES	ZPE	Total
Activation	I	-126	763	636
Activation	E	-358	738	380
Reaction	I	-16928	2089	-14839
Reaction	E	-18122	2333	-15790
M06-2X				
Energy type	E or I carbon	PES	ZPE	Total
Activation	I	-59	773	714
Activation	E	-110	729	619
Reaction	I	-17224	2054	-15170
Reaction	E	-18006	2296	-15710
H$_2$C=CHCH$_3$ + OH				
MPWB1K				
Energy type	E or I carbon	PES	ZPE	Total
Activation	I	-1490	799	-691
Activation	E	-1358	687	-671
Reaction	I	-15736	1692	-14045
Reaction	E	-16088	1825	-14263
M06-2X				
Energy type	E or I carbon	PES	ZPE	Total
Activation	I	-1557	837	-720
Activation	E	-1420	775	-645
Reaction	I	-11299	2160	-9139
Reaction	E	-16772	1901	-14871

S2.4 CCSD(T)-F12/cc-VDZ-F12 validity check

As a further validity check, the interaction energies of the OH-C_3H_n pre-reactive complexes calculated with MPWB1K (DFT) are compared to those calculated with CCSD(T)-F12/cc-VDZ-F12. The interaction energies of the OH-C_3H_n pre-reactive complexes differ by at most 115 K between MPWB1K and CCSD(T)-F12/cc-VDZ-F12 calculations, as shown in Table S2. This shows again that the used functional can accurately describe these reaction paths. For the pre-reactive complex of OH with $H_3CC \equiv CH$ on the exterior carbon atom, convergence is not achieved for the CCSD(T)-F12/cc-VDZ-F12 calculation.

Table S2: Interaction energies of OH with $H_3CC \equiv CH$ and $H_3CCH=CH_2$. E and I refer to the exterior and interior carbon, respectively. All values are in units of Kelvin.

$HC \equiv CCH_3$ + OH		
E or I carbon	PES MPWB1K	PES CCSD(T)-F12/cc-VDZ-F12
I	-1342	-1333
E	-2073	-
$H_3CCH=CH_2$ + OH		
E or I carbon	PES MPWB1K	PES CCSD(T)-F12/cc-VDZ-F12
I	-1543	-1509
E	-1624	-1510

Bibliography

Abplanalp, M. J., Góbi, S., & Kaiser, R. I. 2018, Phys. Chem. Chem. Phys., 21, 5378

Abplanalp, M. J., Gozem, S., Krylov, A. I., et al. 2016, Proc. Natl. Acad. Sci. U.S.A., 113, 7727

Adler, T. B., Knizia, G., & Werner, H.-J. 2007, J. Chem. Phys., 127, 1

Agúndez, M., Fonfría, J. P., Cernicharo, J., Pardo, J., & Guélin, M. 2008, Astron. Astrophys., 479, 493

Alamgir, A. 2018, Therapeutic use of medicinal plants and their extracts: volume 2: phytochemistry and bioactive compounds, Vol. 74 (Cham, Switzerland: Springer)

Arasa, C., Andersson, S., Cuppen, H., van Dishoeck, E. F., & Kroes, G.-J. 2010, J. Chem. Phys., 132, 1

Ball, J. A., Gottlieb, C. A., Lilley, A., & Radford, H. 1970, Astrophys. J., 162, L203

Bernstein, M. P., Sandford, S. A., Allamandola, L. J., Chang, S., & Scharberg, M. A. 1995, Astrophys. J., 454, 327

Boogert, A., Gerakines, P. A., & Whittet, D. C. 2015, Annu. Rev. Astron. Astrophys., 53, 541

Boogert, A., Huard, T., Cook, A., et al. 2011, Astrophys. J., 729, 1

Budin, I. & Szostak, J. W. 2011, Proc. Natl. Acad. Sci. U.S.A., 108, 5249

Burdett, J. L. & Rogers, M. T. 1966, J. Phys. Chem., 70, 939

Butscher, T., Duvernay, F., Rimola, A., Segado-Centellas, M., & Chiavassa, T. 2017, Phys. Chem. Chem. Phys., 19, 2857

Butscher, T., Duvernay, F., Theule, P., et al. 2015, Mon. Not. R. Astron. Soc., 453, 1587

Castellanos, N. P. 2018, PhD thesis

Cernicharo, J., Heras, A. M., Pardo, J. R., et al. 2001, Astrophys. J. Lett., 546, L127

Chang, Q. & Herbst, E. 2012, Astrophys. J., 759, 1

Chen, Y.-J., Ciaravella, A., Caro, G. M., et al. 2013, Astrophys. J., 778, 1

Cherchneff, I. 2011, EAS Publications Series, 46, 177

Chuang, K. 2018, Univ. Leiden, PhD thesis

Chuang, K.-J., Fedoseev, G., Ioppolo, S., van Dishoeck, E. F., & Linnartz, H. 2016, Mon. Not. R. Astron. Soc., 455, 1702

Chuang, K.-J., Fedoseev, G., Qasim, D., et al. 2018, Astron. Astrophys., 617, 1

Chyba, C. F., Thomas, P. J., Brookshaw, L., & Sagan, C. 1990, Science, 249, 366

Collings, M. P., Anderson, M. A., Chen, R., et al. 2004, Mon. Not. R. Astron. Soc., 354, 1133

Comeford, J. & Gould, J. H. 1961, J. Mol. Spectrosc., 5, 474

Contreras, C. S. & Salama, F. 2013, Astrophys. J. Suppl. Ser., 208, 1

Cottin, H., Moore, M. H., & Bénilan, Y. 2003, Astrophys. J., 590, 874

Cuppen, H. & Herbst, E. 2007, Astrophys. J., 668, 294

Cuppen, H., Ioppolo, S., Romanzin, C., & Linnartz, H. 2010, Phys. Chem. Chem. Phys., 12, 12077

Cuylle, S. H., Zhao, D., Strazzulla, G., & Linnartz, H. 2014, Astron. Astrophys., 570, 1

De Rosa, M., Gambacorta, A., & Gliozzi, A. 1986, Microbiol. Rev., 50, 70

Deamer, D., Dworkin, J. P., Sandford, S. A., Bernstein, M. P., & Allamandola, L. J. 2002, Astrobiology, 2, 371

Deegan, M. J. & Knowles, P. J. 1994, Chem. Phys. Lett., 227, 321

Dewick, P. M. 2006, Essentials of organic chemistry: for students of pharmacy, medicinal chemistry and biological chemistry (New York: John Wiley & Sons)

Fedoseev, G., Cuppen, H. M., Ioppolo, S., Lamberts, T., & Linnartz, H. 2015, Mon. Not. R. Astron. Soc., 448, 1288

Fredon, A., Lamberts, T., & Cuppen, H. 2017, Astrophys. J., 849, 1

Fuchs, G., Cuppen, H., Ioppolo, S., et al. 2009, Astron. Astrophys., 505, 629

Gerakines, P., Moore, M. H., & Hudson, R. L. 2000, Astron. Astrophys., 357, 793

Ghosh, J., Hariharan, A. K., Bhuin, R. G., Methikkalam, R. R. J., & Pradeep, T. 2018, Phys. Chem. Chem. Phys., 20, 1838

Gonzalez, J., Caballero, M., Aguilar-Mogas, A., et al. 2011, Theor. Chem. Acc., 128, 579

Hama, T. & Watanabe, N. 2013, Chem. Rev., 113, 8783

Hargreaves, W. R. & Deamer, D. W. 1978, Biochemistry, 17, 3759

Herbst, E. & van Dishoeck, E. F. 2009, Annu. Rev. Astron. Astrophys., 47, 427

Hollis, J. M., Lovas, F. J., Jewell, P. R., & Coudert, L. 2002, Astrophys. J. Lett., 571, L59

Hratchian, H. P. & Schlegel, H. B. 2004, J. Chem. Phys., 120, 9918

Ioppolo, S., Cuppen, H., Romanzin, C., van Dishoeck, E. F., & Linnartz, H. 2008, Astrophys. J., 686, 1474

Ioppolo, S., Cuppen, H., Romanzin, C., van Dishoeck, E. F., & Linnartz, H. 2010, Phys. Chem. Chem. Phys., 12, 12065

Ioppolo, S., Fedoseev, G., Lamberts, T., Romanzin, C., & Linnartz, H. 2013, Rev. Sci. Instrum., 84, 1

Ioppolo, S., Öberg, K., & Linnartz, H. 2014, in Laboratory astrochemistry: from molecules through nanoparticles to grains, ed. S. Schlemmer, T. Giesen, & H. Mutschke (John Wiley & Sons), 289–309

Irvine, W., Hoglund, B., Friberg, P., Askne, J., & Ellder, J. 1981, Astrophys. J., 248, L113

Isokoski, K., Poteet, C., & Linnartz, H. 2013, Astron. Astrophys., 555, 1

Kaifu, N., Ohishi, M., Kawaguchi, K., et al. 2004, Publ. Astron. Soc. Jpn., 56, 69

Kästner, J., Carr, J. M., Keal, T. W., et al. 2009, J. Phys. Chem. A, 113, 11856

Knizia, G., Adler, T. B., & Werner, H.-J. 2009, J. Chem. Phys., 130, 1

Knowles, P. J., Hampel, C., & Werner, H.-J. 1993, J. Chem. Phys., 99, 5219

Knowles, P. J., Hampel, C., & Werner, H.-J. 2000, J. Chem. Phys., 112, 3106

Kobayashi, H., Hidaka, H., Lamberts, T., et al. 2017, Astrophys. J., 837, 1

Kolasinski, K. W. 2012, Surface science: foundations of catalysis and nanoscience (West Chester, PA: John Wiley & Sons)

Kuiper, T., Kuiper, E. R., Dickinson, D. F., Turner, B., & Zuckerman, B. 1984, Astrophys. J., 276, 211

Maity, S., Kaiser, R. I., & Jones, B. M. 2015, Phys. Chem. Chem. Phys., 17, 3081

Malek, S. E., Cami, J., & Bernard-Salas, J. 2011, Astrophys. J., 744, 1

Martín-Doménech, R., Manzano-Santamaría, J., Caro, G. M., et al. 2015, Astron. Astrophys., 584, 1

Matar, E., Congiu, E., Dulieu, F., Momeni, A., & Lemaire, J. 2008, Astron. Astrophys., 492, L17

McGuire, B. A., Shingledecker, C. N., Willis, E. R., et al. 2017, Astrophys. J. Lett., 851, 1

Meisner, J., Markmeyer, M. N., Bohner, M. U., & Kaestner, J. 2017, Phys. Chem. Chem. Phys., 19, 23085

Metz, S., Kästner, J., Sokol, A. A., Keal, T. W., & Sherwood, P. 2014, Wiley Interdiscip. Rev. Comput. Mol. Sci., 4, 101

Miyauchi, N., Hidaka, H., Chigai, T., et al. 2008, Chem. Phys. Lett., 456, 27

Moran, L. A., Horton, H. R., Scrimgeour, G., & Perry, M. 2012, Principles of biochemistry (Upper Saddle River, NJ: Pearson Boston)

Muller, S., Beelen, A., Guélin, M., et al. 2011, Astron. Astrophys., 535, 1

Nykänen, L. & Honkala, K. 2011, J. Phys. Chem. C, 115, 9578

Paardekooper, D., Bossa, J.-B., & Linnartz, H. 2016, Astron. Astrophys., 592, 1

Pascoli, G. & Polleux, A. 2000, Astron. Astrophys., 359, 799

Peterson, K. A., Adler, T. B., & Werner, H.-J. 2008, J. Chem. Phys., 128, 01

Qasim, D., Chuang, K.-J., Fedoseev, G., et al. 2018, Astron. Astrophys., 612, 1

Qasim, D., Fedoseev, G., Chuang, K.-J., et al. 2019, Astron. Astrophys., 627, A1

Qiu, J., Wang, J., Shi, Y., et al. 2018, Astron. Astrophys., 613, 1

Rimola, A., Skouteris, D., Balucani, N., et al. 2018, ACS Earth Space Chem., 2, 720

Romanzin, C., Ioppolo, S., Cuppen, H., van Dishoeck, E. F., & Linnartz, H. 2011, J. Chem. Phys., 134, 1

Schaff, J. E. & Roberts, J. T. 1998, Langmuir, 14, 1478

Shaw, M. F., Osborn, D. L., Jordan, M. J., & Kable, S. H. 2017, J. Phys. Chem. A, 121, 3679

Sherwood, P., de Vries, A. H., Guest, M. F., et al. 2003, J. Mol. Struct.: THEOCHEM, 632, 1

Smith, R. S., May, R. A., & Kay, B. D. 2015, J. Phys. Chem. B, 120, 1979

Snyder, L. & Buhl, D. 1973, Nat. Phys. Sci., 243, 45

Tielens, A. 2013, Rev. Mod. Phys., 85, 1021

Tschersich, K. 2000, J. Appl. Phys., 87, 2565

Tschersich, K., Fleischhauer, J., & Schuler, H. 2008, J. Appl. Phys., 104, 1

Tschersich, K. & Von Bonin, V. 1998, J. Appl. Phys., 84, 4065

Turner, B. E. & Apponi, A. J. 2001, Astrophys. J. Lett., 561, L207

Valiev, M., Bylaska, E. J., Govind, N., et al. 2010, Comput. Phys. Commun., 181, 1477

van Dishoeck, E. F., Herbst, E., & Neufeld, D. A. 2013, Chem. Rev., 113, 9043

van´t Hoff, M. L., Tobin, J. J., Trapman, L., et al. 2018, Astrophys. J. Lett., 864, L23

Vöhringer-Martinez, E., Hansmann, B., Hernandez, H., et al. 2007, Science, 315, 497

Watanabe, N. & Kouchi, A. 2002, Astrophys. J. Lett., 571, L173

Watanabe, N., Shiraki, T., & Kouchi, A. 2003, Astrophys. J. Lett., 588, L121

Weigend, F., Häser, M., Patzelt, H., & Ahlrichs, R. 1998, Chem. Phys. Lett., 294, 143

Werner, H., Knowles, P., Knizia, G., Manby, F., & Schütz, M. 2012, Mol. Sci., 2, 242

Woods, P. M., Millar, T. J., Herbst, E., & Zijlstra, A. A. 2003, Astron. Astrophys., 402, 189

Xu, S. & Lin, M. 2007, Proc. Combust. Inst., 31, 159

Zaverkin, V., Lamberts, T., Markmeyer, M., & Kästner, J. 2018, Astron. Astrophys., 617, 1

Zhao, Y. & Truhlar, D. G. 2004, J. Phys. Chem. A, 108, 6908

Zhao, Y. & Truhlar, D. G. 2008, Theor. Chem. Acc., 120, 215

Zuckerman, B., Turner, B., Johnson, D., et al. 1975, Astrophys. J., 196, L99

Summary

Between (inter) the stars (stellar) lies what is called the interstellar medium (ISM), which consists of highly dilute and very cold clouds of dust and gas. Although this medium is largely composed of gas, the role of the dust in the chemistry of the ISM is significant. The dust acts as a platform for simple atoms and molecules to "accrete, meet, and greet" (i.e., freeze out, directly collide or diffuse on the surface, and react). When these species react with each other on the dust grain, such a reaction typically releases a certain amount of energy, which gets absorbed by phonons in the solid lattice. This is an important stepping stone to the formation of large molecules, as the excess energy could otherwise break apart the product species, as sometimes observed in gas-phase reactions. The dust also contributes to blocking external UV-radiation from penetrating the cloud, which increases the role of 'dark' or 'non-energetic' processes (i.e., processes absent of 'energetic' particles) to the formation of ice species. When the cloud eventually collapses onto itself to form a young stellar object (YSO), the UV-light emitted induces a rich ice chemistry largely governed by 'energetic' processes, as investigated in numerous observational surveys, laboratory experiments, and computational simulations.

This thesis focuses on the 'dark' ice chemistry, which has received less attention in the literature compared to the ice chemistry involving 'energetic' processes, but is equally important to understanding the chemical inventory of interstellar clouds. The formation and formation parameters of simple and complex organic molecules (COMs) through 'non-energetic' processes are experimentally demonstrated and complemented by quantum chemical calculations. The findings from the experimental studies are strongly linked to astronomical observations of both, gas-phase and ice species.

Dark to light ice chemistry in interstellar clouds

At the edges of interstellar clouds, which has a visual extinction (A_V) of just below 1.6 mag, the molecular hydrogen density is relatively low ($\sim 10^3$ cm^{-3}). External UV photons are present, which causes the photodesorption of certain species, like carbon monoxide (CO), from dust grains that have temperatures of $\sim$10-20 K. However, the density is high enough to somewhat shield gas-phase species from 'energetic' particles, which mitigates further ionization of gas-phase species. The ionized species present will recombine (i.e., positive ion combines with electrons or negative ions) to form neutral atoms, such as C, H, N, and O. If not photodesorbed, these simple atoms will hit and stick to the dust surface, and subsequently react to form molecules such as water (H_2O), ammonia (NH_3), and methane (CH_4) ices, with water being the most abundant. Although not yet observationally constrained, recent laboratory experiments, some of which are presented in this thesis, demonstrate that COMs can also be formed in this H_2O-rich ice phase. Carbonaceous grains may contain hy-

drocarbons, such as propyne and acetylene. These molecules can react with nearby OH radicals almost barrierlessly to form aldehydes and alcohols, for example.

Traveling deeper into the cloud (A_V > 9 mag), the density is increased by orders of magnitude ($\sim 10^5$ cm^{-3}), which severely blocks external UV radiation from penetrating the cloud, and also causes a further drop in the temperature (to $\sim$10 K). This is the time period when the 'dark' ice chemistry largely comes into play, as certain 'energetic' particles are not readily available to induce chemical reactions. Much of the remaining carbon in the gas-phase is destroyed by O to form CO. This CO freezes out on top of the H_2O-rich ice "heavily" and then "catastrophically", and is subjected to hydrogenation to form species such as H_2CO, CH_3OH, glycolaldehyde, ethylene glycol, and methyl formate. Recent laboratory experiments from our group have also demonstrated that biologically relevant species can be formed, such as glycerol. In modern life, cell membranes are composed of glycerophospholipids, which contain glycerol molecules. Thus, this 'dark' and 'non-energetic' chemistry can lead to the formation of simple, complex, and biologically relevant organic species.

At a certain point, the cloud will eventually collapse under its own gravity, which then triggers an increase in the density and temperature. A YSO is created and emits radiation, which can process the ices formed in the 'dark' period. Laboratory experiments have demonstrated that radiation-induced processes lead to the formation of residues consisting of polymers and amino acids, in addition to simpler species.

Experimental simulations of dark ice chemistry with SURFRESIDE[3]

All experiments presented in this thesis were performed with the cryogenic ultrahigh vacuum setup, SURFace REaction SImulation DEvice (SURFRESIDE[3]), which is uniquely equipped with three atomic beamlines, along with gas deposition lines, to study solid-state chemical reactions that simply involve radicals. A photograph of the setup is shown in Figure 1 and on the cover of this thesis. For over a decade, SURFRESIDE has been used to study the 'non-energetic' processes that take place in the ices of translucent and dense interstellar clouds. Details on the formation of simple hydrides (e.g., H_2O, NH_3, and CH_4) as well as COMs (e.g., glycolaldehyde, glycerol, and propanal) have been explored, primarily on 10-20 K surfaces cooled by a closed-cycle helium cryostat. The components of the setup are described in the text below.

The three atomic beamlines are collectively able to produce C, H/D, O, and N atoms, along with molecular fragments. The newest addition – the atomic carbon source – produces atomic carbon by the heating of carbon powder within a tantalum tube. This tube is heated to at least $\sim$2000 K in order to sublimate the carbon. The sublimated carbon reacts with the tantalum to form tantalum carbide, which ultimately breaks apart molecular carbon, leading to the formation of atomic carbon that eventually is released into the gas-phase. The hydrogen
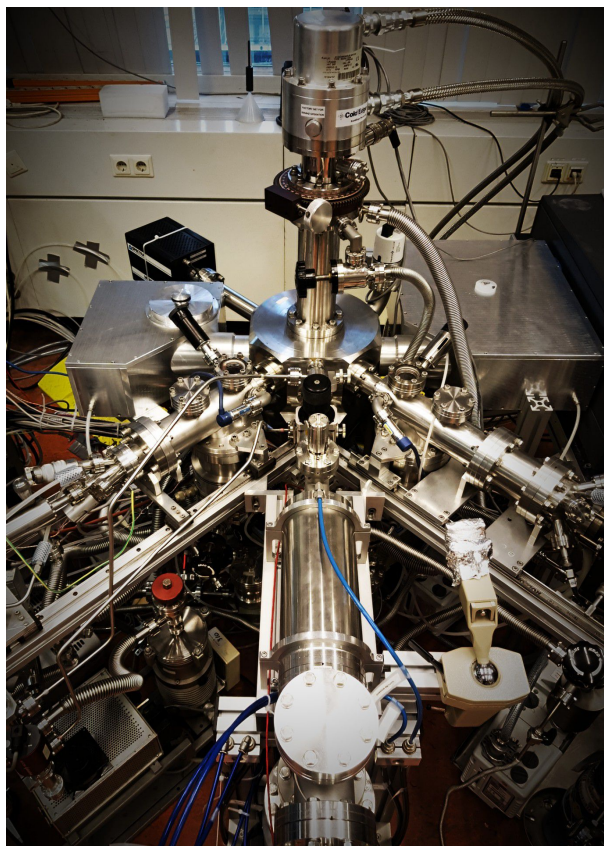
Figure 1: A photo of SURFRESIDE[3].

atom beam source is used primarily to form H(D) atoms by thermally cracking hydrogen (deuterium) molecules with a filament. The microwave atom beam source exploits the electron cyclotron resonance effect to create electrons with kinetic energies sufficient to break apart molecules into atoms and molecular fragments, such as N, O, OH, NH_x, and so on. The absence of a hot filament in the microwave atom beam source allows reactive species, such as oxygen, to be dissociated in the chamber in an experimentally friendly way. For the deposition of stable molecules, two independent dosing lines, which are also pumped by a turbomolecular pump, are used to transfer gases and vapors into the main chamber of SURFRESIDE[3].

Two analytical techniques are collectively used to probe the reactive intermediates and products formed: reflection-absorption infrared spectroscopy (RAIRS) and temperature programmed desorption-quadrupole mass spectrometry (TPD-QMS). With RAIRS, the vibrational signatures of the ice species are probed. This method allows *in situ* observations, however with the disadvantage that vibrational modes are typically broad and semi unique. TPD-QMS is the higher sensitivity technique within the experimental setup that can typically distinguish the different species formed more effectively. However, TPD-QMS is an

ex situ technique as it involves the sublimation of the ice sample, and is also not ideal to probing transient intermediate species. The coupling of RAIRS and TPD-QMS to understand the ice chemistry is powerful, however, in that the disappearance of vibrational signatures and the subsequent rise of desorption signals can be used to piece together the ice species formed. Additional spectroscopic and mass spectrometric information are obtained by using isotopically enriched precursor species.

Non-energetic solid-state formation of simple molecules: CH_4, HCOOH, and CO_2

CH_4 is in the top six most abundant ices to be detected towards young stellar objects. Observational surveys of CH_4 ice show that the probed CH_4 is expected to be formed by the hydrogenation of solid C in H_2O-rich ices. This pathway has also been adapted in some astrochemical models, with however no experimental confirmation of this. In this thesis, it is experimentally demonstrated that CH_4 can be formed by the solid-state hydrogenation of C in a H_2O-rich ice. Additional details to the CH_4 formation pathway are also discussed, such as 1) The formation rate of CH_4 is twice as high in a H_2O-rich ice compared to an ice without H_2O. This is partially due to the increase in the residence time of hydrogen in H_2O ices. 2) Under our laboratory conditions, the competing abstraction reactions appear to not dominate. CH_n radicals readily react with H, as CH_n radicals nor their recombination products are observed. This implies that the H-addition pathway to form CH_4 dominates the H-abstraction pathway to form CH_n radicals, at least with the chosen laboratory settings. As CH_4 is best observed with space-based observatories due to the interference of telluric contamination, the anticipated James Webb Space Telescope (JWST) will be a promising facility to probe CH_4 ice. It's high sensitivity in the mid-IR may also allow direct observations of CH_4 in the H_2O-rich ice phase of quiescent molecular clouds.

HCOOH and CO_2 ices have been recognized through multiple studies to be largely formed also in the H_2O-rich ice phase. Yet, ice observations of CO_2 additionally show that a smaller fraction (~1/3) of the sampled ice is detected in a CO environment. It is explored here the experimental formation of both, HCOOH and CO_2 ices, starting from H_2CO. As H_2CO is a product of CO hydrogenation, this investigation supports the idea that HCOOH and CO_2 should also be formed in the CO-rich ice phase. By combining the experimental results with quantum chemical calculations from the literature, it is found that HOCO and HCO intermediates are responsible for the formation of HCOOH, and that CO_2 is predominantly formed from HOCO. As HCOOH has yet to be securely detected in interstellar ices, this study provides more hope for the presence of HCOOH in the ices of quiescent clouds, as HCOOH ice should be more abundant than previously thought. It is suggested that future observational surveys targeting 'non-energetically' formed HCOOH should not probe beyond the sufficient conversion of H_2CO to CH_3OH in order to reduce complexity in the ice spectra.

The CH₃OH ice dilemma in interstellar clouds

The solid-state CO hydrogenation pathway is regarded as the dominant pathway to forming CH_3OH (ice and gas-phase) in interstellar clouds. But is this scenario truly uniform across all interstellar clouds? Observations of CH_3OH ice in quiescent cloud environments show that CH_3OH upper limits are at least a factor of 3 below CH_3OH ice detections at high visual extinctions (i.e., at cloud depths where CH_3OH should be sufficiently formed). Note, however, that a high visual extinction does not necessarily imply a high density, which would affect CH_3OH formation. This indicates that CH_3OH ice is not effectively formed by the CO hydrogenation pathway in some clouds. Instead, a potential situation may be that CH_3OH is formed by less efficient reactions, such as the CH_4 + OH route, as supported from laboratory experiments presented here. It is found that the CH_4 + OH reaction pathway is around 20 times less efficient than the CO + H pathway to forming CH_3OH. If interstellar CH_3OH ice can also be formed from CH_4, then CH_3OH may be formed earlier than expected. Currently, CH_3OH is constrained to be formed at $A_V \sim 9 \pm 3$ mag, which is after H_2O has formed ($A_V \sim 2$ mag) and after the heavy CO freeze-out ($A_V \sim 3$ mag). Note that the CH_3OH ice formation threshold is only based on 7 detections. Simply based on these formation threshold values, it is thought that the CH_3OH formation threshold should at least be dropped to when CO heavily freezes out.

An updated observational study of CH_3OH ice is presented in this thesis, which includes one additional ice detection and a larger sample of CH_3OH upper limits measured over a range of A_V values (total A_V = 5.1-46 mags). A new CH_3OH ice formation threshold value of $A_V = 7 \pm 4$ mag is found, which shows that more CH_3OH ice observations are warranted due to the large error bar. The upper limits sampled are still much below the detections at high A_V, which confirms previous work that CH_3OH ice is indeed lacking in some clouds. To better understand this puzzling CH_3OH ice dilemma in interstellar clouds, a facility such as the JWST is desired for the following reasons but not limited to: 1) The sensitivity of the JWST in the mid-IR for the 3.53 μm band (S/N ~100) and without the presence of tellurics will be ideal to probe CH_3OH ice. 2) Ice mapping, which allows a large number of sight-lines to be simultaneously probed at a wide range of A_V, is expected to provide a larger sample of CH_3OH ice detections. CH_3OH precursor species, such as CH_4 and CO, can be mapped alongside CH_3OH to observe potential trends between the precursor and product species in different clouds. If the density is indeed low at high A_V for certain clouds, then the CO:CH_3OH ratio will be affected by this, as less CO will be frozen out, and also the higher temperature in less dense regions will reduce the hydrogenation rate of CO to form CH_3OH.

Non-energetic solid-state formation of complex molecules: alcohols and aldehydes

At the low temperature of 10 K and under ultrahigh vacuum conditions, it is shown through experimental simulations complemented with theoretical calculations that various COMs can be formed 'non-energetically' (i.e., COMs can

be formed by 'dark' ice chemistry on interstellar grains, assuming that the starting materials are available). If hydrocarbon radicals are present on/in CO-rich ices, then they should readily react with CO hydrogenation product species to form propanal (aldehyde) and 1-propanol (alcohol). In the experimental investigations, propanal is formed by the barrierless recombination of HCO and H_2CCH/H_3CCH_2 radicals. 1-propanol is formed by the hydrogenation of propanal, which comes with a barrier. The exact barrier value still remains to be explored through computational calculations, however the value is not expected to be below 2560 K, which promotes the idea that other pathways may be more effective to propanol formation. Indeed, it is also shown in this thesis that a variety of 3-carbon COMs, including 1-propanol, can be formed starting from the almost barrierless reaction of propyne/propene and OH radicals. The formation of 3-carbon alcohols can potentially be expanded to the formation of larger, more astrobiologically relevant species, such as fatty alcohols, which may have been part of the primitive material important to life on the early Earth.

In essence, this thesis exploits solid-state experimental techniques to unravel the formation details of simple and complex (organic) molecules on icy interstellar dust grains. Specifically, the study of such molecules through 'dark' or 'non-energetic' ice chemistry is explored to better understand the chemical inventory at the starting point of ice growth in interstellar clouds. Quantum chemical calculations are incorporated to better understand the experimental results, and to also understand the potential astrochemical relevance of certain studied formation pathways. Additionally, a dedicated observational study is presented, which links with experimental and computational findings to understand certain solid-state processes in interstellar ices. Once the JWST is launched and operational, this thesis work will be directly applicable to observational surveys of simple molecules and COMs in numerous quiescent cloud environments.

Samenvatting

Tussen (inter) de sterren (stellair) bevindt zich het zogenaamde interstellaire medium (ISM), dat bestaat uit zeer ijle en koude wolken met daarin stof en gas. Hoewel dit medium grotendeels uit gas bestaat, spelen vooral stofdeeltjes een belangrijke rol voor de chemische verrijking van het ISM. Het stof fungeert namelijk als een oppervlak waarop atomen en eenvoudige moleculen kunnen vastvriezen, zich voortbewegen en zelfs reacties met elkaar kunnen aangaan. Het is dus een plek waar atomen en moleculen zich verzamelen en zich kunnen treffen. Wanneer de atomen en moleculen op de stofdeeltjes met elkaar reageren komt er doorgaans een bepaalde hoeveelheid energie vrij, die wordt geabsorbeerd door het stof. Dit is een belangrijk opstapje naar de vorming van grotere moleculen, in de gasfase zorgt dit overschot aan energie namelijk dat nieuw gevormde moleculen doorgaans direct uit elkaar vallen. Het stof draagt er ook aan bij dat externe UV-straling de wolken minder binnendringt, waardoor het belang van 'donkere' of 'niet-energetische' processen (d.w.z. processen zonder 'energetische' deeltjes) toeneemt in de vorming van ijsmoleculen. Wanneer de wolk onder zijn eigen zwaartekracht ineen stort om een jong stellair object (JSO) te vormen, veroorzaakt het uitgestraalde UV-licht een rijke chemie in het ijs op de stofdeeltjes die grotendeels wordt beheerst door 'energetische' processen, zoals onderzocht in tal van observationele onderzoeken, laboratoriumexperimenten en computationele simulaties.

Dit proefschrift richt zich op de 'donkere' ijschemie, die in de literatuur minder aandacht heeft gekregen dan de ijschemie met 'energetische' processen, maar even belangrijk is voor het begrijpen van de chemische inventaris van interstellaire wolken. De vorming en vormings-parameters van eenvoudige en complexe organische moleculen (COMs) door middel van 'niet-energetische' processen zijn experimenteel onderzocht en aangevuld met kwantumchemische berekeningen. De conclusies van de experimentele studies zijn van belang voor astronomische waarnemingen van zowel gasfase- als ijsmoleculen.

'Niet-energetische' en 'energetische' processen in het ijs van interstellaire wolken

Aan de randen van interstellaire wolken, waar een visuele extinctie (A_V) is van net onder de 1,6 mag, is de dichtheid van moleculair waterstof relatief laag ($\sim 10^3$ cm^{-3}). Er zijn externe UV-fotonen aanwezig die de fotodesorptie veroorzaken van bepaalde moleculen, zoals koolmonoxide (CO), vanaf het oppervlak van ijzige stofdeeltjes met temperaturen van $\sim$10-20 K. De dichtheid is echter hoog genoeg om moleculen in de gasfase enigszins te beschermen tegen 'energetische' deeltjes, zodat verdere ionisatie van moleculen in de gasfase wordt tegengehouden. De geïoniseerde atomen die aanwezig zijn, zullen recombineren (d.w.z. positieve ionen combineren met elektronen of negatieve ionen) om neu-

trale atomen te vormen, zoals C, H, N en O. Deze eenvoudige atomen kunnen het oppervlak van stofdeeltjes raken en blijven plakken, om vervolgens te reageren en moleculen zoals water (H_2O), ammoniak (NH_3) en methaan (CH_4) te vormen. Er wordt een dun ijslaagje gevormd, waarbij water het meest voorkomende molecuul in dit ijs is. Hoewel waarnemingen dit nog niet laten zien, tonen recente laboratoriumexperimenten aan dat COMs ook kunnen worden gevormd in deze H_2O-rijke ijsfase. Zo wordt in dit proefschrift de vorming van aldehyden en alcoholen gepresenteerd. Koolstofhoudende deeltjes kunnen koolwaterstoffen bevatten zoals propyn en acetyleen. Deze moleculen kunnen bijna barriere reageren met nabijgelegen OH-radicalen om bijvoorbeeld aldehyden en alcoholen te vormen.

Dieper in de wolk ($A_V > 9$ mag), is de dichtheid meerdere ordes van grootte hoger ($\sim 10^5$ cm^{-3}), waardoor de externe UV-straling goed geblokkeerd wordt. Dit veroorzaakt ook een verdere daling van de temperatuur naar ongeveer 10 K. Dit is de periode waarin de 'donkere' ijschemie grotendeels aan bod komt, omdat bepaalde 'energetische' deeltjes niet direct beschikbaar zijn om chemische reacties te induceren. Veel van de resterende koolstof atomen in de gasfase worden door zuurstof atomen gebruikt om CO te vormen. Deze CO bevriest bovenop het H_2O-rijke ijs en wordt vervolgens gehydrogeneerd om moleculen zoals H_2CO, CH_3OH, glycolaldehyde, ethyleenglycol en methylformiaat te vormen. Recente laboratoriumexperimenten van onze groep hebben ook aangetoond dat er biologisch relevante moleculen kunnen worden gevormd, zoals glycerol. In het moderne leven bestaan celmembranen uit glycerofosfolipiden, die glycerolmoleculen bevatten. Deze 'donkere' en 'niet-energetische' chemie kan dus leiden tot de vorming van eenvoudige, complexe en biologisch relevante organische moleculen.

Uiteindelijk zal de wolk onder zijn eigen zwaartekracht ineenstorten, waardoor de dichtheid en temperatuur toenemen. Er ontstaat een JSO die straling gaat uitzenden, welke de in de 'donkere' periode gevormde moleculen in het ijs op de stofdeeltjes, chemisch verder kan gaan veranderen. Laboratoriumexperimenten hebben aangetoond dat door straling veroorzaakte processen naast eenvoudige moleculen ook residuen produceren die bestaan uit polymeren en aminozuren.

Experimentele simulaties van 'donkere' ijs chemie met SURFRESIDE[3]

Alle experimenten in dit proefschrift zijn uitgevoerd met een unieke cryogene ultrahoge vacuümopstelling, SURFace REaction SImulation DEvice (SURFRESIDE), die is uitgerust met drie atomaire bundellijnen en twee gas depositie lijnen, om reacties in de vastestofchemie te bestuderen. Een foto van de opstelling is te zien in Figuur 1 en op de omslag van dit proefschrift. SURFRESIDE wordt al meer dan een decennium gebruikt om de 'niet-energetische' processen te bestuderen die plaatsvinden op de ijsdeeltjes van dichte interstellaire wolken. Details over de vorming van eenvoudige hydriden (bijv. H_2O, NH_3 en CH_4) en COMs (bijv. glycolaldehyde, glycerol en propanal) zijn onderzocht, voorname-

lijk op 10-20 K oppervlakken die gekoeld worden met een helium cryostaat. De componenten van de opstelling worden beschreven in de onderstaande tekst.
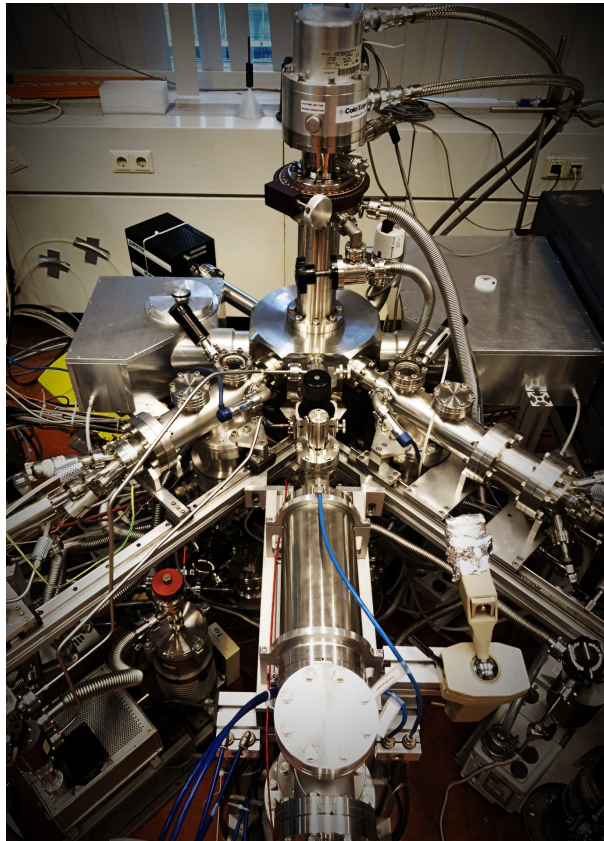
Figuur 1: Een foto van SURFRESIDE[3].

De drie atomaire bundellijnen zijn gezamenlijk in staat om C-, H/D-, O- en N-atomen te produceren, en daarnaast ook moleculaire fragmenten. De nieuwste toevoeging - de atomaire koolstofbron - produceert atomaire koolstof door de verhitting van koolstofpoeder in een tantaalbuis. Deze buis wordt verwarmd tot minimaal ~2000 K om de koolstof te sublimeren. De gesublimeerde koolstof reageert met het tantaal om tantaalcarbide te vormen, dat moleculaire koolstof afbreekt, wat leidt tot de vorming van atomair koolstof die uiteindelijk in de gasfase vrijkomt. De waterstofatoombundelbron wordt voornamelijk gebruikt om H(D)-atomen te vormen door waterstof (deuterium) moleculen thermisch te kraken met een heet filament. De microgolf-atoombundelbron maakt gebruik van het elektron-cyclotron-resonantie-effect om elektronen te creëren met voldoende kinetische energie om moleculen in atomen en moleculaire fragmenten (zoals N, O, OH, NH_x, enzovoort) op te splitsen. Door de afwezigheid van een filament in de microgolf-atoombundelbron kunnen reactieve moleculen, zoals zuurstof, op een experimenteel gemakkelijkere manier worden gedissocieerd. Voor de depositie van stabiele moleculen worden twee aparte depositie lijnen

(die beiden gepompt worden door een turbomoleculaire pomp) gebruikt om gassen in de hoofdkamer van SURFRESIDE[3] over te brengen.

Twee analytische technieken worden gezamelijk gebruikt om de reactieve tussenproducten en gevormde producten te onderzoeken: reflectie-absorptie infraroodspectroscopie (RAIRS) en temperatuurgeprogrammeerde desorptie - quadrupool massaspectrometrie (TPD-QMS). Met RAIRS worden de karakteristieke vibraties van de functionele groepen van ijsmoleculen onderzocht. Deze methode maakt *in situ* waarnemingen mogelijk, maar heeft het nadeel dat karakteristieke trillingen typisch brede spectra vertonen en niet geheel uniek zijn. TPD-QMS is de techniek met hogere gevoeligheid waarmee het mogelijk is de verschillende moleculen die worden gevormd effectiever te onderscheiden. TPD-QMS is echter een *ex situ* techniek omdat het de sublimatie van het ijs vereist, daarbij is het ook geen ideale methode om reactieve tussenproducten te onderzoeken. De combinatie van RAIRS en TPD-QMS om de ijschemie te begrijpen is echter krachtig, omdat bijvoorbeeld het gelijktijdig verdwijnen van karakteristieke trilling signalen en de daaropvolgende stijging van desorptie QMS signalen kan worden gebruikt voor een eenduidige analyse. Aanvullende spectroscopische en massaspectrometrische informatie kunnen worden verkregen door isotopisch verrijkte precursor moleculen te gebruiken.

Niet-energetische vorming van eenvoudige moleculen: CH_4, HCOOH en CO_2

CH_4 staat in de top zes van meest voorkomende ijsmoleculen die kunnen worden gedetecteerd in de buurt van jonge stellaire objecten. Observationeel onderzoek van CH_4-ijs laat zien dat de gedetecteerde CH_4 naar alle waarschijnlijkheid wordt gevormd door de hydrogenering van C-atomen in H_2O-rijk ijs. Deze route wordt ook gebruikt in sommige astrochemische modellen, ondanks dat er nog geen experimentele bevestiging van deze route is gerapporteerd. In dit proefschrift wordt experimenteel aangetoond dat CH_4 kan worden gevormd door de opeenvolgende hydrogenering van C-atomen en gehydrogeneerde reactie producten in H_2O-rijk ijs. Aanvullende details over de CH_4-vormings route worden ook besproken: 1) De vormingssnelheid van CH_4 is tweemaal zo hoog in een H_2O-rijk ijs in vergelijking met een ijs zonder H_2O. Dit komt onder andere door de gemiddeld langere verblijftijd van waterstof in H_2O-ijs. 2) Onder onze laboratoriumomstandigheden lijken de concurrerende abstractiereacties niet te domineren. CH_n-radicalen reageren gemakkelijk met H, aangezien CH_n-radicalen noch hun recombinatieproducten worden waargenomen. Dit impliceert dat het H-additie-pad om CH_4 te vormen het H-abstractie-pad domineert, in ieder geval voor de onderzochte omstandigheden. Omdat CH_4 ijs het beste kan worden waargenomen met ruimtetelescopen vanwege het ontbreken van interferentie met tellurische verontreiniging, zal de verwachte James Webb-ruimtetelescoop (JWST) een veelbelovend instrument zijn om CH_4-ijs te onderzoeken. De hoge gevoeligheid in het mid-infrarood zal ook directe waarneming van CH_4 in het H_2O-rijke ijs mogelijk maken.

Meerdere onderzoeken erkennen dat HCOOH-ijs en CO_2-ijs beiden grotendeels worden gevormd in de H_2O-rijke ijsfase. Toch blijkt uit observaties van CO_2-ijs dat een kleine fractie (~1/3) van het ijs wordt gedetecteerd in een CO-omgeving. In dit proefschrift wordt de experimentele vorming van zowel, HCOOH- als CO_2-ijs, beginnend vanaf H_2CO, verkend. Aangezien H_2CO een product is van CO-hydrogenering, ondersteunt dit onderzoek het idee dat CO_2 en HCOOH ook gevormd worden in de CO-rijke ijsfase. Door de experimentele resultaten te combineren met kwantumchemische berekeningen uit de literatuur, is gebleken dat HOCO- en HCO-tussenproducten verantwoordelijk zijn voor de vorming van HCOOH, en dat CO_2 voornamelijk wordt gevormd uit HOCO. Aangezien HCOOH nog niet eenduidig is gedetecteerd in interstellair ijs, biedt deze studie meer inzicht op de aanwezigheid van HCOOH in het ijs in interstellaire wolken, aangezien HCOOH-ijs meer zou moeten voorkomen dan eerder werd gedacht. Toekomstige observationele zoektochten naar 'niet-energetisch' gevormd HCOOH, moeten zich daarom richten op plekken waar H_2CO nog niet volledig is geconverteerd naar CH_3OH.

Het CH_3OH-ijs dilemma in interstellaire wolken

Het vaste-stof CO-hydrogeneringspad wordt beschouwd als het dominante pad naar CH_3OH (ijs- en gasfase) in interstellaire wolken. Maar is dit scenario werkelijk uniform in alle interstellaire wolken? Waarnemingen van CH_3OH-ijs in dergelijke wolken laten zien dat de bovengrenzen van CH_3OH ten minste een factor 3 lager zijn dan CH_3OH-ijs detecties bij hoge visuele extincties (d.w.z. op wolk-dieptes waar CH_3OH voldoende zou moeten worden gevormd). Merk echter op dat een hoge visuele extinctie niet noodzakelijkerwijs een hoge dichtheid betekent, wat de CH_3OH-vorming zou beïnvloeden. Dit geeft aan dat CH_3OH-ijs in sommige wolken niet effectief wordt gevormd door het CO-hydrogeneringspad. In plaats daarvan is het mogelijk dat CH_3OH wordt gevormd door minder efficiënte reacties, zoals de CH_4 + OH-route. Deze route wordt ondersteund door hier gepresenteerde laboratoriumexperimenten. Hieruit kan geconcludeerd worden dat de CH_4 + OH-reactieroute ongeveer 20 keer minder efficiënt is dan de CO + H-route om CH_3OH te vormen. Als interstellair CH_3OH-ijs ook kan worden gevormd uit CH_4, kan CH_3OH eerder worden gevormd dan tot dusver is aangenomen. Het hier gepresenteerde onderzoek laat zien dat CH_3OH gevormd wordt bij $A_V \sim 9 \pm 3$ mag, hetgeen dus na H_2O vorming is ($A_V \sim 2$ mag) en na de "sterke" CO-accretie ($A_V \sim 3$ mag). Merk op dat de A_V waarde voor CH_3OH-ijs vorming slechts gebaseerd is op 7 detecties. Op basis van deze waarden mag worden aangenomen dat de aanzet van CH_3OH-vorming op zijn minst moet worden verlaagd tot het moment waarop CO effectief vastvriest op stofdeeltjes.

Een observationele vervolgstudie van CH_3OH-ijs wordt gepresenteerd in dit proefschrift, dat een extra ijsdetectie en een grotere hoeveelheid van CH_3OH-bovengrenzen omvat, gemeten over een bereik van A_V-waarden (totaal $A_V =$ 5,1-46 mags). Een nieuwe drempelwaarde voor de vorming van CH_3OH-ijs van $A_V = 7 \pm 4$ mag is gevonden; er zijn duidelijk meer waarnemingen van CH_3OH-ijs nodig om een preciezere uitspraak te kunnen doen. De gevonden bovengren-

zen liggen nog steeds ver onder de detecties bij hoge A_V, wat eerder werk, dat concludeert dat CH$_3$OH-ijs inderdaad in sommige wolken ontbreekt, bevestigt. Om dit raadselachtige CH$_3$OH-ijs dilemma in interstellaire wolken beter te begrijpen, is een faciliteit zoals de JWST gewenst om de volgende redenen: 1) De gevoeligheid van de JWST in het mid-infrarood voor de band van 3,53 μm (S/N ~100) en de afwezigheid van tellurische lijnen is ideaal om CH$_3$OH-ijs te onderzoeken. 2) Het in kaart brengen van ijs, wat inhoudt dat een groot aantal zichtlijnen gelijktijdig kan worden geobserveerd op een breed scala van A_V, zal naar verwachting een grotere steekproef van CH$_3$OH-ijsdetecties opleveren. CH$_3$OH-voorlopers, zoals CH$_4$ en CO, kunnen naast CH$_3$OH in kaart worden gebracht om potentiële trends tussen de precursors en de producten in verschillende wolken te observeren. Als de dichtheid inderdaad laag is bij hoge A_V voor bepaalde wolken, zal de CO: CH$_3$OH-verhouding hierdoor worden beïnvloed, omdat minder CO vastvriest. Ook de hogere temperatuur in minder dichte gebieden zal de hydrogeneringssnelheid verlagen van CO om CH$_3$OH te vormen.

Niet-energetische vorming van complexe moleculen in het ijs: alcoholen en aldehyden

Bij een temperatuur van 10 K, onder ultrahoge vacuüm omstandigheden wordt door experimentele metingen, aangevuld met theoretische berekeningen, aangetoond dat verschillende COMs 'niet-energetisch' kunnen worden gevormd (d.w.z. COMs kunnen worden gevormd door 'donkere' ijschemie op interstellaire stofdeeltjes, ervan uitgaande dat de initiële ingrediënten beschikbaar zijn). Als koolwaterstofradicalen aanwezig zijn op / in CO-rijk ijs, dan zouden ze gemakkelijk moeten reageren met CO-hydrogenering producten om propanal (aldehyde) en 1-propanol (alcohol) te vormen. In de experimentele onderzoeken wordt propanal gevormd door de barrièrevrije recombinatie van HCO en H$_2$CCH/H$_3$CCH$_2$-radicalen. 1-propanol wordt gevormd door de hydrogenering van propanal, wat wel met een barrière gepaard gaat. De exacte grenswaarde moet nog worden onderzocht door middel van computationele berekeningen, maar de waarde zal naar verwachting niet lager zijn dan 2560 K, wat aanduidt dat andere routes effectiever kunnen zijn voor de vorming van propanol. In dit proefschrift wordt inderdaad ook aangetoond dat een verscheidenheid aan 3-koolstof COMs, waaronder 1-propanol, kan worden gevormd uitgaande van de bijna barrièrevrije reactie van propyn / propeen en OH-radicalen. De vorming van 3-koolstofalcoholen kan mogelijk worden uitgebreid tot de vorming van grotere, meer astrobiologisch relevante moleculen, zoals vetalcoholen, die mogelijk deel uitmaakten van het primitieve materiaal dat belangrijk is voor het leven op de vroege aarde.

In essentie maakt dit proefschrift gebruik van experimentele technieken van de vastestofchemie om de details van de vorming van eenvoudige en complexe (organische) moleculen op ijzige interstellaire stofdeeltjes te ontrafelen. In het bijzonder wordt de studie van dergelijke moleculen door middel van 'donkere' of 'niet-energetische' ijschemie onderzocht om de chemische inventarisatie aan het beginpunt van ijsgroei in interstellaire wolken beter te begrijpen. Kwan-

tumchemische berekeningen zijn uitgevoerd om de experimentele resultaten beter te begrijpen en ook om de astrochemische relevantie van bepaalde bestudeerde vormingsroutes in kaart te brengen. Daarnaast worden de resultaten van een observationele studie gepresenteerd, die verband houdt met experimentele en computationele bevindingen om bepaalde vaste stof processen in interstellair ijs te begrijpen. Zodra de JWST is gelanceerd en operationeel is, zal dit proefschrift direct van toepassing zijn op observationele onderzoeken van zowel eenvoudige als complexe moleculen in tal van interstellaire wolken.

List of publications

Publications

13. *A cryogenic ice setup to simulate carbon atom reactions in interstellar ices*
D. Qasim, M.J.A. Witlox, G. Fedoseev, K.-J. Chuang, T. Banu, S.A. Krasnokutski, S. Ioppolo, J. Kästner, E.F. van Dishoeck and H. Linnartz,
Rev. Sci. Instrum. 91 (2020) 054501

12. *An experimental study of the surface formation of methane in interstellar molecular clouds*
D. Qasim, G. Fedoseev, K.-J. Chuang, J. He, S. Ioppolo, E.F. van Dishoeck and H. Linnartz,
Nat. Astron. (2020), in press 10.1038/s41550-020-1054-y

11. *Formation of complex molecules in translucent clouds: Acetaldehyde, vinyl alcohol, ketene, and ethanol via "nonenergetic"processing of C_2H_2 ice*
K.-J. Chuang, G. Fedoseev, **D. Qasim**, S. Ioppolo, C. Jäger, T. Henning, M.E. Palumbo, E.F. van Dishoeck and H. Linnartz,
Astron. Astrophys. 635 (2020) A199

10. *Formation of interstellar propanal and 1-propanol ice: a pathway involving solid-state CO hydrogenation*
D. Qasim, G. Fedoseev, K.-J. Chuang, V. Taquet, T. Lamberts, J. He, S. Ioppolo, E.F. van Dishoeck and H. Linnartz,
Astron. Astrophys. 627 (2019) A1

9. *Extension of the HCOOH and CO_2 solid-state reaction network during the CO freeze-out stage: inclusion of H_2CO*
D. Qasim, T. Lamberts, J. He, K.-J. Chuang, G. Fedoseev, S. Ioppolo, A.C.A. Boogert and H. Linnartz,
Astron. Astrophys. 626 (2019) A118

8. *Alcohols on the rocks: solid-state formation in a $H_3CC{\equiv}CH$ + OH cocktail under dark cloud conditions*
D. Qasim, G. Fedoseev, T. Lamberts, K.-J. Chuang, J. He, S. Ioppolo, J. Kästner and H. Linnartz,
ACS Earth and Space Chemistry 3 (2019) 986–999

7. *H_2 chemistry in interstellar ices: The case of CO ice hydrogenation in UV irradiated CO:H_2 ice mixtures*
K.-J. Chuang, G. Fedoseev, **D. Qasim**, S. Ioppolo, E.F. van Dishoeck, and H. Linnartz,
Astron. Astrophys. 617 (2018) A87

6. *Formation of interstellar methanol ice prior to the heavy CO freeze-out stage*
D. Qasim, K.-J. Chuang, G. Fedoseev, S. Ioppolo, A.C.A. Boogert, and H. Linnartz,
Astron. Astrophys. 612 (2018) A83

5. *Reactive desorption of CO hydrogenation products under cold pre-stellar core conditions*
K.-J. Chuang, G. Fedoseev, **D. Qasim**, S. Ioppolo, E.F. van Dishoeck, and H. Linnartz,
Astrophys. J. 853 (2018) 102

4. *Adsorption of water, methanol, and formic acid on Fe$_2$NiP, a meteoritic mineral analogue*
D. Qasim, L. Vlasak, A. Pital, T. Beckman, N. Mutanda and H. Abbott-Lyon,
J. Phys. Chem. C. 121 (2017) 13645–13654

3. *Formation of glycerol through hydrogenation of CO ice under prestellar core conditions*
G. Fedoseev, K.-J. Chuang, S. Ioppolo, **D. Qasim**, E.F. van Dishoeck, and H. Linnartz,
Astrophys. J. 842 (2017) 52

2. *Production of complex organic molecules: atom addition versus UV irradiation*
K.-J. Chuang, G. Fedoseev, **D. Qasim**, S. Ioppolo, E.F. van Dishoeck, and H. Linnartz,
Mon. Not. R. Astron. Soc. 467 (2017) 2552–2565

1. *The evolution of the surface of the mineral schreibersite in prebiotic chemistry*
N.L. La Cruz, **D. Qasim**, H. Abbott-Lyon, C. Pirim, A.D. McKee, T. Orlando, M. Gull,
D. Lindsay, and M.A. Pasek,
Phys. Chem. Chem. Phys. 18 (2016) 20160–20167

Curriculum Vitae

I was born in Kuwait City, Kuwait on December 29, 1989. My family returned to the US shortly after, where I spent most of my childhood and teenage years in Tucson, Arizona. In 2006, a high school friend forwarded me an application for the Women in Science and Engineering Program at the University of Arizona. I noted in the application that my two favorite classes were chemistry and astronomy, so they paired me with an astrochemist, graduate student Stefanie Milam (now Dr. Stefanie Milam at NASA Goddard Space Flight Center). From there, I developed a passion for astrochemistry. After high school, I enrolled in Northern Arizona University (NAU), where I majored in chemistry and minored in astronomy. During my university years, I participated in two Research Experience for Undergraduates internships: one at Arecibo Observatory and one at the National Radio Astronomy Observatory.

After graduating from NAU in May 2012, I accepted a PhD position at Emory University to specialize in astrochemistry. After a mere one year of enrollment, I was deemed unqualified to continue the graduate program and was immediately dismissed. Long story short, I did not agree with the way I was evaluated, and believed in myself that I could do better. Between the dismissal and entering a new graduate program, I worked at Kimberly-Clark Corporation as a microscopist, where I was trained in scanning electron microscopy and energy dispersive spectrometry. These skills would be later used towards my first publication in my master's.

For many reasons, I decided to enroll in a master's program, rather than a PhD program, at Kennesaw State University. There, I was supervised by Prof. Dr. Heather Abbott-Lyon to experimentally investigate the properties of a meteoritic mineral, schreibersite. This was part of a large collaborative effort with the Center for Chemical Evolution. During this period, I gained a lot of knowledge and within a friendly community, including how to perform ultrahigh vacuum science and how to share my research in public talks. I graduated with two publications – one first-author and one second-author. Such a positive experience gave me the motivation to try a PhD once again.

Dr. Stefanie Milam forwarded me the vacancy announcement for a PhD in the Leiden Laboratory for Astrophysics with Prof. Dr. Harold Linnartz. I was interviewed and then offered to work on SURFRESIDE. In the next years, I went on to publish 6 first-author papers and 5 co-author papers, including a first-author paper in the journal, *Nature Astronomy*. After the PhD, I will continue experimental astrochemistry research as a postdoctoral researcher at NASA Goddard Space Flight Center.

I am diagnosed with mixed receptive-expressive language disorder, which has somewhat impaired my ability to learn and communicate. It is my hope that this CV will motivate particularly those who have language disorders/learning disabilities and wish to pursue a higher education.

Acknowledgements

The Sterrewacht is a truly special place to be as a PhD student. We are encouraged to *work together* to solve problems, *help each other* become successful, and have a lot of fun while doing so! The faculty work hard to provide their students the resources they need to publish. These factors alone result in long-lasting collaborations, success, and friendships, and I will always be grateful to be part of such an exceptional community.

My particular success stands on the shoulders of Team SURFRESIDE within the Laboratory for Astrophysics. Our team is a prime example of those who collectively exploit their individual strengths to help one another achieve. Harold, words cannot express how much I have learned and gained from you as a rising professional in this field. I am a fortunate student to have had your 100% support in me from the beginning to the end. Ewine, you were always available to help me put my work into an astrochemical context, whether it was helping me dig through the literature or connecting me with someone in the field. I have also learned a lot from observing your leadership in astrochemistry on a global scale. Gleb, you were the catalyst to helping me finish my thesis well on time, as you tirelessly went through the details of the experiments, data analysis, and paper writing with me. Ko-Ju, you patiently trained me in experimental laboratory astrochemistry, and from this, I have grown to be confident as a laboratory astrochemist. Sergio, you helped me promote my research and myself as a researcher to the world by inviting and financially supporting me as a speaker to the events you held. Thanja, not only did you enhance my thesis work by contributing quantum chemical calculations, but you taught me theoretical concepts that I struggled to teach myself, and also how to join theory and experiments.

Aart and Martijn – you both were the people who made day-to-day life in the lab smoother. Aart, thank you for patiently helping me get through some very tedious and annoying issues that everyone encounters when working in the lab. Martijn, not only did you help me push through my most difficult (and rewarding) PhD project, but you did something I don't see often – you stood up for me in difficult situations, and I will always remember your courage. Marjan and the secretaries, thank you for being kind and helpful, especially in the beginning when I needed help transitioning from the US to Europe.

Adwin and Daniel – you both took on the very challenging task of training an experimentalist in ice observations, and the body of knowledge I acquired from working with both of you is priceless. Adwin, you went above and beyond as a collaborator, explaining every detail to me (usually halfway across the world), from mathematical derivations to programming in python to interpreting ice observational data. Daniel, you were always available to explain difficult concepts, and I always appreciated that I could ask you anything without feeling bad about it.

I am grateful to everyone in my first two years who made my transition to an entirely new environment welcoming, and to those in my last two years who